Development and applications of new fluorescence techniques to characterize single biomolecules in solution and living cells

Thesis

Department of Mathematics and Natural Sciences
Heinrich-Heine University Düsseldorf

Volodymyr Kudryavtsev
from Kiev
December 2006

Institute of Molecular Physical Chemistry,

Heirich-Heine University Düsseldorf

Printed with the permission of
Department of Mathematics and Natural Sciences
Heinrich-Heine-University Düsseldorf

1. Referee:	Prof. Dr. C.A.M. Seidel
2. Referee:	Prof. Dr. Filipp Oesterhelt

Date of the oral examination: 31.01.2007 to my family

Acknowledgments

This work was carried out under the supervision of Prof. Dr. Claus A. M. Seidel at the Institute of Molecular Physical Chemistry, Heinrich Heine University of Düsseldorf. I would like to take this opportunity to thank all the people who supported me and made this thesis possible.

First, I would like to extend my sincere gratitude to my supervisor, **Prof. Dr. Claus A. M. Seidel**. His sharp eye revealing hidden details, great analytical skills and enthusiasm were the foundation of this work. I'm thankful for his encouragement and fruitful ideas, tolerance and patience.

I gratefully acknowledge

Dr. Suren Felekyan. His support was invaluable not only in science, but also in life experience. It started from the first day of this work and continued until the present. I'm thankful for helpful theoretical discussions on single-molecule analysis, help with programming, his patience and plenty of wise advice. I was happy to learn a lot about Armenian culture and history.

Dr. Ralf Kühnemuth for sharing with me his knowledge and experience, useful discussions, constructive criticism, helpful suggestions and comments.

Alessandro Valeri for interest in my work, helpful discussions and support, patience and sharp sense of humour. It was a big pleasure to work and to live together with you.

Dr. Stanislav Kalinin for sharing with me his knowledge and for helpful theoretical discussions. His valuable suggestions made possible progress in the most difficult parts of this work. I've also enjoyed a lot joint bicycle trips and social activities.

Dr. Alexandr Gaiduk for interest in my work, valuable suggestions, theoretical discussions and constructive criticism of my photos.

Dr. Matthew Antonik, for guidance in Labview programming, useful tricks and exciting discussions on scientific and general subjects.

Prof. Dr. Filipp Oesterhelt for interest in my work, inspiration and helpful advice and suggestions.

Dr. Enno Schweinberger for helpful discussions, guidance in single molecule spectroscopy and exciting free-time activities: sports, fishing, parties.

Dr. Marcelle König and Dr. Anna Wozniak who have provided me advice and inspiration. I'm also thankful to them for organizing social activities.

Martin Schramm for always being nice and positive, helping me with electronic devices and bikes.

Carl Sandhagen and Marcel Merkwitz for help with electronic devices and computers.

Prof. Dr. Claus A. M. Seidel, Dr. Suren Felekyan, Dr. Steven Magennis, Dr. Stanislav Kalinin, Dr. Ralf Kühnemuth, Alessandro Valeri, Dr. Alexandr Gaiduk for reading this thesis**,** helpful comments and constructive critics, which brought this work to the final stage.

Prof. Dr. Jerker Widengren from Stockholm for fruitful collaboration in the project "Identification of multiple species by MFD".

Dr. Manuel Diez, Dr. Boris Zimmermann, Stefan Steigmiller and Dr. Michael Börsch for fruitful collaboration in the investigation of ATP synthase.

I would like to thank all my colleagues for these years when they were always helpful and friendly: **Bärbel Hoffman, Veronika Mendorf, Dr. Manuel M. Lohrengel, Stefan Marawske, Denis Dörr, Daniela Pfiffi, Richard Janissen, Dr. Aike Stortelder, Dr. Peter Karageorgier, Heike Hornen, Stephanie Rehwald, Andreas Renner, Sebastian Overmann, Ming Chang Tsai, Ralf Müller, Opas Tojira, Dr. Nathan Zeitlin, Dr. Sylvia Berger, Dr. Pierre-Alain Müller, Margarita Gerken, Harekrushna Sahoo.**

Finally, I want to extend my greatest gratitude to my family for support and encouragement and during all these years. I'm especially grateful to my farther, Prof. Dr. Yuri V. Kudryavtsev for plenty of helpful advice and criticism.

Volodymyr Kudryavtsev, December 2006

This thesis is based on the following papers:

Multiparameter Fluorescence Imaging to Monitor Dynamic Systems

Kudryavtsev, V., Felekyan, S., Wozniak, A. K., König, M., Sandhagen, C., Kühnemuth, R., Seidel, C. A. M, Oesterhelt, F., 2007,: Anal.Bioanal.Chem, v. 387, p. 71–82.

Single-molecule detection and identification of multiple species by multiparameter fluorescence detection.

Widengren, J., Kudryavtsev, V., Antonik, M., Berger, S., Gerken, M., Seidel, C. A. M. 2006, Analytical Chemistry, v. 78, p. 2039-2050.

Full correlation from picoseconds to seconds by time-resolved and time-correlated single photon detection

Felekyan, S., Kühnemuth, R., Kudryavtsev, V., Sandhagen, C., Becker, W., Seidel, C. A. M. 2005,: Review of Scientific Instruments, v. 76, p. 083104-1-083104-14.

Proton-powered subunit rotation in single membrane-bound F_0F_1-ATP synthase

Diez, M., Zimmermann, B., Börsch, M., König, M., Schweinberger, E., Steigmiller, S., Reuter, R., Felekyan, S., Kudryavtsev, V., Seidel, C. A. M., Gräber, P. 2004, Nature Structural & Molecular Biology, v. 11, p. 135-141.

Time-resolved photon counting allows for new temporal and spatial insights into the nanoworld

Gaiduk, A., Kühnemuth, R., Felekyan, S., Antonik, M., Becker, W., Kudryavtsev, V., König, M., Oesterhelt, F., Sandhagen, C., and Seidel, C. A. M. Proceedings of SPIE – v. 6372.

Oral talks at international conferences:

Applications of multiparameter fluorescence detection (MFD) in chemical analysis

12th International Workshop on "Single Molecule Spectroscopy and Ultra Sensitive Analysis in the Life Sciences" September 20-22, 2006, Berlin, Germany

Posters at international conferences:

Single molecule detection and identification of multiple species by multiparameter fluorescence detection

Volodymyr Kudryavtsev, Jerker Widengren, Margarita Gerken, Sylvia Berger, Claus A M Seidel

9th International Conference on Methods and Applications of Fluorescence (MAF-9), September 04 – 07, 2005, Lissabon, Portugal

Mechanisms of membrane fusion studied by singlemolecule FRET and single-molecule fluorescence images

Volodymyr Kudryavtsev, Marcelle Koenig, Enno Schweinberger, Jerker Widengren, Christina Schuette,Suren Felekyan, Ralf Kuehnemuth, Reinhard Jahn, Claus Seidel

4th International Symposium on Physics, Chemistry & Biology with Single Molecules

February 22-25, 2004, Kloster Banz, Germany

Conformational dynamics of special nucleic acid structures studied by single molecule FRET

AlessandroValeri, Enno Schweinberger, Volodymyr Kudryavtsev, Marcelle König, Pierre-Alain Muller, Rüdiger Dede, Suren Felekyan, Claus A. M. Seidel

9th International Workshop on "Single Molecule Detection and Ultra Sensitive Analysis in the Life Sciences" September 24-26, 2003, Berlin, Germany

Combining FCS and TCSPC: New developments and applications

R. Kühnemuth, S. Felekyan, V. Kudryavtsev, C. Sandhagen, R. Müller, W. Becker and C.A.M. Seidel
10th International Workshop on "Single Molecule Detection and Ultra Sensitive Analysis in the Life Sciences" September 22-24, 2004, Berlin, Germany

Conformational dynamics of special nucleic acid structures studied by single-molecule FRET

V. Kudryavtsev, M. Konig, E. Schweinberger, R. Muller, P.-A. Muller, R. Dede, S. Felekyan, C.A.M. Seidel

8th International Workshop on "Single Molecule Detection and Ultra Sensitive Analysis in the Life Sciences" September 25-27, 2002, Berlin, Germany

Content

1 Introduction

To understand the functions and underlying mechanisms of biological macromolecules, structural and dynamic information of the molecules is required. Nuclear magnetic resonance (NMR) and X-ray crystallography give excellent structural information, but need high amounts of material and give no or very poor dynamic information. Over the last decades, fluorescence-based techniques have become more and more popular for studying biological activities at the single-molecule level. Single-molecule experiments eliminate ensemble averaging and provide direct information on the heterogeneity and kinetics of the system [Kühnemuth and Seidel, 2001]. Distributions of different species in specific states in heterogeneous systems become directly accessible. (Fig.1-1).

Since the first successful experiments on single-molecule detection by optical methods [Hirschfeld, 1976] [Moerner and Kador, 1989], experimental and analytical techniques have significantly improved and at present enable not only fundamental studies of dynamic and conformational properties of single biomolecules[Moerner and Fromm, 2003], but also offer the potential to establish molecular profiles of species present at very low concentrations or quantities.[Anazawa et al., 2002] [Herten et al., 2000] [Knemeyer et al., 2000] [Tinnefeld and Sauer, 2005].

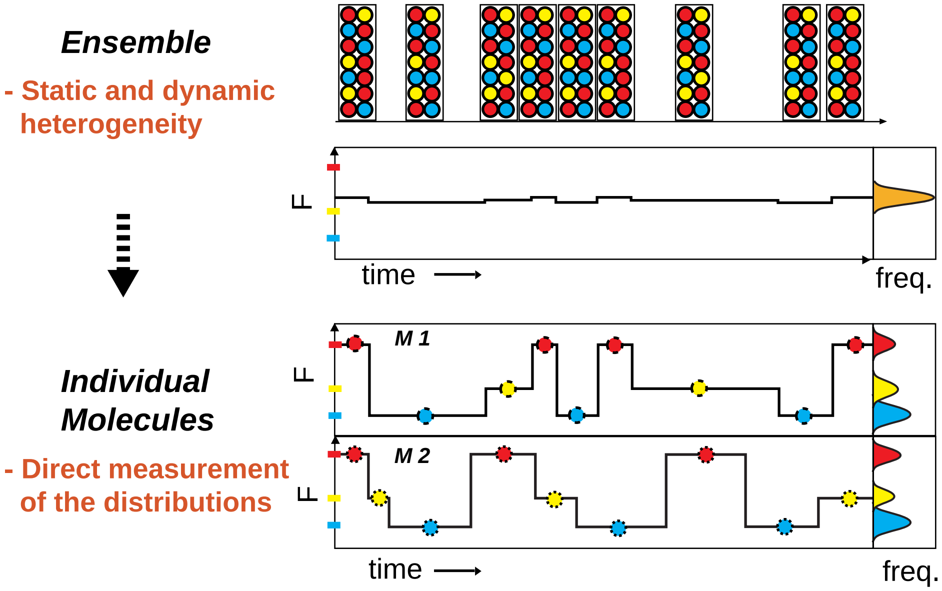

Figure 1-1. Separate detection of individual molecules avoids obscuring by ensemble averaging of unsyncronized state or species dependent properties [from [Kühnemuth and Seidel, 2001]].

Considering molecular systems, changes in fluorescence parameters of a single coupled fluorophore sometimes do not provide enough information for molecular identification or for more detailed investigations of molecular interactions. Further information can be obtained on a single molecule level by having more than one fluorophore per particle involved, thereby increasing the possibilities to determine stoichiometries and interactions of individual particles from photon densities and coincidences[Schmidt et al., 1996] [Weston et al., 2002] Moreover, the use of two fluorescing reporters also makes it possible to determine structural features of particles via fluorescence resonance energy transfer (FRET), quantitatively described by Förster [Förster, 1948]. In FRET energy is transferred from a donor to an acceptor dye. The efficiency of this process depends on the distance between the two dyes and therefore FRET provides a sensitive tool to yield inter and intramolecular distance information. In practice, FRET has frequently and successfully been used to investigate biomolecular structures and to follow dynamic processes, including motor proteins at work, protein and nucleic acid structure fluctuations, and molecular assembly and disassembly. The distances that are accessible with FRET are in the range of 20-100 Å. This distance range matches the dimensions of many biologically relevant molecules. Additionally, the molecules can be studied under physiological conditions, controlling temperature and environment. In general fluorescence techniques are very sensitive, thus FRET measurements need only small amounts of sample and artificial interactions between the molecules under investigation due to high concentrations are avoided. Molecules labelled with a donor or an acceptor only can lead to a wrong calculation of the FRET efficiencies in ensemble measurements. In contrast, single molecule measurements allow them to be distinguished from correctly double labelled ones and be analysed separately. And last but not least the devices needed to perform fluorescence measurements are cheap and easy to handle compared to X-ray or NMR-experiments.

Fluorescence microscopy is a sensitive, specific and non-invasive method that allows one also to assess biochemical information in living cells [Wouters et al., 2001]. Multiparameter Fluorescence Imaging (chapter 4), the combination of confocal microscopy with multi channel, time resolved single-photon counting, makes it possible to gather the complete accessible spectroscopic information in each pixel of an image. The combination of imaging methods with spectroscopic analysis allows one to collect many parameters simultaneously and thus increases the information content per image, which often is crucial for a correct conclusion of functional information.

This work presents an advanced multiparameter fluorescence detection (MFD) technique (experimental and analysis details are described in chapter 2). MFD is now established as a technique in single-molecule fluorescence spectroscopy that allows the simultaneous detection of multiple fluorescence parameters. The spectral properties of absorption and fluorescence, $F(\lambda_A, \lambda_F)$, fluorescence brightness and quantum yield, Φ_F, fluorescence lifetime, τ, [Bowen et al., 2004] [Edman et al., 1996] [Enderlein et al., 1997] [Enderlein and Sauer, 2001] [Maus et al., 2001] [Tellinghuisen et al., 1994] and fluorescence anisotropy, r, [Schaffer et al., 1999] are the five intrinsic properties of a fluorophore that are accessible in a MFD experiment (see Fig. 1.2). These "chromophore parameters" can be deduced from the time-resolved detection of the five observables of the chromophore, which now serves as a tool to report on its local environment. Moreover there are at least three system parameters such as fluorophore separation (FRET), time evolution of the system, and absolute intensity measuring fluorophore concentration.

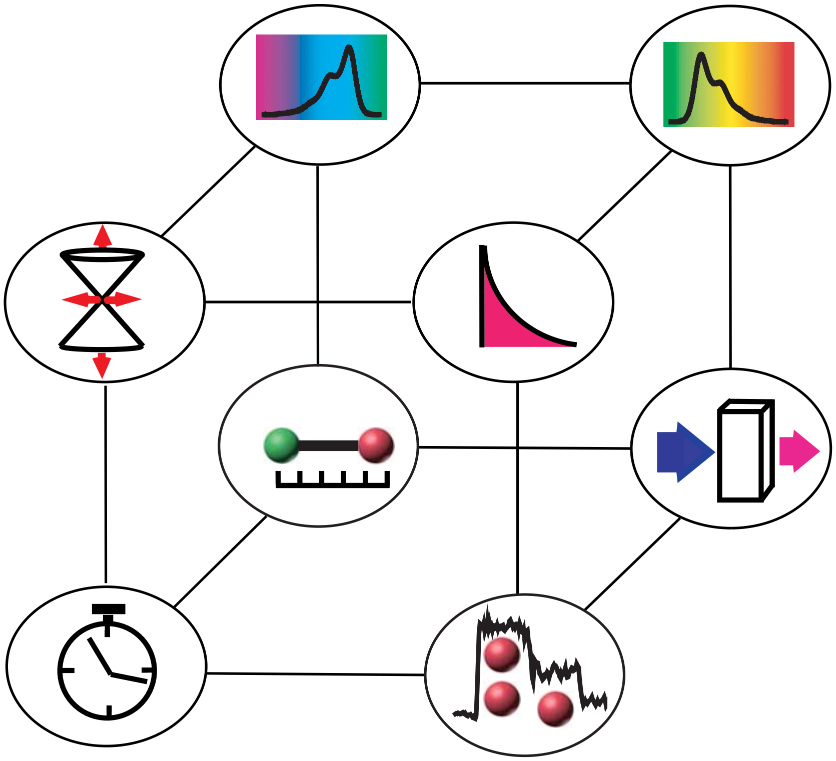

Figure 1.2 Multiple dimensions of fluorescence. Sketches for fluorescence properties at the front face of the cube (starting at the upper left corner with clockwise rotation): fundamental anisotropy, fluorescence lifetime, fluorescence intensity, time; back face: excitation spectrum, fluorescence spectrum, fluorescence quantum yield, and distance between fluorophores.

In this work, MFD was successfully applied on the single molecule level to study freely diffusing molecules in solution (chapter 3) and was combined with an imaging technique to study living cells (chapter 4). It is shown that with MFD it is possible to identify and separate 16 different compounds in a mixture of FRET-labelled oligonucleotides (Chapter 3.1). Such multiplexed assays with single-molecule sensitivity may have a great impact on the screening of species and events that don’t lend themselves so easily to amplification, such as disease-specific proteins and their interactions [Sauer et al., 1997] [Scheffler et al., 2005]. MFD can also deliver detailed information on specific molecular dynamic processes. Investigation of the F_0F_1-ATP synthase subunit rotation during ATP hydrolysis and synthesis is presented in chapter 3.2

Fast movements of fluorescently-labelled molecules can be studied via their resulting signal fluctuations in confocal measurements. Many different methods have been developed to derive information about the molecular dynamics from these fluctuations [Thompson et al., 2002]. As well as the molecule’s mobility parameters, Fluorescence Correlation Spectroscopy (FCS) reveals molecular concentrations, and 2-color Fluorescence Cross Correlation Spectroscopy (FCCS) allows one to detect molecular interactions [Bacia and Schwille, 2003]. FCS can be applied to covalently-labelled molecules or to inherently fluorescent molecules, such as fluorescent proteins [Kohl and Schwille, 2005]. When applying the technique to cells, auto fluorescence background has to be taken into account to obtain correct concentrations [Brock et al., 1998]. It was shown that two-photon excitation (2PE) minimizes photobleaching in spatially restrictive cellular compartments and thereby preserves long-term signal acquisition [Schwille et al., 1999]. In cases where diffusion is restricted to small cytosolic compartments, this has to be considered in the calculation of mobility parameters. Different models have been developed to account for the effect [Gennerich and Schild, 2000].

Instead of analysing the intensity fluctuations at a fixed position, it is possible to scan the focus through the sample while detecting the fluctuating signal. The fluctuations now contain both temporal and spatial information about the sample. The analysis of the fluorescence signal from a circular moving detection volume by scanning the laser beam was used to determine the direction and speed of a flowing dye solution, and the position of immobilized particles [Skinner et al., 2005]. Scanning FCS was also applied to the analysis of surface bound molecules [Xiao et al., 2005] and membrane dynamics [Ruan et al., 2004], and can be used as a tool for testing the resolution and sensitivity of a confocal microscope [Balaji and Maiti, 2005].

Images obtained with a standard laser scanning microscope contain a time structure that can be exploited to measure dynamics of molecules in solution and in cells [Rocheleau et al., 2003]. Image correlation spectroscopy (ICS) analyses the temporal and spatial correlation between neighbouring pixels or successive images and allows molecular diffusion constants on the microsecond to second timescale to be calculated [Digman et al., 2005b] [Digman et al., 2005a]. Due to the spatial information of the diffusion, the direction of molecular movements can also be determined. This was applied to GFP-labelled membrane proteins for protein velocity mapping [Hebert et al., 2005] [Kolin et al., 2006].

FCS has proven to be a powerful technique with single-molecule sensitivity. Recently, it has found a complement in the form of fluorescence intensity distribution analysis (FIDA), which has been very successful in biotechnology and bioanalytics [Fries et al., 1998] [Kask et al., 1999] [Kask et al., 2000] [Palo et al., 2000] [Palo et al., 2002]. There are several combinations of FIDA with other techniques, such as FILDA (time-correlated single photon counting) und FIMDA (FCS). FIDA is especially suitable for calculating precise brightness values of species, even in a complex mixture.

The common technique for FCS recording is the ‘hardware correlator’. The device registers single photon events with a time-resolution in the nanosecond range and correlates the detection times in an internal signal processor. The standard technique for fluorescence lifetime and antibunching experiments is time-correlated single photon counting (TCSPC) [O'Connor and Phillips, 1984]. Both techniques can, of course, be used in combination to obtain independent FCS and lifetime data for the dye and protein under investigation.[Heikal et al., 2000] [Schwille et al., 2000] The drawback is that the lifetime data are not obtained from exactly the same molecules as the FCS data, and lifetime fluctuations cannot be correlated with the fluctuations in the FCS data.

Fully parallel recording of FCS / FCCS and fluorescence lifetime information or antibunching requires a technique that records the fluorescence photons in several independent detection channels and covers a time range of many seconds with picosecond resolution. Furthermore, it must record photon rates up to several 10^5 /s virtually without counting loss.

In this work an advanced TCSPC technique is presented. It was developed in recent years[Becker et al., 2001a] [Becker et al., 2001b] [Becker et al., 2002] [Felekyan et al., 2005] and has now been extended to the recording of FCS, FCCS, fluorescence lifetime and antibunching effects (chapters 2.1, 5).

2 Multiparameter Fluorescence Detection (MFD)

2.1 Experimental setup

2.1.1 Optical setup

During this work four-channel setup based on an Olympus IX70 inverted microscope was used (Fig. 2.1-1) It is described in detail [Eggeling et al., 1998a] [Gaiduk, 2006] [König, 2005]. Freely diffusing molecules can be excited with either argon-ion laser, or krypton ion laser (both provided by Sabre, Coherent). Continuous and pulsed light at different wavelengths is available. Pulsed excitation at a rate of 73.5 MHz with a 200 ps pulse time is obtained with an acoustooptic active modelocker (APE, Berlin). After reflection by a dual-band dichroic mirror, the laser beam is focused by a microscope objective. The fluorescence is collected and then refocused by the same objective to the image plane, where a pinhole is placed.

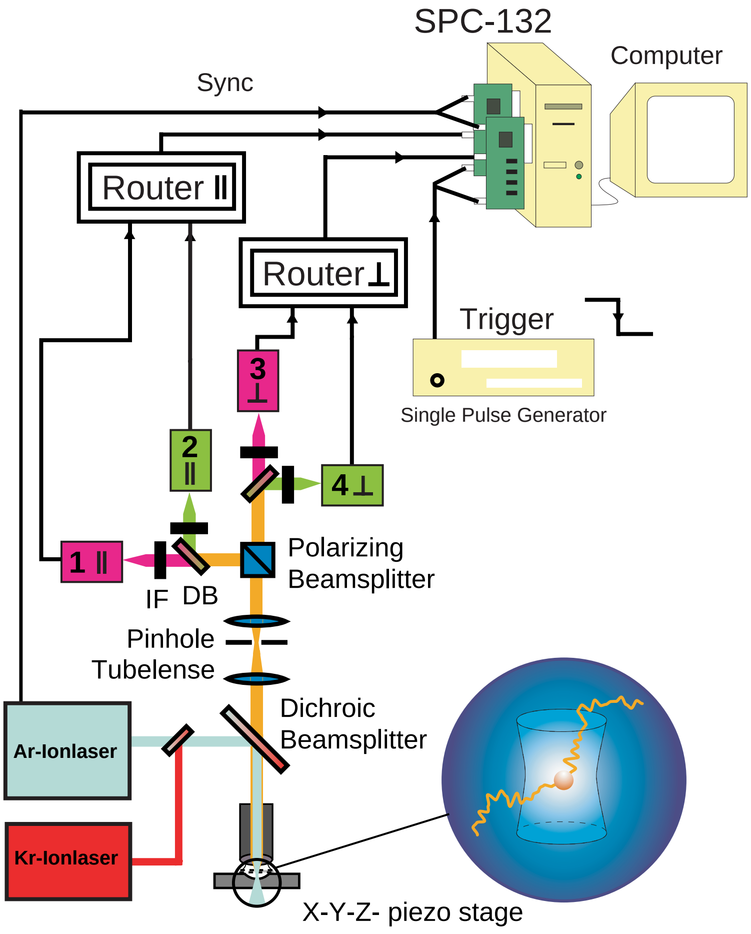

Figure 2.1-1 Four-channel (detectors 1-4) confocal setup. Details are given in text.

After passage through the pinhole, the fluorescence is first separated by a polarizing beam spleatter into parallel and perpendicular components in respect with the laser beam and then divided by a dichroic beam splitter into green and red fractions. Subsequently, band-pass filters are used to discriminate the collected fluorescence of certain spectral range. Detectors (avalanche photodiodes (SPCM-AQR, Perkin-Elmer, USA)) are described in Chapter 2.1.4, the output pulses of which are processed by TCSPC technique (see Chapters 2.1.2-2.1.3).

Scanning. For the generation of MFD images, the sample was moved in a step-wise manner relative to the confocal volume. For this purpose, the sample was mounted on a closed loop piezo-controlled x-y-scanner (Physik Instrumente, Germany) and moved perpendicularly to the optical axis. Accordingly, the pixel size is defined by the step size of the scanning. The resolution is restricted by diffraction and by incomplete illumination of the objective. The diameter of the detection volume is approximately 550 nm for the experiments presented. Back reflection of the laser light from the surface of the cover glass is used for z-position adjustment. The confocal volume is manually positioned in the centre of the object. The scanning process is controlled via a Visual C++-based program. The program generates additional electronic pulses at the moment of pixel and row leaps, which are saved in two supplementary router channels of the SPC 132 board. These signals enable a reconstruction of the picture and the individual evaluation of the photons in each pixel.

2.1.1.1 Optical setup settings for chapter 3.1

Samples were excited by a pulsed, linearly polarized argon-ion laser emitting at 514 nm (Innova Sabre, Coherent) with a repetition rate of 73,5 MHz and an excitation power of 558 μW. After reflection by a dual-band dichroic mirror (DCLP510, AHF Analysentechnik) the laser beam is focused by a microscope objective (Olympus 60 x, NA 1.2, water immersion). The fluorescence is collected and then refocused by the same objective to the image plane, where a pinhole is placed (radius 100 μm). From a FCS diffusion time of freely diffusing Rhodamine 6G (Rh6G) dye of $\tau_D = 256$ μs the detection volume can be estimated to be approximately 3 fl. After passage through the pinhole, the fluorescence is separated by a polarizing beam splitter into parallel and perpendicular components with respect to that of the laser beam. The fluorescence is then divided by a dichroic beam splitter (510DCLX, AHF Analysentechnik) into the fractions originating from the acceptor (Cyanine 5 (Cy5) or

BODIPY650 (BP 650/665)) and donor (Cyanine 3 (Cy3) or Rh6G) fluorophores. Subsequently, band-pass filters are used (HQ730/140 AHF Analysentechnik) for Cy5 and BP 650/665 and (HQ575/70 AHF Analyzentechnik) for Cy3, Rh6G to discriminate the two fractions of the collected fluorescence. Each of the fractions of the fluorescence light is then detected by an avalanche photodiode (SPCM-AQR-14, Perkin Elmer, Canada), the output pulses of which are processed online by a TCSPC-card with a routing unit (SPC 432 Becker&Hickl GmbH, Berlin, Germany).

2.1.1.2 Optical setup settings for chapter 3.2

The samples with Rh110 dye were excited with the 496,5 nm line of a linearly polarized, pulsed argon ion laser (Innova Sabre, Coherent), which was focused in an inverted microscope (IX 70, Olympus, Germany) using a 60x water immersion objective (NA=1.2). The emitted light was collected in the same objective and successively separated into its parallel and perpendicular polarisation (VISHT11, Gsänger, Germany) and into its green and red component (beam splitter 595DCLX, AHF, Germany). The detected spectra are limited by using bandpass filters, HQ 535/50 in the green and HQ 720/150 in the red spectral range, respectively (Chroma Technologies, USA). A confocal pinhole is 150 μm diameter, confocal detection volumes of 2.5 fl was used., The photons were detected by avalanche photodiodes (SPCM-AQR-14, Perkin Elmer, Canada) and counted with PC plug-in TCSPC card (SPC 432, Becker&Hickl, Germany).

2.1.1.3 Optical setup settings for chapter 4

The samples were excited with the 476.5 nm line (yeast cells) or the 496nm line (glutathione-sepharose beads) of a linearly polarized, pulsed argon ion laser (Innova Sabre, Coherent), which was focused in an inverted microscope (IX 70, Olympus, Germany) using a 60x water immersion objective (NA=1.2). The emitted light was collected in the same objective and successively separated into its parallel and perpendicular polarisation (VISHT11, Gsänger, Germany) and into its green and red component (beam splitter 595DCLX, AHF, Germany). The detected spectra are limited by using bandpass filters, HQ 533/46 in the green and HQ 730/140 in the red spectral range, respectively (Chroma

Technologies, USA). A confocal pinhole is 60 μm diameter The photons were detected by avalanche photodiodes (SPCM-AQR-14, Perkin Elmer, Canada) and counted with PC plug-in TCSPC cards (SPC132, Becker&Hickl, Germany).

2.1.1.4 Optical setup settings for chapter 5

The fluorescent molecules are excited by a linearly polarized argon-ion-laser (Innova Sabre, Coherent) at 496 nm, either active-mode-locked (73.5 MHz, 150 ps) or in cw mode. The HF-source for the mode-locker serves as the common time base for sync (TAC stop signal) and the macro time counter for both SPC-132 counting boards. The laser light is focused into the sample by a NA = 1.2 water-immersion objective lens (UPLAPO 60x, Olympus, Hamburg, Germany).

The fluorescence is collected by the same lens and separated from the excitation by a polychroic beamsplitter (488/636 PC, AHF, Tübingen, Germany). A confocal pinhole of 100 μm diameter and the slightly underfilled objective yield a detection volume element of approximately 1 μm diameter and 3 fl size. The collected fluorescence photons are divided first into its parallel and perpendicular components by a polarizing beamsplitter cube (VISHT11, Gsänger, Planegg, Germany), then by dichroic beamsplitters (Q 595 LPXR, AHF) into wavelength ranges below and above 595 nm. Fluorescence bandpass filters (HQ533/46, AHF) block residual laser light and reduce Raman scattering from the solvent.

The detectors used were photomultiplier tubes with GaAsP photokathodes (H7422P-40, Hamamatsu, Germany) or single photon avalanche diodes (SPCM-AQR-14, Perkin Elmer, Canada).

2.1.2 Time-Correlated Single Photon Counting (TCSPC)

Conventional time-correlated single photon counting technique is used for the registration of MFD data. It is based on the measurement of the detection times of individual emitted photons with respect to the time of the excitation. Excitation is achieved with a periodical light source.[O'Connor and Phillips, 1984] This technique has a number of striking benefits:

- The time resolution of TCSPC is limited by the transit time spread, not by the width of the output pulse of the detector. Even early TCSPC systems delivered an instrument response of less than 60 ps full width at half maximum (FWHM).
- TCSPC has a near-perfect counting efficiency and therefore achieves optimum signal-to noise ratio for a given number of detected photons.[Ballew and Demas, 1989] [Carlsson and Philip, 2002] [Köllner and Wolfrum, 1992]

The TCSPC device used for this work is shown in Fig. 2.1-2. One or several light signals are detected simultaneously by a number of photomultiplier tubes (PMTs) or single-photon avalanche photodiodes (SPADs). The recording of the signals is based on the general presumption of TCSPC that the detection of several photons per signal period is unlikely. Under this condition simultaneous detection of several photons in different detectors can be considered unlikely as well. Therefore, the single-photon pulses of all detectors can be processed by a single TCSPC channel. A 'router' combines the single photon pulses in one common timing pulse line, and, simultaneously, delivers a digital 'channel' signal that indicates which detector delivered the current photon pulse [Becker et al., 2001b]. When the TCSPC device detects the photon pulse it writes the corresponding channel word into a channel register. Several additional bits can be read simultaneously with the channel word and be used to synchronize the recording with the experiment.

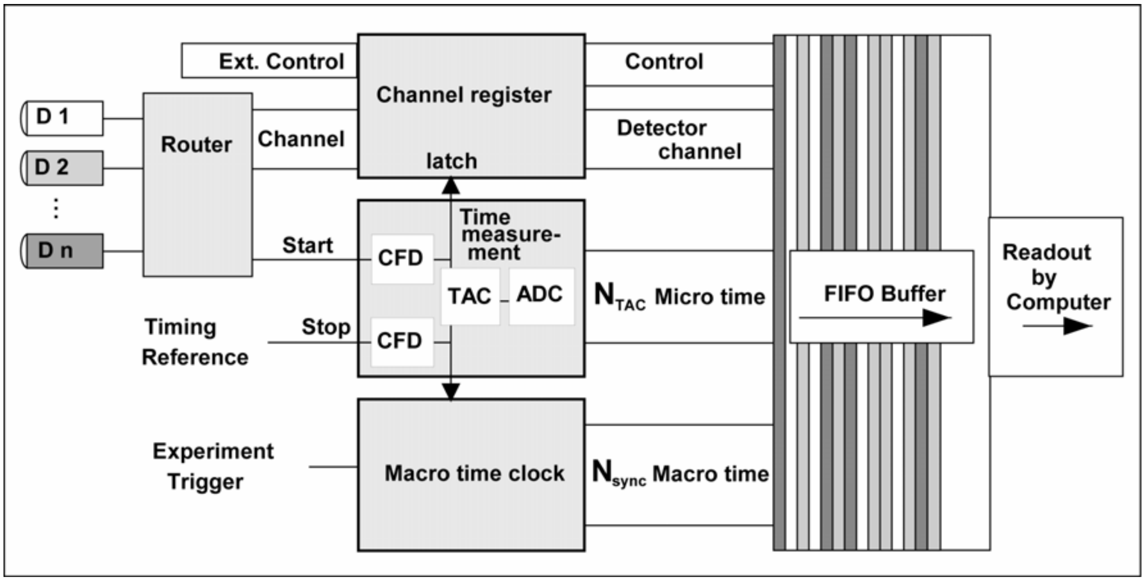

Figure 2.1-2. Block diagram of one TCSPC channel. D1 through Dn - detectors, CFD - constant fraction discriminator, TAC - time-to-amplitude converter, ADC - analog-to-digital converter .

The single photon pulses from the detectors are used as start pulses for the time-measurement block. The time-measurement block employs the traditional architecture of TCSPC. The single-photon pulses and the timing-reference pulses are fed through constant-fraction discriminators, CFD, to remove the amplitude jitter from the timing information. The time between the single-photon pulses and the timing reference is converted into a voltage by a time-to amplitude converter, TAC. The voltage delivered by the TAC is converted into a digital data word by the analog-to-digital converter, ADC. The delivered data word defines the micro time, i.e. the arrival time of the detected photon relative to the reference pulse, by the specified number of micro time channels, N_{TAC}. The width of a micro time channel is usually a few picoseconds. The high speed is obtained by a modified dithering technique. The technique adds an auxiliary signal to the ADC input, which is later subtracted from the output data word. Each photon signal is therefore converted at a different location on the ADC characteristic, resulting in a cancellation of the non-uniformity of the channel width [Becker et al., 1999] [Becker et al., 2001b]. Consequently, the accuracy requirements to the ADC are relaxed, and extremely fast ADC chips can be used. Together with a speed-optimized TAC a dead time down 100 ns is reached.

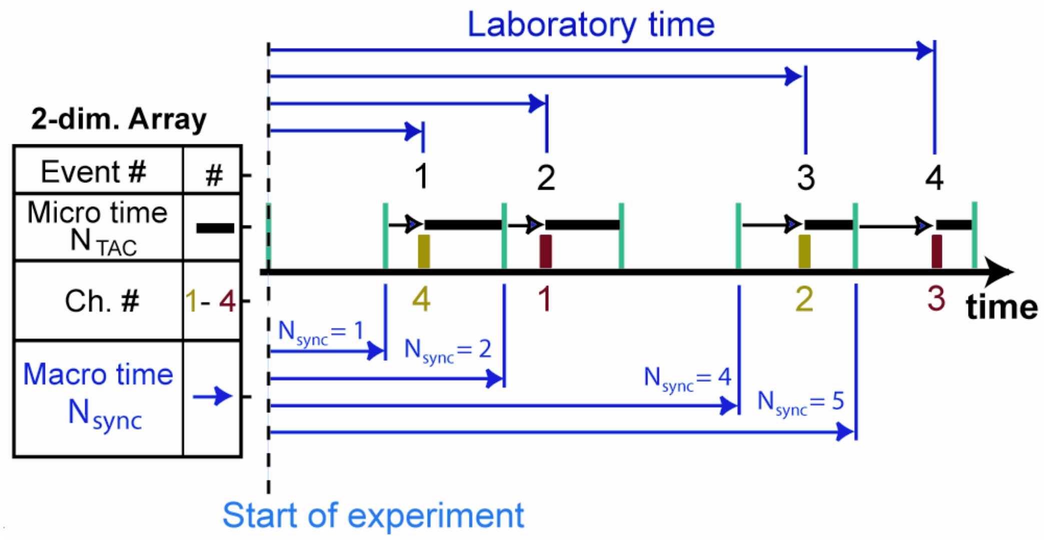

Figure 2.1-3 Data structure in FIFO mode. For each photon micro time (TAC channel N_{TAC}), macro time (sync counter N_{sync}) and detection channel number are recorded.

The laboratory time elapsed from the start of the experiment is obtained by combining the micro and macro time information of the measurement (Fig. 2.1-3). The macro time is measured by the number of periods of a clock oscillator, or, alternatively, the number of TAC stop periods from an external "experiment trigger" pulse, N_{sync}.

The memory of the TCSPC device is configured as a first-in-first-out (FIFO) buffer. When a photon is detected the micro time, the macro time, and the data in the channel register are written into the FIFO. The output of the FIFO is written continuously, and the data are written into the memory or on the hard disc of the host computer.

In many applications the counting efficiency of the recording system is an important parameter. There are several ways a TCSPC setup may lose photons. The most obvious one is the limited efficiency of the optical system and of the detector. The TCSPC device itself may lose photons by the classic pile-up effect, and by counting loss in the dead time after the recording of a previously detected photon.

The dead time in typical TCSPC devices is ‘non paralyzing’, i.e. a photon lost in the dead time of a previous one does not cause new dead time. Moreover, for a TAC stop period shorter than the dead time the counting efficiency covers both the loss by the dead time and the loss by pile-up. For a continuous input signal the counting efficiency, E, is given by the ratio of the recorded count rate, r_{rec}, and the detected count rate, r_{det}, and can be related to the dead time t_d. [Datasheet Single Photon Counting Module, SPCM-AQR Series04] [Becker, 2005]:

$$E = \frac{r_{rec}}{r_{\det}} = \frac{1}{1 + r_{\det} t_d} \quad , \tag{Eq. 2.1}$$

The dead time of the TCSPC modules used for this work is 100 to 125 ns. In a single molecule experiment the burst count rates under reasonable excitation conditions usually don't exceed $5 \cdot 10^5$ s^{-1}, the maximum count rates in the presented data were $3 \cdot 10^5$ s^{-1}. The corresponding counting loss is 5 to 6% and does therefore not result in noticeable distortion of the results.

Another non-ideal effect to be considered is the distortion of the photon distribution by pile-up. Pile-up is caused by the detection of a second photon within one TAC stop period. For a single-exponential fluorescence decay, the pile-up adds virtual lifetime components of τ/2, τ/3...τ/n to the correct lifetime, τ. [Becker, 2005]. The resulting mean intensity-weighted lifetime is approximately

$$\tau_{meani} \approx \tau \left(1 - p/4\right) \quad \text{for}\, p < 0.1, \tag{Eq. 2.2}$$

with p being the average number of photons per TAC stop period. For the TAC stop period of 13.6 ns used in the experiments described below the pile-up results in a lifetime error of less than 0.2 % up to the highest expected count rates in a burst of $5 \cdot 10^5$ s^{-1}.

2.1.3 Dual-Channel TCSPC Setup

A single TCSPC channel of the architecture shown in fig. 2.2 is unable to correlate photons of different detectors within times shorter than the dead time. Correlation of shorter times can, in principle, be obtained by giving the signals different delays[Weston et al., 2002]. If the delay difference for the individual detectors is larger than the dead time of the board, then photons that are detected simultaneously can be recorded separately. However, the photons must be identified by their macro time differences, which is only possible if the count rate is low. However, continuous correlation from the time scale of antibunching to the time scale of diffusion effects is not obtained this way.

To overcome these limitations two synchronized TCSPC boards (SPC-132, custom design, two modified boards of a four board SPC-134 system, Becker & Hickl, Berlin) were combined in one setup [Felekyan et al., 2005]. It is shown in Fig. 2.1-4.

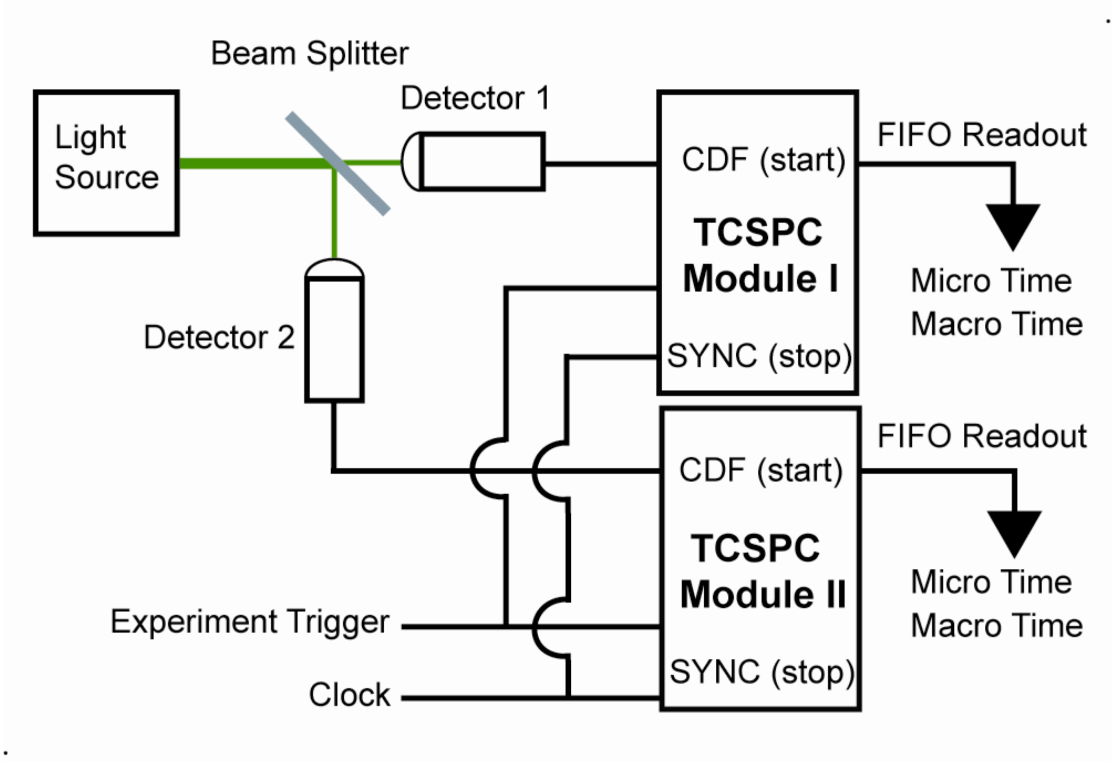

Figure 2.1-4. Dual module setup with synchronized data acquisition.

The events detected in the two detectors are processed in separate TCSPC boards. Both modules use the same timing reference signal at their TAC stop inputs. For experiments with pulsed excitation the timing reference signal is derived from the laser pulse sequence. For continuous excitation an artificial reference signal from a pulse generator was used.

To obtain synchronized, i.e. comparable macro times in both channels the macro time clocks of both channels must be driven by the same clock source. Moreover, the recording must be started synchronously in both channels. TAC stop signal was used as a mother clock of the macro time and start both channels synchronously via their experiment trigger inputs. Thus, every photon is assigned to a defined TAC stop period. The events recorded in both modules are used to calculate a single cross correlation function on a continuous laboratory time scale from picoseconds to milliseconds or seconds, the length of the continuous single photon traces only being limited by the computer memory. This calculation is described in [Felekyan et al., 2005].

2.1.4 Detectors

In general, detectors for TCSPC should have a gain high enough to resolve single photon events, a short transit time spread, and high quantum efficiency. The detector gain and the intrinsic delay must be stable up to a count rate of several 10^6 photons per second. For fluorescence correlation, the quantum efficiency is even more essential. When the detection events are correlated the number of coincidences per time interval drops with the square of the photon number. Thus, the signal-to-noise ratio of the correlation spectrum depends linearly on the rate of photons - not on the square root as for a fluorescence decay curve. Another complication is afterpulsing. Almost any detector has an increased probability to deliver a background pulse for some time after the detection of a photon. Afterpulsing in PMTs is caused by ion feedback and probably dynode fluorescence and glass scintillation. In avalanche photodiodes afterpulses appear when trapped carriers from a previous avalanche are released. Typical afterpulsing time constants are of the order of a few hundred ns, which makes afterpulsing hard to distinguish from triplet effects. The dual detector configurations described above substantially reduces the effect of afterpulsing on the FCS results by applying cross-correlation analysis.

Today there is no detector that is really suitable for correlation experiments down to the picosecond range. Single photon avalanche photodiodes, in principle, are able to yield a high quantum efficiency (exceeding 65% at 650 nm) [Datasheet Single Photon Counting Module, SPCM-AQR Series04] and a good time resolution [Cova et al., 1989] [Ekstrom, 1981] [Yang et al., 2003]. Unfortunately, the commonly used Perkin Elmer SPCM-AQR modules have a poor timing performance. The width of the TCSPC instrument response was found to vary strongly from module to module (FWHM were measured between 190 ps and 620 ps in about 12 different tested modules) and depends on the wavelength (not shown). For all tested modules a strong dependence of the position of the IRF on the count rate was measured (Fig. 2.1.5b), which makes experiments with fluctuating signals cumbersome or impossible to be analyzed quantitatively. Recently, a technical modification of the Perkin Elmer SPCM-AQR modules was shown to yield much better time responses than the ones tested [Cova et al., 2004]. The dead time of the SPCM-AQR can be estimated from the curves of the counting efficiency versus count rate given by the manufacturer [Datasheet Single Photon Counting Module, SPCM-AQR Series04]. The dead time is about 50 ns and thus of the same order as for the TCSCPC modules.

An alternative detector is the Hamamatsu H7422P-40 PMT [Datasheet Photosensor Modules, H7422 Series04]. Due to its GaAsP cathode it has a quantum efficiency approaching 40% around 450 nm, and a relatively short and stable TCSPC instrument response (Fig. 2.1.5a).

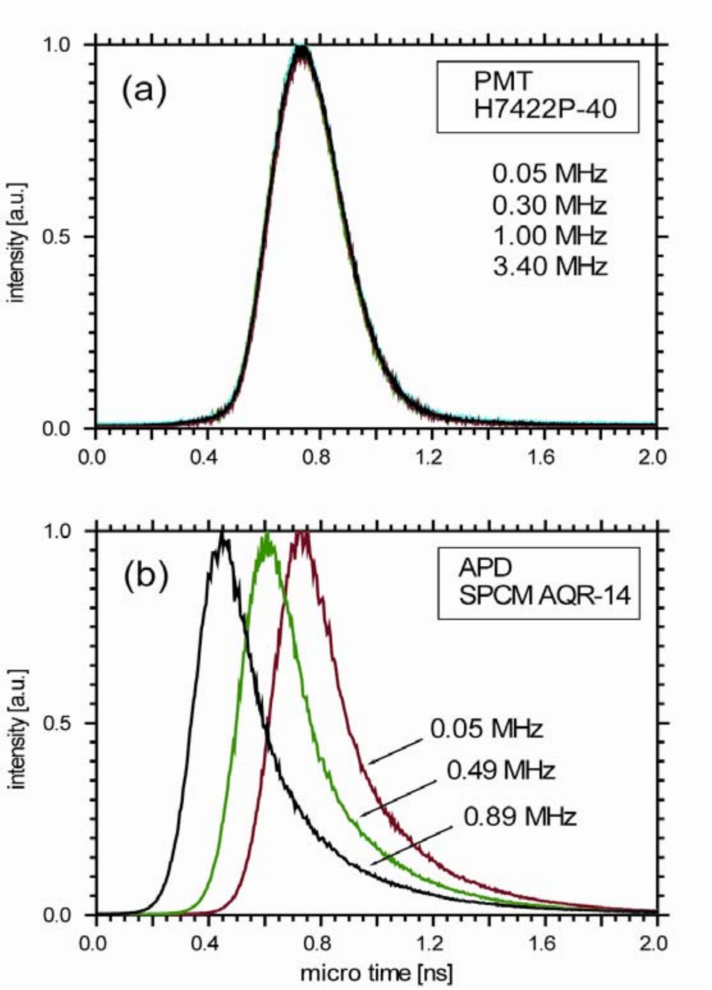

Figure 2.1.5 TCSPC Instrument response functions, measured with Becker & Hickl SPC-132 or SPC-630 TCSPC modules.

(a) H7422P-40: 3.4 MHz, 1 MHz, 0.3 MHz, 0.05 MHz. Diode laser @ 650 nm (BHL-600, Becker & Hickl).

(b) SPCM-AQR-14: count rates 0.05 MHz (right), 0.49 MHz (middle) and 0.89 MHz (left). Modelocked Ar-ion laser @ 496 nm (Coherent).

2.2 Data analysis

By MFD TCSPC technique the following parameters are saved for each detected photon: (i) spectral range, λ_F, of the detected fluorescence (green or red), the polarization of the signal photon (parallel or perpendicular) with respect to the linear polarization of the excitation laser; (ii) the arrival time of the signal photon relative to the incident laser pulse; and (iii) the macroscopic time (number of laser pulses), Δt, to the photon.

Selection of the single molecule bursts is based on the analysis of the interphoton time, Δt. Between two consecutive detected background photons it is very large, whereas fluorescence photons emitted during a dye transit cause a photon burst and thus have a small interphoton time, Δt. A signal with a drop of Δt is classified as fluorescence burst if a certain number of consecutive photons are below a chosen threshold value.

In imaging additional “pixel” and “line” SYNC signals, using two more router channels, are introduced by the instrument control software in order to define pixel coordinates in a photon stream.

Arrival times of the photons in the selected burst or pixel are used to generate fluorescence decay histograms for each of the four detectors (green parallel, $G_{||}$, green perpendicular, $G_{\perp}$, red parallel, $R_{||}$, red perpendicular, $R_{\perp}$). With further analysis, the parameters: signal intensity, lifetime, τ, and anisotropy, r, for each spectral range are determined.

The analysis of experimental data is realized in a LabView-based “Elke”, “Margarita”, “ViewMCS”, “View Burst Traces” programs (see Appendix A for details).

2.2.1 Corrections applied to measured fluorescence signals

The signal intensities, S_G and S_R, of the green and red detection channels are calculated by dividing the number of registered photons by the burst duration or pixel integration time in the case of imaging. To obtain the ratio of corrected donor and acceptor fluorescence F_D/F_A the fluorescence detected in the green F_G and in the red F_R spectral range has to be corrected for the detection efficiencies g_G and g_R respectively.

$$F_D = \frac{F_G}{g_G} = \frac{S_G - B_G}{g_G},$$

$$F_A = \frac{F_R}{g_R} = \frac{(S_R - B_R) - \alpha(S_G - B_G)}{g_R} \qquad \text{(Eq. 2.2-1)}$$

Thereby the experimental fluorescence signals F_G and F_R are calculated from the measured total signals S_G and S_R by subtracting the background signals B_G and B_R, respectively. Additionally the spectral crosstalk α of the donor dye into the red channel has to be taken into account. The spectral crosstalk $\alpha = (S_R - B_R)/(S_G - B_G)$ is calculated by the fluorescence ratio of molecules containing only the donor dye. The ratio of the detection efficiencies g_G/g_R for the specified spectral ranges is obtained by comparing the experimental fluorescence ratio F_G/F_R with the fluorescence ratio measured at a calibrated steady-state fluorescence spectrometer for a single dye.

2.2.2 Fluorescence lifetime

Fluorescence lifetimes were calculated using a maximum likelihood estimator as described in [Schaffer, 2000] which has been shown to be statistically most efficient for the low number of events [Maus et al., 2001].

During the fit superposition of decays from previous pulses is taken into account [Schaffer, 2000]. Correction factors, $l_1 = 0.0308$ and $l_2 = 0.0368$ were applied in order to take into account mixing of polarizations by the microscope objective lenses [Koshioka et al., 1995]. g – factor compensates for slightly different detection efficiencies in the parallel and perpendicular detection channels.

The signal decay histogram registered in the green detection range was described by scattered background and fluorescence decay with a single component. The normalized model pattern, M', of the total signal contains variable fractions, γ, of the scattered background (due to Raman and Rayleigh scattering) , B, and fluorescence F.

$$M'_i(\tau,\gamma) = (1-\gamma)\,F_i(\tau) + \gamma\,B_i \qquad \text{(Eq. 2.2-2)}$$

where fluorescence, F, is given as a convolution of one-exponential decay with instrumental response function, s, taking into account limited arrival time, T_a, and the iterative excitation with the frequency , $1/\omega$.

$$F_i(\tau) = (\sum_{n=0}^{\infty}(s_i \otimes e^{-\frac{t_i}{\tau}})(t + n\omega)) \qquad \text{(Eq. 2.2-3)}$$

One-dimensional minimisation of the fluorescence lifetime, τ, is based on the "schachtelung" algorithm, where variable fraction of the scattered light, γ_S, is determined during every step by a linear regression.

2.2.2.1 *Lifetime fit with a constant background*

Fluorescence lifetime measurements are carried out at high laser repetition rate. The detector afterpulses (see Chapter 2.1.4) from many signal periods accumulate and cause an appreciable signal-dependent background. In the TAC histograms afterpulsing background has a constant profile and makes fitted by eq. 2.2-2 lifetime longer that expected value.

Taking into account the fraction of the constant offset, *u,* the corrected model function of the lifetime fit, $M_i'(\tau,\gamma,u,k)$, is given by eq. 2.2-4:

$$M_i'(\tau,\gamma,u,k) = \frac{u}{k} + (1-u)(M_i(\tau,\gamma)) = \frac{u}{k} + (1-u)((1-\gamma) F_i(\tau) + \gamma B_i); \qquad \text{(Eq. 2.2-4)}$$

where k is a total number of channels in fluorescence decay histogram.

In order to determine the fraction of the constant offset, *u*, sub-ensemble analysis (see chapter 2.2.5) can be applied. All the photons that correspond to selected sub-ensemble are added to get a fluorescence decay of a good statistical quality, which allows for the precise determination of several fit parameters.

2.2.2.2 Global fit of the donor and acceptor decays

In addition to the fluorescence decay of the donor, the acceptor fluorescence decay also delivers information for FRET studies and therefore can be used in the fitting procedure. Global fit of the donor and acceptor decays extracts value of the acceptor lifetime and gives a better estimation of the donor lifetime.

2.2.2.2.1 Model of the time-resolved fluorescence

The rate constants for the donor and acceptor decays of the scheme, shown in Fig. 2.2.2.2-1, can be written as follows [van der Meer et al., 1994]:

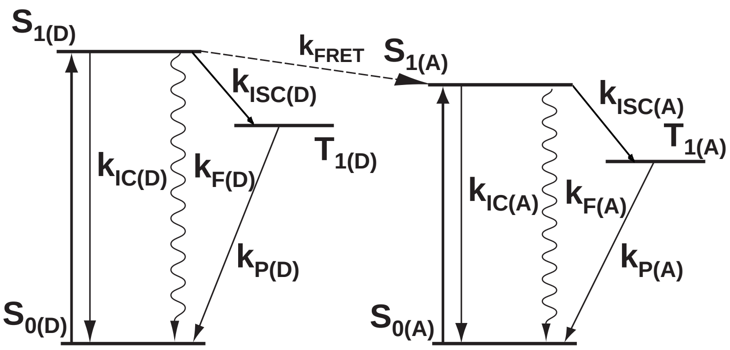

Figure 2.2.2.2-1 Simplified energy–level diagram of resonance energy transfer (adopted from [van der Meer et al., 1994]). $S_{1(D)}$, $S_{0(D)}$, $T_{1(D)}$ refer to the singlet and triplet states of donor, and $S_{1(A)}$, $S_{0(A)}$, $T_{1(A)}$, to the singlet and triplet states of acceptor; $k_{IC(D)}$, $k_{ISC(D)}$, $k_{P(D)}$, $k_{F(D)}$, $k_{IC(A)}$, $k_{ISC(A)}$, $k_{P(A)}$, $k_{F(A)}$,, and k_{FRET} are rate constants: $k_{IC(D)}$, $k_{IC(A)}$ for internal conversion of donor and acceptor, $k_{ISC(D)}$, $k_{ISC(A)}$ for intersystem-crossing of donor and acceptor, and $k_{P(D)}$, $k_{P(A)}$ for phosphorescence and intersystem-crossing from the triplet to singlet state, S_0., k_{FRET} – for energy transfer, and $k_{F(D)}$, $k_{F(A)}$ for fluorescence of donor and acceptor.

$$\frac{d}{dt}p_D = -k_{FRET}\cdot p_D - k_{F(D)}\cdot p_D - k_{ISC(D)}\cdot p_D - k_{IC(D)}\cdot p_D\,; \qquad \text{(Eq. 2.2.2.2-1)}$$

$$\frac{d}{dt}p_A = k_{FRET}\cdot p_D - k_{F(A)}\cdot p_A - k_{ISC(A)}\cdot p_A - k_{IC(A)}\cdot p_A\,; \qquad \text{(Eq. 2.2.2.2-2)}$$

where $p_D = p_D(t)$, $p_A = p_A(t)$ are the probabilities that the donor and acceptor, respectively, are excited at time *t*.

The solution of the differential equation $\frac{d}{dx}y + f(x)\cdot y = g(x)$ is

$$y(x) = M(x)\cdot(\int g(x)\cdot M(x)dx + const);\ where\, M(x) = e^{-\int f(x)dx};$$ (Eq. 2.2.2.2-3)

Solving eqs. 2.2.2.2-1 and 2.2.2.2-2 for the case, when the system is excited with Dirac pulse, and acceptor is excited directly at time *t=0* with probability p_{A0}^{DE}, the following equations are obtained:

$$p_D = p_{D0}\cdot e^{-(k_{FRET}+k_{F(D)}+k_{ISC(D)}+k_{IC(D)})\cdot t};$$ (Eq. 2.2.2.2-4)

$$p_A = \frac{k_{FRET}\cdot(1-p_{A0}^{DE})}{\left(-k_{F(D)}-k_{ISC(D)}-k_{IC(D)}-k_{FRET}+k_{F(A)}+k_{ISC(A)}+k_{IC(A)}\right)}\cdot \\ \cdot\left(e^{-(k_{F(D)}+k_{ISC(D)}+k_{IC(D)}+k_{FRET})t}-e^{-(k_{F(A)}+k_{ISC(A)}+k_{IC(A)})t}\right)+p_{A0}^{DE}\cdot e^{-(k_{F(A)}+k_{ISC(A)}+k_{IC(A)})t}$$ (Eq. 2.2.2.2-5)

In absence of saturation effects either acceptor or donor can be excited, therefore probability that donor is excited is given as p_{D0}=(1- p_{A0}^{DE})

Lifetime of the donor in the presence, $\tau_{D(A)}$, and absence of the acceptor , $\tau_{D(0)}$, as well as lifetime of the acceptor $\tau_{A(0)}$ are inversely proportional to the sum of corresponding rate constants:

$$\tau_{D(A)} = \frac{1}{k_{F(D)}+k_{ISC(D)}+k_{IC(D)}+k_{FRET}};$$ (Eq. 2.2.2.2-6)

$$\tau_{D(0)} = \frac{1}{k_{F(D)}+k_{ISC(D)}+k_{IC(D)}};$$ (Eq. 2.2.2.2-7)

$$\tau_{A(0)} = \frac{1}{k_{F(A)}+k_{ISC(A)}+k_{IC(A)}};$$ (Eq. 2.2.2.2-8)

After substituting eqs. (2.2.2.2-6)-(2.2.2.2-8) into eqs. 2.2.2.2-4 and eqs. 2.2.2.2-5 it follows:

$$p_D = (1-p_{A0}^{DE})\cdot e^{-\frac{t}{\tau_{D(A)}}};$$ (Eq.2.2.2.2-9)

$$p_A = \frac{(1-p_{A0}^{DE})\cdot\left(\tau_{D(0)}-\tau_{D(A)}\right)\cdot\tau_{A(0)}}{\tau_{D(0)}\left(\tau_{D(A)}-\tau_{A(0)}\right)}\cdot\left(e^{-\frac{t}{\tau_{D(A)}}}-e^{-\frac{t}{\tau_{A(0)}}}\right)+p_{A0}^{DE}e^{-\frac{t}{\tau_{A(0)}}};$$ (Eq. 2.2.2.2-10)

Additionally the spectral crosstalk, α, of the donor dye into the red channel (see chapter 2.2.1), different detection efficiencies of the green and red detectors, g_G and g_R, (see chapter

2.2.1) and fluorescence quantum yields, $\Phi_{F(D)}$ and $\Phi_{F(A)}$, have to be taken into account to calculate fluorescence patterns, m''_D and m''_A:

$$m''_D = \Phi_{F(D)} \cdot g_G \cdot (1-\alpha) \cdot p_D = \Phi_{F(D)} \cdot g_G (1-\alpha)(1-p_{A0}^{DE}) e^{-\frac{t}{\tau_{D(A)}}} \qquad \text{(Eq. 2.2.2.2-11)}$$

$$m''_A = \Phi_{F(A)} \cdot g_R \left(p_A + \alpha \cdot \Phi_{F(D)} \cdot p_D\right) =$$
$$= \Phi_{F(A)} \cdot g_R \cdot \left(\frac{\left(\tau_{D(0)} - \tau_{D(A)}\right) \cdot \tau_{A(0)}}{\cdot \tau_{D(0)} \left(\tau_{D(A)} - \tau_{A(0)}\right)} \cdot \left(e^{-\frac{t}{\tau_{D(A)}}} - e^{-\frac{t}{\tau_{A(0)}}} \right) + p_{A0}^{DE} e^{-\frac{t}{\tau_{A(0)}}} + \alpha \cdot \Phi_{F(D)} \cdot\cdot e^{-\frac{t}{\tau_{D(A)}}} \right)$$

(Eq.2.2.2.2-12)

In the case when acceptor triplet state is populated, effective fluorescence quantum yield, $\Phi_{F(A)eff}$, shall be used.

A realistic model of the fluorescence signal can be obtained by convolution of the fluorescence patterns, m''_D and m''_A, with the normalized green and red instrumental response functions, D_G and D_R , taking into account limited arrival time window, T_a, and the iterative excitation with the frequency , 1/ω. The model functions, m'_G, m'_R, contain variable fractions, γ_G and γ_R , of the scattered light (due to Raman and Rayleigh scattering) , D_G and D_R (it is assumed that the scattered light is equal to the instrumental response function). A more advanced model with constant background correction described in previous chapter can be also applied.

$$m'_G(t, \tau_{D(A)}, \gamma_G, \alpha, g_G, \Phi_{F(D)}, D_G) =$$
$$= (1-\gamma_G)(\sum_{n=0}^{\infty} (D_G \otimes m''_D(t, \tau_{D(A)}, \alpha, p_{A0}^{DE}, g_G, \Phi_{F(D)}))(t+n\omega)) + \gamma_G \cdot D_G \qquad \text{(Eq.2.2.2.2-13)}$$

$$m'_R(t, \tau_{D(A)}, \tau_{D(0)}, \tau_{A(0)}, \gamma_R, \alpha, p_{A0}^{DE}, g_R, \Phi_{F(R)}, D_R) =$$
$$= (1-\gamma_R)(\sum_{n=0}^{\infty} (D_R \otimes m''_A(t, \tau_{D(A)}, \tau_{D(0)}, \tau_{A(0)}, \gamma_R, \alpha, p_{A0}^{DE}, g_R, \Phi_{F(A)}))(t+n\omega)) + \gamma_R \cdot D_R$$

(Eq.2.2.2.2-14)

Since the data are accumulated in k arrival channels, the continuous time, t, in the signal patterns is replaced by a discrete channel time, t_i , $t_i = \frac{i \cdot T_a}{k}$. The model function is given by eqs. 2.2.2.2-15 and 2.2.2.2-16:

$$m_{G,i}(\tau_{D(A)}, \gamma_G, T_a, \alpha, p_{A0}^{DE}, g_G, \Phi_{F(D)}, D_G) = (1-\gamma_G)(\sum_{n=0}^{\infty} (D_{G,i} \otimes m''_{D,i})(t_i + n\omega)) + \gamma_G \cdot D_{G,i} \qquad \text{(Eq.2.2.2.2-15)}$$

$$m_{R,i}(\tau_{D(A)},\tau_{D(0)},\tau_{A(0)},\gamma_R,T_a,\alpha,p_{A0}^{DE},g_R,\Phi_{F(A)},D_R)=$$
$$=(1-\gamma_R)(\sum_{n=0}^{\infty}(D_{R,i}\otimes m''_{R,i})(t_i+n\omega))+\gamma_R\cdot D_{R,i}$$
(Eq.2.2.2.2-16)

For the fitting green and red experimental decays that have numbers C_G, C_R of registered photons so that $C_G + C_R = S_c$ two different approaches for normalization of model functions are applied (see next chapter):

1) Normalization by the total number of green and red photons, S_c:

$$M_{j,i}^{t}=S_c\cdot\frac{m_{j,i}}{\sum_{i=1}^{k}m_{G,i}+\sum_{i=1}^{k}m_{R,i}};$$
(Eq.2.2.2.2-17)

$$\sum_{i=1}^{k}M_{j,i}^{t}=M_j^{t};\ M_G{}^{t}+M_R{}^{t}=S_c;$$

where j is a running number of the detector j=[$R;G$]

2) Normalization of the individual decays separately:

$$M_{j,i}^{s}=C_j\ \cdot\frac{m_{j,i}}{\sum_{i=1}^{k}m_{j,i}}$$
(Eq.2.2.2.2-18)

$$M_G^{s}=\sum_{i=1}^{k}M_{G,i}^{s}=C_G;$$

$$M_R^{s}=\sum_{i=1}^{k}M_{R,i}^{s}=C_G\cdot$$

2.2.2.2.2 Fit quality parameter.

For the fluorescence decay analysis with the low number of counts a maximum likelihood estimator (MLE) [Schaffer et al., 1999] [Schaffer, 2000] was shown to be statistically more efficient then the more commonly used weighted least-squares method [Maus et al., 2001] because the underlying the assumption of a Gaussian instead of Poisson or multinomial distribution of errors is incorrect [Bajzer et al., 1991] [Baker and Cousins, 1984] [Hall and Selinger, 1981].

The MLE method is based on the calculation of the likelihood function, which is given as [Brand, 1998] [Schaffer, 2000]:

$$L'(C \mid M(\vec{x})) = \prod_{i=1}^{k} w(C_i \mid M_i(\vec{x})), \qquad \text{(Eq. 2.2.2.2-19)}$$

where $w(C_i \mid M_i(\vec{x}))$ represents the probability that C_i counts in the *i*-th channel of the experimental decay histogram $C=(C_1, C_2, ..., C_k)$ are detected. k is a total number of channels, $M(\vec{x}) = (M_1(\vec{x}), M_2(\vec{x}), ..., M_k(\vec{x}))$ is a model function of the expectation values, which is defined by a set of parameters $\vec{x}$.

It is convenient to apply the logarithm and to normalize the likelihood function $L'(C \mid M(\vec{x}))$ with the likelihood of the absolutely exact fit $L'(C \mid C)$. In this way the MLE fit quality parameter $2I^*$ can be obtained [Schaffer et al., 1999]:

$$2I^* = -2ln\frac{L(C \mid M(\vec{x}))}{L(C \mid C)} = -2ln\prod_{i=1}^{k}\frac{w(C_i \mid M_i(\vec{x}))}{w(C_i \mid C_i)} = -2\sum_{i=1}^{k} ln\frac{w(C_i \mid M_i(\vec{x}))}{w(C_i \mid C_i)}; \qquad \text{(Eq. 2.2.2.2-20)}$$

During the FRET experiment fluorescence is detected in two (red and green) histograms, which correspond to acceptor and donor fluorescence, respectively. In this case the probability, $w(C_i^j \mid M_i^j(\vec{x}))$, that $C^j{}_i$ counts are detected in the detector *j* (green or red) and *i*-th channel of the experimental decay, has to be calculated.

One has to consider two processes: (A) from total of S_c photons C_j photons will fall into detector *j* and (B) from these C_j photons $C_{j,i}$ photons will fall into channel *i*. According to [Bronstein 91] the joint probability, $w(A \cap B)$, of two (*A* and *B)* events in conjunction is given as

$$w(B \cap A) = w(A) \cdot w(B \mid A) \qquad \text{(Eq. 2.2.2.2-21)}$$

where conditional probability, $w(B \mid A)$, is the probability of event B, given the occurrence of event A.

In the experimental setup (chapter 2.1.1) photons are spit into the red and green channels with a dichroic beamsplitter which can be described by a binomial distribution:

$$w(C_j \mid S_c, M_j^t) = \frac{S_c!}{C_j! \cdot (S_c - C_j)!} \cdot p_j^{C_j} \cdot (1 - p_j)^{S_c - C_j} \qquad \text{(Eq. 2.2.2.2-22)}$$

where p is the probability that photon is detected by detector j, which is defined by the model:

$$p_j = \frac{\sum_{i=1}^{k} M_{j,i}^t}{S_c} = \frac{M_j^t}{S_c}, \qquad \text{(Eq. 2.2.2.2-23)}$$

where S_c is a total number of photons in green and red channels, j is a running number of the detector j=[$R;G$], $M_{j,i}^t$ is given by eq. 2.2.2.2-17.

The probability to collect the set of a $\{C_{j,1} ... C_{j,k}\}$ photons out of total C_j detected by the detector j, is given by the multinomial distribution[Brand, 1998] [Köllner, 1993]:

$$w(C_{j,1} ... C_{j,k} \mid C_j, M_{j,1}^s ... M_{j,k}^s) = \prod_{i=1}^{k} w(C_{j,i} \mid C_j, M_{j,i}^s) = C_j! \prod_{i=1}^{k} \frac{{M_{j,i}^s}^{C_{j,i}}}{C_j^{C_{j,i}} \cdot C_{j,i}!}; \qquad \text{(Eq. 2.2.2.2-24)}$$

When a photon is already detected by one of detectors, it will fall into one of it's TAC channels with probability 1:

$$\sum_{i=1}^{k} w(C_{j,i} \mid C_j, M_{j,i}^s) = 1; \qquad \text{(Eq. 2.2.2.2-25)}$$

According to Eq. 2.2.2.2-19 the likelihood function for the signal can be written as

$$L(C \mid M) = w(C_j \mid S_c, M_j^t) \prod_{j=G,R} \prod_{i=1}^{k} w(C_{j,i} \mid C_j, M_{j,i}^s) \qquad \text{(Eq. 2.2.2.2-26)}$$

Substituting eq. (2.2.2.2-22) — (2.2.2.2-24) into eq. 2.2.2.2-20 the $2I^*$ parameter for the global fit of green and red decays is obtained:

$$2I^* = -2\ln L = 2\left[\left(C_G \ln\frac{C_G}{M_G^t} + C_R \ln\frac{C_R}{M_R^t}\right) + \sum_i C_{G,i}\ln\frac{C_{G,i}}{M_{G,i}^s} + \sum_i C_{R,i}\ln\frac{C_{R,i}}{M_{R,i}^s}\right] \quad \text{(Eq. 2.2.2.2-27)}$$

normalized $2I_r{}^*$ fit parameter is given by eq . 2.2.2.2-28

$$2I_r{}^* = -\frac{2\ln L}{k-\zeta-1} = \frac{2}{k-\zeta-1}\left[\left(C_G \ln\frac{C_G}{M_G^t} + C_R \ln\frac{C_R}{M_R^t}\right) + \sum_i C_{G,i}\ln\frac{C_{G,i}}{M_{G,i}^s} + \sum_i C_{R,i}\ln\frac{C_{R,i}}{M_{R,i}^s}\right] \quad \text{(Eq. 2.2.2.2-28)}$$

where ζ is the number of fitted parameters.

The first term in eq. 2.2.2.2-28,

$$k_{bi} = \left(C_G \ln\frac{C_G}{M_G^t} + C_R \ln\frac{C_R}{M_R^t}\right) \quad \text{(Eq. 2.2.2.2-29)}$$

corresponds to the contribution of the probability, $w(C^j \mid N, M_j^t)$, that photon is detected by one of two (green and red) detectors and given by a binomial distribution.

It can be shown, that eq. (Eq. 2.2.2.2-28) is equivalent to eq. (Eq. 2.2.2.2-30)

$$2I_r{}^* = \frac{2}{k-\zeta-1}\left[\sum_i C_{G,i}\ln\frac{C_{G,i}}{M_{G,i}^t} + \sum_i C_{R,i}\ln\frac{C_{R,i}}{M_{R,i}^t}\right] \quad \text{(Eq. 2.2.2.2-30)}$$

Calculation of the normalized model function, $M_{j,i}^t$, can be difficult due to large number of parameters; Some of them ($\alpha, p_{A0}^{DE}, g_G, \Phi_{F(D)}, g_R, \Phi_{F(A)}$) are not always determined easily. In this case a "simplified" global fit can be done by setting $k_{bi} = 0$ (eq. 2.2.2.2-31). Calculation of the model function $M_{j,i}^t$ is therefore no longer necessary.

$$2I_{rs}{}^* = \frac{2}{k-\zeta-1}\left[\sum_i C_{G,i}\ln\frac{C_{G,i}}{M_{G,i}^s} + \sum_i C_{R,i}\ln\frac{C_{R,i}}{M_{R,i}^s}\right] \quad \text{(Eq. 2.2.2.2-31)}$$

A similar approach describing calculation of $2I_r{}^*$ parameter for the system with two (parallel and perpendicular) detectors is presented in [Schaffer, 2000] (corresponding eq. 4.3-14) and [Schaffer et al., 1999] (corresponding eq. 12):

$$2I_r{}^* = -\frac{2\ln L}{k-\zeta-1} = \frac{2}{k-\zeta-1}\left[2K\left(C_G \ln\frac{C_G}{M_G^t} + C_R \ln\frac{C_R}{M_R^t}\right) + \sum_i C_{G,i}\ln\frac{C_{G,i}}{M_{G,i}^t} + \sum_i C_{R,i}\ln\frac{C_{R,i}}{M_{R,i}^t}\right] \quad \text{(wrong)}$$

Nomenclature in the equation of J. Schaffer is changed to be consistent with this thesis. Indexes of parallel and perpendicular detectors are replaced with the green and red detectors.

Two mistakes are found in this equation:

1) Normalization of the model function in the last two terms is wrong ($M^t_{j,i}$ is used instead of $M^s_{j,i}$,. eq. 2.2.2.2-25 is then no longer true)
2) The first term, k_{bi}, is multiplied with coefficient *2k*. This is wrong, because the probability, $w(C_j \mid S_c, M^t_j)$, that a photon is detected by one of two (green and red) detectors should appear only once in the formula of likelihood function, *L*.

2.2.2.2.3 Applications to simulated data

Single-molecule FRET data were simulated to test the developed fitting procedure. Simulation algorithm uses experimentally obtained distribution of a photon number in a single-molecule burst and applies binomial distribution (see eq. 2.2.2.2-22) to generate photon numbers in the green and red detectors. The probability, p_j that a photon is detected by detector j, is an input parameter for simulation software. After number of photons in a detector is obtained, lifetime histograms are generated based on the model functions, given by the eqs. (2.2.2.2-15) and (2.2.2.2-16) using Poisson distribution of photons in each TAC channel. The following input parameters are used: the donor lifetime in absence, $\tau_{D(0)}$, and in presence, $\tau_{D(A)}$, of the acceptor; the acceptor lifetime, $\tau_{A(0)}$; spectral crosstalk, α, the probability, p_{A0}^{DE}, that acceptor is excited directly, donor and acceptor quantum yields, Φ_D,Φ_A; green and red instrumental response functions, D_G, D_R. and number of TAC channels, k.

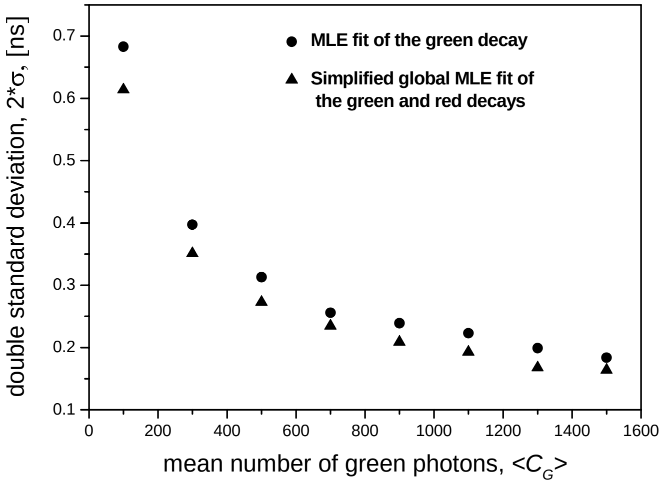

Figure 2.2.2.2-2. Double standard deviation, 2σ, of the donor lifetime in presence of acceptor, $\tau_{D(A)}$, plotted versus mean number of green photons,$<C_G>$. Calculations were carried out for the simulated FRET sample (p_R=0.4885; $\tau_{D(0)}$=4.0 ns; $\tau_{D(A)}$=1.954 ns; $\tau_{A(0)}$=2.93 ns; α=0; $p_{A0}^{DE}=0$; $\Phi_D=\Phi_A=1$; k=256) using MLE fit of only the green decay (triangles) and "simplified" global MLE fit of green and red decays, using eq. 2.2.2.2-31 (circles). Standard deviations were obtained by fitting the calculated lifetime distributions with the Gaussian curve: $y(x) = y_0 + \frac{A}{\sigma\sqrt{2\cdot\pi}} \cdot e^{-\frac{(x-\mu)^2}{2\sigma^2}}$

Fig. 2.2.2.2-2 shows the double standard deviation, 2σ, of the donor lifetime in presence of acceptor, $\tau_{D(A)}$, plotted versus mean number of green photons,$<C_G>$. Calculations were carried out for the simulated FRET sample (p_R=0.4885; $\tau_{D(0)}$=4.0 ns; $\tau_{D(A)}$=1.954 ns; $\tau_{A(0)}$=2.93 ns; α=0; p_{A0}^{DE} =0; Φ_D=Φ_A=1; k=256) using two fitting procedures:

1) MLE fit of the green decay only (described in detail by [Schaffer, 2000])
2) "Simplified" global MLE fit of green and red decays, which applies eq. 2.2.2.2-31.

Second approach gives a better estimation of the donor lifetime than first one.

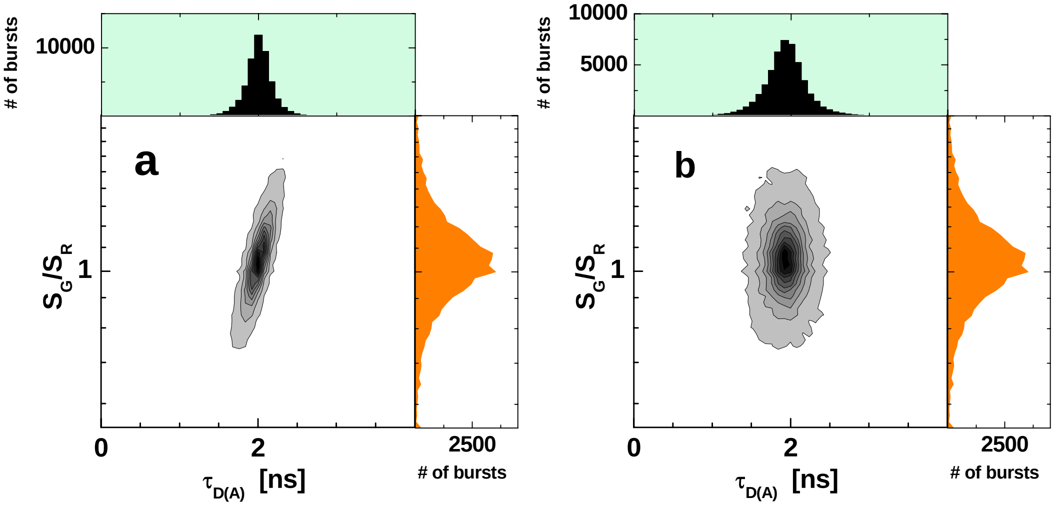

Figure 2.2.2.2-3. Fluorescence signal ratio, S_G /S_R , is plotted versus donor lifetime, $\tau_{D(A)}$, for simulated FRET sample (p_R=0.4885; $\tau_{D(0)}$=4.0 ns; $\tau_{D(A)}$=1.954 ns; $\tau_{A(0)}$=1.3 ns; α=0; $p_{A0}{}^{DE}$=0; Φ_D=Φ_A=1; k=512). Donor lifetimes, $\tau_{D(A)}$, were calculated by the fitting procedures applying: a) eq. 2.2.2.2-28 (standard global fit) and b) eq. 2.2.2.2-31 ("simplified" global fit).

Figure 2.2.2.2-3 shows a two-dimensional histogram, with the bursts of the simulated FRET sample (p_R=0.4885; $\tau_{D(0)}$=4.0 ns; $\tau_{D(A)}$=1.954 ns; $\tau_{A(0)}$=1.3 ns; α=0; p_{A0}^{DE} =0; Φ_D=Φ_A=1; k=512) sorted with respect to the fluorescence signal ratio, S_G /S_R , and the donor lifetime in presence of the acceptor, $\tau_{D(A)}$, calculated by the fitting procedures applying: a) eq. 2.2.2.2-28 (standard global fit) and b) eq. 2.2.2.2-31 ("simplified" global fit). In both cases fitted value of the donor lifetime stays in a good correspondence with the simulation parameter: $\tau_{D(A)}$=1.954 ns. Standard global fit produces more narrow distribution of the donor lifetime, than the "simplified" global fit. Correlation with the fluorescence signal ratio is observed in the case of standard global fit since the model function, $M^{t}_{j,i}$ (eq. 2.2.2.2-17), predicts exact values of green and red intensities.

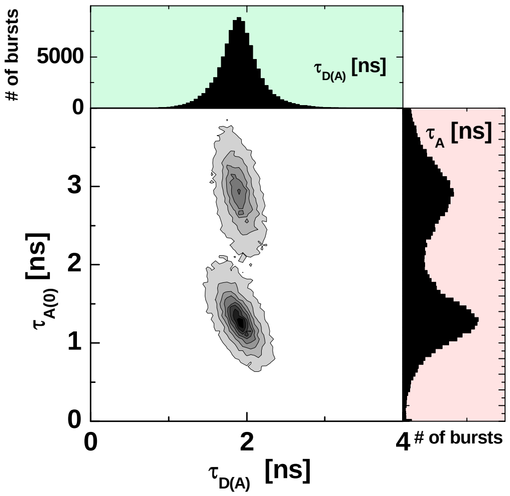

Figure 2.2.2.2-4. Acceptor lifetime, $\tau_{A(0)}$, is plotted versus donor lifetime, $\tau_{D(A)}$, for simulated FRET sample (p_R=0.4885; $\tau_{D(0)}$=4.0 ns; $\tau_{D(A)}$=1.954 ns; $\tau_{A(0)1}$=1.3 ns; $\tau_{A(0)2}$=2.93 ns α=0; $p_{A0}{}^{DE}$=0; Φ_D=Φ_A=1; k=256). Fitting procedure applying eq. 2.2.2.2-31 (“simplified” global fit) was used.

The simulated FRET sample having two species differing in the acceptor lifetime (p_R=0.4885; $\tau_{D(0)}$=4.0 ns; $\tau_{D(A)}$=1.954 ns; $\tau_{A(0)1}$=1.3 ns; $\tau_{A(0)2}$=2.93 ns; α=0; p_{A0}^{DE}=0; Φ_D=Φ_A=1; k=256) was analyzed. Figure 2.2.2.2-4 shows a two-dimensional histogram, with the bursts sorted with respect to the acceptor lifetime, $\tau_{A(0)}$, and the donor lifetime in presence of the acceptor, $\tau_{D(A)}$ calculated using eq. 2.2.2.2-31 (“simplified” global fit).

Both acceptor lifetimes were recovered with good accuracy. Correlation of the acceptor and donor lifetimes is observed because the model function, $M_{j,i}^{s}$ (eq. 2.2.2.2-18) depends on both of these parameters.

Analysis of simulated data shows that the MLE global fit of the donor and acceptor decays gives better estimation of the donor lifetime than MLE fit of only green decay and in addition extracts acceptor lifetime with good accuracy.

2.2.3 Fluorescence anisotropy

The anisotropy was primarily analyzed in the green range. The steady-state anisotropy is formally given by

$$r_G = \int_0^\infty r_G(t)F_G(t)dt \Big/ \int_0^\infty F_G(t)dt\,, \tag{Eq. 2.2.3-1}$$

where

$$r_G(t) = \frac{F_{G\|}(t) - F_{G\perp}(t)}{F_{G\|}(t) + 2\cdot F_{G\perp}(t)} \tag{Eq. 2.2.3-2}$$

is the time-dependent anisotropy, and $F_{G\|}(t)$and $F_{G\perp}(t)$ are the fluorescence detected with a polarization parallel and perpendicular to that of the excitation light, respectively. $F_G(t)= F_{G\|}(t)+2F_{G\perp}(t)$ is the total fluorescence intensity.

In this study, the anisotropy of the fluorescence detected from a single molecule in the green channels was determined as by [Schaffer et al., 1999].

$$r_G = \frac{gF_{G//} - F_{G\perp}}{(1-3l_2)gF_{G//} + (2-3l_1)F_{G\perp}}\,, \tag{Eq. 2.2.3-3}$$

where $F_{G\|}$ and $F_{G\perp}$ are the average fluorescence count rates detected with a polarization parallel and perpendicular to that of the excitation light, respectively.

2.2.4 Fluorescence correlation spectroscopy (FCS)

Fluorescence correlation spectroscopy (FCS) exploits the correlation between the fluorescence intensities in different time intervals and delivers information about following processes:

- Translational diffusion
- Rotational diffusion
- Photophysical processes (triplet formation, photobleaching)
- Photochemical processes (protonation kinetic, quenching kinetic)

FCS is also able to estimate the average number of detected molecules in the focal volume.

FCS demonstrates huge potential in imaging applications (see Chapter 4). It can be combined with image correlation spectroscopy (ICS), that analyses the temporal and spatial correlation between neighbouring pixels or successive images and allows to calculate molecular diffusion constants in the microsecond to second timescale [Digman et al., 2005b] [Digman et al., 2005a].

The common technique for FCS recording is the ‘hardware correlator’. The device registers single photon events with a time-resolution in the ns range and correlates the detection times in an internal signal processor. It can be used in combination with the standard TCSPC technique [O'Connor and Phillips, 1984] to obtain independent FCS and lifetime data for the molecules under investigation [Heikal et al., 2000] [Schwille et al., 2000]. The drawback is that the lifetime data are not obtained from exactly the same molecules as the FCS data, and lifetime fluctuations cannot be correlated with the fluctuations in the FCS data.

This work was carried out with the advanced TCSPC technique (Chapters 2.1.2, 2.1.3) and correlation software, described in the next chapter, which is extended for the simultanious recording of FCS, FCCS, fluorescence lifetime and antibunching effects.

2.2.4.1 *Software correlation*

In FCS, fluctuations, $\delta F(t)$, of the fluorescence intensity, $F(t)$, with time, t, around an equilibrium value, $<F>$, ($\delta F(t)=F(t)-<F>$) are statistically investigated by calculating the normalized second order autocorrelation function, $G^{(2)}(t_c)$. In practice the fluorescence signal is often split and directed onto two separate detectors to overcome deadtime problems of the detectors and associated electronics. The resulting two signals are then cross-correlated to yield the correlation curve, with the correlation or lag time t_c.

$$G^{(2)}(t_c) = \frac{\langle F_1(t)F_2(t+t_c)\rangle}{\langle F_1\rangle\langle F_2\rangle} = 1 + \frac{\langle \delta F_1(t)\delta F_2(t+t_c)\rangle}{\langle F_1\rangle\langle F_2\rangle} \qquad \text{(Eq. 2.2.4-1)}$$

A multi-tau software correlator was developed to correlate the data (see Appendix A, “Kristine” program). The algorithm uses the asynchronous single photon intensity information of the TCSPC data without requiring the construction of a multichannel scaler (MCS) trace, as needed for conventional intensity correlation algorithms. As shown previously, [Magatti and Ferri, 2003] [Wahl et al., 2003] [Wohland et al., 2001] this is the most efficient way to correlate single photon data at low or moderate count rates.

2.2.4.1.1 Time-axis generation and TAC linearization

Laboratory time: For the FCS/FCCS curve generation it is required to restore the exact laboratory time from start of the experiment with ps resolution for each photon from the saved data. For this purpose the macro- and micro- (TAC) time information was used for each event for the generation of a combined arrival time with TAC resolution (Fig. 2.1-3):

$$t_{lab} = t_{sync} \cdot N_{sync} + t_{TAC} \cdot N_{TAC} \qquad \text{(Eq. 2.2.4-2)}$$

where t_{lab} is the laboratory time since the start of the experiment, t_{sync} is the time between the synchronization pulses, N_{sync} is the macro time counter (number of SYNC pulses since the start of the experiment), t_{TAC} is the calibrated width of a TAC channel in ns and N_{TAC} the number of TAC-channels between a photon and the previous sync pulse. The combination of the time axes is only possible when the master clock for the macro timer (t_{sync}) and the stop signal for the TAC (t_{TAC}) are the same, as achieved in dual channel TCSPC setup.

Nonlinearity: Any nonlinearity of the TAC characteristic will cause periodic distortions in the reconstructed time axis, as discussed before. These -reproducible- artefacts were corrected by applying a rebinning algorithm to yield equal time-bins, which makes use of a calibration table containing calibration factors for each channel of the two TACs.

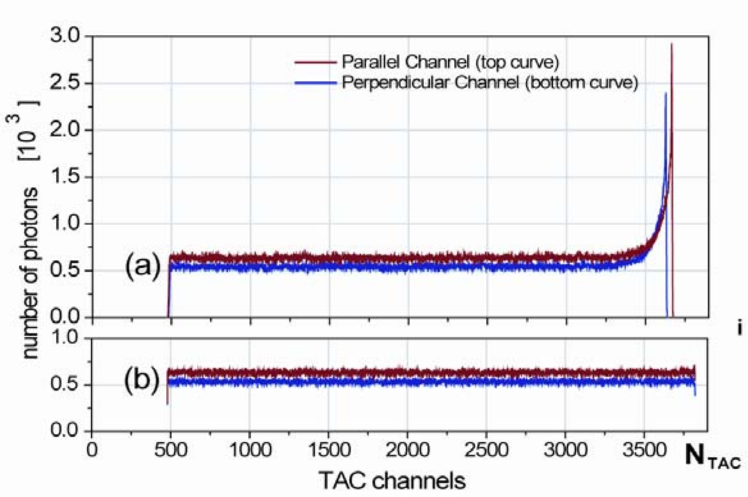

Figure 2.2.4-1: TAC-histograms.

(a) Original histograms diplaying nonlinearities in both channels/boards.

(b) Corresponding linearized histograms.

The first step in the generation of this linearization table is the acquisition of TAC histograms consisting of at least 10^6 randomly distributed photons to record the characteristic for each TAC with sufficient accuracy. To preserve the original factory-set calibration of the TAC the approximately linear part of the histograms is used to calculate a mean number of counts per channel, n_{mean} (i.e. from channels 550-3000 in Fig. 2.2.4-1a). Within the shot-noise limit the counts in every channel, $n(k)$, of an ideal TAC should equal this number of photons. The deviations observed in practice for certain regions of the full range will be corrected for as follows:

The TAC histogram is normalized with n_{mean}. The obtained numbers, $n(k)/n_{mean}$, represent the deviation from the mean of the width of the corresponding TAC channel. From these relative bin-widths a table of corrected times, $N_{TAC}^{fract}(i)$, for each channel i is generated by defining:

$$N_{TAC}^{fract}(i) = f\sum_{k=0}^{i} \frac{n(k)}{n_{mean}}, \qquad \text{(Eq. 2.2.4-3)}$$

where $n(k)/n_{mean}$ is the measured width of the nonlinear bins and f a stretching factor. The factor f was needed to avoid gaps in the time axis, i.e. to make the TAC scales of both modules identical and match the macro time spacing by correcting the slight and unavoidable variations in the individual calibrations. It corrects for inaccuracies in the TAC calibration which usually is performed by the manufacturer only for the linear part. As a result of this stretching/shrinking each TAC range yields the same number of channels required to fill the lag between two SYNC pulses with bins of the calibrated width (3343 bins of 4.069 ps (= t_{TAC}) for a 13.6 ns (= t_{sync}) time window). The corrected times for each TAC bin, $N_{TAC}^{fract}(i)$, still refer to the units of the original time-bins but are rational numbers and no longer integers. Since efficient and fast correlation of the data requires equal time bins (see below) a rebinning of the photons has to be performed.

Rebinning of photons: The next step of the linearization process is the redistribution of the photons on the time axis from the original nonlinear TAC bins, i, into corresponding bins of equal width, N_{TAC}. A relative width $n(k)/n_{mean} > 1$ suggests a division of that particular bin into smaller bins. A redistribution of single photons is performed one by one according to the calculated probability of the photon belonging to a certain corrected time-bin. To this end a random number, u, is assigned to the considered photon and, after beeing multiplied by the respective bin-width, added to the corrected time of the previous bin:

$$N_{TAC} = N_{offset} + \left\lceil N_{TAC}^{fract}(i-1) + u\left(N_{TAC}^{fract}(i) - N_{TAC}^{fract}(i-1)\right) \right\rceil \quad \text{with} \quad i > N_{offset}, \qquad \text{(Eq. 2.2.4-4)}$$

where $0 \leq u < 1$ is a random number generated by the standard LabVIEW random number generator, N_{offset} the number of empty TAC channels (about 500 in Fig. 2.2.4-1a) and $\lceil\ \rceil$ increases the enclosed argument to the nearest higher integer. N_{TAC} gives the new channel number for the considered photon.

The result of the linearization is demonstrated in Fig. 2.2.4-1. Histograms of fluorescence of Rhodamine 110 solutions excited by polarized cw laserlight and detected in the two perpendicularly polarized channels are displayed before and after the linearization procedure (Fig. 2.2.4-1a and Fig. 2.2.4-1b, respectively).

Synchronization of the board specific switching points of the macro time counter with the TAC time scale: Besides the TAC nonlinearity a second property of the analog circuitry potentially producing artefacts in the combined time axis is an offset between TAC ramp and macro timer. Despite the use of a single external clock signal to "simultaneously" advance the macro time counters and stop the TACs of both boards, internal delays in general cause a switching of the macro timer not exactly at the end of a TAC ramp but rather during the ramp and different for both modules. As a result, an identical photon train simultaneously arriving at both boards, i.e. a single detector signal split by a powersplitter, would occasionally generate "photon pairs" stamped with identical TAC time but a macro time differing by one count. The corresponding Δt histogram for short times ($|\Delta t = t_{lab}(\text{det } 1) - t_{lab}(\text{det } 2)| < 100$ ns) would peak at $\Delta t = 0$ but also show satellites $\Delta t = \pm\, t_{sync}$. Moving by software of the switching points of both modules to the same end of the TAC ramp vastly reduces these satellites. Allthough a complete correction was not possible due to a slight jitter of the counting electronics, the remaining uncertainty was less than five TAC channels of 4.069 ps width each.

The TCSPC data allows recovery of the photon detection laboratory time with the accuracy of the TAC channel calibration time (4.069 ps). From $t_{sync} = t_{TAC} \cdot N_{TAC}^{\max}$ ($N_{TAC}^{\max}$ is the number of TAC channels within one macrotiming clock cycle t_{sync}) and eq. (1) it follows that also the laboratory times t_{lab} of the photon detection are integer multiples of the TAC channel calibration time t_{TAC}. This "single photon MCS trace" differs from conventional MCS traces by containing only the time information of the registered photons instead of intensity information for equally spaced bins. In this way the same information is stored in a much more efficient way, equivalent to only saving the filled bins and not the much more frequent empty ones. Developed fast correlation algorithm makes use of this fact.

Correlation of the data with full (ps) time resolution up to the milliseconds or seconds range would still require enormous computation time and at the same time gain little information. Therefore a reduction of the time resolution for larger correlation times t_c was carried out using a multi tau scheme. Calculation of $G^{(2)}(t_c)$ with pseudo-logarithmically spaced lag times was first proposed by Schätzel[Schätzel, 1985] [Schätzel and Peters, 1991] and then used in commercial hardware correlators. An equivalent procedure was adopted by this algorithm. Here a fixed number N_c of time bins with equal spacing (one cascade) is followed by consecutive cascades with bin-widths that, starting with the third cascade, double each time.

The number of equal time-bins per cascade can be chosen arbitrarily in the algorithm. For the full correlation curves presented in this thesis the number of correlation times per cascade $N_c = 8$ was used in analogy with the standard design of commercial hardware-correlators. This results in the following array of lag times in units of t_{TAC} for the first four cascades: $\{t_c\}=\{(1,2,...,7,8),(9,10,...,15,16),(18,20,...,30,32),(36,40,\ldots,60,64),...\}$. The general analytical representation of this array of lag times $t_c(k)$ is:

$$t_c(k)=\begin{cases} 1 & \text{if} \quad k=0 \\ t_c(k-1)+1 & \text{if} \quad 0<k<2N_c \\ t_c(k-1)+2^{\lfloor (k/N_c)-1 \rfloor} & \text{if} \quad k \geq 2N_c \end{cases} \qquad \text{(Eq. 2.2.4-5)}$$

where $\lfloor \ \rfloor$ returns the integer part of the enclosed expression, which for $k > 2N_c$ is the cascade number K.

Developed algorithm works directly on two arrays of laboratory times $t_1(i)$ and $t_2(j)$, which for the first two cascades correspond to single photon events. As a consequence of the time binning multiple events per bin for cascades $K \geq 2$ are possible. To take that into account, in parallel to the two arrays of laboratory times $t_1(i)$ and $t_2(j)$ an additional pair of arrays $F_1(i)$ and $F_2(j)$ is generated which carries the photon number or intensity information. The initial values for the first two cascades are $F_1(i) = F_2(j) =1$. The algorithm runs in a cycle for each cascade to find the coincident photons for the corresponding range of lag times. For a given element i in array $F_1(i)$ the corresponding bin in $F_2(j)$ is found via its associated time in the range from $t_2^{start}(K,N_c,t_1(i))$ to $t_2^{end}(K,N_c,t_1(i))$:

$$\begin{aligned} t_2^{start} &= \frac{t_c(k=KN_c)}{b}+t_1(i) \\ t_2^{end} &= t_2^{start}+N_c \end{aligned} \text{, with the binning factor } b=\begin{cases} 1 & \text{if} \quad K=0 \\ 2^{K\text{-}1} & \text{if} \quad K>0 \end{cases} \qquad \text{(Eq. 2.2.4-6)}$$

The number of cascades is defined by the maximum correlation time chosen by the user, which can be up to one fifth of the length of the data set.

For the correlation an array $P(t_c)$ containing the sums of the products of the photon numbers for each lag time, i.e. the number of pairs, is generated.

$$P(t_c)=\sum F_1(t_1(i))F_2(t_1(i)+t_c) \qquad \text{(Eq. 2.2.4-7)}$$

Starting with the first element of the first channel $F_1(t_1(i=0))$, the algorithm searches an element in the second channel $F_2(t_2(j))$ in the range $t_2^{start} \leq t_2(j) < t_2^{end}$. It then generates the possible products $F_1(t_1(i))F_2(t_1(i)+t_c)$ in that cascade and adds them to their corresponding bins $P(t_c)$, with $t_c = t_2(j)-t_1(i) = t_c(t_2(j)-t_2^{start}+KN_c)$.

After completing the first two cascades rebinning of the data has to be performed. For the following cascades the widths of the time-bins of both channels are doubled each time by dividing the elements of the time arrays t_1 and t_2 by 2. Since these values are stored as 64 bit integers, the divison by 2 is performed by a right-shift. Elements of the intensity arrays $F_1(t_1(i))$ and $F_2(t_2(j))$, that as a result now belong to the same laboratory time bin, are grouped:

$$\left.\begin{aligned} F_{i+1}(K) &= F_i(K-1)+F_{i+1}(K-1)\\ F_i(K) &= 0\end{aligned}\right\}\quad \text{for}\quad t_i(K)=t_{i+1}(K) \qquad \text{(Eq. 2.2.4-8)}$$

The application of eq. 2.2.4-8 is schematically displayed in Fig. 2.2.4-2:

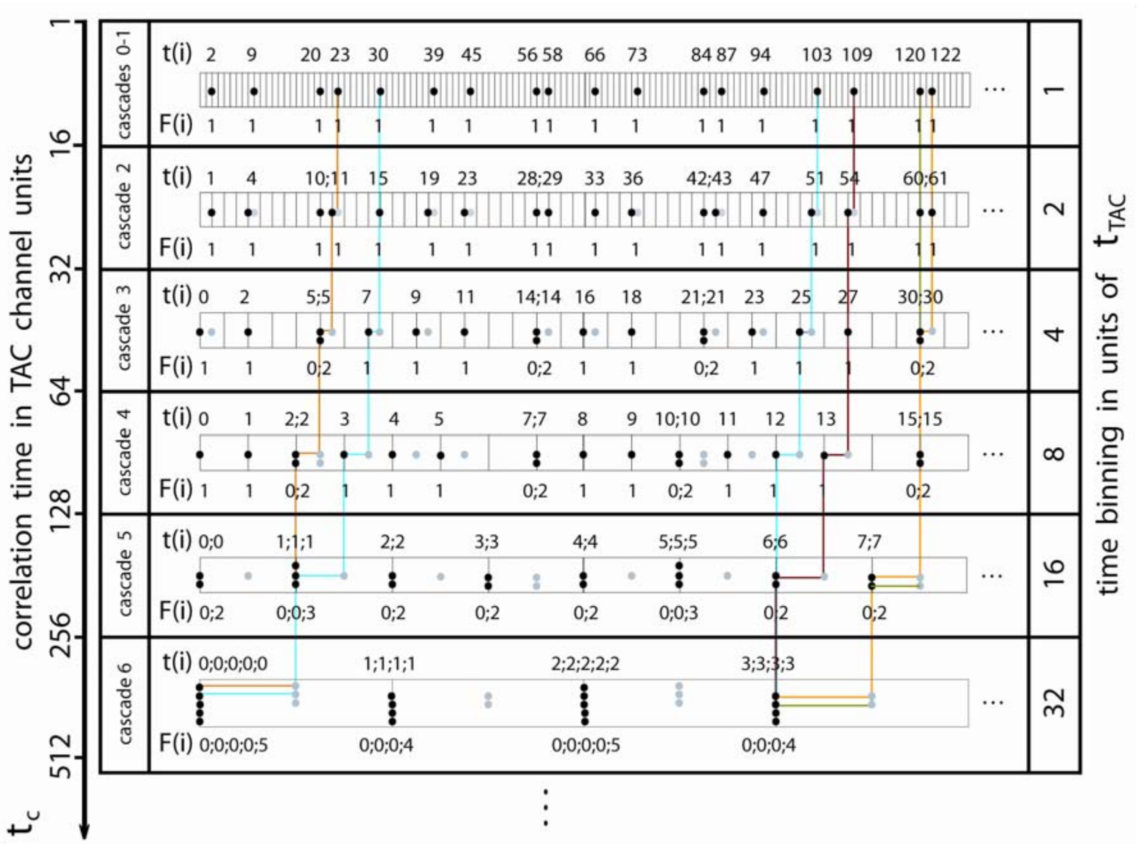

Figure 2.2.4-2: Architecture of the rebinning algorithm.

The values $G^{(2)}(t_c)$ of the second order cross-correlation of the two intensity channels, F_1 and F_2, are obtained by normalizing $P(t_c)$:

$$G^{(2)}(t_c) = \frac{\langle F_1(t) F_2(t+t_c)\rangle}{\langle F_1(t)\rangle \cdot \langle F_2(t)\rangle} = \frac{\left(\dfrac{\sum_i F_1(t_i) F_2(t_i+t_c)}{min(t_1^{\max}, t_2^{\max} - t_c)}\right)}{\left(\dfrac{\sum_i F_1(t_i)}{t_1^{\max}}\right) \cdot \left(\dfrac{\sum_j F_2(t_j)}{t_2^{\max}}\right)} = \frac{\left(\dfrac{P(t_c)}{t_{cor}}\right)}{\left(\dfrac{N_1}{t_1^{\max}}\right)\left(\dfrac{N_2}{t_2^{\max}}\right)}. \quad \text{(Eq. 2.2.4-9)}$$

N_1 and N_2 are the total numbers of photons in channel 1 and 2, $min(t_1^{\max},\ t_2^{\max} - t_c) = t_{cor}$ returns the smaller number of $t_1^{\max}$ and ($t_2^{\max} - t_c$), and $t_1^{\max}$ and $t_2^{\max}$ are the time-bin numbers of the last photons in detection channel 1 and 2, respectively. Please note that for the different cascades t^{max} is expressed in different multiples of t_{TAC}. Thus the normalization by t^{max} automatically compensates for the different numbers of possible pairs of bins in the different time binnings. Since in this work the focus is on short time correlations, symmetrical normalization as in eq. (2.2.4-9) was chosen to reduce computation time. As shown previously, noise reduction by in general more appropriate asymmetrical normalization becomes significant only at larger lag times.[Schätzel et al., 1988]

More sophisticated techniques like time-gated correlation[Eggeling et al., 2001a] which selects photons according to their arrival time after pulsed laser excitation for correlation analysis, or selective correlation, (Chapter 2.2.5) i.e. selection of specific single-molecule events in a fluorescence time trace, are implemented in the software and can be applied as well.

2.2.4.2 FCS modeling

Every process leading to statistical fluctuations in the fluorescence signal (e.g., rotational or translational diffusion, triplet formation) will induce a characteristic decay or rise time in the correlation curve (see Fig 2.2.4-3).

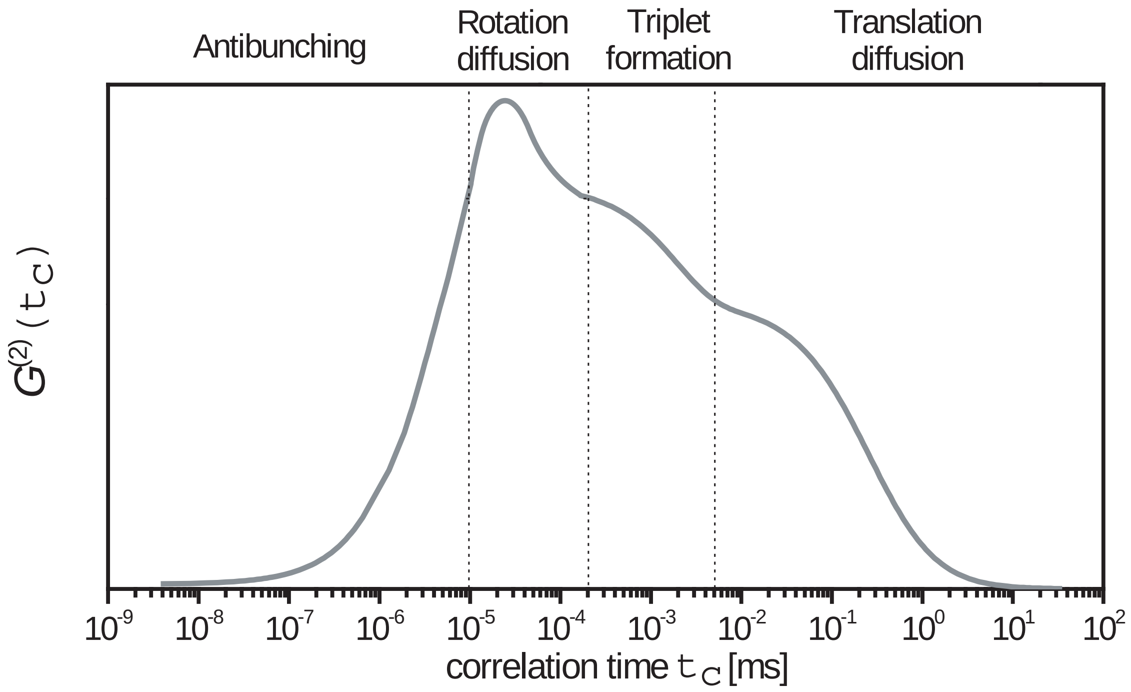

Figure 2.2.4-3 Schematic representation of the fluorescence correlation curve.

Continuous wave (*cw*) *excitation*: For the independent, i.e. uncorrelated processes their contribution is additive to the complete correlation curve. If translational diffusion, triplet formation and single molecule photon antibunching are the only noticeable processes causing fluorescence intensity fluctuations, the normalized correlation function, $G^{(2)}(t_c)$, can be approximated by the sum of a diffusional term $G_D(t_c)$, a characteristic triplet term $G_T(t_c)$ and an antibunching term $G_A(t_c)$, scaled with the mean reciprocal particle number ($1/N$) in the detection volume element and superimposed on the poissonian contribution $G(\infty) = 1$[Mets, 2001] [Widengren, 2001].

$$\begin{aligned} G^{(2)}(t_c) &= 1+\frac{1}{N}\left[G_D(t_c)+G_T(t_c)+G_A(t_c)\right] \\ &= 1+\frac{1}{N}\left[\left(\frac{1}{1+(t_c/t_D)}\right)\left(\frac{1}{1+\left(\frac{\omega_0}{z_0}\right)^2 (t_c/t_D)}\right)^{1/2} + \frac{T}{m(1-T)}\exp(-t_c/t_T) - \frac{1}{m(1-T)}\exp(-t_c/t_A)\right] \quad \text{(Eq. 2.2.4-10)} \end{aligned}$$

This model assumes a 3-dimensional Gaussian shaped volume element with spatial distribution of the detection probabilities:

$$w(x,y,z) = \exp\left(-2\left(x^2+y^2\right)/\omega_0^2\right)\exp\left(-2z^2/z_0^2\right). \quad \text{(Eq. 2.2.4-11)}$$

The $1/e^2$ radii in x and y or in z direction are denoted by ω_0 or z_0, respectively. The characteristic diffusion time t_D can be used to estimate the diffusion coefficient D: $t_D = \omega_0^2/4D$. From the equilibrium fraction of molecules in the triplet state, T_{eq}, and the triplet correlation time, t_T, the rate constants for intersystem crossing, k_{ISC}, and triplet decay, k_T, can be derived. The characteristic rise time of the antibunching term t_A is the reciprocal sum of the rate constants for excitation k_{01} and fluorescence decay k_0: $t_A = 1/(k_{01} + k_0)$. A variable m is included to take into account the possibility of multiple independent fluorophores per diffusing particle. A possible uncorrelated background due to darkcounts or scatter is not considered here but should be taken into account for quantitative interpretation of the amplitude $1/N$ [Koppel, 1974].

If the timescales of all the effects are at least an order of magnitude different, the correlation curve can be modelled by the product of their respective correlation functions. Translational diffusion, triplet formation, rotational diffusion and fluorescence antibunching effects are included in the correlation function equation as given by [Mets and Rigler, 1994]:

$$G^{(2)}(t_c) = 1 + \underbrace{\frac{1}{N}\left(1+\frac{t_c}{t_d}\right)^{-1}\left[1+\frac{t_c}{t_d}\left(\frac{\omega_0}{z_0}\right)^2\right]^{-1/2}}_{\text{translational diffusion term}} \underbrace{\left[1-T+T\cdot\exp\left(-\frac{t_c}{t_T}\right)\right]}_{\text{triplet term}} \cdot \underbrace{\left[1+R\cdot\exp\left(-\frac{t_c}{t_R}\right)\right]}_{\text{rotational diffusion term}} \cdot \underbrace{\left[1-A\cdot\exp\left(-\frac{t_c}{t_A}\right)\right]}_{\text{antibunching term}}$$

(Eq. 2.2.4-11a)

where R is the rotational fraction of the correlation function amplitude, t_R is a characteristic rotational diffusion time, A is the antibunching fraction of the correlation function amplitude, t_A is the characteristic photon antibunching which reflects the quantum nature of light emission and is defined by the excitation and fluorescence decay rates.

For freely diffusing molecules with a single fluorophore (m = 1, eq. 2.2.4-10), the amplitude of the correlation curve at time zero, $G(0)$, is equal to 1 and independent on the number of molecules in the sample volume. For $m > 1$, e.g. for multiply labelled molecules, complexes etc. this no longer holds. From eq. 2.2.4-10 follows:

$$G^{(2)}(0) = 1 + \frac{1}{N}\left[1-\frac{1}{m}\right] > 1. \qquad \text{(Eq. 2.2.4-12)}$$

This effect can be used to estimate the number of independent fluorophores per particle.

Pulsed excitation and short-time correlation: For simultaneous lifetime and correlation measurements pulsed excitation is required. The nonclassical photonbunches of the laserlight will result in a train of equally spaced correlation peaks superimposed on the correlation function, broadened by the fluorescence lifetime ($\tau = (k_0)^{-1}$) and the instrumental response function (IRF). Due to the pseudo-logarithmic time-binning used in the software correlation this modulation vanishes at higher times due to averaging of many excitation periods. In the constant time-binning regime and assuming single exponential decay of the detected fluorescence, a sum of shifted exponentials can be used to fit the data [Beveratos et al., 2002] [Felekyan et al., 2005]:

$$G^{(2)}(t_c) = C_{i=0}\exp\left(-\frac{|t_c - t_0|}{\tau_d}\right) + \sum_{i=1}^{n} C_i\left(\exp\left(-\frac{|t_c - t_0 + it_L|}{\tau_d}\right) + \exp\left(-\frac{|t_c - t_0 - it_L|}{\tau_d}\right)\right)$$

(Eq. 2.2.4-13)

C_i are the amplitudes of the central/lateral peaks, t_0 a possible offset between detection channels, t_L the time between laser pulses and τ_d the signal decay time, which for negligible width of the IRF equals the fluorescence lifetime. The amplitudes C_i can be related to the normalized correlation amplitude values $G(i \cdot t_L)$ that would be measured in a cw experiment at $t_c = i \cdot t_L$ by eq. 2.2.4-14.

$$G(i \cdot t_L) = C_i \frac{2\tau_d}{t_L} \qquad \text{(Eq. 2.2.4-14)}$$

At high repetition rates, i.e. with spacings between the laserpulses of the order of the fluorescence decay time, the peaks in the correlation curve partially overlap. In this case only fitting of a model function like eq. 2.2.4-3 allows one to approximately resolve coincident photon pairs originating from excitation pulses with defined spacing. By that means the undisturbed correlation amplitude at time zero, $G(0)$, can be calculated which e.g. is necessary to determine the number of independent emitters with eq. 2.2.4-12.

At reduced repetition rates, i.e. $t_L \gg \tau_d$, correlation of the macro-times or building histograms of coincident photons [Weston et al., 2002] is sufficient to calculate $G(0)$. A quantitative interpretation still requires knowledge of the complete correlation curve, e.g. the degree of triplet excitation T and other dark states and, for investigations of mobile emitters, the number of independently diffusing particles N. Reducing the repetition rate to avoid overlapping decays reduces the time resolution and, in case the observation time is limited, also the efficiency of the experiment. In these cases high repetition rate laser excitation followed by analysis of the correlation curves with eq. 2.2.4-13 and 2.2.4-14 might be an alternative.

Fitting of the above model functions to the data is performed by a Levenberg-Marquardt routine. Constant weighting was applied for correlation curves with equal time-binning, while for variable binning according to eq. 2.2.4-6 a modified procedure based on the work of Koppel was applied [Koppel, 1974].

2.2.4.2.1 Simplified modelling of the FCS parameters.

For the case of short-time measurements (for example in imaging, see Chapter 4) obtained correlation curves have high sort noise, therefore fitting procedure with the model functions described above does not give a reasonable outcome. In order to characterize main features of such a curves the following descriptive parameters can be calculated:

The mean correlation amplitude, g_m, of the correlation function, $G^2(t_c)$, is defined for a certain range of correlation times, $t_c(c_{start})$ to $t_c(c_{end})$, where the correlation amplitude reaches a saturation level (eq. 2.2.4-1)).

$$g_m = \frac{\sum_{c_{start}}^{c_{end}} G^2(c_i)}{c_{end} - c_{start}}, \qquad \text{(Eq. 2.2.4-15)}$$

The correlation decay time, t_m, is a descriptive parameter and is calculated using a geometric approximation to reduce shot noise. Taking into account that the correlations times t_c have a pseudo-logarithmic time axis, where the values are ordered in a linear array of time channels c_i, the mean channel number, c_m, is calculated first. Then it is converted by linear interpolation to the corresponding correlation decay time t_m (eq. 2.2.4-16).

$$c_m = \frac{\sum_i (G^2(c_i) - 1)}{g_m - 1} \qquad \text{(Eq. 2.2.4-16)}$$

2.2.4.3 FCS for the short measurement times

The approach for calculating the FCS curves, described in chapter 2.2.4.1 is applicable for cases where the measurement time window is significantly bigger than the correlation time of interest. However, this is not the case in imaging, where the approached integration time per pixel T is of the order of the defined correlation time t_c.

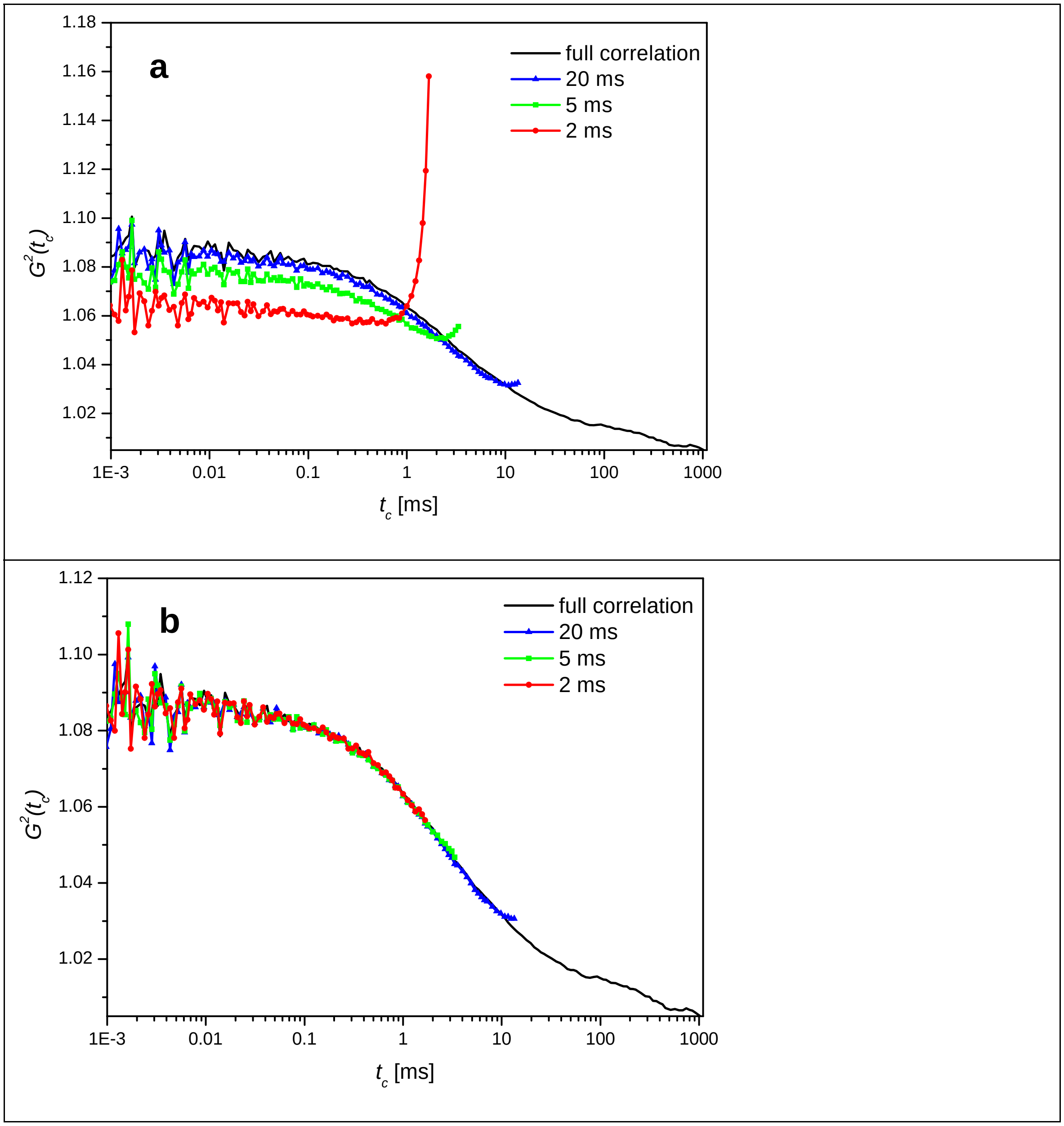

Figure 2.2.4-4. Correlation curves, calculated for simulated time windows of 2, 5 and 20 ms and for complete continuous trace. Calculations were done according to eq. 2.2.4-17 (a) and eq. 2.2.4-18 (b)

The influence of different measurements times on the correlation function was tested in the following way. For data that were taken continuously at one spot of the yeast cell (see Chapter 4.2 for sample details) time windows (pixels) of 2, 5 and 20 ms were simulated by cutting the fluorescence trace in K time windows (pixels). Fig. 2.2.4-4a shows cumulative correlation curves which were obtained by averaging over all the time windows with defined duration according to eq. 2.2.4-17 (for details on selective analysis see next chapter). The correlation curve for the complete continuous measurement is shown as well.

$$G^{(2)}(t_c)=\frac{\left(\dfrac{\sum\limits_{k=1}^{K}P_k(t_c)}{\sum\limits_{k=1}^{K}t_{mcs}(k)}\right)}{\left(\dfrac{\sum\limits_{k=1}^{K}N_1(k)}{\sum\limits_{k=1}^{K}t_1^{\max}(k)}\right)\left(\dfrac{\sum\limits_{k=1}^{K}N_2(k)}{\sum\limits_{k=1}^{K}t_2^{\max}(k)}\right)}, \qquad \text{(Eq. 2.2.4-17)}$$

where the un-normalized correlation function (number of pairs), $P_k(t_c)$, is calculated for each separate time window k by eq. 2.2.4-7, $N_1(k)$ and $N_2(k)$ are the total numbers of photons in channel 1 and 2, $t_1^{\max}(k)$ and $t_2^{\max}(k)$ are the time-bin numbers of the last photons in detection channel 1 and 2, respectively, K is the total number of time windows.

Figure 2.2.4-4a shows a decrease in the time window duration leads to a drop in the amplitude and produces a strong artifact at long correlation times. The durations of MCS traces, $t_1^{\max}(k)$, $t_2^{\max}(k)$, are calculated for eq. 2.2.4-17 by the difference of the first and the last photon bin number in the corresponding channel and for low countrates can strongly differ from the original simulated duration of the time window. Therefore in this case a modified eq. 2.2.4-18, should be applied:

$$G^{(2)}(t_c)=\frac{\left(\dfrac{\sum\limits_{k=1}^{K}P_k(t_c)}{K\cdot T}\right)}{\left(\dfrac{\sum\limits_{k=1}^{K}N_1(k)}{K\cdot T}\right)\left(\dfrac{\sum\limits_{k=1}^{K}N_2(k)}{K\cdot T}\right)} \qquad \text{(Eq. 2.2.4-18)}$$

where T corresponds to the duration of the simulated time windows or to the integration time of the pixel.

Correlation curves, calculated for a given integration time according to eq. 2.2.4-18 are shown in Fig. 2.2.4-4b. They show the same correlation as the complete trace, i.e. even if the size of pixel integration time window is too small to get the full correlation curve, the data are still sufficient to obtain a correct shape and absolute amplitude.

For cases where the measurement time window is comparable with the correlation time of interest not all intensity values of the time trace with bin width t_{bin} must be used to calculate the mean intensities. For these cases, a corrected algorithm is applied for calculation of the mean intensity. The pixel integration time T and the correlation time t_c can be expressed by the corresponding bin integer numbers N_T and N_c. of a given time binning t_{bin}: $T = t_{bin}\, N_T$ and $t_c = t_{bin}\, N_c$. In this way the number of intensities used for calculation is given by N_T-N_c.

$$G(t_c) = \frac{\frac{1}{\left(N_T - N_c\right)} \sum_{i=1}^{N_T - N_c} F_1(t_i) \cdot F_2(t_i + t_c)}{\frac{1}{N_T - N_c} \sum_{i=1}^{N_T - N_c} F_1(t_i) \cdot \frac{1}{N_T - N_c} \sum_{i=N_c}^{N_T} F_2(t_i + t_c)} \qquad \text{(Eq. 2.2.4-19)}$$

2.2.5 Selective and sub-ensemble analysis

With the MFD technique it is possible to select a sub-ensemble in a heterogenic sample by characteristic fluorescence properties and separate it for further analysis. All photons that correspond to the selected sub-ensemble can be added together to reduce the shot noise for better determination of fluorescence parameters.

This approach can be applied not only in the investigation of freely diffusing molecules in solution [Eggeling et al., 2001b] [Schaffer, 2000], but also in imaging [Kudryavtsev et al., 2006].

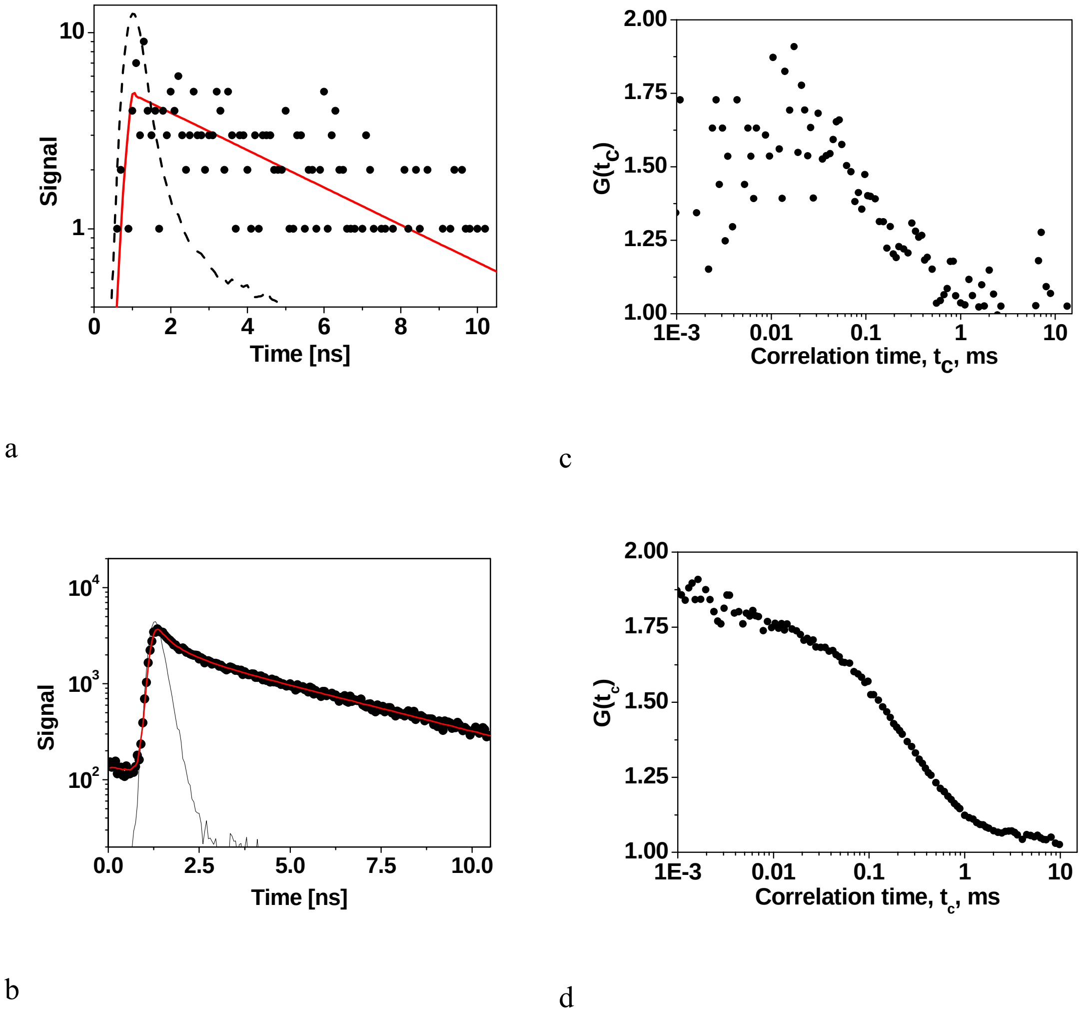

a

c

b

d

Figure 2.2.4-5 Pixelwise and pixel-selective analysis: Fluorescence lifetime decay of a single pixel (a) and of a selected set of pixels (b). The red line corresponds to the fitted model function, the dashed line indicates the instrumental response function. Correspondingly, correlation curves are calculated for a single pixel (c) as well as for a selected set of pixels (d).

Fig. 2.2.4-5a displays fluorescence decay for a single pixel, which is characterized by a high noise level, so that only a single fluorescence lifetime of 3.9 ns can be estimated by a maximum likelihood estimator (chapter 2.2.2).

If, however, a fluorescence arrival time histogram is accumulated for a sub-ensemble of selected pixels or single-molecule bursts, noise is reduced and a much higher level of accuracy can be reached (Fig. 2.2.4-5b), which allows one to detect more than a single fluorescent species. Besides 10 % scattered background the fitted model function has two fluorescent components with the lifetimes τ_{long}= 4.5 ns (64%) and τ_{short}= 0.6 ns (36%).

Considering the fast scanning speed of confocal laser scanning microscopy, fluorescence lifetime imaging (FLIM) with a high accuracy can only be reached for the analysis of a pixel subensemble but not for a single pixel. MFD-imaging shows that the issues of speed or accuracy do not exclude each other but they can be combined in a single measurement with suitable data acquisition and analysis.

Similar arguments can also be applied for FCS [Eggeling et al., 2001b]. All photons from a set of single molecule bursts or pixels that correspond to a given sub-ensemble can be used for calculating one cumulative correlation function, $G^{(2)}(t_c)$, according to eq. 2.2.4-17. This equation should be applied if analysed subpopulation is homogeneous and the mean fluorescence signal is constant over time. If this is not a case, another kind of normalization should be used (eq. 2.2.4-20):

$$G^{(2)}(t_c) = \frac{1}{K}\sum_{\mathrm{k}=1}^{K} \frac{\left(\dfrac{P_k(t_c)}{t_{mcs}(k)}\right)}{\left(\dfrac{N_1(k)}{t_1^{\max}(k)}\right)\left(\dfrac{N_2(k)}{t_2^{\max}(k)}\right)} \qquad \text{(Eq. 2.2.4-20)}$$

Fig 2.2.4-5c displays a FCS curve calculated from photons detected in a single pixel using an integration time of 20 ms. It is evident, that the curve has an amplitude > 1 and a bunching term in the range of 0.1 to 1 ms. The statistical significance of this observation is validated by the pixel sub-ensemble analysis shown in fig. 2.2.4-5d. This means that even if the noise of correlation curves of single pixels is high, it is still possible to derive statistically meaningful correlation functions by sub-ensemble averaging.

3 MFD of freely diffusing molecules in solution

Following chapter presents applications of MFD in study of the freely diffusing molecules in solution on the single molecule level. It is shown, that with MFD it is possible to identify and separate 16 different compounds in the mixture of FRET-labelled oligonucleotides (Chapter 3.1). MFD can also deliver detailed information on specific molecular dynamic processes. In chapter 3.2 investigation of the F_0F_1-ATP synthase subunit rotation during ATP hydrolysis and synthesis is presented.

3.1 Identification of multiple species by MFD

A general strategy to identify and quantify single molecules in dilute solution employing MFD was developed and applied in this work. Here a dye labelling scheme of oligonucleotides is demonstrated, by which it is possible to identify and separate 16 different compounds in the mixture. Such multiplex assays with single-molecule sensitivity may have a great impact on the screening of species and events that don't lend themselves so easily to amplification, such as disease-specific proteins and their interactions [Sauer et al., 1997] [Scheffler et al., 2005].

Experiment was carried out on a set-up, described in chapter 2.1, all the fluorescence parameters were calculated according to chapter 2.2.

This investigation was done in cooperation with Prof. Dr. Jerker Widengren, Royal Institute of Technology, Stockholm and presented in [Widengren et al., 2006].

3.1.1 Sample

For this studies, a deoxyoligonucleotide *N1* containing 27 nucleobases in a random sequence was synthesized using the standard phosphoamidite-technology: 5'-d(TTG AAA ACG AGA GAG ACA TAA ACG ATC). The 5'-d of this deoxyoligonucleotide was labeled via a C6 amino link either with the N-hydroxysuccinimide (NHS)-ester of Cyanine 3 (Cy3) (Amersham Pharmacia Biotech) or Rhodamine 6G (Rh6G) (Molecular Probes, Eugene (OR)) as donor dyes. Using a postlabeling reaction the acceptor dyes (BP650/665) (Molecular Probes, Eugene (OR)) or Cyanine 5 (Cy5) (Amersham Pharmacia Biotech) were covalently attached to an 5'-C6-Amino-2'd**T** at a defined position (with 9, 13 or 17 base-pairs (bp) between the linked dyes) on the complementary deoxyoligonucleotide *N2*: 5'-d(GAT CGT TTA **T**GT C**T**C TC**T** CGT TTT CAA). The oligonucleotides were double HPLC-purified and additionally PAGE-purified.

Schematic representation of the oligonucleotide labelled with Rh6G donor and Cy5 acceptor dyes is shown in Fig. 3.1-1.

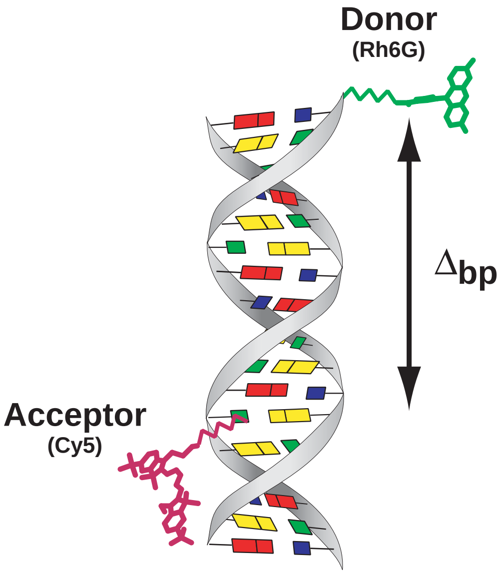

Figure 3.1-1. Schematic representation of the oligonucleotide labelled with Rh6G donor and Cy5 acceptor dyes.

All synthesis and purification was done by IBA GmbH (Göttingen, Germany). Hybridization was performed in a buffer containing 180 mM NaCl, 12 mM Na-citrate, and 25 µM $MgCl_2$ (pH 7.5). To obtain the FRET-active molecules, complementary donor and acceptor labeled strands (N1 and N2) were mixed in a 1:1 ratio and slowly cooled from 95 to 20 °C. In all experiments, a sodium phosphate buffer with 180 mM NaCl, 10 mM NaH_2PO_4/Na_2HPO_4, and 400 µM Na-ascorbate (pH 7.5) was used. The following 16 molecules were analyzed: Cy3-Cy5(9, 13 or 17 bp), Cy3-BP650/665(9, 13 or 17 bp), Cy3-oligonucleotide, Rh6G-Cy5(9, 13 or 17 bp), Rh6G-BP650/665(9, 13 or 17 bp), Rh6G-oligonucleotide and two fluorescent impurities of unknown structure ***I1*** and ***I2***.

3.1.2 Spectrofluorimetric and TCSPC measurements.

The labeled single-stranded oligonucleotides were investigated in a spectrofluorometer (Jobin-Yvon Fluorolog 3) with respect to the excitation and fluorescence spectra of the dyes attached to them. The fluorescence lifetimes were investigated by time-correlated-single-photon-counting (TCSPC), performed by the MFD instrumentation (Chapter 2.1) at concentrations of approximately 100 pM. In the TCSPC experiments, the donor (Rh6G and Cy3) and the acceptor (Cy5, BP650/665) dyes were excited by the argon-ion (514nm) and the krypton-ion (647nm) laser, respectively. The measured fluorescence lifetimes of the dyes and their maximum absorption and emission wavelengths are given in table 3.1-1 and the spectra in Fig. 3.1-2.

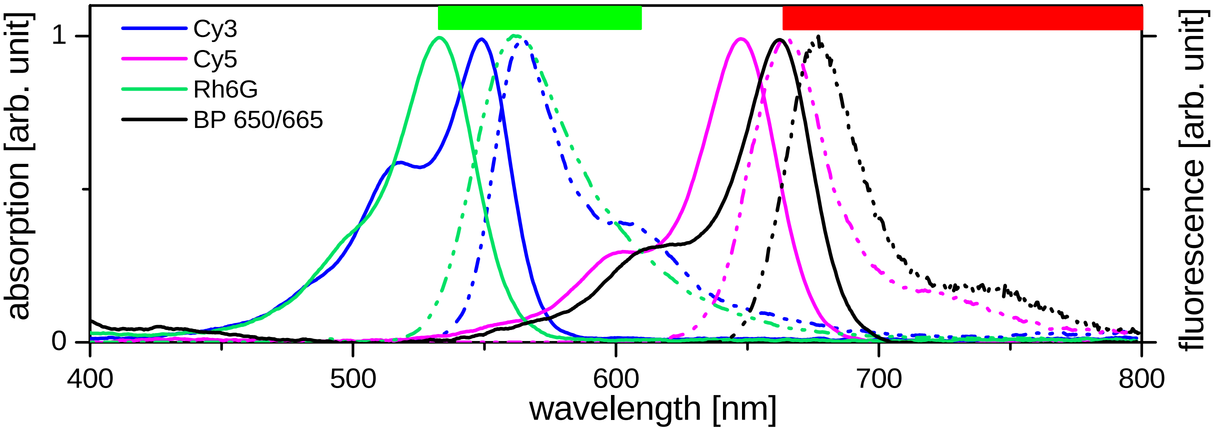

Figure 3.1-2 Absorption (solid line) and emission (dashed line) spectra of Rh6G, Cy3, Cy5, BP650/665 dyes. Bars on the top indicate transmission range of the filters for single molecule spectroscopy.

Dye label at oligonucleotide	τ [ns] [a]	λ_{Abs} / λ_F [nm]	Spectral detection [nm]
Rh6G	4.0	534 / 564	535 - 605
Cy3	0.8 [b]	550 / 565	535 - 605
BP650/665	4.3	663 / 678	665 - 800
Cy5	1.0	649 / 665	665 - 800

Table 3.1-1

[a]: The experimentally measured fluorescence lifetimes using the avalanche APDs of the Series "AQR" are increased due to a count rate dependent jitter by approx. 10 %. The listed τ values are corrected for this effect, but the τ-histograms shown in Fig 3.1.4 - 3.1-7 were not corrected for this effect.

[b]: Surprisingly the Cy3 labeled DNA samples contain large amounts of a fluorescent species with a fluorescence lifetime of 1.5 ns. It is classified as an impurity because is not quenched by FRET as the species with $\tau = 0.8$ ns. It is assumed that the species with $\tau = 1.5$ ns are not attached to the oligonucleotide.

3.1.3 Graphical MFD analysis

The different oligonucleotides were measured and analysed burstwise with respect to all their fluorescence parameters on the single molecule level by MFD, as described in the chapter 2.2. For each type of the dye-labeled oligonucleotides, the detected molecules were measured and sorted into a multi-dimensional cumulative histogram, based on their determined fluorescence parameters. The fluorescence bursts from all the different oligonucleotides were then arranged into one joint histogram.

In Figure 3.1.3, a two-dimensional projection of this histogram is shown, where the fluorescence bursts from all the measured compounds have been arranged with respect to their count rates in the green and red emission ranges, S_G and S_R.

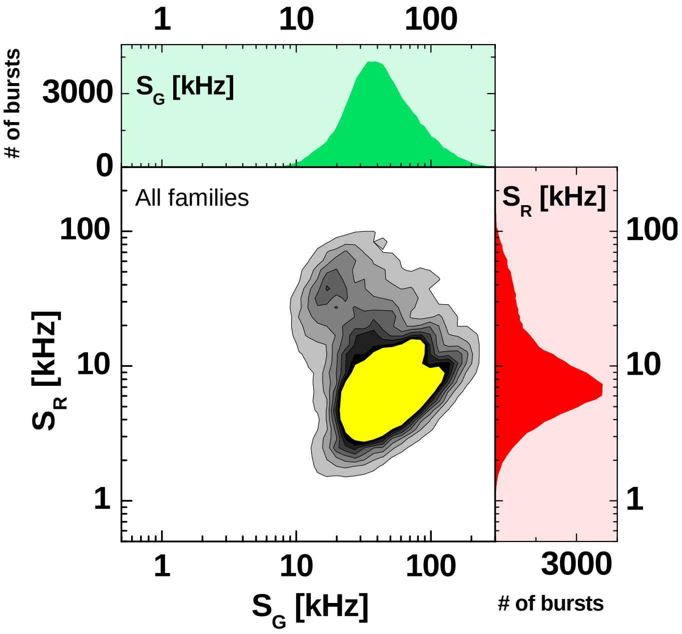

Figure 3.1-3. Cumulative histogram of all compounds. Red signal, S_R is plotted versus green signal S_G. Frequency is coded by gray scale. To visualize also small subpopulations, a Z-magnified view is presented, where all frequencies above 0.2 of the maximum are displayed in yellow as a single level. Total number of molecules $A_{total} = 92694$

Even though recording takes place at the single molecule level, which should in principle provide the possibility to reveal subpopulations within an ensemble of molecules, it is clear that at least a characterization based on only S_G and S_R is in this case not sufficient to identify the different subpopulations. From this histogram, it is also not possible to extract from how many different compounds the data have been recorded. To demonstrate the full dynamic range of MFD figures 3.1.3 and 3.1-5 - 3.1-9 are present in Z-magnified views with the last level indicated in uniform yellow (see), that focuses the dynamic range of the gray scale to the border zones between the different populations.

To better distinguish between the species, a procedure where the subpopulations are identified based on a set of parameters, and where a systematic selection of subpopulations within different ranges of the detected parameters will be performed in several steps(see Diagram 3.1-1). The general rationale for this multi-step selection procedure is that the different compounds differ distinctly from each other with respect to at least one measurable parameter, or that combinations of parameter values can be used to enhance differences between compounds that do not differ distinctly with respect to a single parameter.

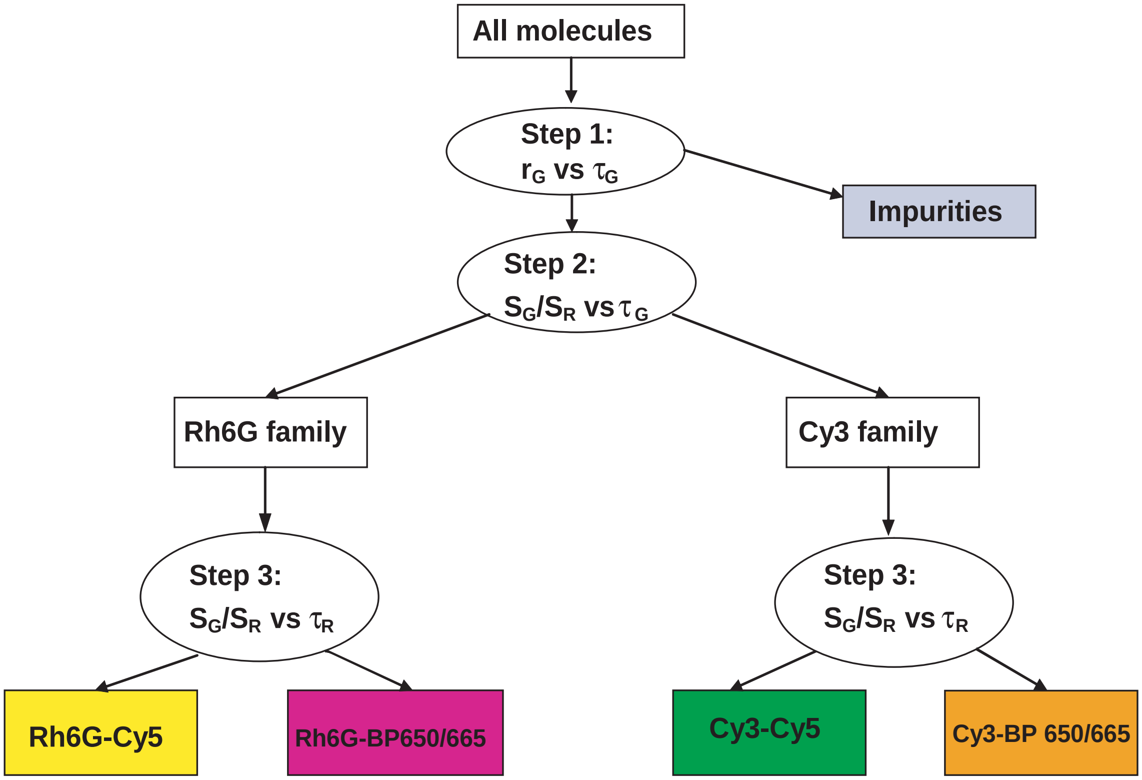

Diagram 3.1-1. General approach for species sorting.

In this study, differences between the compounds in rotational mobilities (characterized by different anisotropies, r_G, for free and labeled fluorophores), FRET efficiencies (different dye-to-dye distances reflected in S_G, S_R, τ_G, τ_R), and differences due to the identities of the donor and acceptor dye labels (S_G, S_R, τ_G, τ_R), or differences in combinations of the parameters are exploited within the frame of this general strategy for systematic selection. As shown in table 3.1.1, donor dyes (Rh6G and Cy3) and acceptor dyes (BP650/665 and Cy5) with a long and a short fluorescence lifetime, respectively, have been chosen for the green and the red spectral windows. Based on their characteristic fluorescence lifetimes, four distinct oligonucleotide families (Rh6G-BP650/665, Rh6G-Cy5, Cy3-BP650/665 and Cy3-Cy5) with different DA distances have been studied.

3.1.3.1 Step 1: selection in the r_G vs τ_G parameter plane.

As a first step, the multi-dimensional cumulative histogram was projected onto a two-dimensional histogram, with the bursts sorted with respect to the measured fluorescence anisotropy, r_G, and the fluorescence lifetimes, τ_G, of their donor fluorophores (r_G - τ_G-histogram). Given its formal expression (see methods section), it is clear that r_G will increase with shorter fluorescence lifetimes. This is illustrated in the r_G - τ_G histogram of Fig. 3.1-4.

For comparison, lines corresponding to mean rotational correlation times ρ of 0.2 ns, 2.0 ns and 7.0 ns are included, which are calculated from the Perrin equation, $r_G = r_0/(1+\tau/\rho)$, using a fundamental anisotropy $r_0 = 0.375$.

In view of the broad range of fluorescence lifetimes covered, the observed anisotropy, broadened by shot noise, is also very wide. The anisotropies of the major subpopulations consisting of the donor dyes linked to the oligonucleotides are well described by a mean rotational correlation time of $\rho = 2.0$ ns. However, there are two subpopulations, marked as ***I1*** and ***I2***, with fluorescence lifetimes τ_G = 1.8 and 4 ns, which have very small mean rotational correlation times of approx.0.2 ns (blue line). The small rotational correlation time is evidence for the existence of free impurities, which emit in the green spectral range and are not subject to FRET-mediated quenching of their fluorescence.

Based on this, a limit was defined such that only labeled oligonucleotides with $r_G >$ 0.107 (red line) were selected for further analysis. Thereby, the highly rotationally mobile fluorescent impurities ***I1*** and ***I2*** with rotational correlation times short enough not to be attributed to the rotation of donor-labeled oligonucleotides could be sorted out with high certainty but rather attributed to free dye.

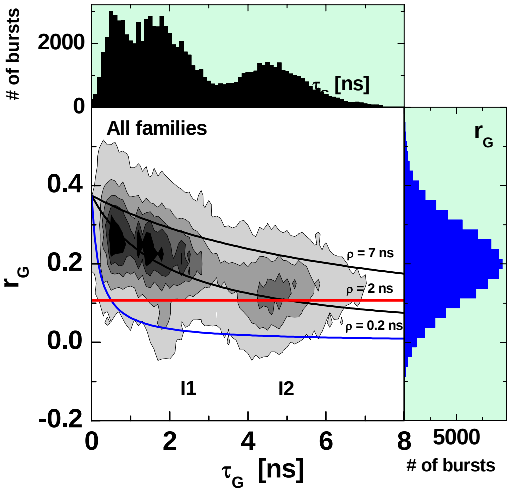

Figure 3.1-4. Green lifetime, τ_G is plotted versus anisotropy, $r_{G,}$ together with an overlaid Perrin equation computed for 3 rotational correlation times (0.2, 2, 7 ns). Molecules under the red line were excluded from further analysis. Total number of molecules A_{total} = 92628.

3.1.3.2 Generation of characteristic patterns.

In the present qualitative analysis, the aim is to detect the presence of an individual subpopulation. For this generated characteristic patterns of different individual species of donor-acceptor labeled oligonucleotides were generated. These characterisitic patterns guide the definition of the areas in various parameter planes as belonging to a particular species. Specific patterns were generated for all two-dimensional parameter planes by analyzing the individual subpopulations separately. In addition to free dye molecules, fractions of molecules which are not labeled at all or which are not completely labeled remain in practically all labeling procedures. In order to distinguish fully labeled molecules from incompletely labeled ones, one can refer back to the cumulative histograms of the individual oligonucleotide species from which free dye molecules have been sorted out by use of the criterion of step 1. Figures 3.1-5 A-C show three typical two-dimensional histograms, with oligonucleotides labeled with Rh6G (donor) and Cy5 (acceptor) with different distances between the labeling sites. The measurements can be evaluated by depicting the ratios of their signal intensities detected in the green (S_G) divided by those in the red (S_R) wavelength range, S_G/S_R, along the ordinate, and their donor fluorescence lifetimes, τ_G, along the abscissa.

It can be seen from these S_G/S_R - τ_G histograms that the fractions of oligonucleotides that are not labeled with acceptor dyes can be clearly distinguished from those labeled with both dyes. Oligonucleotides that were labeled with both donor and acceptor dyes (DA-oligonucleotides) show FRET-mediated quenching of the donor fluorescence and a concomitant FRET-sensitized fluorescence of the acceptor dye when the donor dye is excited by laser light at 514 nm. With higher FRET efficiencies increasingly lower ratios of S_G/S_R and shorter τ_G appear. DA-oligonucleotides accumulate in distinct fractions with lower S_G/S_R and shorter τ_G, well separable from oligonucleotides, having just a donor fluorophore labeled to them (D-oligonucleotides). Acceptor labeled oligonucleotides (A-oligonucleotides) are practically not excited at an excitation wavelength of 514 nm, and are thus not detectable in the current experiment.

Further, for DA-oligonucleotides labeled with the same donor-acceptor dye pair, the positions of the population of DA-oligonucleotides in the histograms differ distinctly depending on the dye-to-dye distance (distances between the two dyes in Figures 3.1-5A, 3.1-5B, and 3.1-5C of 17, 13 and 9 base-pairs, respectively). The differences of the individual histograms should thus provide patterns from which it is possible to separate D-oligonucleotides from DA-oligonucleotides, and to distinguish between the DA-oligonucleotides in the joint histograms via their specific FRET-efficiencies defined by the distances between the labeling sites of their donor and acceptor fluorophores.

For this graphical analysis it is sufficient to approximate the characteristic patterns by variable ellipses with characteristic colors for the four families of DA oligonucleotides

[Rh6G-BP650/665 (magenta), Rh6G-Cy5 (yellow), Cy3-BP650/665 (orange) and Cy3-Cy5 (olive)] and for the D-oligonucleotides of Rh6G and Cy3 (black). The size of these elliptic patterns in the contour plots is defined by the area in which the frequency is 20% of the maximum value or higher. For histogram containing a mixture of species, such elliptic patterns guide the definition of areas within which the different individual species are confined.

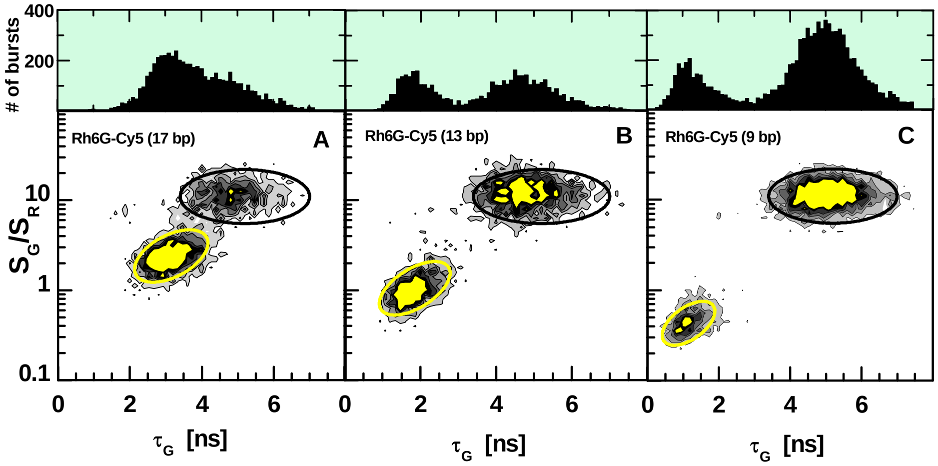

Figure 3.1-5 Fluorescence count rate ratio S_G /S_R is plotted versus green lifetime, τ_G for individual populations of oligos labeled with Rh6G (donor) and Cy5 (acceptor) with different distances between the labelling sites (17 (A), 13 (B) and 9 base-pairs (C)).

Black ellipses show patterns for donor-only labeled oligos, yellow ones – for oligos labeled with both donor and acceptor. Z-magnified view, where all frequencies above 0.4 of the maximum are displayed in yellow as a single level. Total number of molecules: (A) A_{total} = 5856, (B) A_{total} = 4768, (C) A_{total} = 9804.

3.1.3.3 Step 2: Selection in the S_G/S_R vs τ_G parameter plane.

After separation of free dyes from the mixture in step 1 above, differences in the macroscopic fluorescence properties of the fluorophores (Table 3.1-1) were exploited in sequential steps to separate the subpopulations of the remaining oligonucleotides. First, the oligonucleotides were separated into two main groups based on the differences in the intrinsic fluorescence lifetimes of their donor fluorophores (Rh6G (4 ns) and Cy3 (0.8 ns)). This was performed by displaying the detected oligonucleotides in a S_G/S_R versus τ_G histogram. As mentioned above, higher efficiencies of FRET generates increasingly lower ratios of S_G/S_R and shorter τ_G. However, irrespective of the degree of quenching of the donor dye due to FRET, oligonucleotides labeled with Rh6G can be separated from those labeled with Cy3. This separation is possible by virtue of the distinct differences in the measured τ_G between the molecules, which follow from the prominent difference in the intrinsic lifetimes of the two donor fluorophores. The separation of Cy3-labeled oligonucleotides from their Rh6G labeled counterparts is indicated by a red line in Fig. 3.1-6.

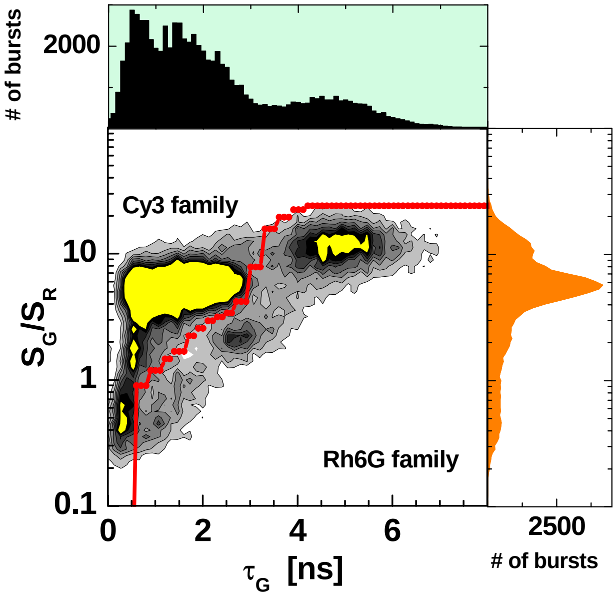

Figure 3.1-6 Fluorescence signal ratio S_G/S_R is plotted versus green lifetime, τ_G , for all measured compounds. Red line shows separation between populations of oligos labeled with Rh6G and Cy3 dyes. Z-magnified view, where all frequencies above 0.2 of the maximum are displayed in yellow as a single level. Total number of molecules $A_{total} = 74758$.

3.1.3.4 Step 3: Selection in the S_G/S_R vs τ_R parameter plane.

Following the separation of oligonucleotides based on the intrinsic donor fluorescence lifetimes (Fig. 3.1-6), oligonucleotides labeled with either Cy3 or Rh6G as donors were separated with respect to what acceptor dye was attached to them. This separation step is possible due to a large difference in the intrinsic lifetimes of the two acceptor dyes Cy5 (1.0 ns) and BP650/665 (4.3 ns) (see Table 3.1-1). In Fig. 3.1-7A and 3.1-7B, the histograms selected based on the different intrinsic donor lifetimes of the Cy3- and Rh6G-labeled oligonucleotides according to step 2 are each projected in a plane defined by the ratio S_G/S_R and the measured decay time in the red detection channels, τ_R. Here, a clear distinction can be seen for those oligonucleotides labeled with BP650/665 (4.3 ns) as the acceptor dye from those with Cy5 (1.0 ns). Disregarding the effect of the duration of the laser excitation pulses (which is subject to deconvolution), the measured acceptor fluorescence intensity is a convolution product of the donor and acceptor fluorescence intensity decay following a Dirac pulse, i.e. $F_A(t) \propto \int_0^t \exp(-t'/\tau_D) \times \exp(-(t-t')/\tau_A)dt'$ for mono-exponential fluorescence decays, where τ_D and τ_A are the lifetimes of the donor and acceptor dye, respectively. In contrast to the determination of the donor fluorescence lifetime from the complete fluorescence response curve it is at present sufficient that only decaying part of the complex fluorescence response of the acceptor is judged by a single exponential decay without deconvolution having a characteristic signal decay time, τ_R [Eggeling et al., 2001b]. Short D-A distances generate short donor lifetimes, and thus also a shorter time over which excitation by energy transfer to the acceptor dye can take place. Consequently, for oligonucleotides with shorter D-A distances, typically a shorter time interval passes after the excitation pulse until the acceptor dye is excited and subsequently fluoresces, although the intrinsic fluorescence lifetime of the acceptor remains the same. This effect can most clearly be seen for those oligonucleotides having Rh6G as a donor dye (Fig. 3.1-7B), since the absolute changes in fluorescence lifetime upon FRET are larger with Rh6G than with Cy3, due to the shorter intrinsic fluorescence lifetime of Cy3. Likewise, with a relatively short intrinsic fluorescence lifetime of the acceptor dye, the relative effect of convolution by the donor fluorescence decay is more prominent and distinct as can be seen for the Rh6G-Cy5 labeled oligonucleotides in Fig. 3.1-7B. Considering the specific patterns, all DA combinations of the Rh6G family can easily be distinguished, which allows for the simultaneous detection of seven oligonucleotides: Rh6G-Cy5(9, 13 and 17 bp), Rh6G-BP650/665(9, 13 and 17 bp), and Rh6G-oligonucleotide (D-oligonucleotide).

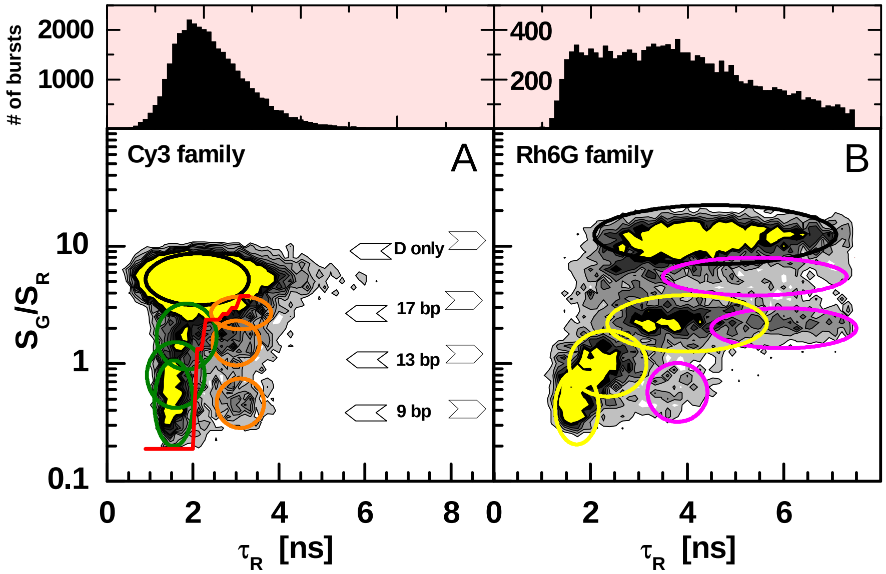

Figure 3.1-7. Fluorescence signal ratio, S_G/S_R, is plotted versus red decay time, τ_R, for oligos, labeled with Cy3 (A) and Rh6G (b) donor dyes. Green ellipses indicate patterns for Cy3-Cy5 populations, orange – Cy3-BP 650/665 populations, yellow – Rh6G-Cy5 populations, pink – Rh6G-BP 650/665 populations, black – donor-only labeled oligos. Red line shows separation between Cy3- BP 650/665 and Cy3- Cy5 populations. Z-magnified view, where all frequencies above 0.075 of the maximum are displayed in yellow as a single level. Total number of molecules: (A) A_{total} = 37275; (B) A_{total} = 14398.

3.1.3.5 Step 4: Selection in the S_R vs S_G parameter plane.

As indicated in Fig. 3.1-7A, a separation relying on D-A distances can be difficult when based solely on the S_G/S_R vs τ_R projection. Considering the Cy3 family, a substantial overlap of the oligonucleotides with different D-A distances can be noticed. For the case of overlap between populations of different species, additional projections can be used to increase the specificity of the separation of the different species from each other. In figures 3.1-8A and 3.1-8B the projections of the Cy3-Cy5 and Cy3-BP650/665 populations, both included in Figure 3.1-7A, are after separation (indicated by the red line in Figure 3.1-7A) plotted along S_G and S_R. In this case, this projection provides an additional criterion, enabling an improved separation of the oligonucleotides labeled with Cy3 as a donor, and either Cy5 (olive) or B650 (orange) as an acceptor, based on their D-A distances. In this way, the remaining seven oligonucleotides are identified: Cy3-Cy5(9, 13 and 17 bp), Cy3-BP650/665(9, 13 and 17 bp), Cy3-oligonucleotide (D-oligonucleotide).

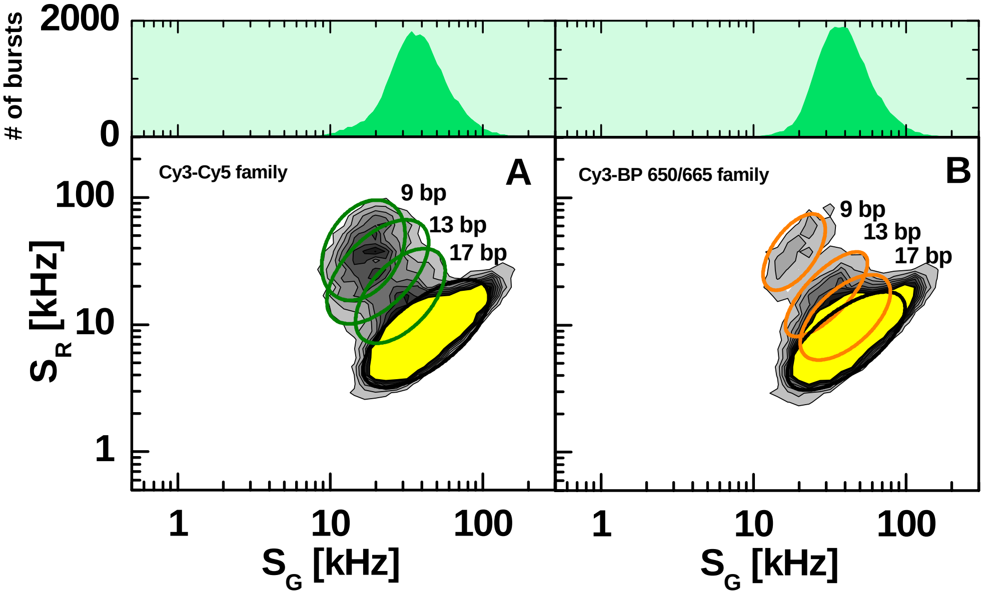

Figure 3.1-8. Red fluorescence signal S_R is plotted versus green, S_G, for Cy3-Cy5 populations (A) and Cy3- BP 650/665 populations (B). Green ellipses indicate patterns for Cy3-Cy5 populations, orange – Cy3-BP 650/665 populations. Z-magnified view, where all frequencies above 0.06 of the maximum are displayed in yellow as a single level. Total number of molecules: (A) A_{total} = 29035; (B) A_{total} = 29306.

3.1.4 Quantitative identification of the detected molecules.

The visual identification procedure, performed in sequential steps, as outlined above, forms the principal basis of an automated identification procedure which can determine the relative fractions of each species. The accuracy of such an approach would ideally be limited only by the ability to identify properly single molecule bursts for each species in the data. The following section presents, a procedure, which exploits the multi-dimensionality of the measured data, and which lends itself well for fast, stable, and reliable species identification of the detected species.

3.1.4.1 *Procedure.*

The core of the procedure is the estimation of the probability, $\Psi(m|\{\upsilon_{k\,exp}\}_\alpha)$. It states the probability that a detected molecule α, possessing a set of K independent experimentally determined fluorescence parameter values, $\{\upsilon_{1\,exp}, . , , \upsilon_{K\,exp}\}$, belongs to species m out of N different species with the index $n = 1$ to N. In the K-dimensional set $\{\upsilon_{k\,exp}\}_\alpha$, each of the K values corresponds to a unique fluorescence parameter, e.g. lifetime, anisotropy, etc.

As an intermediate step in determining Ψ, it is first necessary to determine a set of $K \times N$ probability distributions, $\{P_{k,m}(\upsilon_k), k = 1 \text{ to } K, n = 1 \text{ to } N\}$, which describes the probability that a molecule known to be of species m has a value for the k^{th} fluorescence parameter given by υ_k (or more precisely, has a value which falls into a bin centered around υ_k). In this report, the $P_{k,m}(\upsilon_k)$ distributions are generated from histograms obtained from the same MFD data used to determine the characteristic patterns above (for example, see 1D projections in Fig. 3.1.5), whereby the DA-oligonucleotides were first separated from the D-oligonucleotides and impurity species. The relevant histograms are normalized such that for each species m and parameter k, $\sum_\upsilon P_{k,m}(\upsilon_k) = 1$ (remembering that the values for υ are restricted to a finite set of bin centers). The probability $\Psi(m|\{\upsilon_{k\,exp}\}_\alpha)$ is calculated from the set of distributions $\{P_{k,m}(\upsilon_{k\,exp})\}$ as follows:

$$\Psi\left(m\middle|\left\{\upsilon_{k\,exp}\right\}_\alpha\right)=\frac{\prod_{k=1}^{K}P_{k,m}\left(\upsilon_{k\,exp}\right)}{\sum_{n=1}^{N}\prod_{k=1}^{K}P_{k,n}\left(\upsilon_{k\,exp}\right)} \tag{Eq. 3.1-1}$$

This ratio expresses the probability of a molecule from species *m* displaying the particular set of parameters $\{\upsilon_{k\ exp}\}$ (calculated in the numerator) relative to the probability that the set $\{\upsilon_{k\ exp}\}$ will be displayed by *any* of the *N* species (denominator). In absence of conformational dynamics (which is here the case) shot noise limited distributions for the individual parameters are measured. For each individual molecule α, a set of *N* probabilities, $\{\Psi(1|\{\upsilon_{k\ exp}\}_{\alpha}), \ldots \Psi(N|\{\upsilon_{k\ exp}\}_{\alpha})\}$, is calculated by Eq. 3.1-1 using the set of experimentally determined fluorescence parameters for that molecule, $\{\upsilon_{1\ exp}, .\, ., \upsilon_{K\ exp}\}_{\alpha}$. Since a molecule must belong to one of the *N* species, $\sum_n \Psi(n|\{\upsilon_{k\ exp}\}_{\alpha}) = 1$ for each molecule α. The molecule is then classified as belonging to that species m for which $\Psi(m|\{\upsilon_{k\ exp}\}_{\alpha})$ is the highest.

For each of the $n_d = 1, \cdot, m, \cdot, N$ DA- oligonucleotide data sets, a histogram was generated that counted how many molecules in that data set were assigned to each of the *N* species. The classification probability $\Omega(m|n_d)$, stating the probability that a molecule of the dataset n_d (i.e. originating from species $n=m$) is classified as species *m, is* obtained by normalizing the sum of each of these histograms to unity. By restricting analysis to a single dataset n_d, the classification probability $\Omega(m|n_d)$ can be defined as $\Omega(m|n_d) = \frac{a_m}{\sum_{n=1}^{N} a_n}$,

where $\{a_{n=1}; \ldots a_N\}$ are the numbers of molecules from dataset n_d assigned to species *m*.

3.1.4.2 Classification of single molecules.

The classification probabilities obtained for each of the $N = 12$ DA-oligonucleotide species are shown in Fig. 3.1-9 (for detailed values see Table 3.1-2). If $\Omega(n=n_d|n_d) = 1$, then there is no errors in classification. However, not all of the molecules of an individual data set n_d are indeed classified as belonging to species *m*, i.e. $\Omega(m=n_d|n_d) < 1$. This error is due to overlap of the one-dimensional probability distributions, $P_{k,n,}$, between the different species. However, by increasing the number of dimensions, *K*, the classification confidence can be improved. The classification probabilities shown in Fig. 3.1-9 use four fluorescence dimensions: green lifetime, τ_G, green anisotropy, r_G, red signal decay time, τ_R, and signal intensity ratio, S_G/S_R. Analysing $\Omega(m|n_d)$ in Fig. 3.1-9, the likelihood that a molecule of dataset is properly assigned to a species (i.e. the correct classification, $\Omega(n=n_d|n_d)$ always dominates over the other classification probabilities $\Omega(n\neq n_d|n_d)$, and exceeds 0.5 for all datasets with n_d.

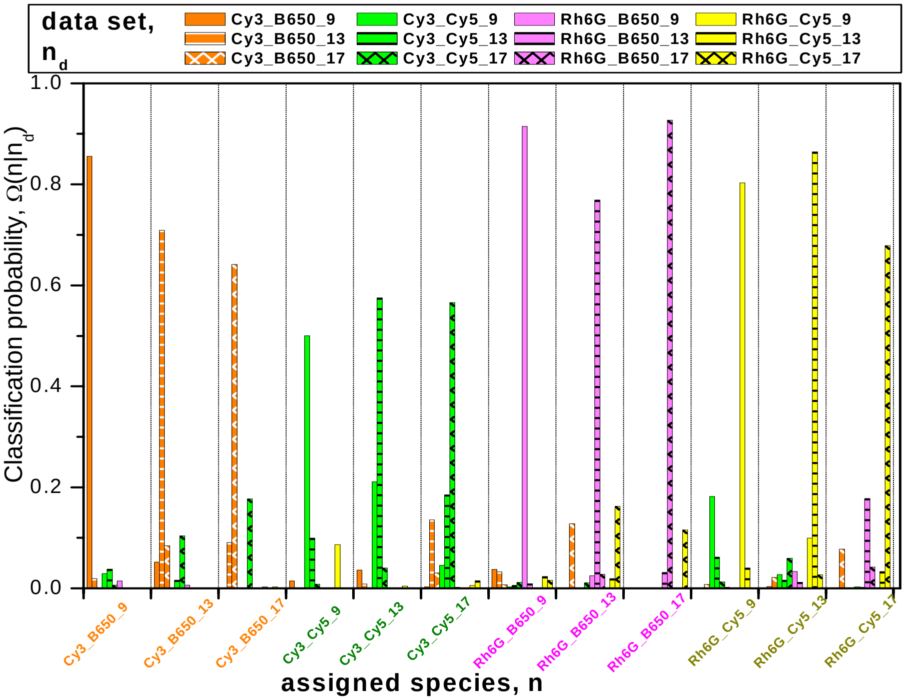

Figure 3.1-9. Classification probability, $\Omega(n|n_d)$, that an DA-oligonucleotide molecule of the data set n_d is classified as a species *n*. Calculations were based on the procedure, described in the text, using 4 fluorescence dimensions: green lifetime, τ_G, green anisotropy, r_G , red decay time, τ_R, and signal intensity ratio, S_G/S_R**.** (For detailed values see Table 3.1-2).

Dataset\species	Cy3_B650_9	Cy3_B650_13	Cy3_B650_17	Cy3_Cy5_9	Cy3_Cy5_13	Cy3_Cy5_17	Rh6G_B650_9	Rh6G_B650_13	Rh6G_B650_17	Rh6G_Cy5_9	Rh6G_Cy5_13	Rh6G_Cy5_17
Cy3_B650_9	**0.85521**	**0.05208**	**0**	**0.01458**	**0.03646**	**0.00312**	**0.0375**	**0**	**0**	**0.00104**	**0**	**0**
Cy3_B650_13	**0.01917**	**0.70919**	**0.09055**	**0**	**0.00859**	**0.13549**	**0.03305**	**0.00066**	**0**	**0**	**0.0033**	**0**
Cy3_B650_17	**0**	**0.08423**	**0.6413**	**0**	**0.00037**	**0.03066**	**0.00702**	**0.12819**	**0.00074**	**0.00776**	**0.0218**	**0.07795**
Cy3_Cy5_9	**0.02912**	**0.00104**	**0**	**0.50052**	**0.21109**	**0.04541**	**0.00312**	**0**	**0**	**0.18198**	**0.02773**	**0**
Cy3_Cy5_13	**0.03809**	**0.01632**	**0.0006**	**0.09976**	**0.57497**	**0.18561**	**0.00605**	**0**	**0**	**0.06227**	**0.01632**	**0**
Cy3_Cy5_17	**0.00656**	**0.10394**	**0.17724**	**0.00821**	**0.04048**	**0.56565**	**0.01149**	**0.01094**	**0**	**0.01313**	**0.05963**	**0.00274**
Rh6G_B650_9	**0.01461**	**0.00626**	**0**	**0**	**0**	**0.00209**	**0.9144**	**0.02505**	**0**	**0.00209**	**0.0334**	**0.00209**
Rh6G_B650_13	**0**	**0**	**0**	**0**	**0**	**0**	**0.00945**	**0.7689**	**0.03179**	**0**	**0.01203**	**0.17784**
Rh6G_B650_17	**0**	**0**	**0.00312**	**0**	**0**	**0**	**0**	**0.0281**	**0.92662**	**0**	**0**	**0.04215**
Rh6G_Cy5_9	**0**	**0.00061**	**0**	**0.08634**	**0.0049**	**0.00612**	**0**	**0**	**0**	**0.80282**	**0.0992**	**0**
Rh6G_Cy5_13	**0**	**0**	**0.00305**	**0.00076**	**0**	**0.01523**	**0.02361**	**0.01904**	**0**	**0.04037**	**0.86443**	**0.03351**
Rh6G_Cy5_17	**0**	**0**	**0.00037**	**0**	**0**	**0**	**0.01563**	**0.16263**	**0.11574**	**0**	**0.0268**	**0.67882**

Table 3.1-2. Classification probability, $\Omega(n|n_d)$, that an DA-oligonucleotide molecule of the data set n_d (rows) is classified as a species *n* (columns). Calculations were based on the procedure, described in the text, using 4 fluorescence dimensions: green lifetime, τ_G, green anisotropy, r_G , red decay time, τ_R, and signal intensity ratio, S_G/S_R**.**

3.1.4.3 Analysis of an ensemble of molecules.

In general, having a definition for the classification probabilities $\Omega(n=1|n_d)$ to $\Omega(n=N|n_d)$ for a given data set n_d with a separate species n allows us to generalize the definition for a_n to include all of the analyzed datasets. Thereby, the frequency histogram for the classification of corresponding single molecules can be predicted with the frequency of the assigned molecules described by $\vec{a}=\{a_{n=1};\ \dots\ a_N\}$, where the total number of detected molecules A_{total} is given by $\sum_{n=1}^{N} a_n$. Due to shot noise broadened fluorescence parameters, the patterns overlap which has the consequence that the recognition of single-molecules can not be not perfect (Fig. 3.1-9). Because of these statistical classification problems in the first step, which can be described by error probabilities, all molecules should be analyzed together in a second step to improve the classification on the basis of the knowledge of the mean classification error. In this way a much better result for the number of detected molecules of the ensemble c_n is obtained than at the single molecule level.

The actually calculated numbers for each species in this mixture $\vec{c}=\{c_{n=1};\ \dots\ c_N\}$ are obtained by solving the following system of linear equations with the classification probabilities $\Omega(n|n_d)$ and the experimentally obtained numbers of assigned molecules $\vec{a}$.

$$\begin{pmatrix} \Omega(n=1|n_d=1) & \dots & \Omega(n=1|n_d=N) \\ \dots & \dots & \dots \\ \Omega(n=N|n_d=1) & \dots & \Omega(n=N|n_d=N) \end{pmatrix} \begin{pmatrix} c_{n=1} \\ \dots \\ c_N \end{pmatrix} = \begin{pmatrix} a_{n=1} \\ \dots \\ a_N \end{pmatrix} \qquad \text{(Eq. 3.1-2)}$$

In order to give an example for the substantial improvement by using Eq. 2 an independently measured test sample was analyzed. This sample contained a total number A_{total} = 4143 molecules from three of the 12 DA-oligonucleotides. For the discussion of the results the molecule numbers $\vec{a}$ and $\vec{c}$ were normalized by A_{total} defining relative fractions of experimentally assigned molecules $\vec{a_r}$ and relative species fractions calculated for the ensemble $\vec{c_r}$, respectively. The actual sample composition $\vec{c}_{r\ sample}$={a_3(Cy3-BP650/665(17bp))=0.33; a_4(Cy3-Cy5(9bp))=0,35; a_{12}(Rh6G-Cy5(17bp))=0.32} is very well recovered by single-molecule counting analysis $\vec{c}_{r\ analysis}$={a_3=0.32; a_4=0,35; a_6=0.01; a_8=-0.01; a_{11}=-0.01; a_{12}=0.34}. The negative fractions of $\vec{c}_{r\ analysis}$ are solely result of the mathematical solution and have of course no chemical meaning. In contrast to $\vec{c}_{r\ analysis}$, please note that the fractions obtained in the first step by the single molecule classification $\vec{a}_r=\{0.01; 0.03; \underline{0.21}; \underline{0.17}; 0.08; 0.03; 0.01; 0.09; 0.04; 0.06; 0.02; \underline{025}\}$ (Eq. 3.1-1) indicate a level of misclassification of up to 10% which results in false positive and false negative classified molecules on the single-molecule level. This result is equivalent to the case of the overlap of ellipses for different species in the graphical analysis (e.g. Fig. 3.1-7). However, using Eq. 3.1-2 $\vec{a}_r$ is converted with high accuracy to $\vec{c}_{r\,analysis}$ in the second step of the single-molecule counting analysis. The comparison of $\vec{c}_{r\,sample}$ with $\vec{c}_{r\,analysis}$ indicates a very low statistical noise level of only one to two percent.

3.1.5 Conclusions and outlook

The purpose of this study was to demonstrate the feasibility and huge dynamic range of single-molecule measurements for identifying a larger number of different species, based on multi-parameter detection and a multi-dimensional single-molecule counting analysis. By MFD, free dye molecules and incompletely labeled species could be excluded from the analysis, and all 16 different compounds (four families of DA-oligonucleotides, Cy3-Cy5, Cy3-BP650/665, Rh6G-Cy5, and Rh6G-BP650/665, each with 9, 13, 17 bp separation between the dyes, D-oligonucleotides labeled with Cy3 or Rh6G, impurities) were separated, based on the multidimensional information contained in the fluorescence of the analyzed molecules.

Following arrangement of the detected molecules into a multi-dimensional cumulative histogram, identification of the different species was first demonstrated by use of sequential two-dimensional projections of the histogram in different parameter planes, employing different "border lines" between the populations projected in each plane. However, apart from this visual approach demonstrating the feasibility, a more quantitative identification procedure can be employed, based on an algorithm that offers fast and automated species identification with reasonable fidelity on a single molecule level. This approach can also regenerate concentration profiles of species in a mixed sample with very high accuracy, and there is still a clear potential for implementing additional criteria and procedures. Apart from the "traditional" "chromophore" fluorescence parameters providing the criteria for the species identification in this study, fluctuation analysis of the fluorescence intensity (such fluorescence correlation spectroscopy or some other parameter of the detected fluorescence) can yield additional independent parameters. To such characteristic fluctuation parameters, within the category of parameters referred to as “environment/system parameters” above, belong triplet state transitions,[Widengren et al., 1995] trans-cis isomerization,[Widengren and Schwille, 2000] charge transfer[Widengren et al., 1997] or even transport properties.[Eggeling et al., 2001b] In a recent study, the determination of up to 14 different parameters from one individual molecule was claimed, including transition rates to and from the triplet state and spatial parameters.[Prummer et al., 2004]

Finally it is important to mention that an analysis of a sample, where the analysed fluorescence bursts have been selected from fluorescence intensity time trace via an intensity threshold criterion, can give only an qualitative picture on the sample composition, because the chance of bright molecules to be selected and to be subsequently analysed is higher than that of less bright molecules. Thus the multi-dimensional single-molecule counting analysis performed here is very well suited to check for presence of even very small amounts of molecules yielding a qualitative sample survey. Moreover, Fries et al. [Fries et al., 1998] have shown that the analysis of the obtained burst size distributions allows one to identify fluorescent sample molecules also in a quantitative manner. Thus the introduced method of multi-dimensional single-molecule counting harbors the potential for a complete characterization and quantitative analysis of a highly diluted sample in homogenous assays.

3.2 Dynamics by MFD: Proton-powered subunit rotation in single membrane-bound F_0F_1–ATP synthase

In mitochondria, chloroplasts and bacteria, membrane-bound F_0F_1-ATP synthases catalyze the synthesis of ATP by coupling the chemical reaction with an exergonic proton translocation across the membrane. To analyze subunit rotation during ATP hydrolysis and synthesis, active F_0F_1-ATP from *Escherichia coli* was reconstituted into liposomes and the subunits γ and b of the enzyme were selectively labelled with a donor and acceptor dye to study FRET. Freely diffusing liposomes containing a single F_0F_1-ATP were measured with a confocal set-up for single-molecule detection (see chapter 2.1) and analyzed with MFD-techniques according to chapter 2.2. During ATP synthesis, repeating sequences of three conformational states with distinct FRET efficiencies indicated rotation of the γ-subunit in 120 degree steps. For the first time, it was shown that rotation occurs during ATP synthesis by opposite direction compared to hydrolysis.

This work was carried out in cooperation with Prof. Gräber (Institut für Physikalische Chemie II, Albert-Ludwigs-Universität, Freiburg) and was already published [Diez et al., 2004]. Experiments were mainly supported by Dr. Marcelle König and Dr. Suren Felekyan, Heinrich-Heine University, Düsseldorf.

3.2.1 F_0F_1–ATP synthase from Escherichia coli

ATP (Adenosin-5'-Triphosphat) functions as a carrier of energy in all living organisms. It captures the chemical energy released by the combustion of nutrients and transfers it to reactions that require energy, e.g. the building up of cell components, transmission of nerve messages, muscle contraction, and many other functions. The central metabolic role of the F_0F_1-ATP synthase has initiated much experimental work to study its mechanism [Abrahams et al., 1994] [Boyer, 1998] [Junge et al., 1996] [Mitchell, 1961].

F_0F_1-ATP synthase catalyzes the formation of ATP from Adenosin-5'-Diphosphat (ADP) and phosphate. The enzyme consists of two parts, F_1 and F_0, which have in E. coli the subunit composition $\alpha_3\beta_3\gamma\delta\varepsilon$ and ab_2c_n (Fig. 3.2-1a). ATP synthesis from ADP and phosphate takes place at the three β-subunits of the F_1 part. According to the binding change theory, these β-subunits sequentially adopt different conformations during catalysis [Boyer, 1998].

Determined by the interaction of each β-subunit with the γ-subunit, three possible conformations exist called 'tight', 'loose' and 'open'. All three conformations have directly been observed in the X-ray structure of F_1 [Abrahams et al., 1994]. A sequential conversion of the conformations of the catalytic sites is caused by rotation of the γ-subunit that is located in the center of the $\alpha_3\beta_3$-complex. Rotation of the γ-subunit - together with ε - is thought to be coupled mechanically to proton translocation by a rotational movement of the c-ring of F_0 [Junge et al., 1996]. Therefore, the subunits are also defined as 'rotor' ($\gamma\varepsilon c_{10-12}$; blue in Fig. 3.2.1) and 'stator' ($\alpha_3\beta_3\delta ab_2$, orange in Fig. 3.2-1).

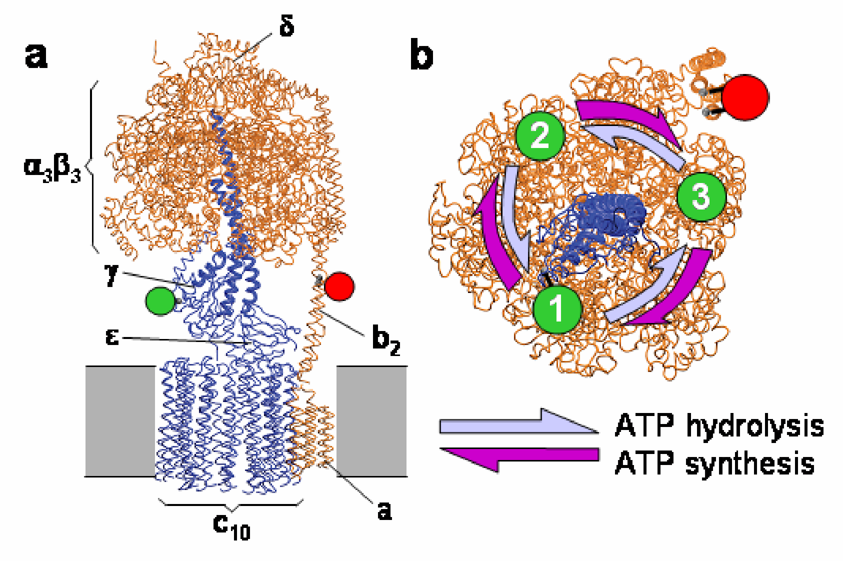

Figure 3.2-1. Model of F_0F_1-ATP synthase from *E. coli*. **a**, Side view. The FRET donor is bound to the γ-subunit (green circle), the FRET acceptor Cy5bis to the b-subunits (red circle). 'Rotor' subunits are blue, 'stator' subunits are orange. **b**, Cross section at the fluorophore level, viewed from the F_0 part. Cy5bis (red) crosslinks the b-subunits. Donor position 1 (green) of cysteine γ-T106C exhibits the largest distance to bQ64C. Rotation of the γ-subunit by 120 degree results in two additional donor positions 2 and 3. [Borsch et al., 2002].

For ATP hydrolysis, the rotation taking place in F_1 was demonstrated by the pioneering video-microscopic experiment using a fluorescent actin filament connected to the γ-subunit as a marker of its orientation in single immobilized F_1 subcomplexes [Noji et al., 1997] [Yasuda et al., 2001]. Hydrolysis of three ATP leads to a full rotation of the γ-subunit involving three 120 degree steps. Recently, substeps were revealed [Junge et al., 1996] [Yasuda et al., 2001]. The direction of rotation of the γ-subunit is counter-clockwise, when viewed from F_0 to F_1 (Fig. 3.2.1b). The actin filament method has been employed to show rotation of the c-subunits using immobilized complexes [Sambongi et al., 1999]. However, the direction of the rotational coupling during ATP synthesis has still to be validated.

3.2.2 Specific experimental details

Single molecule fluorescence measurements under conditions of ATP hydrolysis (1mM ATP) and AMPPPNP binding (1mM AMPPNP) were performed in a buffer (pH8) containing 20 mM succinic acid, 20 mM tricine, 2.5 mM $MgCl_2$, 80 mM NaCl and 0.6 mM KCl. ATP synthesis was measured after preincubation of the liposomes in 20 mM succinic acid buffer (pH 4.7), containing 5 mM NaH_2PO_4, 0.6 mM KOH, 2.5 mM $MgCl_2$, 100 µM ADP, 20 µM valinomycin. The transmembrane ΔpH was generated by mixing the acidic liposomes with the basic buffer containing 200 mM Tricine (pH 8.8), 5 mM NaH_2PO_4, 160 mM KOH, 2.5 mM $MgCl_2$ and 100 µM ADP in a T-shaped flow chamber with two syringes. This generated an initial transmembrane pH difference ΔpH = 4.1 with an additional electric potential difference $\Delta\phi$= 126 mV [Diez, 2003] [König, 2005]. All the samples of the double-labeled F_0F_1 were diluted to the concentration of ~ 90 pM.

F_1 of ATP-Synthase from *E. coli* carrying the cysteine mutation γ-T106C was prepared in Freiburg as described [Gogol et al., 1989] using the plasmid pRA144 [Aggeler and Capaldi, 1992] expressed in strain RA1 [Aggeler et al., 1997]. To exclude specific photophysical effects of the dyes, two alternative FRET donor fluorophores were used: Tetramethylrhodamine-maleimide (TMR, Molecular Probes) or Rhodamine110-maleimide (Rh110, Evotec) were bound to the γ-subunit at residue 106 (green circles in Fig 3.2-1a and 3.2-1b). The FRET acceptor, the bifunctional Cyanine-5-bismaleimide (Cy5bis), crosslinked the two cysteines at position 64 in the b-subunit dimer of F_0F_1 avoiding the ambiguity in location of the dye [Borsch et al., 2002]. Gel electrophoresis revealed that more than 90 % of the b-subunits were crosslinked by Cy5bis.

Labelling efficiencies were 54 % for TMR and 67 % for Rh110 at γ, and 64 % for Cy5bis at b_2. Rates of ATP synthesis and ATP hydrolysis were measured at 23° C with an enzyme concentration of 0.15 nM (hydrolysis) and 0.2 nM (synthesis).

To avoid any perturbations from surfaces, the labelled holoenzyme was investigated in freely diffusing liposomes which proved to be fully functional. The catalytic rates of these double-labeled enzymes were R_S=(23±3) s^{-1} for ATP synthesis and R_H=(67±6) s^{-1} for ATP hydrolysis which is similar to those of the unlabelled F_0F_1-ATP synthase [Borsch et al., 2002]. Upon addition of 40 μM of the inhibitor N,N'-dicyclohexylcarbodiimide (DCCD), ATP synthesis was reduced to R_S=(4±3) s^{-1} and ATP hydrolysis to R_H=(2±2) s^{-1}, confirming that catalysis was coupled to proton transport.

Background count rates (usually between 0.5 and 2 kHz) obtained in each experiment form measurements of solutions without labelled samples, were subtracted from the burst count rates. In addition crosstalk (photons from the donor in the detection channel of the acceptor), as well as differences in the detection efficiencies of the donor and acceptor channels of the instrument were corrected, resulted in corrected fluorescence intensities for donor (F_D) and acceptor (F_A).

3.2.3 Stepwise γ-subunit rotation during ATP-hydrolysis

Rotary movements during ATP hydrolysis were analyzed in the presence of 1 mM ATP. Fig. 3.2-2a shows a long-lasting photon burst with large fluctuations of the fluorescence intensities of donor and acceptor, F_D (green) and F_A (red). To correlate these fluctuations with changes in the intramolecular FRET efficiency, i.e. with changes in distance, the ratio of corrected fluorescence intensities F_D/F_A was determined (orange lines in Fig. 3.2-2). This ratio is directly related to the distance R_{DA} between donor and acceptor dye [Perlin et al., 1983]. For the observed photon burst three different constant levels of F_D/F_A were found (level1, level2, level3) interchanging in sudden jumps between the levels which occur faster than the time resolution (binning time 1ms). The burst in Fig. 3.2-2a displays a sequence of four steps of the F_D/F_A levels. In addition, traces of the fluorescence lifetime of the donor in presence of the acceptor, $\tau_{D(A)}$, were simultaneously measured to exclude artefacts from photophysics of the donor dyes in FRET analysis (Fig. 3.2-2b).

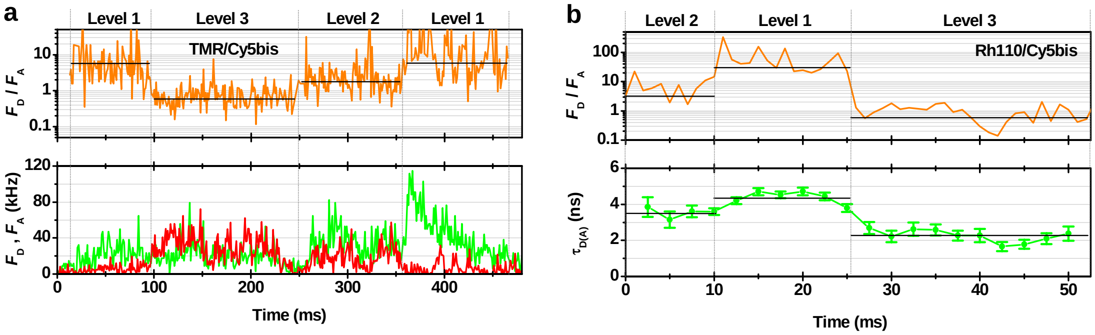

Figure 3.2-2. Photon bursts from single liposomes with one double-labelled F_0F_1-ATP synthase during ATP hydrolysis in presence of 1 mM ATP. Fluorescence donor is TMR in trace a), Rh110 in trace b), Cy5bis is the fluorescence acceptor in all traces. Fluorescence intensity traces of the donor, F_D, are shown in green, those of the acceptor, F_A, in red. The corrected intensity ratios F_D /F_A are depicted in orange, showing the different levels of energy transfer, indicated as level 1, 2 or 3 at the top of the figure. Fluorescence lifetimes of Rh110 in double-labelled F_0F_1 are shown in the bottom trace b). Data for the TMR traces are provided by Dr. M. Diez, Dr. M. Börsch, Albert-Ludwigs Universität, Freiburg

High FRET efficiencies are characterized by low ratios F_D/F_A and a short $\tau_{D(A)}$. The coincident steps in the levels of F_D/F_A and $\tau_{D(A)}$ prove that the jumps are caused by changes in

FRET efficiencies and not by temporally photophysical effects [PERLIN et al., 1983] of the reporter dyes. FRET levels change within a single burst during ATP hydrolysis in the order 1→3→2→1 (Fig. 3.3.2a) and 2→1→3 (Fig. 3.2-2b) respectively. By analyzing 222 traces of single F_0F_1-ATP synthases, the predominant sequence of the FRET level transitions is found to be 1→3→2→1→.. for more than 72 % of the bursts. The fact that not all bursts displayed the same sequence is due to the kinetics of ATP hydrolysis. In this analysis only levels with a duration of at least 5 ms are recognized as individual levels. The observed average ATP turnover time of 19 ms (see later) together with an exponential distribution of the F_D/F_A level durations, leads to a number of only 77 % of levels that last for more than 5 ms and thus are recognized as individual levels. Therefore, apparently 'wrong' sequences resulted from the fact that sometimes short F_D/F_A levels were missed. One can conclude, that during ATP hydrolysis the inter-conversion of well-defined FRET levels clearly indicates a stepwise rotary movement of the γ-subunit in membrane-integrated F_0F_1-ATP synthase. The actin filament method determined the rotation direction in F_1 subcomplexes during ATP hydrolysis to be counter-clockwise when viewed from the F_0-part. Therefore the sequence 1→3→2→1→.., observed during ATP hydrolysis, was attributed to the counter-clockwise direction of rotation [Noji et al., 1997] of the γ-subunit.

3.2.4 Stepwise γ-subunit rotation during ATP-synthesis

To observe subunit movements during ATP synthesis, a transmembrane pH difference (ΔpH) and an electric potential difference (Δϕ) was generated across the liposome membrane. The flow chamber was inserted into the confocal microscope and fluorescence intensity traces were recorded (see Fig. 3.2-3 a and b). Similar as during ATP hydrolysis, well defined constant levels of F_D/F_A are observed with stepwise changes between these levels. The burst shown in Fig. 3.2-3a with TMR/Cy5bis as donor/acceptor displays three distinct levels with the sequence 3→1→2→3. Fig. 3.2-3b shows a burst using Rh110/Cy5bis with the sequence, 1→2→3→1 were in addition to the intensity ratio the fluorescence lifetime of Rh110 is depicted. Again each state is defined by a constant ratio of donor to acceptor intensity (duration > 5 ms) and the fluorescence lifetime of the donor. During ATP synthesis in more than 83 % of the 188 analysed bursts the sequence of level transitions was found 1→2→3→1→.... For both donors TMR and Rh110 with Cy5bis as acceptor an identical behavior was found.

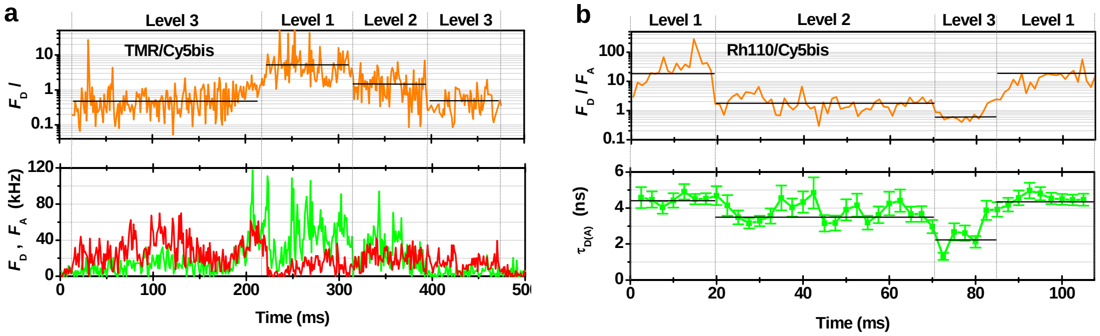

Figure 3.2-3. Photon bursts from single liposomes with one double-labelled F_0F_1-ATP synthase during ATP synthesis in the presence of ADP and phosphate at an initial transmembrane pH difference of ΔpH = 4.1. Fluorescence donor is TMR in trace a), Rh110 in trace b), Cy5bis is the fluorescence acceptor in all traces. Fluorescence intensity traces of the donor, F_D, are shown in green, those of the acceptor, F_A, in red. The corrected intensity ratios F_D /F_A are depicted in orange, showing the different levels of energy transfer, indicated as level 1, 2 or 3 at the top of the figure. Fluorescence lifetimes of Rh110 in double-labelled F_0F_1 are shown in the bottom trace b). Data for the TMR traces are provided by Dr. M. Diez, Dr. M. Börsch, Albert-Ludwigs Universität, Freiburg

This sequence of FRET levels is reversed compared to the sequence during ATP hydrolysis, what leads to the conclusion that the direction of rotation for ATP synthesis is opposite to ATP hydrolysis.

3.2.5 Fluorophore distances and γ-subunit orientations

Single-molecule FRET data revealed additional structural information. From the homology model of F_0F_1 (Fig. 3.2-1), the largest distance between the Cα atoms of the amino acids b-Q64C and γ-T106C was estimated to be 73 Å. Rotation of the γ subunit by 120° and 240° resulted in two shorter distances in the range of 40–60 Å. According to the Förster theory of FRET, two effects can influence F_D / F_A levels, donor-acceptor distances and orientations in transition dipole moments (factor κ^2) of the donor relative to the acceptor dye. Apparent donor-acceptor distances, R' DA, were calculated from the measured fluorescence parameters. These apparent distances of 52, 65 and 80 Å, representing mean values during catalysis and AMPPNP binding for the three FRET states within the enzyme, agree with estimates obtained from the model.

3.2.6 Discussion

MFD technique based on the intramolecular single-molecule FRET approach was applied to show subunit rotation in the liposome-reconstituted holoenzyme F_0F_1-ATP synthase powered by proton flow. Here, one fluorophore was attached to the rotating γ subunit of F_1 and the other to the static, nonrotating b-subunit dimer of F_0. The FRET efficiency depends on the distance between the two fluorophores. Therefore, FRET efficiency changes between the two fluorophores at a single ATP synthase are expected to describe trajectories of the relative motion of the two labeled subunits during catalysis. Upon addition of AMPPNP as a nonhydrolyzable substrate for the enzyme, three well-defined and distinct FRET levels were found. They correspond to three distances of the labeled residue 106 at a protruding part (‘off-axis position’) of the γ subunit with respect to the b subunits. The calculated ratio of corrected fluorescence intensities F_D/ F_A between FRET donor and acceptor in the photon bursts of a single ATP synthase is independent of intensity fluctuations of the double-labeled enzyme on its transit pathway through the confocal detection volume. In addition to this intensity ratio, each FRET level is defined by a specific FRET donor fluorescence lifetime $\tau_{(DA)}$, and therefore, other photophysical causes effecting the quantum yields of the FRET fluorophores are unlikely. These stable FRET levels during a photon burst indicate the trapping of the γ subunit by AMPPNP in one of three distinguishable orientations. The three intramolecular distances calculated from the FRET efficiencies of these levels are in good agreement with the distances derived from the model of F_0F_1-ATP synthase and the expected positions of the γ subunit. FRET-labeled ATP synthase in a freely diffusing liposome carries out proton transport-coupled ATP synthesis and hydrolysis almost undisturbed during real-time observation. Given this direct correlation between FRET level and γ-subunit orientation, γ-subunit rotation in F_0F_1-ATP synthase occurs stepwise in both modes of catalysis and the direction of rotation during ATP synthesis is reversed compared with that during ATP hydrolysis. Using the actin-filament method, the rotation direction of the γ subunit in F_1 subcomplexes during ATP hydrolysis has been determined to be counterclockwise when viewed from F_0 [Noji et al., 1997]. Therefore the FRET level sequence 1→3→2→1→... observed during ATP hydrolysis was attributed to the counterclockwise direction of rotation of the γ subunit (Fig. 3.3.1b). Stepwise rotation of the γ subunit during ATP hydrolysis has been discussed for F_1-ATPase [Yasuda et al., 2001] and for F_0F_1-ATP synthase [Borsch et al., 2002] earlier and is confirmed here. In the present work, proton-driven ATP synthesis is also accompanied by a three-step rotary movement of the γ subunit and not by a quasi-ontinuous rotation, which might have been expected from the stoichiometry of at least nine translocated protons per 360° revolution and from the multistep rotational motion of the c subunits of F_0 during ATP synthesis. These distinct distances between the FRET fluorophores remain constant throughout the dwell time of one γ-subunit orientation, before a consecutive 120° rotary movement of the γ subunit takes place, as has been shown unequivocally with immobilized F_1 subcomplexes for the case of ATP hydrolysis at millimolar concentrations [Yasuda et al., 2001]. The mean stopping positions of the γ subunit upon ATP synthesis are similar to those observed in the AMPPNP-trapped states and those during ATP hydrolysis at millimolar ATP concentrations. As anticipated in molecular dynamics simulations and derived from theoretical considerations of microscopic reversibility, a reversed rotary motion of the γ subunit during ATP synthesis was predicted, and is now strongly supported by this work. The rotary subunit movement is indicated by repeating sequences of three FRET levels, which are induced by distance changes between the FRET pair. In most cases, a consecutive order of the three γ-subunit orientations was observed, and in an opposite direction during ATP synthesis from that during ATP hydrolysis. Thus, unidirectional rotary motion of the γ subunit during both modes of catalysis seems very improbable. Any two-state model, including contracting-and-stretching modes of the γ subunit or back-and-forth swiveling modes between only two of the three catalytic sites, are not consistent with the repeating sequences of three FRET levels. Oscillations between two FRET states were rarely observed and can be attributed either to omitted levels or to an equilibrium state between a weak proton-motive force competing with the ATP hydrolysis backreaction. The significant broadening of the three FRET levels during ATP synthesis allows us to predict the occurrence of substeps comparable to those observed in F_1 subcomplexes during ATP hydrolysis. As first hints and as rare events more than three FRET levels (substeps) in some photon bursts of F_0F_1 were identified during ATP synthesis. The origin of these substeps remains to be clarified. In principle, a hypothetical ADP-(plus Pi)-waiting state of the enzyme at one angular position of the γ subunit and a conformational state associated with the catalytic reaction or product release at another angular position can be discriminated by the dependence of substrate concentration. Detecting one ATP synthase in freely diffusing liposomes, as has been shown in this work, limits the observation time to several hundred milliseconds. Therefore, concentration dependencies must be studied by a modified approach, for instance with surface-immobilized liposomes using a streptavidin-biotin multilayer. Monitoring single enzymes at work under kinetic control in both directions of catalysis will reveal insights into the mechanism of the 'rotary nanomachine' F_0F_1-ATP synthase.

4 MFD-Imaging.

In single-molecule fluorescence spectroscopy photon bursts are analysed due to a transit of a molecule. The photon bursts can be defined as packages of photons, which are randomly distributed on the time axis. In imaging a pixel is now interpreted also as a photon package which is well defined by scanning track. All known single-molecule techniques can be applied to photon packages defined by pixels instead of burst coordinates.

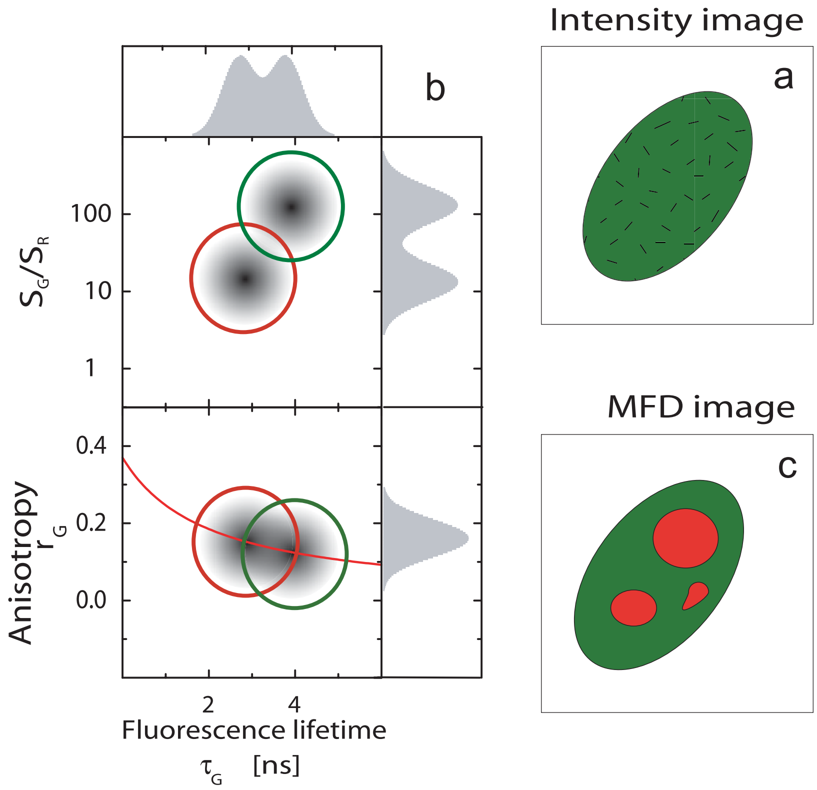

Figure 4.1 Sketched representation of the MFD-Imaging features. a) The intensity image of the cell shows a rather homogenous distribution of fluorescence inside the cell. b) The sorting of pixels into a histograms according to various calculated parameters allows one to better distinguish between different species (e.g. green and red). c) The two species can subsequently be allocated in the cell and give information about varying conditions.

Fig. 4.1 shows the basic principles of MFD-Imaging (MFDi). For each pixel in Fig. 4.1a not only the signal intensity is known but also all other fluorescence parameters. However, it is quite difficult in parameter images to judge the statistical significance of the observed spread of the fluorescence parameter values for all pixels. Thus it is useful to generate fluorescence parameters histograms for a given set of pixels (image). In MFDi it is possible to display pairs of parameters in two dimensional frequency histograms, where the number of pixels is displayed in a colour scheme, where black corresponds to the highest value. Moreover, the corresponding one-dimensional histograms are given as projection. Fig. 4.1b displays as an example a stack of the 2D histograms, which are important in FRET measurements [Rothwell et al., 2003]. Here the fluorescence lifetime of the donor dye τ_G is plotted versus the ratio of signals in the green and red channel S_G/S_R and the fluorescence anisotropy r_G. In this way the heterogeneity of a set of pixels for a given image or a series of images is easily detected. By selecting a subpopulation of pixels (green and red circles, respectively) and displaying them in a joint image, more detailed spatial and fluorescence information of validated statistical significance is obtained for the image of the cell (Fig. 4.1c).

The analysis of imaging data is realized in a LabView-based “Marcelle” and “Margarita” programs (see Appendix A for details).

4.1 Imaging of the Rh110 dye located inside and outside a glutathione-sepharose bead.

To demonstrate the ability of the multiparameter fluorescence imaging (MFDi) technique, a test system that exhibits spatial variation of the molecular mobility was analysed. Therefore glutathione-sepharose beads pressed between two cover slides that allowed the fluorophore Rh110 to diffuse also inside the bead was used as a model system. Fig. 4.2 shows five images with different fluorescence parameters of the green detection channels: green signal S_G (a), fluorescence lifetime τ_G (b), stationary anisotropy r_G (c), mean correlation amplitude (d) and correlation decay time (e). All the parameters were calculated from a single MFD image scan as described in Chapter 2.2.

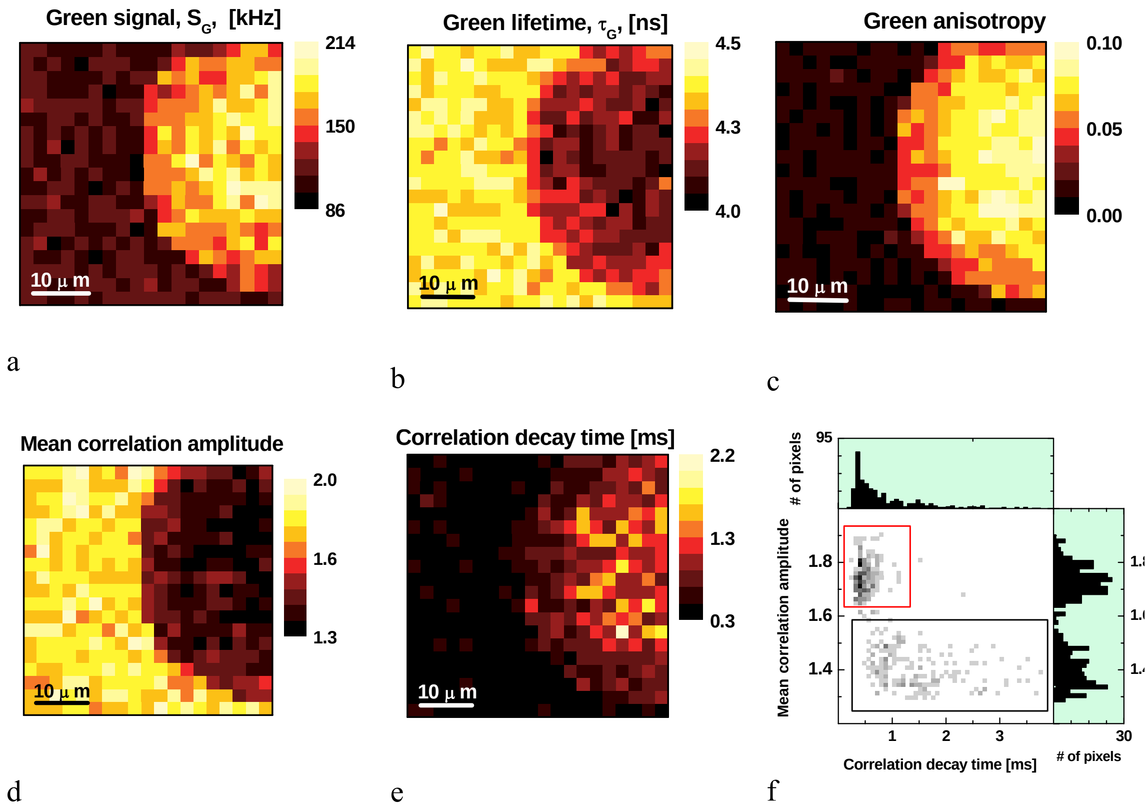

Figure 4.2. MFD-Imaging of the Rh110 dye located inside and outside a glutathione-sepharose bead. The bead is located at the right hand side of the pictures, singeled out by a round shape. The following MFD parameters have been calculated: a) Green signal, S_G; b) Green lifetime, τ_G ; c) Green anisotropy, r_G; d) mean correlation amplitude; e) Correlation decay time. f) A 2D histogram of the single pixel values from pictures d and e. The correlation amplitude is plotted versus the correlation decay time. The corresponding one-dimensional histograms are given as projections. The black box highlights the pixels inside the bead, the red one corresponds to the pixels outside the bead. The integration time per pixel is 300 ms. All the parameters are calculated as described in Chapter 2.2.

The intensity image (Fig. 4.2a) shows that the bead is brighter than the surroundings, which indicates an accumulation of fluorescent dyes inside the bead. Due to the interaction with the polymer network, their fluorescence (Fig. 4.2b) is quenched. The fluorescence lifetime is reduced from τ_{out} = 4.15 ns outside the bead to τ_{in} = 3.68 ns inside the bead. The anisotropy image (Fig. 4.2c) shows the higher r values inside the bead than outside. Calculating average anisotropies for the selected areas inside and outside the bead, anisotropy values of 0.02 and 0.086 are found, respectively. Using a value of the fundamental anisotropy r_0 = 0.375 in the Perrin equation ($\rho = r\ \tau/(r_0\text{-}r)$), mean rotational correlation times ρ_{out} = 0.23 ns and ρ_{in} = 1.1

ns are calculated. Thus the reduced rotational mobility directly proves the dye's interaction with the polymer network.

For the anisotropy, intensity and the fluorescence lifetime, an increased influence of the polymer matrix is visible when going from the edge towards the centre of the bead. This may originate from the fact that the beads were clamped between two cover slides to fix them for stable imaging. This results in a compression of the polymer beads to approximately half of their thickness and thus increases the polymer density, mainly at the centre of the bead. Performing the pixel-wise fluorescence correlation analysis, information on the number of fluorescent particles in the confocal volume is obtained via the correlation amplitude in each pixel (chapter 2.2). The mean correlation amplitude image (Fig. 4.2d) shows the change in concentration between the surrounding and the inner of the bead. Since the correlation amplitude is given by the inverse number of molecules in the focal volume, the lower amplitude inside the bead shows the accumulation of fluorophores, which is consistent with the higher intensity inside the bead.

Simultaneously, the image of the correlation decay time is also obtained. It reflects the diffusion coefficient of the fluorophore in the different surroundings (Fig. 4.2e). This image clearly proves a restricted translational diffusion indicated by longer correlation decay times within the bead, which is in accordance with the reduced rotational diffusion measured by the increase of the anisotropy.

In the fluorescence parameter images it is quite difficult to analyse the statistical properties of the values at each pixel. In MFDi it is possible to display pairs of parameters in two dimensional frequency histograms, where the number of pixels is displayed in a colour scheme, where black corresponds to the highest value. Fig. 4.2f displays the 2D histogram of the correlation amplitude versus the correlation decay time together with the corresponding one-dimensional histogram given as projection. Here the two populations are clearly visible, whereby the population of free dyes (red box) has much smaller distribution of correlation decay times t_m than those inside the bead (black box), which can be seen only in the 2D histogram. The very broad t_m distribution of dyes inside the bead cannot be explained by statistical variations only and thus reflects nicely the heterogeneity of the microenvironments inside the bead.

4.1.1 Calculation of concentrations.

There are two possibilities to calculate the concentration of fluorescent molecules. First, the average number of fluorescent particles N_P that diffuse through the confocal volume can be calculated from the correlation amplitude of the FCS curve (chapter 2.2.4.2). Second, the number of emitting fluorophores N_F can be deduced from the fluorescence intensity F by taking the brightness Q of the dye into account. These two methods have been applied for the analysis of the bead images (Fig. 4.2). The number $N_{F(in)}$ of fluorophores in the confocal volume inside the bead is calculated according to

$$N_{F(in)} = \frac{S_{in} - B_{in}}{Q_{in}} = \frac{F_{in}}{Q_{in}} \qquad \text{(eq. 4.1)}$$

where S_{in} = 183.7 kHz is the average fluorescence intensity inside the bead and B_{in} = 11.3 kHz is the average background intensity measured in a bead without Rh110. The brightness (i.e. signal counts per molecule) Q_{in} inside the bead was estimated by extrapolation using the brightness outside the bead Q_{out} as a reference value. The latter one has to be corrected in order to account for the fluorescence quenching observed within the bead.

$$Q_{in} = Q_{out} \cdot \frac{\tau_{in}}{\tau_{out}} \qquad \text{(eq. 4.2)}$$

The correction factor τ_{in} / τ_{out} results from the linear relationship between the fluorescence quantum yield Φ_F and the fluorescence lifetime τ, which is given by $\Phi = k_F \cdot \tau$, where k_F is the intrinsic rate constant of fluorescence. The average fluorescence lifetimes τ_{in} = 3.68 ns and τ_{out} = 4.15 ns were calculated by fitting all photon data of the respective selected pixels, taking also constant background into account, which could not be done in most of the cases for the single pixel lifetime analysis due to high shot noise.

Using the average correlation amplitudes of the selected areas outside the bead, the number of diffusing particles was calculated $N_{P(out)}$ = 1.3. Moreover, the fluorescence intensity is proportional to the number of emitting fluorophores N_F in the confocal volume. If the sample would consist of diffusing particles containing n fluorophores, the number of fluorophores N_F estimated from the fluorescence intensity would be n times the number of particles calculated according to the correlation amplitude. Assuming that the fluorophores outside the bead do not aggregate, $N_{F(out)}=N_{P(out)}$ = 1.3. With the average signal per pixel of S_{out} = 111.4 kHz, background B_{out} = 1.98 kHz and the number $N_{F(out)}$ of 1.3 fluorophores in the confocal volume derived from the FCS, the brightness of the Rh110 outside the bead amounts to Q_{out} = 81 kHz/molecule. The number of fluorophores in the focus thus is calculated to $N_{F(in)}$ = 2.40, which agrees well with the number of diffusing particles $N_{P(in)}$ = 2.5. This result indicates that the fluorophore do not aggregate.

It is known, that the calculation of exact concentrations from a fluorescence correlation analysis is limited due to several uncertainties such as: (1) shape and size of the confocal detection volume, which can vary with the local index of refraction, (2) varying contributions of background. Nevertheless, the results show that the accuracy in FCS calculation is high enough to decide from the comparison of the intensity and correlation amplitude images whether particles contain only one or more than one fluorophore. This is of high relevance especially for studying the interaction of labelled proteins in cells.

4.2 Imaging the distribution and diffusion of GFP labelled Mal3 proteins in yeast cells

MFD imaging technique was applied to single cells of fusion yeast *Schizosaccharomyces pombe* that express the GFP labelled Mal3 protein. Yeast cells undergo a very dynamic cycle of polymerizing and depolymerising microtubules, that grow from the cell center towards the cell ends [Busch and Brunner, 2004] [Kerres et al., 2004].

The Mal3 protein assembles along the microtubule, localizing in particles preferentially at their growing ends, promoting the initiation of microtubule growth and preventing degradation catastrophes. At the cell ends, the microtubule tip-associated Mal3 particles disappear, followed by rapid microtubule degradation. This process allows the cell to target the cell ends, helping to maintain the cellular bipolarity.

MFDi was applied to this highly dynamic system to show its potentials in giving better insight in cellular systems compared to simple intensity images. Time series taken with the MFDi system (data not shown) showed the typical rapid microtubule polymerisation and successive degradation within minutes. The imaged cell shown in Fig. 4.3 is in a state shortly after cell division, exhibiting a septum in the centre part indicated by low fluorescence intensity.

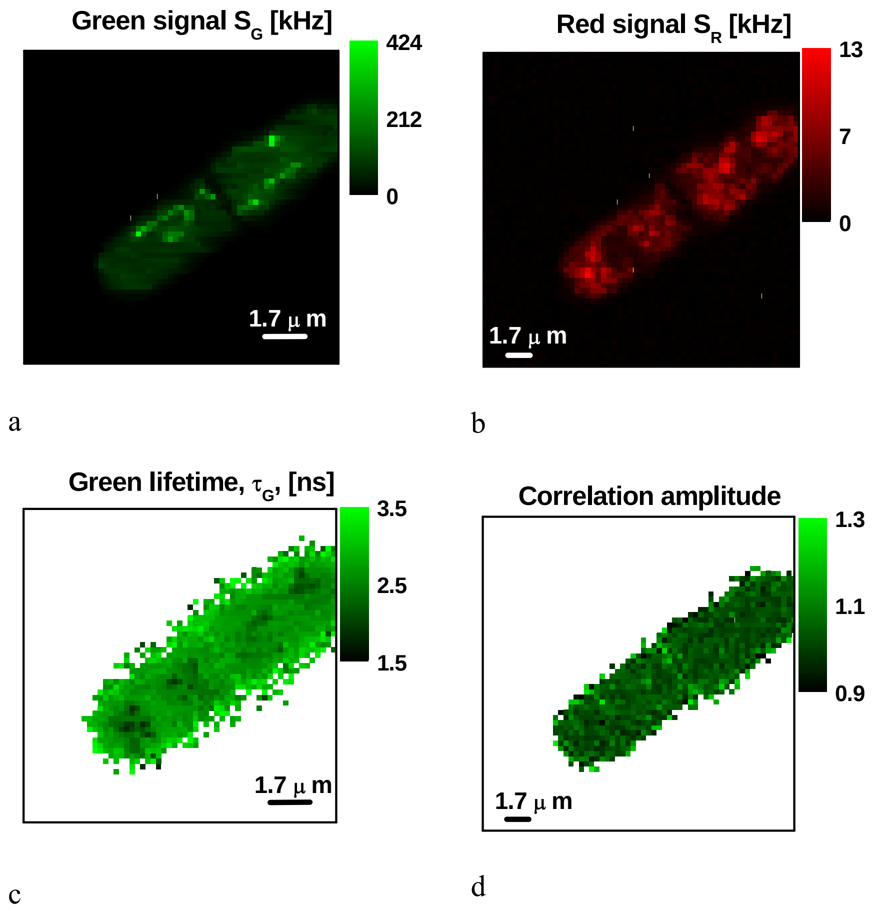

Figure 4.3 MFD-Imaging of Mal3-pk-GFP proteins in *Schizosaccharomyces pombe* yeast cells. Intensity image of a) the green, S_G and b) the red signal, S_R; c) Green fluorescence lifetime, τ_G ; d) Correlation amplitude. The cells were excited at 1.7 µW. The integration time per pixel was 20 ms. All the parameters are calculated as described in Chapter 2.2.

An image showing the microtubule in the polymerizing phase, exhibiting bright particles at the growing tips containing a high concentration of bound Mal3-pk-GFP was selected for detailed analysis. Beside these bright spots, also a weaker fluorescence in the rest of the cell is visible due to Mal3-pk-GFP that is not bound to the microtubule. Due to the high concentration of Mal3-pk-GFP and the low excitation intensity of 1.7 µW the contribution of the autofluorescence background in the green channel is not dominating (Fig. 4.3a) (see below). In the simultaneously detected signal of the red channel a significant contribution of red auto fluorescence resulting from green excitation is visible, which shows cellular structures. In the centre of the lower part of the cell, a vacuole structure is visible.

Because of the high rotational correlation time of GFP itself which is longer than its fluorescence lifetime [Striker et al., 1999], the anisotropy does not strongly increase due to a decreased rotational movement upon interaction of the Mal3-pk-GFP protein with other protein complexes. Accordingly, it was found the same anisotropy 0.26 value throughout the whole cell, which is slightly smaller than the steady-state anisotropy of 0.32 [Schaffer et al., 1999] [Sekar and Periasamy, 2003]. Only variations at decreased fluorescence intensities were found at the border of the cell, where the calculated anisotropy values vary more strongly due to shot noise [Schaffer et al., 1999]. Interestingly, an anisotropy decrease due to possible homo fluorescence energy transfer is not visible, even not for the areas of highest Mal3-pk-GFP concentration in the particles at the microtubule ends. This indicates that the different Mal3-pk-GFP proteins do neither interact directly within these particles nor do they form multimers (within a distance of approximately 8 nm) when not being bound to the microtubules.

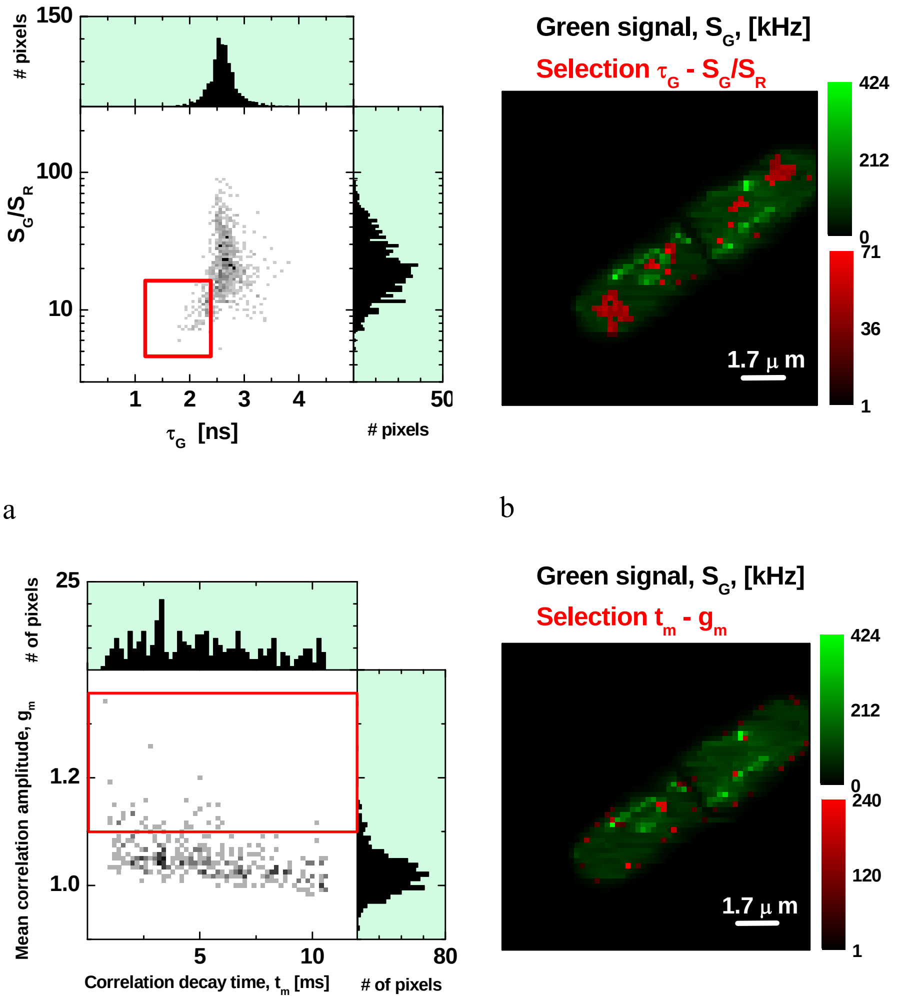

a

b

c

d

Figure 4.4 MFD-Imaging of Mal3-pk-GFP proteins in *Schizosaccharomyces pombe* yeast cells. Selection of sub-species according to their MFD-parameters. a) Selection of a short-lifetime, τ_G, low green-to-red intensity ratio, S_G/S_R, species in a 2D-histogram (red box), corresponding to the high amount of autofluorescence. b) The species is represented in the green signal MFD-Image by a red colour scale, as compared to the remaining pixels in a green colour scale. c) Another selection has been done by choosing a high-correlation amplitude species. d) Again, the selection is highlighted by a red colour scale in the green signal MFD-Image. The cells were excited at 1.7 μW. The integration time per pixel was 20 ms. All the parameters are calculated as described in Chapter 2.2.

Figure 4.4a shows a 2-D histogram where the ratio of green to red intensity S_G/S_R is displayed versus the fluorescence lifetime τ_G for all individual pixels. A typical lifetime of 2.6 ns is found for most of the pixels, which is also slightly smaller than the mean GFP fluorescence lifetime of approximately 3 ns. Moreover at intensity ratios S_G/S_R smaller than 10, an additional species becomes visible exhibiting lower lifetimes of approximately 2.2 ns. Please note that in the 1D-histogram of fluorescence lifetime this species would not have been detected. Selecting the corresponding pixels (red frame), they easily can be located in the intensity image of the yeast cell shown in Fig. 4.4b by assigning a red colour scale to the selected pixels only. Locally different fluorescence lifetimes might indicate a variation of the surroundings when using fluorophores sensitive to pH or other parameters. But in spite of GFP showing a pH sensitive transition between a bright and a dark state that affects its average brightness, this does not strongly affect its fluorescence lifetime.

This shows that the simultaneous measurement of several parameters is crucial for detecting systematic errors in quantitative fluorescence imaging and a correct interpretation. Especially in the case of high noise due to low photon counts, the analysis of all pixel data in two dimensional histograms allows to reveal systematic trends.

Fig. 4.3d shows the fluorescence correlation amplitudes calculated for each individual pixel. Due to the short measurement time of 20 ms per pixel and thus the relatively low number of photons per pixel of approximately 1500, the image shows a considerable noise. From the 2D histogram of correlation amplitude g_m vs correlation decay time t_m (fig. 4.3c) an average amplitude of 1.03 was obtained while the correlation decay times for the Mal3-pk-GFP protein show a broad distribution in the range of several milliseconds. This is consistent with the diffusion time of free GFP in aqueous buffer of approximately 0.4 ms, which was calculated from reference experiments (data not shown). Due to the high concentration of proteins and cellular components, the mobility of Mal3-pk-GFP within the cell will be reduced.

The 2D histogram shows few pixels (9.5%) having amplitudes above 1.10. Due to the high noise, one has to be careful with interpreting single pixel amplitudes. However, fig 4.4d shows the location of the selected pixels displayed with a red colour scale in the intensity image. It is evident that the selected pixels are not randomly distributed in the cell. Two classes of pixels are detectable: (i) located at the bright ends of the microtubules, and (ii) location at the edge of the cell. While the high amplitudes at the edge of the cell may be due to fluctuations based on the low photon counts, this does not hold for the bright pixels in the cell. In this respect it is important to note that the correlation amplitude is strongly increased if the signal changes from the start to the end of the measurement time window of the pixel. At positions of high fluorescence intensity contrast such a change of the intensity within the measurement time window occurs due to the delayed approach of a new pixel in the closed loop operation mode of the piezo scanner. To avoid corruption of the calculated correlation parameters by this relative movement of the confocal detection volume one easily can exclude the photons taken in the first several ms from the data analysis. This on the other hand would lead to an increased noise due to lower photon counts or requires an increased time for image recording. However for most of the pixels within the cell where no high intensity contrast occurs, this interference with the calculated correlation amplitude was found being small compared to the noise due to low photon counts.

5 Full correlation

An improved time-correlated single photon counting (TCSPC) technique for simultaneous fluorescence lifetime and correlation experiments was developed. It allows calculation of the full correlation curve from the same photons emitted from single or very few, molecules used in MFD analysis.

The method offers two main advantages for experiments at low concentrations over conventional single molecule fluorescence detection:

1) The rotational correlation times of large macromolecules, which are much bigger than the fluorescence lifetimes are now accessible in a TCSPC experiment with high time resolution (many proteins exhibit rotational correlation times between 10 and 100 ns.) Accessing the rotational diffusion via commercial hardware correlators is not possible at present, since they are limited to time resolutions of 5 ns or less. The presented technique bridges the gap between anisotropy decay analysis and currently available commercial correlators.
2) The number of independent fluorophores on a single molecule can be determined (e.g. the number of monomers in a complex) by measuring coincident photons simultaneously with all other fluorescence parameters. Alternatively, in suitable systems photophysical processes like singlet-singlet-annihilation or singlet-triplet-annihilation can be studied with high precision. Besides applications in the investigation of multichromophoric entities, this technique, which is based on the quantum mechanical phenomenon of antibunching, might also be promising for applications in molecular biology.

The technique is applicable to immobilized molecules as well as to solutions of fluorophores. In heterogeneous samples species selective correlation analysis (see chapter 2.2.5) is possible after sorting single molecule events by software.

This work was carried out in cooperation with Becker & Hickl GmbH, Berlin. Experiments and programming were mainly supported by Dr. Suren Felekyan, Heinrich-Heine Universität, Düsseldorf.

5.1 Full correlation with a continuous wave (cw) excitation.

Complete correlation curves generated from single photon data ranging from picoseconds up to 35 milliseconds are shown in Fig. 5-1. Here Rh110 solutions were excited by cw laser light and the fluorescence was detected with Hamamatsu H7422P-40 PMTs.

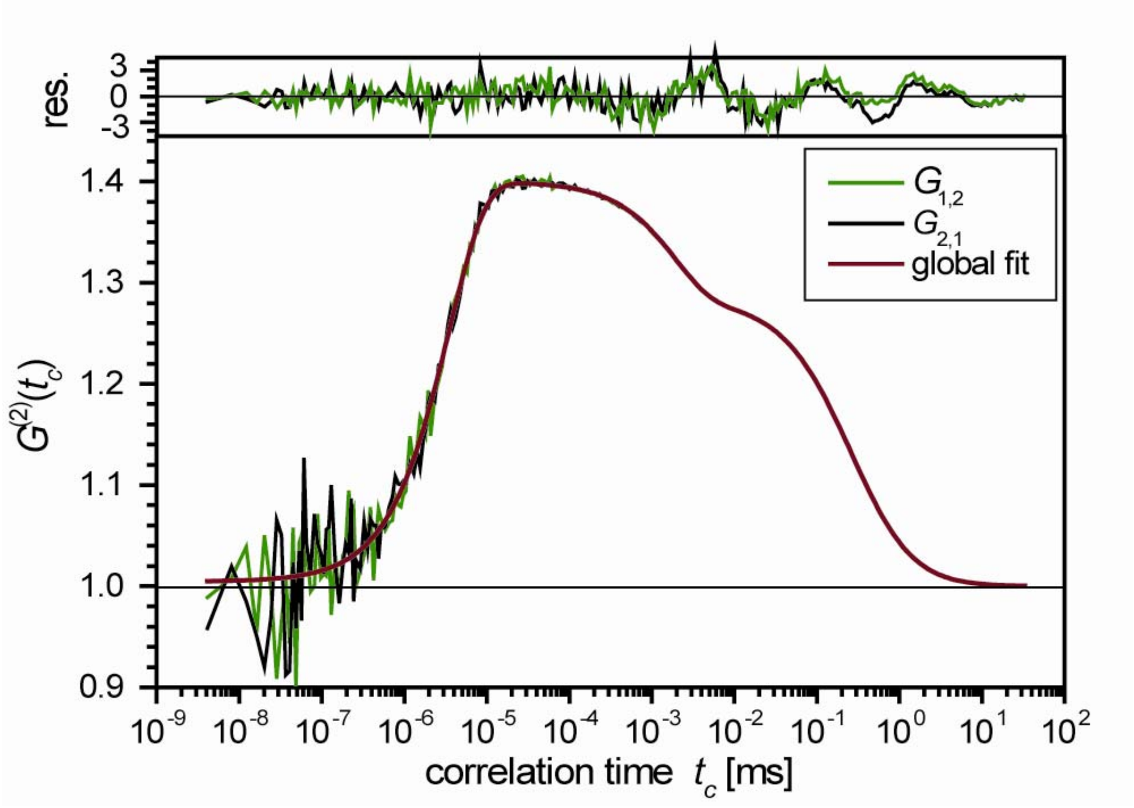

Figure 5-1. Correlation curves $G_{1,2}$ and $G_{2,1}$ of Rhodamine 110 aqueous solutions. Excitation at 496 nm, measured with PMT detectors. Recording time 16 min. Fit to eq. 12 (N=3.5, z_0/ω_0=1.5, t_D=0.3ms, T_{eq}=0.29, t_T=1.9µs, m=1.02, t_A=3.5ns).

A pseudo-logarithmic binning procedure was used starting with the highest time resolution at a correlation time t_c = 4.069 ps. To demonstrate the symmetry of the setup both cross-correlations $G_{1,2}$ and $G_{2,1}$ are presented. For Rh110, a small molecule with a rotational correlation time that is short on the timescale of its excited state lifetime and as a consequence exhibiting a very small steady state anisotropy, no measurable differences between both cross-correlations are to be expected. The experimental curve is well reproduced by a weighted fit to the model function (eq. 2.2.4-10) which neglects rotational effects. Slight deviations of both correlation curves at longer times that can be seen in the residuals are expected and can be explained by partial singlet and triplet saturation as well as photobleaching caused by the relatively high mean excitation power ($I_0/2$) [Eggeling et al., 1998b] of 90 kW/cm^2. The detected countrate added from both channels was 526 kHz, which by normalizing to the mean number of Rh110 molecules in the detection volume element of N = 3.5 corresponds to 150 kHz per molecule.

The high excitation power is also denoted by the observed mean triplet population of 29%. No artefacts around 13.6 ns are observed, confirming the accurate combination of the micro- and the macroscopic time information to a unified time axis.

5.1.1 Short time regime: dual board data acquisition

Many of the possible experimental artefacts will manifest in the short time regime of a correlation curve. This part of the correlation curve is dominated by photon antibunching from single Rh110 molecules. The normalized amplitude at zero delay, $G^{(2)}(t_c=0)$, is expected to approach one for single emitters freely diffusing in solution.

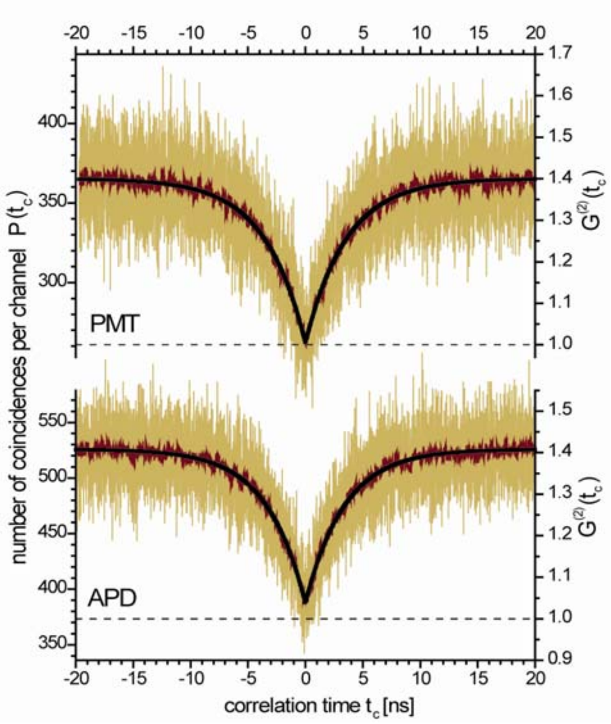

Figure 5-2. Short-time correlation curves of Rhodamine 110 aqueous solutions measured with PMT (top) and APD detectors (bottom). Experimental conditions as in fig. 9. Recording time 16 min. Fit to eq. 12 (black line): antibunching time t_A = 3.6 ns (PMT) and t_A = 3.4 ns (APD), m = 1.01 (PMT) and m = 1.10 (APD).

A thorough investigation of the times between -20 ns < t_c < 20 ns, covering the critical region around the junction of the micro- and the macro-time axis at 13.6 ns, recalculated from the data taken with H7422P-40 PMTs and shown in fig. 5-1, is presented in Fig. 5-2 (top). Besides the data acquisition electronics mainly detector performance affects the signal quality. Data with Perkin Elmer SPCM AQR-14 avalanche photodiodes under otherwise comparable experimental conditions was recorded for a comparison (fig. 5-2, bottom).

To generate the curves two settings in the correlation software had to be used that have not been described previously:

(1) Correlation algorithm described in chapter 2.2.4.1 only uses positive correlation times ($t_c \geq 0$). To facilitate computation, channel 2 was given an artificial positive offset which was subtracted after correlation. This way the whole time intervall shown with positive and negative correlation times between -20 ns < t_c < 20 ns could be calculated in one run.

(2) The curves were calculated with the full (electronical) time resolution of 4.069 ps by setting N_c to a number sufficiently large to have the desired time range fall inside the first two cascades, by that means avoiding time-binning. For the data in fig. 5-2a cascade size of N_c = 5000 and an offset for channel 2 of Δt_2 = 5000 was used.

The number of coincidences per channel in a correlation experiment, $P(t_c)$, is calculated from eq 2.2.4-7. The fit (black line) as well as the smoothed data (dark grey) confirm the inferior time resolution of the APDs as compared to the PMTs: the correlation of the APD data cannot reproduce the amplitude at t_c = 0 of $G(0) = 1$, as would be expected for freely diffusing single fluorophores and is found with the PMTs. This cannot be attributed to the timing jitter of the detectors: The full width at half maximum (FWHM) of the instrumental response functions (IRF) was measured to be around 0.30 ns for the PMT detectors and 0.19 and 0.23 ns for the APDs used. Besides an increased afterpulsing probability for the APDs (not shown, afterpulsing does not significantly affect the shape of the cross-correlation curves), the main origin of the poorer performance of the APDs is their unstable IRF which drifts with countrate (Fig. 2.1.5). The time constant of the drift was found to be of the order of 0.1 s (not shown).

In some experiments at low light levels APDs could still be the better choice. APDs can achieve much higher quantum efficiencies (QE) than PMTs over wide wavelength ranges. Based on the count rate per molecule (180 kHz vs. 150 kHz) a 20% higher sensitivity for the APDs was found compared to the PMTs in the wavelength range around 533 nm (see Fig. 5-2 and 5-3); the manufacturers specifications for typical modules at 580 nm would predict a difference around 40% [Datasheet Single Photon Counting Module, SPCM-AQR Series04]

[Datasheet Photosensor Modules, H7422 Series04]. When the dominant source for uncertainty in the determination of the characteristic antibunching time is shot-noise the detectors with highest QE shout be preferred.

5.1.2 Short time regime: single board data acquisition

The common way to obtain inter-photon arrival time histograms for short delay times t_d, which are equivalent to the cross-correlation curves in Fig. 5-2 employs a Hanbury-Brown and Twiss (HBT) setup [Basché et al., 1992] [Hanbury-Brown and Twiss, 1956]. Here only a single TAC is used to directly record t_d, therefore not requiring the construction of synchronized macroscopic time-axes (Fig. 5-3).

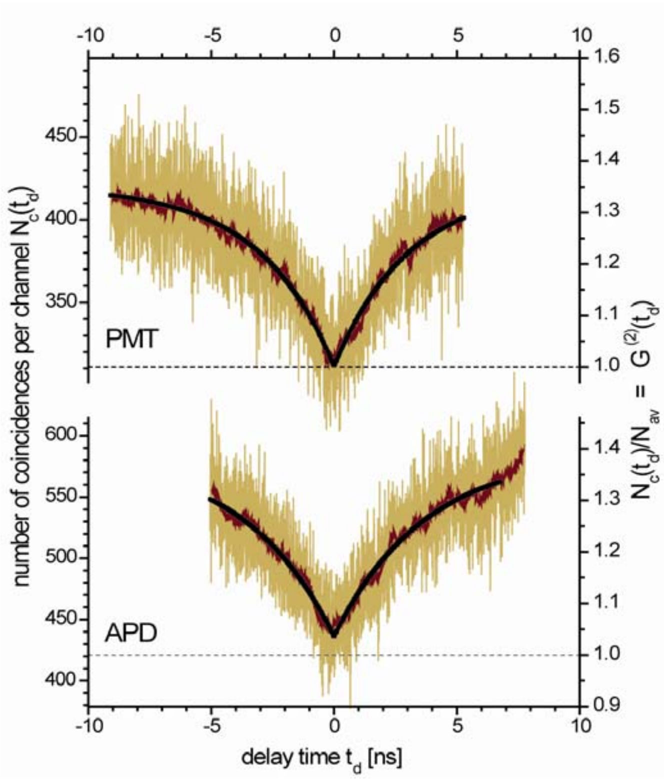

Figure 5-3. Δt (TAC) histograms of Rhodamine 110 aqueous solutions measured with PMT (top) and APD detectors (bottom). Recording time 14 min. Fit to eq. 10 (black line): antibunching time t_A=3.0 ns (PMT) and t_A=3.7 ns (APD).

Data was recorded in the histogram mode of the board, i.e. only the number of stop events per TAC channel $N_c(t_d)$ but no macro time information was stored. Normalization to obtain the correlation amplitude was done by dividing $N_c(t_d)$ by the average number of coincidences N_{av} that are expected for poissonian noise. N_{av} was calculated from the mean countrate by eq. 5-1:

$$N_{av} = \left(\frac{F}{t}\right)_{av}^{2} t_{TAC} t_{\exp} \ , \qquad \text{(Eq. 5-1)}$$

with $(F/t)_{av}$ being the mean countrate per detection channels, t_{TAC} the TAC channel width and $t_{\exp}$ the total data acquisition time. The mean number of fluorophores N in the detection volume element was determined to $N = 4.0$ by separate FCS preceding the HBT experiment. Having countrates per molecule comparable to the FCS experiment (Fig. 5-2), the higher number of coincidences per channel in the HBT experiment can be explained by the slightly higher concentration.

Compared to the recording and correlation of high resolution photon time traces the comparably simple HBT arrangement has a number of drawbacks:

(1) Depending on the length of the TAC ramp only a limited time range is accessible. The same TAC setting as in Fig. 5-2, i.e. a bin-width of 4.069 ps, was used in Fig. 5-3.

(2) In principle, as with the used electronics, macro time recording of the photons that stop the TAC is possible. Since this is only a small fraction of the total number of photons detected by both detectors, (long-time) correlation curves generated from these data would be correspondingly noisy. In the classical HBT experiment the macro time information is lost. Consequently the full correlation curve and therefore information about fluorophore concentrations is in general not available.

(3) Electronic interference between the two channels destorting the time axis can be seen on the smoothed curve (dark grey) and is harder to minimize in a single board setup than in a dual board experiment.

The antibunching time t_A from all four experiments (Figs. 5-2, 5-3) is in average 3.4 ns ± 10%, the HBT-data having the bigger error due to the smaller time-window available for fitting. From $t_A = 1/(k_{01} + k_0)$ and the excitation rate constant $k_{01} = \sigma_{01} \cdot \mathrm{I}_0/2 \cdot \lambda/\mathrm{hc}$, with λ/hc being wavelength of the exciting light divided by Planck's constant and the speed of light, the known absorption cross section σ_{01} can now be used to predict t_A [Mets et al., 1997]. For a fluorescence lifetime of $(k_0)^{-1} = 4.01$ ns, an applied mean excitation intensity of $\mathrm{I}_0/2 = 90$ kW/cm^2 at a wavelength of $\lambda = 496$ nm and an absorption cross section for Rh110 in water of $\sigma_{01} = 2.62 \cdot 10^{-16}$ cm^2 at that wavelength [Eggeling, 1999] $t_A = 3.24$ ns is obtained. This is well within the experimental error of the measured value. The limited instrumental resolution was not taken into account in this consideration, its effect was estimated to be smaller than the scattering of the experimental values for the antibunching relaxation times but would make the difference between prediction and mean experimental value even smaller.

5.2 Full correlation with a pulsed excitation.

Cw experiments can, via measuring of antibunching relaxation times, yield information about the fluorescence lifetimes but requires knowledge of the excitation rates. The more direct and, for a given number of detected photons statistically far more accurate way to determine lifetimes employs pulsed excitation. In the following its effect on the correlation curves will be discussed.

In fluorescence experiments with pulsed laser excitation the system is probed at the repetition rate of the light source as opposed to random excitation with a cw light source. Consequently, for time intervals of the order of or smaller than the pulse distance, correlation of the data results in significantly different FCS curves for the two excitation modes. As shown for Rhodamine 110 solutions (Fig. 5-4), the pulse train of the excitation pulses is reflected in the statistics of the emitted photons. The highly correlated fluorescence signal results in correlation curves exhibiting strong bunching/antibunching behaviour at timescales of the laser repetition rates.

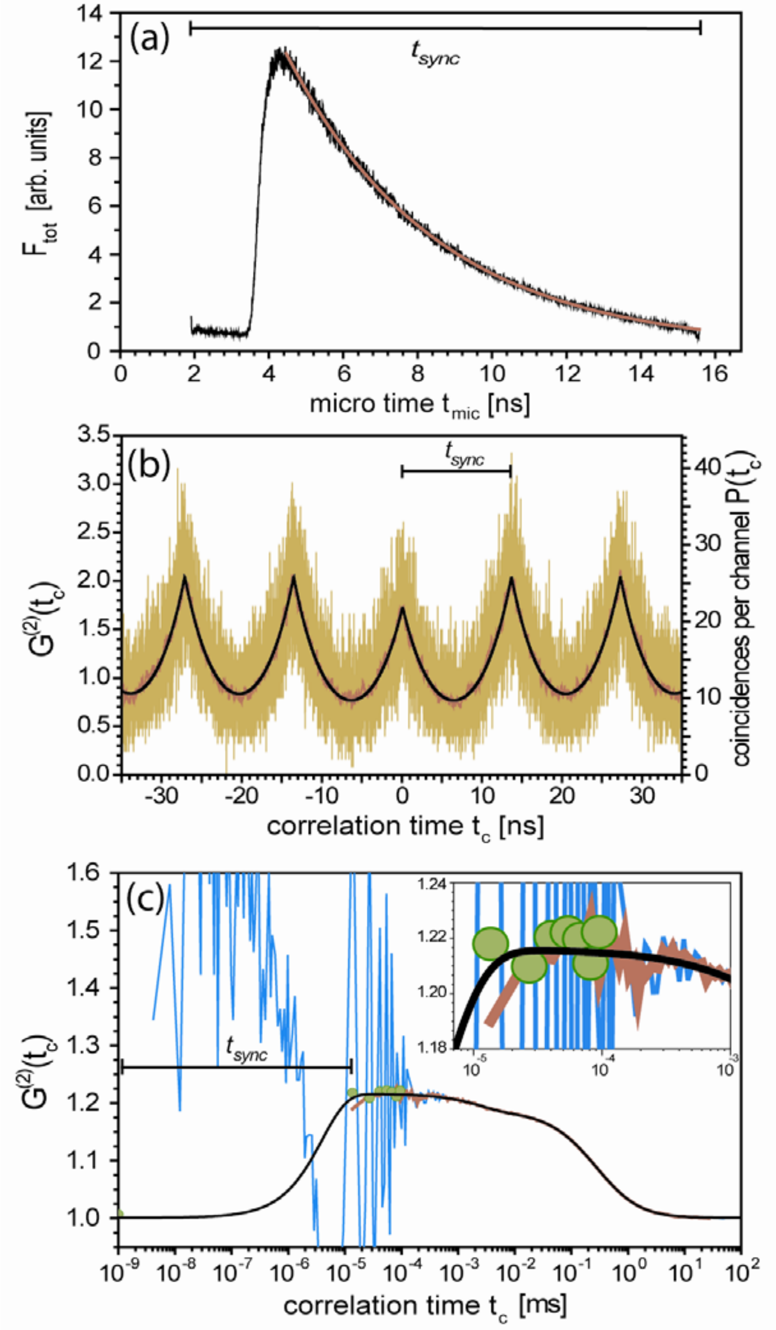

Figure 5-4. MFD of Rhodamine 110 aqueous solutions with APD detectors, pulsed excitation at 496 nm, mean intensity 24 kW/cm^2. Recording time 40s. t_{sync} is the synchronisation signal for the macro time counter and is obtained from the modelocker of the pulsed laser

a) Micro time t_{mic} histogram showing fluorescence decay (black) with single exponential fit (red). Fit results: τ = 4.01 ns, F_{offs} = 0.0206.

b) Short-time correlation curves (green) with 50 point average (red) and fit to eq. 13 (black). Time channel width is 4.069 ps. Fit results: C_0 = 1.48, C_1 = 1.81, C_2 = 1.80, t_{del} = 13.6 ns, τ_d = 4.14 ns. A linear offset was set to 0.113 (see text).

c) Full correlation curve (blue) with macro time correlation curve (red), short-time correlation amplitudes from eq. 14 (green dots) and simulation according to eq. 12 (black). Simulation parameters: N = 5.4, z_0/ω_0 = 2.0, t_D = 0.3 ms, T_{eq} = 0.135, t_T = 2.4 µs, m = 1.01, t_A = 4.0 ns. The insert shows an enlarged part of the time regime around the intersection of micro and macro time axis.

Fluorescence was detected with APDs after excitation by pulsed laser light at 496 nm and a repetition rate of 73.5 MHz. The mean intensity was set to 24 kW/cm^2, the mean number of Rh110 molecules in the confocal volume element was $N = 5.4$.

5.2.1 Fluorescence decay:

Histogramming the photon arrival times t_{mic} (micro time $t_{mic} = t_{TAC} \cdot N_{TAC}$) yields fluorescence decay curves F_{par} and F_{perp} for the parallel and perpendicular detection channel, respectively. Assuming isotropic distribution of the molecules the total fluorescence signal decay $F_{tot}(t_{mic})$ can be reconstructed by eq. 5-4.

$$F_{tot}(t_{mic}) = (1-3l_2)F_{par}(t_{mic}) + (2-3l_1)gF_{perp}(t_{mic}) \qquad \text{(Eq. 5-2)}$$

The correction factors $l_1 = 0.0308$, $l_2 = 0.0368$ compensate for mixing of polarizations in the high N.A. objective, the g-factor (in this case $g = 0.91$) corrects intensities for slight anisotropies in the individual detection efficiencies of the different channels (see chapter 2.2). A total fluorescence decay $F_{tot}(t_{mic})$ is shown in fig. 5-4a together with a fitted single exponential. The APD modules used in this experiment showed significant afterpulsing. Afterpulsing occurs on timescales larger than the detector deadtime and generates a flat offset in the TAC histogram. To account for that a constant offset ,*u,* was used and in the fit added to the time-dependent fluorescence signal (Chapter 2.2.2.1). The offset in Fig. 5-4a amounts to 5.8% of the total signal. The fluorescence lifetime was found to be $\tau = 4.01$ ns.

5.2.2 Short-time correlation:

The FCS for lag times between -100 ns < t_c < 100 ns is shown in Fig. 5-4b (light grey) together with a fit to eq. 2.2.4-13 (black) and a smoothed curve of the data (dark grey). The amplitude at $t_c = 0$, corresponding to the central peak, is smaller than at the lateral peaks as a result of single molecule photon antibunching, but does no longer represent the absolute minimum of the FCS as in the case of cw excitation. By setting an offset to 0.113, corresponding to the measured offset of 5.8% in the fluorescence decay (Fig. 5-4a) a decay time for the correlation peaks of $t_d = 4.14$ ns was found. t_d is expected to be slightly larger than τ derived from the fluorescence decay analysis since no deconvolution with the instrumental response function was performed and in the FCS two IRF (one per channel) enter to broaden the signal.

The contrast of the pulse pattern in this time regime is a function of the experimental conditions and will vanish, for a given fluorescence lifetime, at high repetition rates ($t_L << \tau_d$) or at low instrumental resolution ($t_L << FWHM_{IRF}$).

5.2.3 Full correlation:

For pseudo logarithmic binning (multiple tau correlation) the long-time portion of the full correlation resembles a cw experiment (Fig. 5-4c). Here the time-bins cover (and average) many excitation periods. A fit to eq. 2.2.4-10 for $t_c > 10^{-4}$ ms, extrapolated to shorter times with fixed parameters $t_A = 4.0$ ns and $m = 1$ is shown as black overlay in the figure. Correlation of the macro-times yields a low-resolution curve starting at 13.6 ns (red). The first points of theat curve with spacings of 13.6 ns suffer from overlapping of the fluorescence decays originating from adjacent laser pulses. Here fitting of the the short-time correlation curve (Fig. 5-3b) and application of eq. 2.2.4-12 yields more accurate results by taking these artefacts into account (dots). The amplitude at time zero (t_c=0) as it would be expected in a cw experiment is indicated at $t_c = 10^{-9}$ ms. In pulsed experients with high repetition rates this amplitude can only be derived in the described way and is not available by macro-time correlation.

The three different ways to analyse the data from pulsed excitation can give information

(1) via correlation, about molecular and photophysical dynamics with a time resolution of the pulse distance,

(2) via decay analysis, about fluorescence lifetime and faster rotational correlation times and

(3) at $t_c = 0$, i.e. in the photon antibunching regime, about coincident photons and numbers of independent fluorophores.

6 SUMMARY

This thesis presents the development and applications of novel experimental and analytical techniques for the quantitative investigation of single biological molecules in solution and living cells. In contrast to ensemble experiments, single molecule measurements eliminate averaging over a population of molecules and deliver direct structural and dynamic information. Multiparameter fluorescence detection (MFD) is now established as a technique in single-molecule fluorescence spectroscopy and allows for the simultaneous measurement of the full fluorescence information: the spectral properties, fluorescence brightness and quantum yield, fluorescence lifetime and fluorescence anisotropy.

Identification of multiple species

A general strategy to identify and quantify single molecules in dilute solution employing MFD was developed. Twelve identical oligonucleotides differing in the combination of the fluorescence reporters labeled to them (Rh6G-Cy5, Rh6G-BP 650/665, Cy3-Cy5, Cy3-BP 650/665) and in the distance between them (with 9, 13 or 17 base-pairs), were measured at the single molecule level. Including free dye molecules and incompletely labeled oligonucleotides, 16 different compounds were identified and separated from the mixture, based on the multidimensional information contained in the fluorescence of the analyzed molecules.

Identification of the different species was first demonstrated by use of sequential two-dimensional projections of histograms in different fluorescence parameter planes, employing different “border lines” between the populations projected in each plane. However, in addition to this visual approach demonstrating the feasibility, a more quantitative identification procedure was employed, based on an algorithm that offers fast and automated species identification with reasonable fidelity on a single molecule level. This approach can also regenerate concentration profiles of species in a mixed sample with very high accuracy and there is still a clear potential for implementing additional criteria and procedures.

Such multiplexed assays with single-molecule sensitivity may have a great impact on the screening of species and events that don't lend themselves so easily to amplification, such as disease-specific proteins and their interactions.

Subunit rotation in single membrane-bound F_0F_1 –ATP synthase.

MFD was shown to be a powerful tool for studies of dynamic and conformational properties of single biomolecules. γ-subunit rotation of F_0F_1-ATP synthase was studied during ATP synthesis and hydrolysis. F_0F_1-ATP synthases from *Escherichia coli* were labelled with fluorescence reporters and incorporated into liposomes. By analyzing the fluorescence information, it was found that the γ-subunit rotates stepwise during proton transport–powered ATP synthesis, showing three distinct distances to the b subunits in repeating sequences. The average durations of these steps correspond to catalytic turnover times upon ATP synthesis as well as ATP hydrolysis. The direction of rotation during ATP synthesis is opposite to that of ATP hydrolysis.

MFD-Imaging (MFDi)

A new general strategy based on MFD was introduced to register and quantitatively analyse fluorescence images. MFD delivers the complete accessible spectroscopic information in each pixel of an image and thus increases the information content per image, which often is crucial for a correct interpretation of functional information.

By analyzing 2D histograms of the fluorescence parameters, specific pixels can be selected for subsequent sub-ensemble analysis to improve statistical accuracy of the estimated parameters. MFDi avoids sequential measurements, because the registered data allows one to perform many analysis techniques such as fluorescence correlation spectroscopy (FCS) in an off-line mode.

To demonstrate the ability of this technique, two systems were analyzed:

1) interactions of the fluorescent dye Rhodamine 110 inside and outside of a glutathione-sepharose bead;

2) microtubule dynamics in live yeast cells of *Schizosaccharomyces pombe* using a fusion protein of Green Fluorescent Protein (GFP) with Minichromosome Altered Loss Protein 3 (Mal3), which is involved in the dynamic cycle of polymerizing and depolymerising microtubules.

Full correlation

MFD can be combined with fluorescence correlation spectroscopy (FCS), which reveals molecular concentrations as well as the molecule's mobility parameters.

An improved time-correlated single photon counting (TCSPC) technique for simultaneous fluorescence lifetime and correlation experiments was developed. It allows calculation of the full correlation curve from the same photons emitted from single or very few, molecules.

A fast multi-tau software correlator was developed to correlate the data. The algorithm uses the asynchronous single photon intensity information of the TCSPC data without requiring the construction of a multichannel scaler (MCS) trace, as needed for conventional intensity correlation algorithms.

The method offers two main advantages for experiments at low concentrations over conventional single molecule fluorescence detection:

3) Short (nanosecond time-scale) and long (ms time scale) correlation times are now simultaneously accessible in a TCSPC experiment with high resolution. The presented technique bridges the gap between anisotropy decay analysis and currently available commercial correlators.
4) The number of independent fluorophores on a single molecule can be determined (e.g. the number of monomers in a complex) by measuring coincident photons simultaneously with all other fluorescence parameters.

The technique is applicable to immobilized molecules as well as to free fluorophores in solution.

7 Literature

Datasheet Photosensor Modules, H7422 Series Hamamatsu Photonics Deutschland (2004)

Datasheet Single Photon Counting Module, SPCM-AQR Series PerkinElmer Optoelectronics (2004)

Abrahams, JP, A G W Leslie, R Lutter, J E Walker. *Structure at 2.8-angstrom resolution of* F_1*-ATPase from bovine heart-mitochondria*. Nature **370**, p. 621-628 (1994).

Aggeler,R, R A Capaldi. *Cross-linking of the gamma-subunit of the escherichia-coli ATPase (ecf(1)) via cysteines introduced by site-directed mutagenesis*. Journal of Biological Chemistry **267**, p. 21355-21359 (1992).

Aggeler,R, I Ogilvie, R A Capaldi. *Rotation of a gamma-epsilon subunit domain in the Escherichia coli* F_1F_0*-ATP synthase complex - The gamma-epsilon subunits are essentially randomly distributed relative to the alpha(3)beta(3)delta domain in the intact complex*. Journal of Biological Chemistry **272**, p. 19621-19624 (1997).

Anazawa, T, H Matsunaga, E S Yeung. *Electrophoretic quantitation of nucleic acids without amplification by single-molecule imaging*. Analytical Chemistry **74**, p. 5033-5038 (2002).

Bacia, K, P Schwille. *A dynamic view of cellular processes by in vivo fluorescence auto- and cross-correlation spectroscopy*. Methods **29**, p. 74-85 (2003).

Bajzer, Z, T M Therneau, J C Sharp, F G Prendergast. *Maximum likelihood method for the analysis of time-resolved fluorescence decay curves*. European Biophysics Journal **20**, p. 247-262 (1991).

Baker, S, R D Cousins. *Clarification of the use of chi-square and likelihood functions in fits to histograms*. Nucleic Instruments & Methods in Physics Research **221**, p. 437-442 (1984).

Balaji, J, S Maiti. *Quantitative measurement of the resolution and sensitivity of confocal microscopes using line-scanning fluorescence correlation spectroscopy*. Microscopy Research and Technique **66**, p. 198-202 (2005).

Ballew, RM, J N Demas. *An error analysis of the rapid lifetime determination method for the evaluation of single exponential decays*. Analytical Chemistry **61**, p. 30-33 (1989).

Basché, T, W E Moerner, M Orrit, H Talon. *Photon Antibunching in the Fluorescence of a Single Dye Molecule Trapped in a Solid.* Physical Review Letters **69**, p. 1516-1519 (1992).

Becker, W. *Advanced time-correlated single photon counting techniques*. Springer Berlin Heidelberg New York (2005).

Becker, W, K Benndorf, A Bergmann, C Biskup, K Koenig, U Tirlapur, T Zimmer. *FRET measurements by TCSPC laser scanning microscopy*. Proceedings of SPIE-The International Society for Optical Engineering **4431**, p. 94-98 (2001a).

Becker, W, A Bergmann, C Biskup, T Zimmer, N Kloecker, K Benndorf. *Multiwavelength TCSPC lifetime imaging*. Proceedings of SPIE-The International Society for Optical Engineering **4620**, p. 79-84 (2002).

Becker, W, A Bergmann, H Wabnitz, D Grosenick, A Liebert. *High-count-rate multichannel TCSPC for optical tomography*. Proceedings of SPIE-The International Society for Optical Engineering **4431**, p. 249-254 (2001b).

Becker, W, H Hickl, C Zander, K H Drexhage, M Sauer, S Siebert, J Wolfrum. *Time-resolved detection and identification of single analyte molecules in microcapillaries by time-correlated single-photon counting (TCSPC)*. Review of Scientific Instruments **70**, p. 1835-1841 (1999).

Beveratos, A, S Kuhn, R Brouri, T Gacoin, J-P Poizat, P Grangier. *Room temperature stable single-photon source*. European Physical Journal D **18**, p. 191-196 (2002).

Borsch, M, M Diez, B Zimmermann, R Reuter, P Graber. *Stepwise rotation of the gamma-subunit of EF(0)F(1)-ATP synthase observed by intramolecular single-molecule fluorescence resonance energy transfer*. FEBS Letters **527**, p. 147-152 (2002).

Bowen, BP, A Scruggs, J Enderlein, M Sauer, N Woodbury. *Implementation of neural networks for the identification of single molecules*. Journal of Physical Chemistry A **108**, p. 4799-4804 (2004).

Boyer, PD. *ATP synthase - past and future*. Biochimica et Biophysica Acta-Bioenergetics **1365**, p. 3-9 (1998).

Brand, L. *Zeitaufgelöster Nachweis einzelner Moleküle in Lösung*. Thesis Georg-August-Universität Göttingen (1998).

Brock, R, M A Hink, T M Jovin. *Fluorescence correlation microscopy of cells in the presence of autofluorescence*. Biophysical Journal **75**, p. 2547-2557 (1998).

Busch, KE, D Brunner. *The microtubule plus end-tracking proteins mal3p and tip1p cooperate for cell-end targeting of interphase microtubules*. Current Biology **14**, p. 548-559 (2004).

Carlsson, J, J Philip. *Theoretical investigation of the signal-to-noise ratio for different fluorescence lifetime imaging techniques*. Proceedings of SPIE-The International Society for Optical Engineering **4622**, p. 70-78 (2002).

Cova, S, M Ghioni, A Lotito, I Rech, F Zappa. *Evolution and prospects for single-photon avalanche diodes and quenching circuits*. Journal of Modern Optics **51**, p. 1267-1288 (2004).

Cova, S, A Lacaita, M Ghioni, G Ripamonti, T A Louis. *20-ps timing resolution with single-photon avalanche diodes*. Review of Scientific Instruments **60**, p. 1104-1110 (1989).

Diez, M. *H+-ATPsynthase aus E. coli: Beobachtung der Protonen angetriebenen Rotation der γ-Untereinheit mit Einzelmolekül Fluoreszenzspektroskopie.* Thesis Albert-Ludwigs Universität (2003).

Diez, M, B Zimmermann, M Börsch, M König, E Schweinberger, S Steigmiller, R Reuter, S Felekyan, V Kudryavtsev, C. A. M. Seidel, P Gräber. *Proton-powered subunit rotation in single membrane-bound F_0F_1-ATP synthase*. Nature Structural & Molecular Biology **11**, p. 135-141 (2004).

Digman, MA, C M Brown, P Sengupta, P W Wiseman, A R Horwitz, E Gratton. *Measuring fast dynamics in solutions and cells with a laser scanning microscope*. Biophysical Journal **89**, p. 1317-1327 (2005a).

Digman, MA, P Sengupta, P W Wiseman, C M Brown, A R Horwitz, E Gratton. *Fluctuation correlation spectroscopy with a laser-scanning microscope: Exploiting the hidden time structure*. Biophysical Journal **88**, p. L33-L36 (2005b).

Edman, L, Ü Mets, R Rigler. *Conformational transitions monitored for single molecules in solution*. Proc.Natl.Acad.Sci.U.S.A. **93**, p. 6710-6715 (1996).

Eggeling, C. Thesis, Georg-August-Universität Göttingen, Germany (1999).

Eggeling, C, S Berger, L Brand, J R Fries, J Schaffer, A Volkmer, C A M Seidel. *Data registration and selective single-molecule analysis using multi-parameter fluorescence detection*. Journal of Biotechnology **86**, p. 163-180 (2001a).

Eggeling, C, J R Fries, L Brand, R Günther, C A M Seidel. *Monitoring conformational dynamics of a single molecule by selective fluorescence spectroscopy*. Proc.Natl.Acad.Sci.U.S.A. **95**, p. 1556-1561 (1998a).

Eggeling, C, J Schaffer, C A M Seidel, J Korte, G Brehm, S Schneider, W Schrof. *Homogeneity, transport, and signal properties of single Ag particles studied by single-molecule surface-enhanced resonance Raman scattering*. Journal of Physical Chemistry A **105**, p. 3673-3679 (2001b).

Eggeling, C, J Widengren, R Rigler, C A M Seidel. *Photobleaching of Fluorescent Dyes under Conditions used for Single-Molecule-Detection: Evidence of Two-Step Photolysis*. Analytical Chemistry **70**, p. 2651-2659 (1998b).

Ekstrom, PA. *Triggered-avalanche detection of optical photons*. Journal of Applied Physics **52**, p. 6974-6979 (1981).

Enderlein, J, P M Goodwin, A van Orden, W P Ambrose, R Erdmann, R A Keller. *A maximum likelihood estimator to distinguish single molecules by their fluorescence decays*. Chemical Physics Letters **270**, p. 464-470 (1997).

Enderlein, J, M Sauer. *Optimal Algorithm for Single-Molecule Identification with Time-Correlated Single-Photon Counting*. Journal of Physical Chemistry A **105**, p. 48-53 (2001).

Felekyan, S, R Kühnemuth, V Kudryavtsev, C Sandhagen, W Becker, C A M Seidel. *Full correlation from picoseconds to seconds by time-resolved and time-correlated single photon detection*. Review of Scientific Instruments **76**, p. 083104-1-083104-14 (2005).

Förster, T. *Zwischenmolekulare Energiewanderung und Fluoreszenz*. Annalen der Physik **2**, p. 55-75 (1948).

Fries, JR, L Brand, C Eggeling, M Köllner, C A M Seidel. *Quantitative identification of different single-molecules by selective time-resolved confocal fluorescence spectroscopy*. Journal of Physical Chemistry A **102**, p. 6601-6613 (1998).

Gaiduk, A. Thesis Heinrich-Heine-Universität Düsseldorf, Germany (2006).

Gennerich, A, D Schild. *Fluorescence correlation spectroscopy in small cytosolic compartments depends critically on the diffusion model used*. Biophysical Journal **79**, p. 3294-3306 (2000).

Gogol, EP, U Lucken, T Bork, R A Capaldi. *Molecular architecture of escherichia-coli* F_1 *adenosine-triphosphatase*. Biochemistry **28**, p. 4709-4716 (1989).

Hall, P, B Selinger. *Better Estimates of Exponential Decay Parameters*. Journal of Physical Chemistry **85**, p. 2941-2946 (1981).

Hanbury-Brown, R, R Q Twiss. *Correlation between photons in 2 coherent beams of light*. Nature **177**, p. 27-29 (1956).

Hebert, B, S Costantino, P W Wiseman. *Spatiotemporal image correlation spectroscopy (STICS) theory, verification, and application to protein velocity mapping in living CHO cells*. Biophysical Journal **88**, p. 3601-3614 (2005).

Heikal, AA, S T Hess, G S Baird, R Y Tsien, W W Webb. *Molecular spectroscopy and dynamics of intrinsically fluorescent proteins: Coral red (dsRed) and yellow (Citrine)*. Proceedings of the National Academy of Sciences of the United States of America **97**, p. 11996-12001 (2000).

Herten, DP, P Tinnefeld, M Sauer. *Identification of single fluorescently labelled mononucleotide molecules in solution by spectrally resolved time-correlated single-photon counting*. Applied Physics B **71**, p. 765-771 (2000).

Hirschfeld, T. *Quantum efficiency independence of the time integrated emission from a fluorescent molecule*. Applied Optics **15**, p. 3135-3139 (1976).

Junge, W, D Sabbert, S Engelbrecht. *Rotatory catalysis by F-ATPase: Real-time recording of intersubunit rotation*. Berichte der Bunsen-Gesellschaft-Physical Chemistry Chemical Physics **100**, p. 2014-2019 (1996).

Kask, P, K Palo, N Fay, L Brand, Ü Mets, D Ullmann, J Jungmann, J Pschorr, K Gall. *Two-Dimensional Fluorescence Intensity Distribution Analysis: Theory and Application* . Biophysical Journal **78**, p. 1703-1713 (2000).

Kask, P, K Palo, D Ullmann, K Gall. *Fluorescence-intensity distribution analysis and its application in biomolecular detection technology*. Proc.Natl.Acad.Sci.U.S.A. **96**, p. 13756-13761 (1999).

Kerres, A, C Vietmeier-Decker, J Ortiz, I Karig, C Beuter, J Hegemann, J Lechner, U Fleig. *The fission yeast kinetochore component Spc7 associates with the EB1 family member Mal3 and is required for kinetochore-spindle association*. Molecular Biology of the Cell **15**, p. 5255-5267 (2004).

Knemeyer, J-P, N Marmé, M Sauer. *Probes for detection of specific DNA sequences at the single-molecule level*. Analytical Chemistry **72**, p. 3717-3724 (2000).

Kohl, T, P Schwille. *Fluorescence correlation spectroscopy with autofluorescent proteins*. Microscopy Techniques **95**, p. 107-142 (2005).

Kolin, DL, S Costantino, P W Wiseman. *Sampling effects, noise, and photobleaching in temporal image correlation spectroscopy*. Biophysical Journal **90**, p. 628-639 (2006).

Koppel, DE. *Statistical accuracy in fluorescence correlation spectroscopy*. Physical Review A **10**, p. 1938-1945 (1974).

Koshioka, M, K Saski, H Masuhara. *Time-Dependent Fluorescene Depolarization Analysis in Three Dimensional Microscopy*. Applied Spectroscopy **49**, p. 224-228 (1995).

Köllner, M. *Statistische und experimentelle Untersuchungen des ultraempfindlichen, selektiven Nachweises von Biomolekülen mit Hilfe von Multiplex-Farbstoffen*. Thesis Ruprecht-Karls-Universität, Heidelberg (1993).

Köllner, M, J Wolfrum. *How many photons are necessary for fluorescence-lifetime measurements?* Chemical Physics Letters **200**, p. 199-204 (1992).

König, M. *Multiparameter-fluoreszenzspektroskopische Untersuchungen zur molekularen Dynamik an einzelnen Biomolekülen*. Thesis (2005).

Kudryavtsev, V, S Felekyan, A K Wozniak, M König, C Sandhagen, R Kühnemuth, C. A. M. Seidel, F Oesterhelt. *Multiparameter Fluorescence Imaging to Monitor Dynamic Systems*. Anal.Bioanal.Chem. (2006).

Kühnemuth, R, C A M Seidel. *Principles of Single Molecule Multiparameter Fluorescence Spectroscopy*. Single Molecules **2** , p. 251-254 (2001).

Magatti, D, F Ferri. *25 ns software correlator for photon and fluorescence correlation spectroscopy*. Review of Scientific Instruments **74**, p. 1135-1144 (2003).

Maus, M, M Cotlet, J Hofkens, T Gensch, F C De Schryver, J Schaffer, C A M Seidel . *An Experimental Comparison of the Maximum Likelihood Estimation and Nonlinear Least-Squares Fluorescence Lifetime Analysis of Single Molecules*. Analytical Chemistry **73**, p. 2078-2086 (2001).

Mets, Ü, R Rigler. *Submillisecond Detection of Single Rhodamine Molecules in Water*. Journal of Fluorescence **4**, p. 259-264 (1994).

Mets, Ü, J Widengren, R Rigler. *Application of the antibunching in dye fluorescence - measuring the excitation rates in solution*. Chemical Physics **218**, p. 191-198 (1997).

Mitchell, P. *Coupling of phosphorylation to electron and hydrogen transfer by a chemi-osmotic type of mechanism*. Nature **191**, p. 144-& (1961).

Moerner, WE, D P Fromm. *Methods of single-molecule fluorescence spectroscopy and microscopy* . Review of Scientific Instruments **74**, p. 3597-3619 (2003).

Moerner, WE, L Kador. *Optical Detection and Spectroscopy of Single Molecules in a Solid*. Physical Review Letters **62**, p. 2535-2538 (1989).

Noji, H, R Yasuda, M Yoshida, K Kinosita. *Direct observation of the rotation of F-1-ATPase*. Nature **386**, p. 299-302 (1997).

O'Connor, DV, D Phillips. *Time-correlated Single Photon Counting*. Academic Press New York (1984).

Palo, K, L Brand, C Eggeling, S Jäger, P Kask , K Gall. *Fluorescence intensity and lifetime distribution analysis: Toward higher accuracy in fluorescence fluctuation spectroscopy*. Biophysical Journal **83**, p. 605-618 (2002).

Palo, K, Ü Mets, S Jäger, P Kask, K Gall. *Fluorescence Intensity Multiple Distributions Analysis: Concurrent Determination of Diffusion Times and Molecular Brightness*. Biophysical Journal **79**, p. 2858-2866 (2000).

PERLIN,DS, D N COX, A E Senior. *Integration of F_1 and the membrane sector of the proton-ATPase of escherichia-coli - role of subunit-b (uncf-protein)*. Journal of Biological Chemistry **258**, p. 9793-9800 (1983).

Prummer, M, B Sick, A Renn, U P Wild. *Multipararneter microscopy and spectroscopy for single-molecule analytics*. Analytical Chemistry **76**, p. 1633-1640 (2004).

Rocheleau, JV, P W Wiseman, N O Petersen. *Isolation of bright aggregate fluctuations in a multipopulation image correlation spectroscopy system using intensity subtraction*. Biophysical Journal **84**, p. 4011-4022 (2003).

Rothwell, PJ, S Berger, O Kensch, S Felekyan, M Antonik, B M Wöhrl, T Restle, R S Goody, C A M Seidel. *Multi-parameter Single-molecule Fluorescence Spectroscopy reveals Heterogeneity of HIV-1 Reverse Transcriptase:primer/template Complexes*. Proc.Natl.Acad.Sci.U.S.A. **100**, p. 1655-1660 (2003).

Ruan, Q, M A Cheng, M Levi, E Gratton, W W Mantulin. *Spatial-temporal studies of membrane dynamics: Scanning fluorescence correlation spectroscopy (SFCS)*. Biophysical Journal **87**, p. 1260-1267 (2004).

Sambongi, Y, Y Iko, M Tanabe, H Omote, A Iwamoto-Kihara, I Ueda, T Yanagida, Y Wada, M Futai. *Mechanical rotation of the c subunit oligomer in ATP synthase (F_0F_1): Direct observation*. Science **286**, p. 1722-1724 (1999).

Sauer, M, C Zander, R Müller, B Ullrich, K H Drexhage, S Kaul, J Wolfrum. *Detection and identification of individual antigen molecules in human serum with pulsed semiconductor lasers*. Applied Physics **65**, p. 427-431 (1997).

Schaffer, J. *Charakterisierung von Einzelmolekülen durch selektive Fluoreszenzspektroskopie*. Thesis Georg-August-Universität Göttingen (2000).

Schaffer,J, A Volkmer, C Eggeling, V Subramaniam, G Striker, C A M Seidel. *Identification of single molecules in aqueous solution by time-resolved fluorescence anisotropy*. Journal of Physical Chemistry A **103**, p. 331-336 (1999).

Schätzel, K. *New concepts in correlator design*. Institute of Physics Conference Series **77**, p. 175-184 (1985).

Schätzel, K, M Drewel, S Stimac. *Photon Correlation Measurements at Large Lag Times: Improving Statistical Accuracy*. Journal of Modern Optics **35**, p. 711-718 (1988).

Schätzel, K, R Peters. *Noise on multiple-tau photon correlation data*. Proceedings of SPIE-The International Society for Optical Engineering **1430**, p. 109-115 (1991).

Scheffler, S, M Sauer, H Neuweiler. *Monitoring antibody binding events in homogeneous solution by single-molecule fluorescence spectroscopy*. Zeitschrift fur Physikalische Chemie-International Journal of Research in Physical Chemistry & Chemical Physics **219**, p. 665-678 (2005).

Schmidt, Th, G J Schütz, H J Gruber, H Schindler. *Local stoichiometries determined by counting individual molecules*. Analytical Chemistry **68**, p. 4397-4401 (1996).

Schwille, P, U Haupts, S Maiti, W W Webb. *Molecular Dynamics in Living Cells Observed by Fluorescence Correlation Spectroscopy with One- and Two-Photon Excitation*. Biophysical Journal **77**, p. 2251-2265 (1999).

Schwille, P, S Kummer, A A Heikal, W E Moerner, W W Webb. *Fluorescence correlation spectroscopy reveals fast optical excitation-driven intramolecular dynamics of yellow fluorescent proteins*. Proceedings of the National Academy of Sciences of the United States of America **97**, p. 151-156 (2000).

Sekar, RB, A Periasamy. *Fluorescence resonance energy transfer (FRET) microscopy imaging of live cell protein localizations*. Journal of Cell Biology **160**, p. 629-633 (2003).

Skinner, JP, Y Chen, J D Müller. *Position-sensitive scanning fluorescence correlation spectroscopy*. Biophysical Journal **89**, p. 1288-1301 (2005).

Striker, G, V Subramaniam, C A M Seidel, A Volkmer. *Photochromicity and fluorescence lifetimes of green fluorescent protein* . Journal of Physical Chemistry B **103**, p. 8612-8617 (1999).

Tellinghuisen, J, P M Goodwin, W P Ambrose, J C Martin, R A Keller. *Analysis of Fluorescence Lifetime Data for Single Rhodamine Molecules in Flowing Sample Streams*. Analytical Chemistry **66**, p. 64-72 (1994).

Thompson, NL, A M Lieto, N W Allen. *Recent advances in fluorescence correlation spectroscopy*. Current Opinion in Structural Biology **12**, p. 634-641 (2002).

Tinnefeld, P, M Sauer. *Branching out of single-molecule fluorescence spectroscopy: Challenges for chemistry and influence on biology*. Angewandte Chemie-International Edition **44**, p. 2642-2671 (2005).

van der Meer, BW, G Cooker, S Y Chen. *Resonance Energy Transfer: Theory and Data*. VCH Publishers New York (1994).

Wahl,M, I Gregor, M Patting, J Enderlein. *Fast calculation of fluorescence correlation data with asynchronous time-correlated single-photon counting*. Optics Express **11**, p. 3583-3591 (2003).

Weston, KD, M Dyck, P Tinnefeld, C Muller, D P Herten, M Sauer. *Measuring the number of independent emitters in single-molecule fluorescence images and trajectories using coincident photons*. Analytical Chemistry **74**, p. 5342-5349 (2002).

Widengren, J, J Dapprich, R Rigler. *Fast interactions between Rh6G and dGTP in water studied by fluorescence correlation spectroscopy.* Chemical Physics **216**, p. 417-426 (1997).

Widengren, J, V Kudryavtsev, M Antonik, S Berger, M Gerken, C A M Seidel. *Single-molecule detection and identification of multiple species by multiparameter fluorescence detection*. Analytical Chemistry **78**, p. 2039-2050 (2006).

Widengren, J, Ü Mets, R Rigler. *Fluorescence Correlation Spectroscopy of Triplet States in Solution: A Theoretical and Experimental Study*. Journal of Physical Chemistry **99**, p. 13368-13379 (1995).

Widengren, J, P Schwille. *Characterization of photoinduced isomerization and back-isomerization of the cyanine dye Cy5 by fluorescence correlation spectroscopy*. Journal of Physical Chemistry A **104**, p. 6416-6428 (2000).

Wohland, T, R Rigler, H Vogel. *The Standard Deviation in Fluorescence Correlation Spectroscopy*. Biophysical Journal **80**, p. 2987-2999 (2001).

Wouters, FS, P J Verveer, P I H Bastiaens. *Imaging biochemistry inside cells*. Trends in Cell Biology **11**, p. 203-211 (2001).

Xiao, Y, V Buschmann, K D Weston. *Scanning fluorescence correlation spectroscopy: A tool for probing microsecond dynamics of surface-bound fluorescent species*. Analytical Chemistry **77**, p. 36-46 (2005).

Yang, H, G B Luo, P Karnchanaphanurach, T M Louie, I Rech, S Cova, L Y Xun, X S Xie. *Protein conformational dynamics probed by single-molecule electron transfer*. Science **302**, p. 262-266 (2003).

Yasuda, R, H Noji, M Yoshida, K Kinosita, H Itoh . *Resolution of distinct rotational substeps by submillisecond kinetic analysis of F-1-ATPase*. Nature **410**, p. 898-904 (2001).

8 APPENDIX A. Description of custom-written software

8.1 ELKE

"Elke" is the LabView based, custom-written program for primary MFD analysis (see Chapter 2.2). It reads SPC data, selects single molecule bursts, and calculates lifetime, anisotropy, and intensity for each separate burst. For all or selected single molecule bursts time window analyses with shifted intervals option can be applied. Programming by Dr. Cristian Eggeling, Dr. Jorg Schäffer, Dr. Elke Haustein, Dr. Suren Felekyan, Dr. Matthew Antonik, Volodymyr Kudryavtsev.

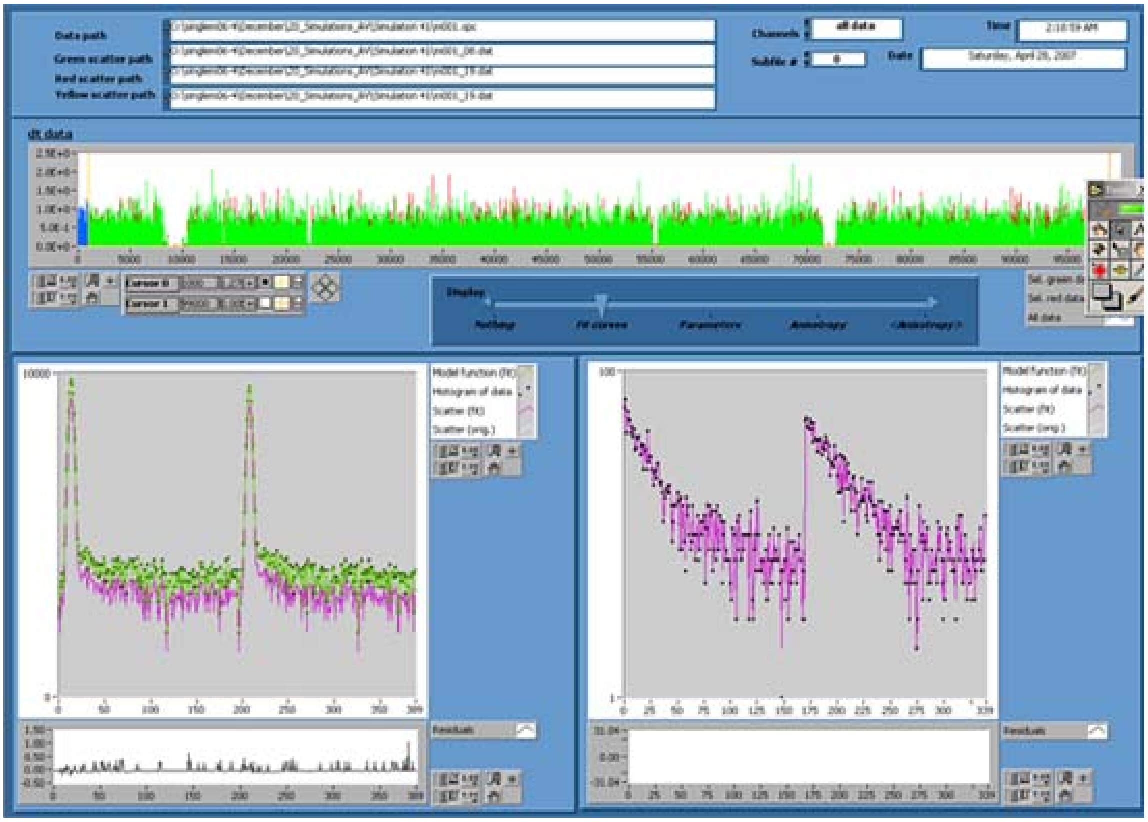

Figure 8.1 Front panel of the "Elke" program.

8.2 Margatita

"Margarita" is the LabView based, custom-written program, which reads the files produced by ELKE, and generates user specified 2D and 1D histograms. Burst coordinates (burst ID) for selected species can be exported for farther analyses. The third fluorescence parameter values can be used for species selection. Programming by Dr. Matthew Antonik.

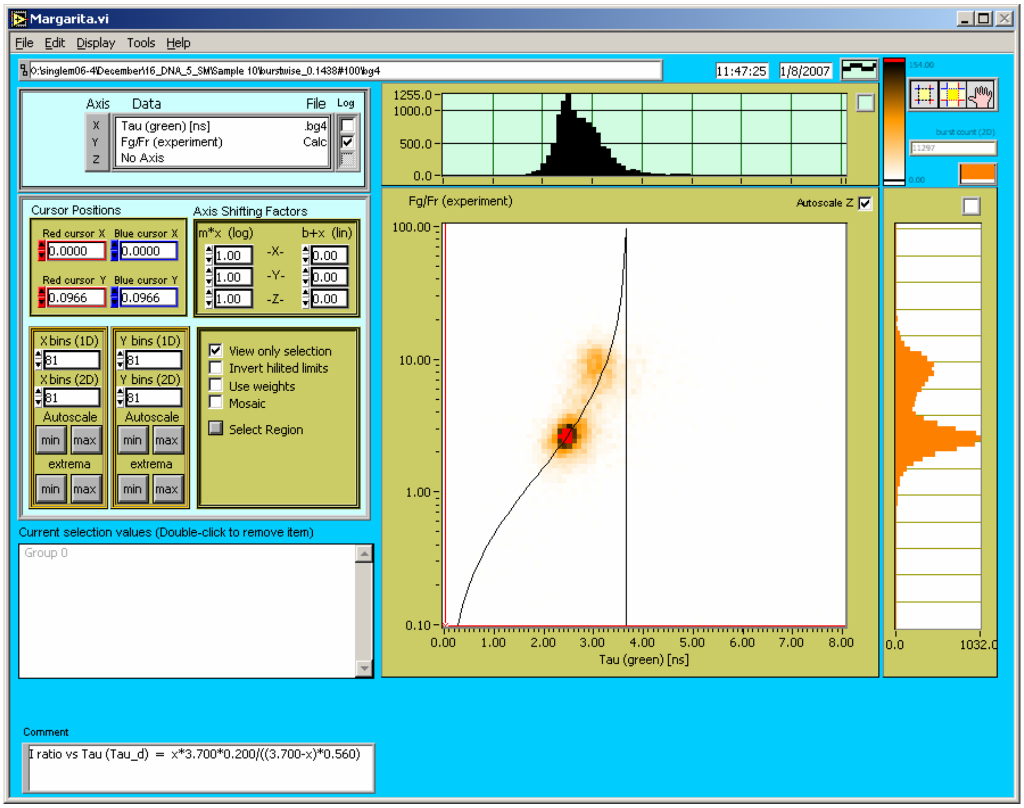

O:\singlem06-4\December\16_DNA_5_SM\Sample 10\burstwise_0.1438#100\bg4

11:47:25 1/8/2007

Axis	Data	File	Log
X	Tau (green) [ns]	.bg4	☐
Y	Fg/Fr (experiment)	Calc	☑
Z	No Axis		

Autoscale Z ☑

burst count (2D): 11297

Cursor Positions

Red cursor X: 0.0000
Blue cursor X: 0.0000
Red cursor Y: 0.0966
Blue cursor Y: 0.0966

Axis Shifting Factors

m*x (log)		b+x (lin)
1.00	-X-	0.00
1.00	-Y-	0.00
1.00	-Z-	0.00

X bins (1D): 81
X bins (2D): 81
Y bins (1D): 81
Y bins (2D): 81

☑ View only selection
☐ Invert hilited limits
☐ Use weights
☐ Mosaic
☐ Select Region

Current selection values (Double-click to remove item)

Group 0

Comment

I ratio vs Tau (Tau_d) = x*3.700*0.200/((3.700-x)*0.560)

Figure 8.2 Front panel of the "Margarita" program.

8.3 *VIEW BURST TRACES*

"View burst traces" is the LabView based, custom-written program which reads files produced by ELKE. For analyses which have been performed on bursts divided into either time or photon windows, it allows the user to view the parameters as a function of time within each burst. Programming by Volodymyr Kudryavtsev.

Total 727 bursts loaded

O:\singlem06-4\December\16_DNA_5_SM\Sample 10\tw_3.00ms__0.1480#100\tg4

Inverse ☑

Selected burst 0 0

x_axis 7

Smoothing m 1

Mean Macrotime (red) [ms]

Burst # 9 File # 0 SubFile # 0 # 9

Burst # 1

Figure 8.3. Front Panel of the "View burst traces" program.

8.4 *View MCS*

"View MCS" computes an MCS trace using user specified MCS bin width and time gating from SPC files. Reads burst ID's generated by "Margarita" and computes an MCS trace using user specified MCS bin width and time gating. Multiple burst filtering options are available. It histograms dwell times, S_G/S_R ratio frequencies from all bursts. Programming by Volodymyr Kudryavtsev, Dr. Matthew Antonik, Dr. Suren Felekyan.

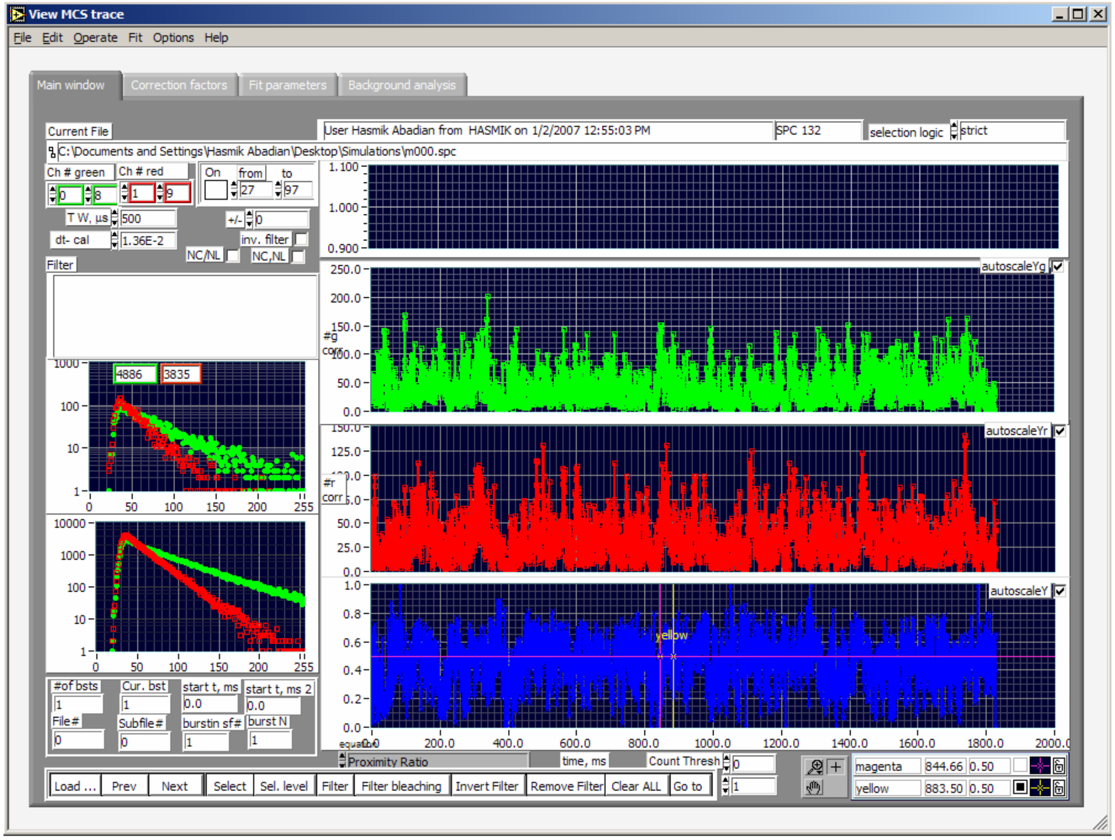
View MCS trace

Current File: C:\Documents and Settings\Hasmik Abadian\Desktop\Simulations\m000.spc

User Hasmik Abadian from HASMIK on 1/2/2007 12:55:03 PM

SPC 132

selection logic: strict

Ch # green: 0, 8

Ch # red: 1, 9

On: ☐ from 27 to 97

T W, µs: 500

dt- cal: 1.36E-2

+/-: 0

inv. filter ☐

NC/NL ☐

NC,NL ☐

4886

3835

#of bsts: 1

Cur. bst: 1

start t, ms: 0.0

start t, ms 2: 0.0

File#: 0

Subfile#: 0

burstin sf#: 1

burst N: 1

Proximity Ratio

Count Thresh: 0, 1

magenta 844.66 0.50

yellow 883.50 0.50

autoscaleYg ☑

autoscaleYr ☑

autoscaleY ☑

Figure 8.4. Front Panel of the "View MCS" program.

8.5 *KRISTINE*

"Kristine" is the Labview based software correlator and fitting routine. Full correlation from picoseconds to seconds for TCSPC data, TAC gated FCS ae possible. Countrate filter can be applied to SPC files. Species selective FCS (Burst ID correlation). Time-resolved FCS or component selective correlation (with Jörg Enderlein filters). More than 100 fitting functions with up to 32 parameters and 32 constants are implemented. Global fitting is possible. Programming by Dr. Suren Felekyan, Volodymyr Kudryavtsev.

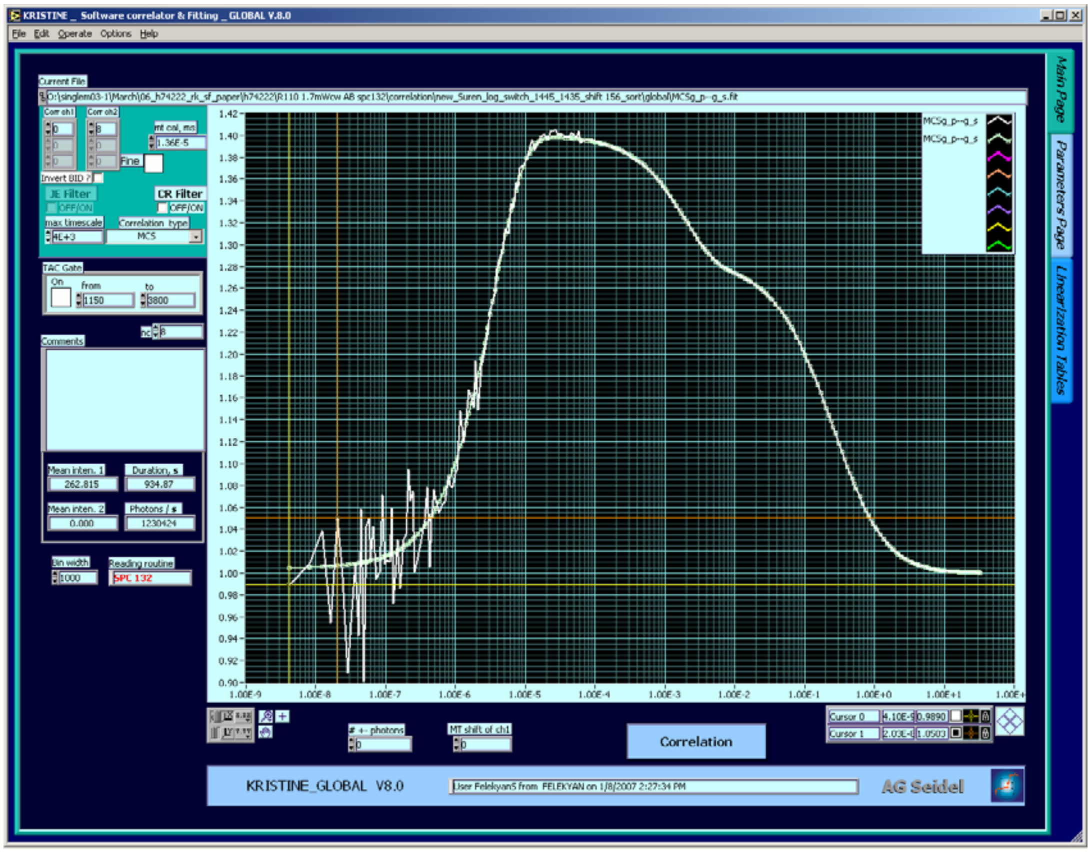

Current File: O:\singlem03-1\March\06_h74222_rk_sf_paper\h74222\R110 1.7mWcw AB spc132\correlation\new_Suren_log_switch_1445_1435_shift 156_sort\global\MCSg_p--g_s.fit

Corr ch1: 0, 0, 0

Corr ch2: 8, 0, 0

mt cal, ms: 1.36E-5

Fine ☐

Invert BID ? ☐

max timescale: 4E+3

Correlation type: MCS

TAC Gate: On ☐ from 1150 to 3800

nc: 8

Mean inten. 1: 262.815

Duration, s: 934.87

Mean inten. 2: 0.000

Photons / s: 1230424

Bin width: 1000

Reading routine: SPC 132

+- photons: 0

MT shift of ch1: 0

Cursor 0: 4.10E-9, 0.9890

Cursor 1: 2.03E-0, 1.0503

User Felekyan5 from FELEKYAN on 1/8/2007 2:27:34 PM

Figure 8.5. Front Panel of "Kristine" program.

8.6 *Marcelle*

"Marcelle" is a custom written Labview based program for MFD-Imaging (see Chapter 4). It finds the proper photons for each pixel of 2D scan and recovers the image from SPC files, calculates correlation curve and TAC histogram for each pixel or for the selection of the pixels. For each pixel lifetime, anisotropy, intensity, correlation diffusion time, correlation amplitude can be calculated. Marcelle exports the calculated parameters for "Margarita", pixel coordinates in format of burst ID. Most of above mentioned software can analyze the pixel photons like photons from bursts, so all fluorescence parameters can be calculated for each pixel and all types of fluorescence parameter images can be constructed. Generates movies from the series of frames, saving for each movie frame all the calculated parameters as well as raw data. Programming by Volodymyr Kudryavtsev, Dr. Suren Felekyan.

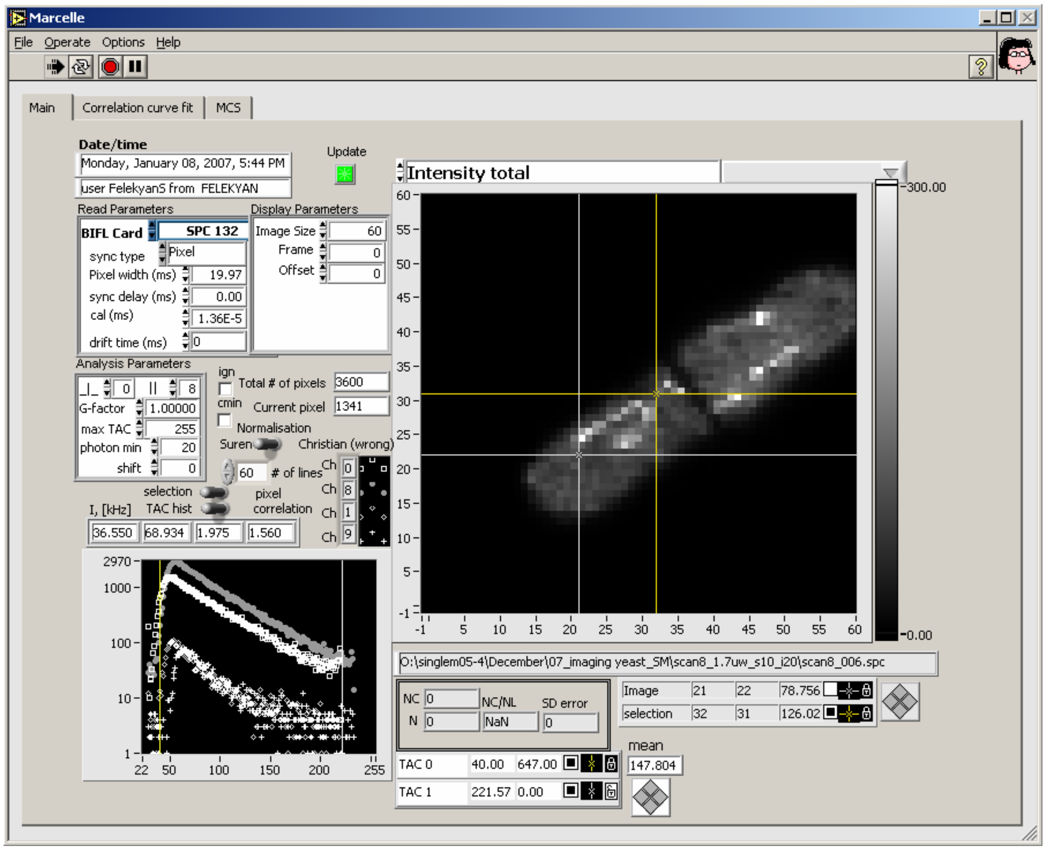

Date/time
Monday, January 08, 2007, 5:44 PM
user FelekyanS from FELEKYAN

BIFL Card: SPC 132
sync type: Pixel
Pixel width (ms): 19.97
sync delay (ms): 0.00
cal (ms): 1.36E-5
drift time (ms): 0

Image Size: 60
Frame: 0
Offset: 0

_|_: 0
||: 8
G-factor: 1.00000
max TAC: 255
photon min: 20
shift: 0

☐ Total # of pixels: 3600
☐ Current pixel: 1341
# of lines: 60
Ch 0
Ch 8
Ch 1
Ch 9

36.550 | 68.934 | 1.975 | 1.560

O:\singlem05-4\December\07_imaging yeast_SM\scan8_1.7uw_s10_i20\scan8_006.spc

NC: 0
N: 0
NC/NL: NaN
SD error: 0

Image	21	22	78.756
selection	32	31	126.02

TAC 0	40.00	647.00
TAC 1	221.57	0.00

mean: 147.804

Figure 8.6. Front Panel of "Marcelle" program.

VOLUME 11 NUMBER 2 FEBRUARY 2004
www.nature.com/natstructmolbiol

nature structural & molecular biology

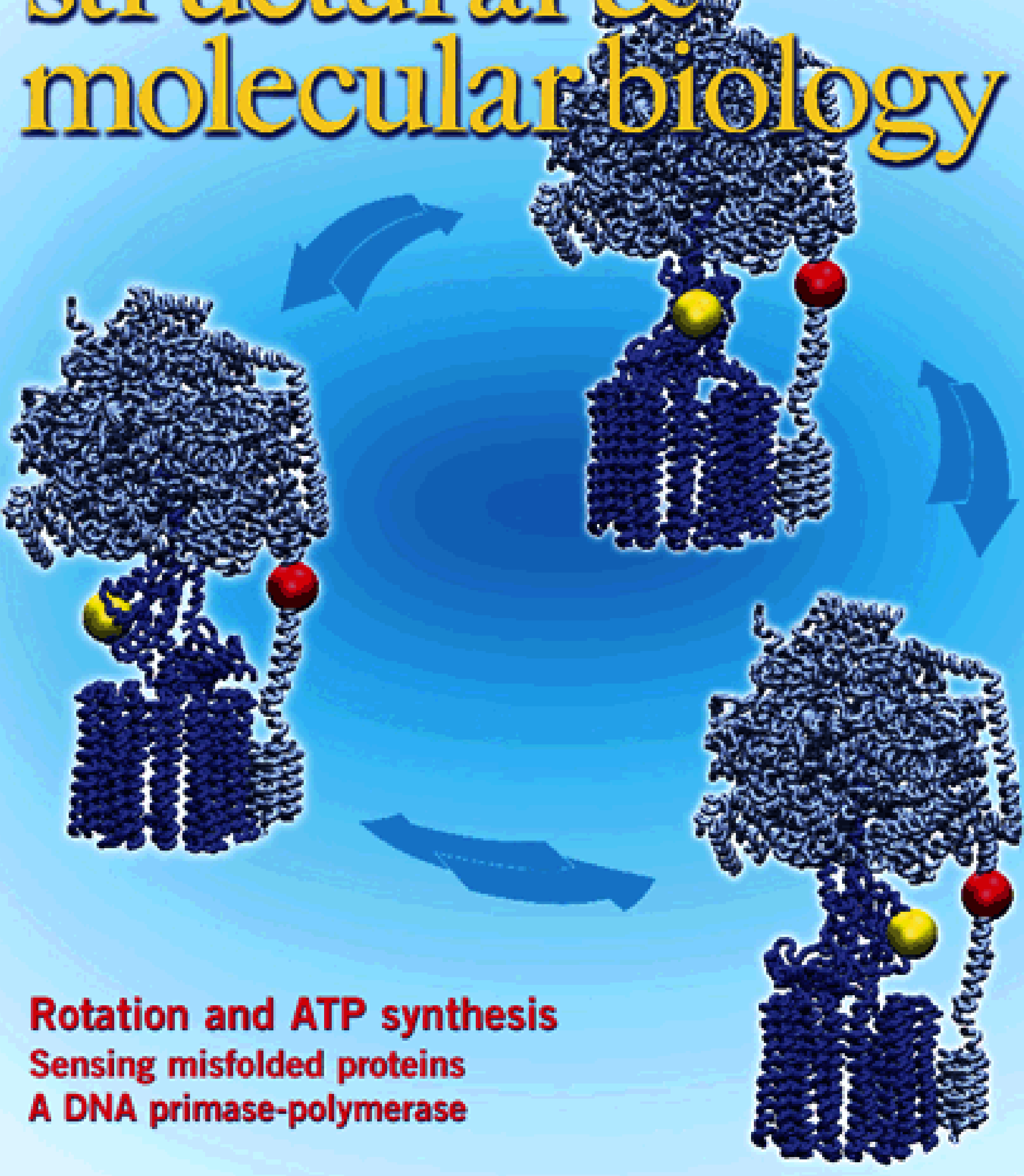

Rotation and ATP synthesis

Sensing misfolded proteins

A DNA primase-polymerase

nature
structural &
molecular biology

Proton-powered subunit rotation in single membrane-bound F_0F_1-ATP synthase

Manuel Diez[1], Boris Zimmermann[1], Michael Börsch[2], Marcelle König[3], Enno Schweinberger[3], Stefan Steigmiller[1], Rolf Reuter[1], Suren Felekyan[3], Volodymyr Kudryavtsev[3], Claus A M Seidel[3] & Peter Gräber[1]

Synthesis of ATP from ADP and phosphate, catalyzed by F_0F_1-ATP synthases, is the most abundant physiological reaction in almost any cell. F_0F_1-ATP synthases are membrane-bound enzymes that use the energy derived from an electrochemical proton gradient for ATP formation. We incorporated double-labeled F_0F_1-ATP synthases from *Escherichia coli* into liposomes and measured single-molecule fluorescence resonance energy transfer (FRET) during ATP synthesis and hydrolysis. The γ subunit rotates stepwise during proton transport–powered ATP synthesis, showing three distinct distances to the b subunits in repeating sequences. The average durations of these steps correspond to catalytic turnover times upon ATP synthesis as well as ATP hydrolysis. The direction of rotation during ATP synthesis is opposite to that of ATP hydrolysis.

To clarify the central role of energy transduction and the rotary mechanism of F_0F_1-ATP synthase, much experimental work has focused on the mechanistic events in this molecular motor[1–17]. F_0F_1-ATP synthase catalyzes the formation of ATP from ADP and phosphate in bacteria, mitochondria and chloroplasts, and this reaction is driven by conversion of Gibbs free energy derived from a transmembrane electrochemical proton gradient[1]. The enzyme consists of two parts, F_1 and F_0, which in *E. coli* have the subunit composition $\alpha_3\beta_3\gamma\delta\varepsilon$ and ab_2c_n with an expected number n of c subunits between 10 and 12, respectively (**Fig. 1a**). ATP synthesis takes place at the three β subunits of F_1, which sequentially adopt different conformations during catalysis[2]. Due to different interactions of each β subunit with the γ subunit, three possible conformations of the catalytic binding sites are found in the X-ray structure[3]. A sequential conversion of the conformations of the catalytic sites is caused by rotation of the γ subunit, which is located in the center of the $\alpha_3\beta_3$ complex. Rotation of the γ subunit is assumed to be coupled mechanically to proton translocation by a rotational movement of the c-ring[4] of F_0. Therefore, the subunits are also defined as 'rotor' ($\gamma\varepsilon c_n$, **Fig. 1**) and 'stator' ($\alpha_3\beta_3\delta ab_2$, **Fig. 1**)[5–8].

In single immobilized F_1 subcomplexes, subunit rotation during ATP hydrolysis has been demonstrated by video-microscopic experiment using a fluorescent actin filament connected to the γ subunit as a marker of its orientation[9]. Hydrolysis of ATP led to rotation of the γ subunit in 120° steps. Recently, resolution of substeps[10,11] has shown that the binding event of ATP at a relative γ-subunit position of 0° (or 120° and 240°, respectively) and the catalytic processes of ATP hydrolysis and product release at a relative γ-subunit position between 80° and 90° are associated with different angular orientations of the γ subunit. The direction of rotation was counterclockwise when viewed from F_0 to F_1 (**Fig. 1b**). Actin-filament attachment has also been used to show rotation of the c subunits of F_0 using immobilized complexes[12,13]; and by a single-fluorophore polarization experiment[14]. 'Molecular dynamics' simulations of the direction of ATP synthesis showed induced conformational changes within F_1 when an external rotary force was applied to the γ subunit[15,16].

However, up to now the rotation of the central γ subunit during proton-powered ATP synthesis could only be demonstrated indirectly[17]. The following questions must be investigated: (i) can we observe a rotation of the γ subunit coupled to proton translocation during ATP synthesis, that is distinguishable from an oscillation mode between only two positions for the γ subunit? (ii) Is the direction of rotation during ATP synthesis opposite or identical to that during ATP hydrolysis; that is, is this enzyme a bidirectional or unidirectional motor? (iii) Is the movement of the γ subunit during proton translocation continuous or stepwise? Because consecutive conformational motions in protein machines are stochastic and thus can hardly be synchronized, the subunit movements in F_0F_1-ATP synthase must be studied at the single-molecule level. Here we present the use of intramolecular single-molecule FRET to observe the rotary movement of the γ subunit during proton-powered ATP synthesis by single F_0F_1-ATP synthase. The FRET donor was attached at the rotating γ subunit and the FRET acceptor crosslinked the nonrotating b-subunit dimer. During catalysis, fluctuating FRET efficiencies indicate the relative movement of the labels because their distances sequentially interchange as a result of the rotation of the γ subunit.

---

[1]Institut für Physikalische Chemie, Albert-Ludwigs-Universität Freiburg, Albertstrasse 23 a, 79104 Freiburg, Germany. [2]3. Physikalisches Institut, Universität Stuttgart, Pfaffenwaldring 57, 70569 Stuttgart, Germany. [3]Max-Planck-Institut für Biophysikalische Chemie, Am Fassberg 11, 37077 Göttingen, Germany. Correspondence should be addressed to M.B. (michael.boersch@physchem.uni-freiburg.de).

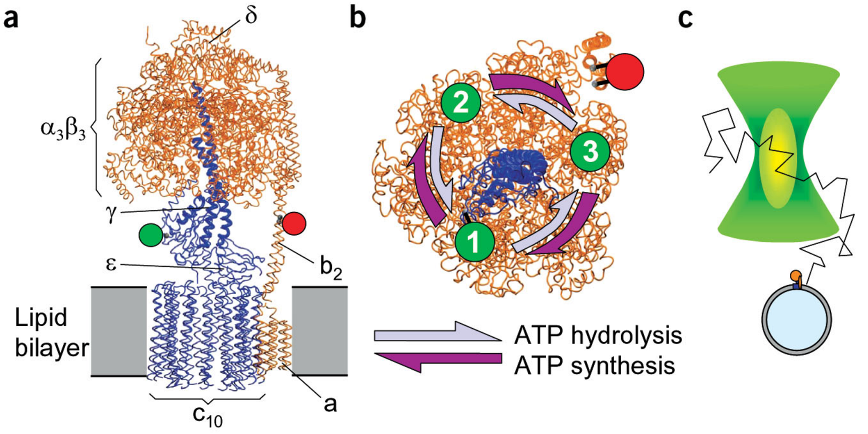

Figure 1 Model of F_0F_1 from *E. coli* (see Methods). (**a**) Side view. The FRET donor is bound to the γ subunit (green circle), the FRET acceptor Cy5bis to the b subunits (red circle). 'Rotor' subunits are blue, 'stator' subunits are orange. (**b**) Cross-section at the fluorophore level, viewed from F_0. Cy5bis (red) crosslinks the b subunits. Donor position 1 (green) of cysteine γ-T106C is farthest away from b-Q64C. Rotation of the γ subunit by 120° and 240° results in donor positions 2 and 3, respectively. (**c**) Photon bursts are observed when a freely diffusing single liposome with a single FRET-labeled F_0F_1 traverses the confocal detection volume (yellowish) within the laser focus (green).

RESULTS

Reconstituted F_0F_1-ATP synthase with FRET labels

To study intersubunit rotation of the membrane-bound F_0F_1-ATP synthase (referred to as F_0F_1 below) from *E. coli* under conditions of ATP synthesis and hydrolysis, the following prerequisites must be met: (i) preparation of the fully functional holoenzyme F_0F_1 in a quasi-native environment without additional immobilization; (ii) generation of a proton gradient across the lipid membrane; (iii) attachment of reporters for rotation that are small enough to allow undisturbed subunit movement during catalysis. We met these requirements by incorporating F_0F_1 into a liposome and by specifically labeling the b-subunit dimer and the γ subunit with two different fluorophores suitable for single-molecule FRET. To exclude specific photophysical effects of the dyes, we used two alternative FRET donor fluorophores, either tetramethylrhodamine-maleimide (TMR) or rhodamine110-maleimide (Rh110) bound to the γ subunit at residue 106 (**Fig. 1a,b**). The FRET acceptor, the bifunctional cyanine-5-bismaleimide (Cy5bis), crosslinked the two cysteines at position 64 in the b-subunit dimer of F_0F_1, avoiding ambiguity in the location of the dye[18].

To avoid any perturbations from surfaces, the labeled holoenzyme was investigated in freely diffusing liposomes that proved to be fully functional. The catalytic rates of these double-labeled enzymes were $v_S = (23 \pm 3)\ s^{-1}$ for ATP synthesis and $v_H = (67 \pm 6)\ s^{-1}$ for ATP

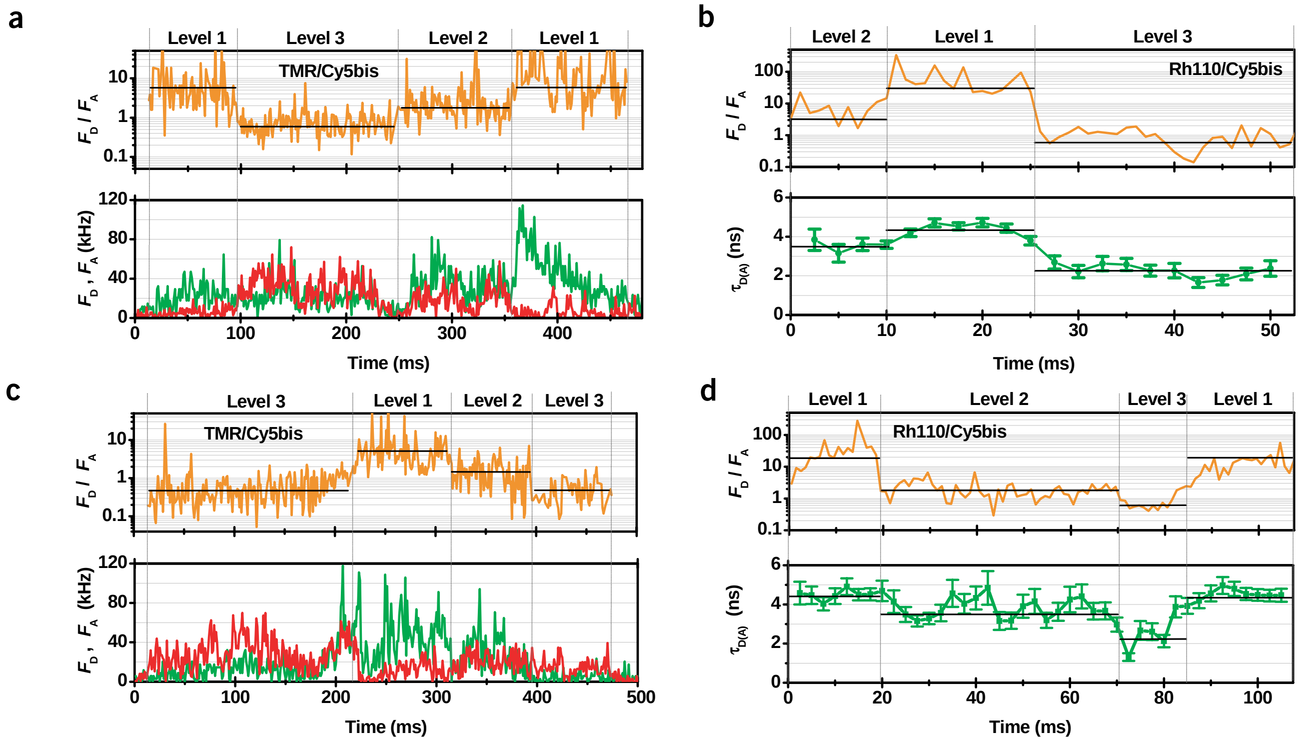

Figure 2 Photon bursts from single F_0F_1-ATP synthases in liposomes. (**a**,**b**) Photon bursts during ATP hydrolysis. (**c**,**d**) Photon bursts during ATP synthesis. FRET donor is TMR in **a** and **c**, Rh110 in **b** and **d**; FRET acceptor is Cy5bis in all traces. Fluorescence intensity traces of the donor, F_D, and acceptor, F_A, are green and red, respectively, in **a** and **c** (time window 1 ms). Corrected intensity ratios F_D / F_A are orange in all panels (time window 1 ms), and fluorescence lifetimes of the donor Rh110 are green in **b** and **d** (total time window 5 ms, shifted by 2.5 ms per data point). Three distinct FRET levels are attributed (1, 2 or 3) at top of panels. Black horizontal lines indicate the mean FRET levels from the distributions in **Figure 4** (additional traces are shown in **Supplementary Fig. 2** online).

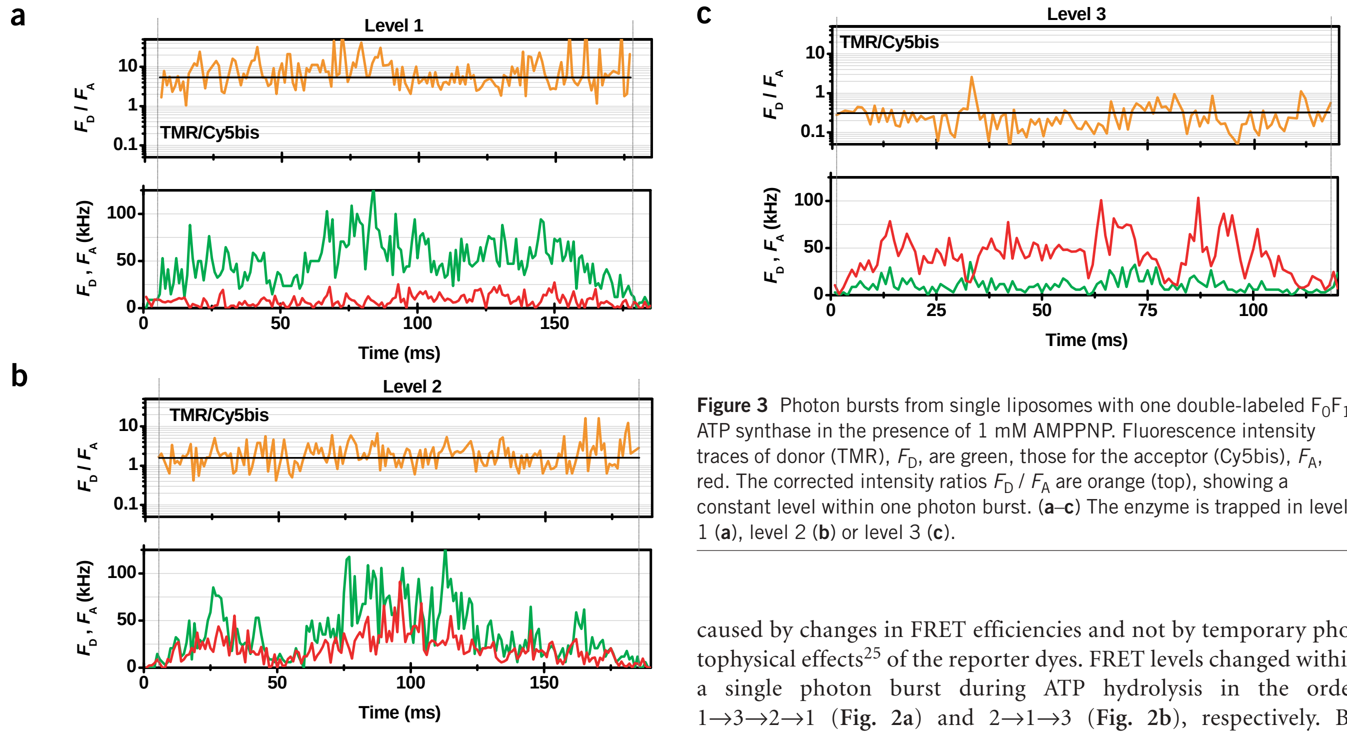

Figure 3 Photon bursts from single liposomes with one double-labeled F_0F_1-ATP synthase in the presence of 1 mM AMPPNP. Fluorescence intensity traces of donor (TMR), F_D, are green, those for the acceptor (Cy5bis), F_A, red. The corrected intensity ratios F_D / F_A are orange (top), showing a constant level within one photon burst. (**a**–**c**) The enzyme is trapped in level 1 (**a**), level 2 (**b**) or level 3 (**c**).

hydrolysis, both of which are similar to those of the unlabeled F_0F_1-ATP synthase[19,20]. Upon addition of 40 μM of the inhibitor *N*,*N*′-dicyclohexylcarbodiimide (DCCD), ATP synthesis was reduced to $v_S = (4 \pm 3)\ s^{-1}$ and ATP hydrolysis to $v_H = (2 \pm 2)\ s^{-1}$, confirming that catalysis was coupled to proton transport[21,22].

Stepwise γ-subunit rotation during ATP hydrolysis

First, we analyzed rotary movements during ATP hydrolysis in the presence of 1 mM ATP. Using intramolecular single-molecule FRET[18,23,24] and single-molecule multiparameter fluorescence detection[25], we obtained quantitative fluorescence information (intensity, lifetime and anisotropy in two spectral regions) from the attached reporters at high time resolution. Single FRET-labeled enzymes incorporated into liposomes were detected by their fluorescence photon bursts while traversing the confocal detection volume (**Fig. 1c**). **Figure 2a** shows a long-lasting photon burst with large fluctuations of the fluorescence intensities of donor, F_D (green) and acceptor, F_A (red). The ratio of corrected fluorescence intensities F_D / F_A was calculated (**Fig. 2**) to correlate these fluctuations with changes in the intramolecular FRET efficiency; that is, with distance changes between the two fluorophores. For the observed photon bursts, we found three different constant levels of F_D / F_A (levels 1, 2 and 3) corresponding to three distinct distances between the labels at the γ and b subunits. These FRET states interchanged in sudden jumps among the levels, with a transition time faster than the time resolution (binning time 1 ms). The burst in **Figure 2a** shows a sequence of four steps of the F_D / F_A levels.

In addition, time traces of the fluorescence lifetime of the donor in the presence of the acceptor, $\tau_{D(A)}$, were simultaneously measured (**Fig. 2b**). Each F_D / F_A level corresponded to a well-defined $\tau_{D(A)}$: high FRET efficiencies (level 3, short distance) were characterized by a short $\tau_{D(A)}$, medium FRET efficiencies (level 2, medium distance) by a larger $\tau_{D(A)}$, and low FRET efficiencies (level 1, long distance) by high ratios of F_D / F_A and a long $\tau_{D(A)}$. The coincident steps in the levels of F_D / F_A and $\tau_{D(A)}$ proved that these jumps were caused by changes in FRET efficiencies and not by temporary photophysical effects[25] of the reporter dyes. FRET levels changed within a single photon burst during ATP hydrolysis in the order 1→3→2→1 (**Fig. 2a**) and 2→1→3 (**Fig. 2b**), respectively. By analyzing 222 traces of single F_0F_1-ATP synthases with two or more FRET levels, the predominant sequence of level transitions was found to be 1→3→2→1→... and so forth for >72% of the bursts. We conclude that during ATP hydrolysis at high ATP concentrations this interconversion of well-defined FRET levels clearly indicates a three-step rotary movement of the γ subunit in membrane-integrated F_0F_1-ATP synthase.

The fact that not all bursts exhibited the same sequence is due to the fast kinetics of ATP hydrolysis. In our analysis, only levels with duration of at least 5 ms were considered separate levels. From the average ATP turnover time and assuming an exponential distribution of the F_D / F_A level durations, we calculated a probability of 77% for levels that last for 5 ms or longer and thus are recognized as distinct levels during ATP hydrolysis. Therefore, apparently 'wrong' sequences were observed because short F_D / F_A levels were sometimes missed.

Stepwise γ-subunit rotation during ATP synthesis

To monitor subunit movements during ATP synthesis, we generated a transmembrane pH difference (ΔpH) plus an additional electric potential difference (Δϕ) across the liposome membrane[19,20] immediately before fluorescence measurements. In **Figure 2c,d**, typical photon bursts of TMR/Cy5bis- and Rh110/Cy5bis-labeled ATP synthases are shown (for additional traces see **Supplementary Fig. 2c,d** online). Three distinct FRET levels were identified within these photon bursts, characterized by constant F_D / F_A and $\tau_{D(A)}$ levels, which interchange in coincident jumps to the next level. After mixing the two buffers in the microscopic flow chamber, ΔpH and Δϕ with initial maximum values dissipated within 3–5 min, partly used by F_0F_1- ATP synthase for ATP synthesis and parly lost in a distinct process by proton leakage across the lipid membrane. Therefore, fluctuating FRET efficiencies within the photon bursts of liposome-embedded ATP synthase were observable only for the first few minutes. Several minutes after mixing, FRET states of F_0F_1 remained constant within the bursts. Rarely, oscillations between two FRET states were detected.

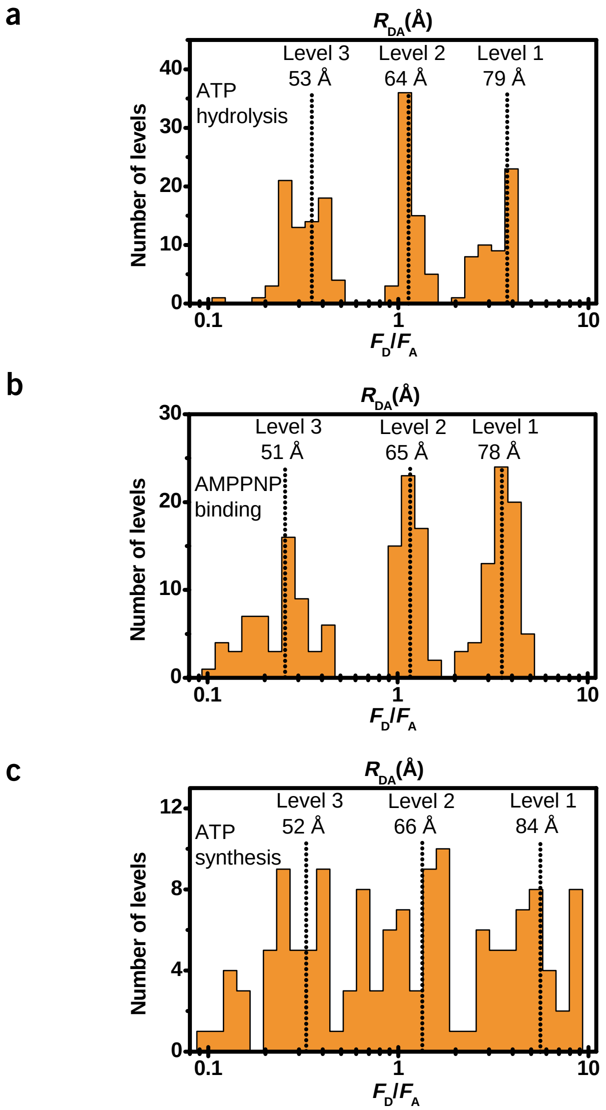

Figure 4 Histograms of the fluorescence intensity ratios F_D / F_A of single FRET-labeled F_0F_1. Top, most probable donor-acceptor distances, R'_{DA} (see Methods). (**a**) During ATP hydrolysis (1 mM ATP), 48 photon bursts with three or more steps (that is, 207 FRET level altogether) were analyzed. (**b**) Binding of AMPPNP (1 mM) with data from 185 photon bursts. (**c**) During ATP synthesis (100 µM ADP, 5 mM phosphate, initial ΔpH = 4.1), 32 photon bursts containing three or more steps (that is, 129 FRET level altogether) were analyzed.

In contrast to ATP hydrolysis, the order of level transitions was reversed for both pairs of FRET fluorophores. The observed sequences are 3→1→2→3 (**Fig. 2c**) and 1→2→3→1 (**Fig. 2d**), respectively. Repeating F_D/F_A and $\tau_{D(A)}$ sequences in the direction 1→2→3→1→... were found for >83% of 188 analyzed bursts with two or more FRET levels. As the sequence of FRET levels is reversed, we conclude that the direction of γ rotation during ATP synthesis is opposite compared with that during ATP hydrolysis.

Three AMPPNP-trapped γ-subunit orientations

The existence of three distinct FRET levels was corroborated by an independent experiment. Upon addition of nonhydrolyzable adenosine-5′-(β,γ-imido)triphosphate (AMPPNP) the enzyme was expected to be trapped in one of three different orientations of the γ subunit with respect to the b subunits. In this case, the traces of single-particle events showed F_D / F_A levels that remained constant throughout each burst. The observation of three distinct FRET efficiencies upon addition of AMPPNP supports the proper discrimination of the anticipated γ-subunit orientations (**Fig. 3a–c**).

Level histograms of the three FRET states

The statistical significance of the individual traces of F_0F_1 was evaluated by the analysis of the FRET level histograms of ATP synthases during catalysis and AMPPNP binding (**Fig. 4**). We selected 48 photon bursts from single F_0F_1 with three or more FRET levels during ATP hydrolysis. In the histogram of F_D / F_A levels (**Fig. 4a**), three peaks are clearly separated. In **Figure 4b**, the F_D / F_A level histogram in the presence of AMPPNP is shown. Three F_D / F_A levels are found also, with the center of the distribution of each level similar to those observed during ATP hydrolysis. At millimolar concentrations, ATP binds rapidly to the free nucleotide-binding site and the rate-limiting step is expected to be the release of ADP. The resting positions of the enzyme should therefore be the same as those after binding of AMPPNP, resulting in almost identical maxima of the F_D / F_A level histograms in the presence of ATP or AMPPNP.

The histogram of F_D / F_A levels, obtained from of 32 photon bursts during ATP synthesis (**Fig. 4c**), shows again three subpopulations. When F_D / F_A level distributions are fitted with three Gaussians, the centers of the distributions are almost identical to those for ATP hydrolysis and AMPPNP binding. In the case of ATP synthesis, the maxima of the distribution were similar; however, the distributions were significantly broadened.

Dwell times of the FRET states during catalysis

The durations of the different F_D / F_A levels during ATP hydrolysis and ATP synthesis were considered as dwell times of conformational states. A monoexponential fit to the level durations during ATP hydrolysis resulted in an average dwell time of 19 ms (**Fig. 5a**). This value agrees well with a turnover time of 15 ms for the hydrolysis of one ATP obtained from bulk experiments. For ATP synthesis, a monoexponential fit to the level durations yielded an average dwell time of 51 ms (**Fig. 5b**), in accordance with a turnover time of 43 ms for the synthesis of one ATP calculated from the initial rates in bulk experiments. This comparison indicates that the duration of the FRET states is directly correlated with the catalytic event.

Fluorophore distances and γ-subunit orientations

Single-molecule FRET data revealed additional structural information. From the homology model of F_0F_1 (**Fig. 1**), the largest distance between the Cα atoms of the amino acids b-Q64C and γ-T106C was estimated to be 73 Å. Rotation of the γ subunit by 120° and 240° resulted in two shorter distances in the range of 40–60 Å. According to the Förster theory of FRET[26,27], two effects can influence F_D / F_A levels, donor-acceptor distances and orientations in transition dipole moments (factor κ^2) of the donor relative to the acceptor dye. We calculated apparent donor-acceptor distances, $R'_{DA,}$ from the measured fluorescence parameters. These apparent distances of 52, 65 and 80 Å (**Fig. 4**), representing mean values during catalysis and AMPPNP binding for the three FRET states within the enzyme, agree with estimates obtained from the model.

DISCUSSION

We applied an intramolecular single-molecule FRET approach to show subunit rotation in the liposome-reconstituted holoenzyme F_0F_1-ATP

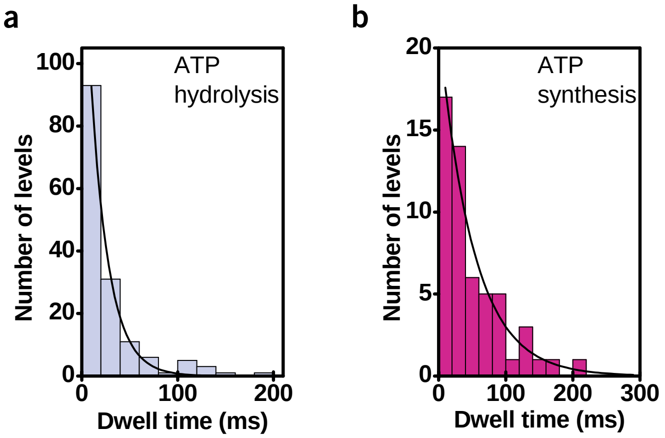

Figure 5 Level duration distributions of FRET states. (**a**,**b**) Distributions during ATP hydrolysis (**a**) and ATP synthesis (**b**). Fits with monoexponential decay functions yield mean dwell times of 19 ms upon ATP hydrolysis and 51 ms upon ATP synthesis.

synthase powered by proton flow. Here, one fluorophore was attached to the rotating γ subunit of F_1 and the other to the static, nonrotating b-subunit dimer of F_0. We achieved high-specificity labeling by separately labeling cysteines in F_1 and F_0 and subsequently reassembling and reconstituting the enzyme into liposomes. The FRET efficiency depends on the distance between the two fluorophores. Therefore, FRET efficiency changes between the two fluorophores at a single ATP synthase are expected to describe trajectories of the relative motion of the two labeled subunits during catalysis.

Upon addition of AMPPNP as a nonhydrolyzable substrate for the enzyme, we find three well-defined and distinct FRET levels and conclude that these levels correspond to three distances of the labeled residue 106 at a protruding part (‘off-axis position’) of the γ subunit with respect to the b subunits. The calculated ratio of corrected fluorescence intensities F_D / F_A between FRET donor and acceptor in the photon bursts of a single ATP synthase is independent of intensity fluctuations of the double-labeled enzyme on its transit pathway through the confocal detection volume. In addition to this intensity ratio, each FRET level is defined by a specific FRET donor fluorescence lifetime $\tau_{(DA)}$, and therefore, other photophysical causes effecting the quantum yields of the FRET fluorophores are unlikely. These stable FRET levels during a photon burst indicate the trapping of the γ subunit by AMPPNP in one of three distinguishable orientations. The three intramolecular distances calculated from the FRET efficiencies of these levels are in good agreement with the distances derived from our model of F_0F_1-ATP synthase and the expected positions of the γ subunit.

FRET-labeled ATP synthase in a freely diffusing liposome carries out proton transport-coupled ATP synthesis and hydrolysis almost undisturbed during real-time observation. The dwell times of the FRET levels correspond to the bulk rates of catalysis, during ATP hydrolysis as well as ATP synthesis, thereby independently excluding photophysical causes for interchanging FRET levels.

Given this direct correlation between FRET level and γ-subunit orientation, γ-subunit rotation in F_0F_1-ATP synthase occurs stepwise in both modes of catalysis and the direction of rotation during ATP synthesis is reversed compared with that during ATP hydrolysis. Using the actin-filament method, the rotation direction of the γ subunit in F_1 subcomplexes during ATP hydrolysis has been determined to be counterclockwise when viewed from F_0 (ref. 9). Therefore we attribute the FRET level sequence 1→3→2→1→... observed during ATP hydrolysis to the counterclockwise direction of rotation of the γ subunit (**Fig. 1b**). Stepwise rotation of the γ subunit during ATP hydrolysis has been discussed for F_1-ATPase[10,11,28] and for F_0F_1-ATP synthase[18] earlier and is confirmed here. In the present work, proton-driven ATP synthesis is also accompanied by a three-step rotary movement of the γ subunit and not by a quasi-continuous rotation, which might have been expected from the stoichiometry of at least nine translocated protons per 360° revolution and from the multistep rotational motion of the c subunits of F_0 during ATP synthesis. These distinct distances between the FRET fluorophores remain constant throughout the dwell time of one γ-subunit orientation, before a consecutive 120° rotary movement of the γ subunit takes place, as has been shown unequivocally with immobilized F_1 subcomplexes for the case of ATP hydrolysis at millimolar concentrations[10]. The mean stopping positions of the γ subunit upon ATP synthesis are similar to those observed in the AMPPNP-trapped states and those during ATP hydrolysis at millimolar ATP concentrations.

As anticipated in molecular dynamics simulations[15,16] and derived from theoretical considerations of microscopic reversibility, a reversed rotary motion of the γ subunit during ATP synthesis was predicted, and is now strongly supported by our experiments. The rotary subunit movement is indicated by repeating sequences of three FRET levels, which are induced by distance changes between the FRET pair. In most cases, a consecutive order of the three γ-subunit orientations was observed, and in an opposite direction during ATP synthesis from that during ATP hydrolysis. Thus, unidirectional rotary motion of the γ subunit during both modes of catalysis seems very improbable. Any two-state model, including contracting-and-stretching modes of the γ subunit or back-and-forth swiveling modes between only two of the three catalytic sites, are not consistent with the repeating sequences of three FRET levels. Oscillations between two FRET states were rarely observed and can be attributed either to omitted levels or to an equilibrium state between a weak proton-motive force competing with the ATP hydrolysis backreaction.

The significant broadening of the three FRET levels during ATP synthesis allows us to predict the occurrence of substeps comparable to those observed in F_1 subcomplexes during ATP hydrolysis. As first hints and as rare events we identified more than three FRET levels (substeps) in some photon bursts of F_0F_1 during ATP synthesis. The origin of these substeps remains to be clarified. In principle, a hypothetical ADP-(plus P_i)-waiting state of the enzyme at one angular position of the γ subunit and a conformational state associated with the catalytic reaction or product release at another angular position can be discriminated by the dependence of substrate concentration. Detecting one ATP synthase in freely diffusing liposomes, as has been shown in this work, limits the observation time to several hundred milliseconds. Therefore, concentration dependencies must be studied by a modified approach, for instance with surface-immobilized liposomes using a streptavidin-biotin multilayer. Monitoring single enzymes at work under kinetic control in both directions of catalysis will reveal insights into the mechanism of the ‘rotary nanomachine’ F_0F_1-ATP synthase.

METHODS

FRET-labeled F_0F_1-ATP synthase from *E. coli*. F_1 of ATP synthase of *E. coli* carrying the cysteine mutation γ-T106C was prepared as described[29] using the plasmid pRA144 (ref. 30) expressed in strain RA1 (ref. 31). Specific substoichiometric labeling of the γ subunit was achieved with tetramethylrhodamine-maleimide (TMR, Molecular Probes) or Rhodamine110-maleimide (Rh110, Evotec) with labeling efficiencies between 50 and 60% (refs. 18,32). F_1 with γ-T106C contains several buried cysteines[33]. However, at the given reaction conditions only γ-T106C is labeled[32,33], as checked by fluorograms after SDS-PAGE. F_0F_1-ATP synthases of *E. coli* carrying the cysteine mutation b-Q64C were prepared separately[19] using the plasmid pRR76 (ref. 18) expressed in strain RA1. The cysteines of the b subunits were crosslinked with the cyanine dye Cy5-bis-C_5-maleimide synthesized from (5-maleimidyl)-pentyl-1-amine and Cy5-bis-*N*-hydroxysuccinimidylester (bisreactive Cy5 NHS-ester obtained from Amersham Biosciences). Cy5-labeling efficiency of the b-subunit dimer was 64% with a yield of crosslinking of ~90%. The a and c subunits of F_0 were not labeled as checked by fluorograms after SDS-PAGE. Cy5-labeled F_0F_1 was reconstituted into liposomes (diameter ~100 nm), F_1 was removed and Cy5-labeled F_0 was reassembled with TMR- or Rh110-labeled F_1 to yield the FRET-labeled F_0F_1-ATP synthase in liposomes, as described[18]. ATP synthesis rates were measured[19,20] at 23 °C, yielding $v_S = 59 \pm 1\ s^{-1}$ for the nonlabeled b-mutant F_0-b64-F_1, $v_S = 48 \pm 3\ s^{-1}$ for the labeled F_0-b64-Cy5–F_1, $v_S = 24 \pm 2\ s^{-1}$ for the reassembled TMR-labeled F_0-b64–F_1-γ106-TMR and $v_S = 23 \pm 3\ s^{-1}$ for the FRET-labeled F_0-b64-Cy5–F_1-γ106-TMR. ATP hydrolysis rates at 23 °C were $v_H = 186 \pm 12\ s^{-1}$ for F_0-b64–F_1, $v_H = 108 \pm 24\ s^{-1}$ for F_0-b64-Cy5–F_1 and $v_S = 67 \pm 6\ s^{-1}$ for the reassembled and FRET-labeled F_0-b64-Cy5–F_1-γ106-TMR. Reassembly causes slower rates[18,21]. All hydrolysis rates were inhibited by 40 μM DCCD to remaining activities of 6 ± 4%.

Single-molecule FRET measurements. Single-molecule FRET measurements were carried out as described[18] using continuous wave-excitation at 532 nm for TMR and pulsed excitation at 496 nm for Rh110. Confocal detection volumes of 6.8 fl for TMR/Cy5bis and 2.5 fl for Rh110/Cy5bis were used. Mean diffusion times through the confocal volume of 10–30 ms for the labeled F_0F_1 in liposomes were determined by fluorescence correlation spectroscopy. Single-molecule fluorescence measurements under conditions of ATP hydrolysis (1 mM ATP) and AMPNP binding (1 mM AMPPNP) were carried out in a buffer (pH 8) containing 20 mM succinic acid, 20 mM tricine, 2.5 mM $MgCl_2$, 80 mM NaCl and 0.6 mM KCl. ATP synthesis was measured after preincubation of the liposomes in 20 mM succinic acid buffer, pH 4.7, containing 5 mM NaH_2PO_4, 0.6 mM KOH, 2.5 mM $MgCl_2$, 100 μM ADP, 20 μM valinomycin. The transmembrane ΔpH was generated by mixing the acidic liposomes with the basic buffer containing 200 mM tricine, pH 8.8, 5 mM NaH_2PO_4, 160 mM KOH, 2.5 mM $MgCl_2$ and 100 μM ADP in a T-shaped flow chamber with two syringes. This generated an initial transmembrane pH difference ΔpH = 4.1 with an additional electric potential difference Δϕ = 126 mV (refs. 19,20). All samples of the double-labeled F_0F_1 were diluted to a final concentration of ~90 pM.

F_0F_1 identification in photon bursts. Background count rates (usually between 0.5 and 2 kHz), obtained in each experiment from measurements of buffer solutions without labeled enzymes, were subtracted from the burst count rates. In addition, crosstalk (photons from the donor in the detection channel of the acceptor) and differences in the detection efficiencies of the donor and acceptor channels of the instrument were corrected, resulting in corrected fluorescence intensities for donor (F_D) and acceptor (F_A). A photon burst was considered 'significant' when the sum of photon counts in the donor and acceptor channel was >15 counts per ms. To eliminate events of remaining donor-labeled F_1 that were not bound to F_0 in liposomes, we excluded photon bursts with a duration <45 ms and, when Rh110 was used, with a donor anisotropy <0.12 (see **Supplementary Fig. 1** online).

Calculation of intramolecular FRET distances. The reduced Förster radii[25] $R_{0r} = 9{,}780\ (J(\lambda)\ \kappa^2\ n^{-4})^{1/6}$ for the FRET pairs TMR/Cy5bis and Rh110/Cy5bis were calculated using $n = 1.33$ for the index of refraction and $\kappa^2 = 2/3$. The spectral overlap (J) was determined from the respective donor emission and acceptor absorption spectra resulting in $R_{0r} = 76$ Å for TMR/Cy5bis and 55.5 Å for Rh110/Cy5bis. Anisotropies of donor and acceptor were 0.2. Even in this case, it is still sufficient to assume $\kappa^2 = 2/3$, because our estimate for κ^2 lies well in the range of possible κ^2 values assuming the case of linear and planar (due to rotation) transition moments of donor and acceptor[27]. Based on these assumptions, it is appropriate to calculate apparent donor-acceptor distances, R'_{DA} from the measured fluorescence parameters using $R'_{DA} = R_{0r}\ [\phi_A\ (F_D / F_A)]^{1/6}$.

The apparent distances between donor and acceptor dyes were calculated from the maxima of the Gaussian distributions of F_D / F_A for the different levels. The effective acceptor fluorescence quantum yield in single-molecule experiments was $\phi_A = 0.32$ for Cy5bis[25]. These distances are compared with geometrically estimated values from a model of F_0F_1. Therefore, homology alignment[34] of structures of the ($\alpha_3\beta_3\gamma$) subcomplex from the mitochondrial enzyme, δ, ε plus γ and c subunits from X-ray[3,35] and NMR[36,37] analyses were combined with postulated structures of the c_{10}-ring[8] and a and b subunits[38] for an overview of intramolecular distances within F_0F_1-ATP synthase.

Note: Supplementary information is available on the Nature Structural & Molecular Biology website.

ACKNOWLEDGMENTS
This work is dedicated to the memory of K. Süss, who died on 17 March 2002. We thank R.H. Fillingame for his help with the b-mutants, R.A. Capaldi and R. Aggeler for the gift of the γ-mutant, O. Hucke for refinement of the F_0F_1 model, and M. Antonik and E. Haustein for analytical software. We thank H. Grubmüller, R. Jahn, B.A. Melandri and P. Turina for critical reading the manuscript and helpful discussions and A. Börsch-Haubold for editorial suggestions. C.A.M.S. acknowledges financial support by the Bundesministerium für Bildung und Forschung (BioFuture grant 0311865).

COMPETING INTERESTS STATEMENT
The authors declare that they have no competing financial interests.

Received 12 September; accepted 12 November 2003

1. Mitchell, P. Coupling of phosphorylation to electron and hydrogen transfer by chemi-osmotic type of mechanism. *Nature* **191**, 144–152 (1961).
2. Boyer, P.D. ATP synthase—past and future. *Biochim. Biophys. Acta* **1365**, 3–9 (1998).
3. Abrahams, J.P., Leslie, A.G.W., Lutter, R. & Walker, J.E. Structure at 2.8 Å resolution of F_1-ATPase from bovine heart mitochondria. *Nature* **370**, 621–628 (1994).
4. Junge, W., Sabbert, D. & Engelbrecht, S. Rotatory catalysis by F-ATPase: Real-time recording of intersubunit rotation. *Ber. Bunsenges. Phys. Chem.* **100**, 2014–2019 (1996).
5. Yoshida, M., Muneyuki, E. & Hisabori, T. ATP synthase – a marvelous rotary engine of the cell. *Nat. Rev. Mol. Cell. Biol.* **2**, 669–677 (2001).
6. Capaldi, R.A. & Aggeler, R. Mechanism of the F_1F_0-type ATP synthase, a biological rotary motor. *Trends Biochem. Sci.* **27**, 154–160 (2002).
7. Weber, J. & Senior, A.E. ATP synthesis driven by proton transport in F_1F_0-ATP synthase. *FEBS Lett.* **545**, 61–70 (2003).
8. Fillingame, R.H., Angevine, C.M. & Dmitriev, O.Y. Coupling proton movements to c-ring rotation in F_1F_0 ATP synthase: aqueous access channels and helix rotations at the a-c interface. *Biochim. Biophys. Acta* **1555**, 29–36 (2002).
9. Noji, H., Yasuda, R., Yoshida, M. & Kinosita, K. Jr. Direct observation of the rotation of F_1-ATPase. *Nature* **386**, 299–302 (1997).
10. Yasuda, R., Noji, H., Yoshida, M., Kinosita, K. & Itoh, H. Resolution of distinct rotational sub-steps by submillisecond kinetic analysis of F_1-ATPase. *Nature* **410**, 898–904 (2001).
11. Yasuda, R. *et al.* The ATP-waiting conformation of rotating F_1-ATPase revealed by single-pair fluorescence resonance energy transfer. *Proc. Natl. Acad. Sci. USA* **100**, 9314–9318 (2003).
12. Sambongi, Y. *et al.* Mechanical rotation of the c subunit oligomer in ATP synthase (F_0F_1): direct observation. *Science* **286**, 1722–1724 (1999).
13. Junge, W. *et al.* Inter-subunit rotation and elastic power transmission in F_0F_1-ATPase. *FEBS Lett.* **504**, 152–160 (2001).
14. Kaim, G. *et al.* Coupled rotation within single F_0F_1 enzyme complexes during ATP synthesis or hydrolysis. *FEBS Lett.* **525**, 156–163 (2002).
15. Böckmann, R.A. & Grubmüller, H. Nanosecond molecular dynamics simulation of primary mechanical energy transfer steps in F_1-ATP synthase. *Nat. Struct. Biol.* **9**, 198–202 (2002).
16. Ma, J. *et al.* A dynamical analysis of the rotation mechanism for conformational change in F_1-ATPase, *Structure* **10**, 921–930 (2002).
17. Zhou, Y., Duncan, T.M., Cross, R.L. Subunit rotation in *Escherichia coli* F_0F_1-ATP synthase during oxidative phosphorylation. *Proc. Natl. Acad. Sci.* USA **94**, 10583-10587 (1997).
18. Börsch, M., Diez, M., Zimmermann, B., Reuter, R. & Gräber, P. Stepwise rotation of the γ-subunit of EF_0F_1-ATP synthase observed by intramolecular single-molecule fluorescence resonance energy transfer, *FEBS Lett.* **527**, 147–152 (2002).
19. Fischer, S. & Gräber, P. Comparison of ΔpH- and Δϕ-driven ATP synthesis catalyzed by the H^+-ATPases from *Escherichia coli* or chloroplasts reconstituted into liposomes. *FEBS Lett.* **457**, 327–332 (1999).
20. Fischer, S., Gräber, P. & Turina, P. The activity of the ATP synthase from *Escherichia coli* is regulated by the transmembrane proton motive force. *J. Biol. Chem.* **275**, 30157–30162 (2000).
21. Lötscher, H.R., deJong, C. & Capaldi, R.A. Modification of the F_0 portion of the H^+-

translocating adenosinetriphosphatase complex of *Escherichia coli* by the water-soluble carbodiimide 1-ethyl-3-[3-(dimethylamino)propyl]carbodiimide and effect on the proton channeling function. *Biochemistry* **23**, 4128–4134 (1983).

22. Perlin, D.S., Cox, D.N. & Senior, A.E. Integration of F_1 and the membrane sector of the proton-ATPase of *E. coli*. *J. Biol. Chem.* **258**, 9793–9800 (1983).
23. Weiss, S. Measuring conformational dynamics of biomolecules by single molecule fluorescence spectroscopy. *Nature Struct. Biol.* **7**, 724–729 (2000).
24. Ha, T. Single-molecule fluorescence resonance energy transfer. *Methods* **25**, 78–86 (2001).
25. Rothwell, P.J. *et al.* Multi-parameter single-molecule fluorescence spectroscopy reveals heterogeneity of HIV-1 reverse transcriptase: primer/template complexes. *Proc. Natl. Acad. Sci. USA* **100**, 1655–1660 (2003).
26. Förster, T. Zwischenmolekulare Energiewanderung und Fluoreszenz. *Ann. Phys.* **2**, 55–70 (1948).
27. Van der Meer, B.W., Cooker, G. & Chen, S.S.-Y. *Resonance Energy Transfer: Theory and Data* (VCH, New York, 1994).
28. Häsler, K., Engelbrecht, S. & Junge, W. Three-stepped rotation of subunits Q and O in single molecules of F-ATPase as revealed by polarized, confocal fluorometry. *FEBS Lett.* **426**, 301–304 (1998).
29. Gogol, E.P., Luecken, U., Bork, T. & Capaldi, R.A. Molecular architecture of *Escherichia coli* F1 adenosinetriphosphatase. *Biochemistry* **28**, 4709–4716 (1989).
30. Aggeler, R. & Capaldi, R.A. Cross-linking of the γ subunit of the *Escherichia coli* ATPase (ECF_1) via cysteines introduced by site-directed mutagenesis. *J. Biol. Chem.* **267**, 21355–21359 (1992).
31. Aggeler, R., Ogilvie, I. & Capaldi, R.A. Rotation of a γ-ε subunit domain in the *Escherichia coli* F_1F_0-ATP synthase complex. *J. Biol. Chem.* **272**, 19621–19624 (1997).
32. Börsch, M. *et al.* Conformational changes of the H^+-ATPase from *Escherichia coli* upon nucleotide binding detected by single molecule fluorescence. *FEBS Lett.* **437**, 251–254 (1998).
33. Turina, P. & Capaldi, R.A. ATP hydrolysis-driven structural changes in the γ-subunit of *Escherichia coli* ATPase monitored by fluorescence from probes bound at introduced cysteine residues. *J. Biol. Chem.* **269**, 13465–13471 (1994).
34. Engelbrecht, S. & Junge, W. ATP synthase: a tentative structural model. *FEBS Lett.* **414**, 485–491 (1997).
35. Rodgers, A. & Wilce, M. Structure of the γ/ε complex of ATP synthase: the camshaft in the rotary motor of life. *Nat. Struct. Biol.* **7**, 1051–1054 (2000).
36. Wilkens, S., Dunn, S., Chandler, J., Dahlquist, F.W. & Capaldi, R.A. Solution structure of the N-terminal domain of the δ subunit of the *E. coli* ATP synthase (ECF_1F_0). *Nat. Struct. Biol.* **4**, 198–201 (1997).
37. Girvin, M.E., Rastogi, V.K., Abildgaard, F., Markley, J.L. & Fillingame, R.H. Solution structure of the transmembrane H^+-transporting subunit c of the F_0F_1 ATP synthase. *Biochemistry.* **37**, 8817–8824 (1998).
38. Del Rizzo, P.A., Dunn, S.D., Bi, Y. & Shilton, B.H. The 'second stalk' of *Escherichia coli* ATP synthase: structure of the isolated dimerization domain. *Biochemistry* **41**, 6875–6884 (2002).

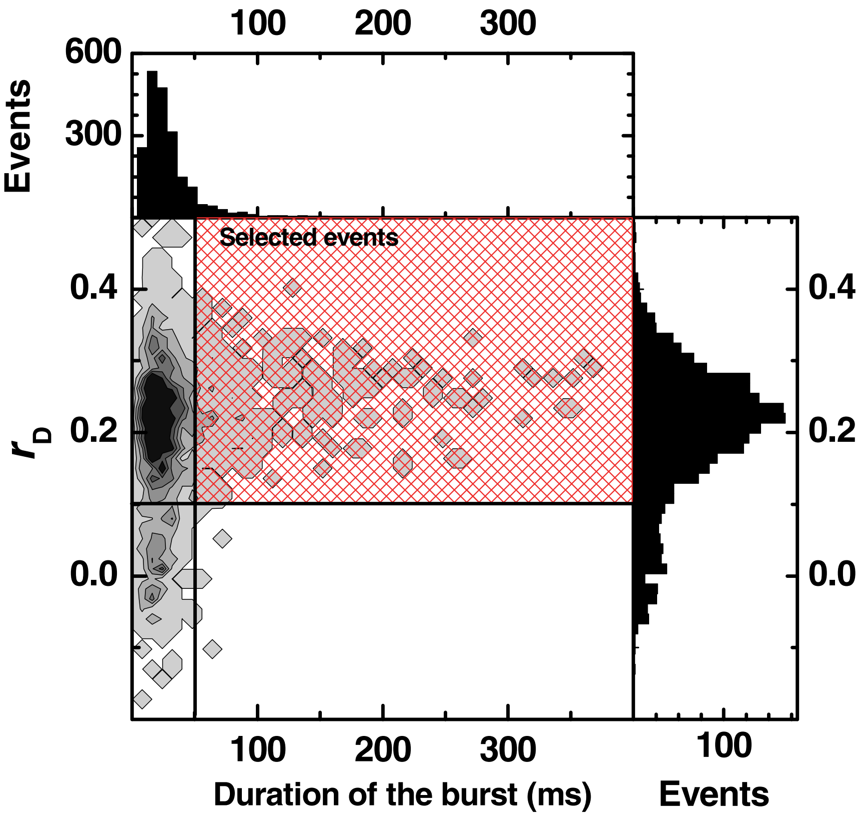

Supplementary Figure 1: Two-dimensional histogram of photon burst duration (i.e. diffusion time through the confocal detection volume) versus anisotropy r_D of the donor fluorophore (Rhodamine 110) attached to the γ-subunit of F_0F_1-ATP synthase during ATP hydrolysis. The events resulting from the FRET-labeled holoenzyme incorporated in a liposome can be distinguished from unbound dye and remaining donor labeled F_1 parts (not bound to F_0) by their high r_D. The probability to observe a transition between two FRET levels within a photon burst depends on the duration of the event. Therefore, only photon bursts within the red shaded area are considered for further analysis (i.e. 382 bursts of 2127 bursts with $r_D > 0.12$).

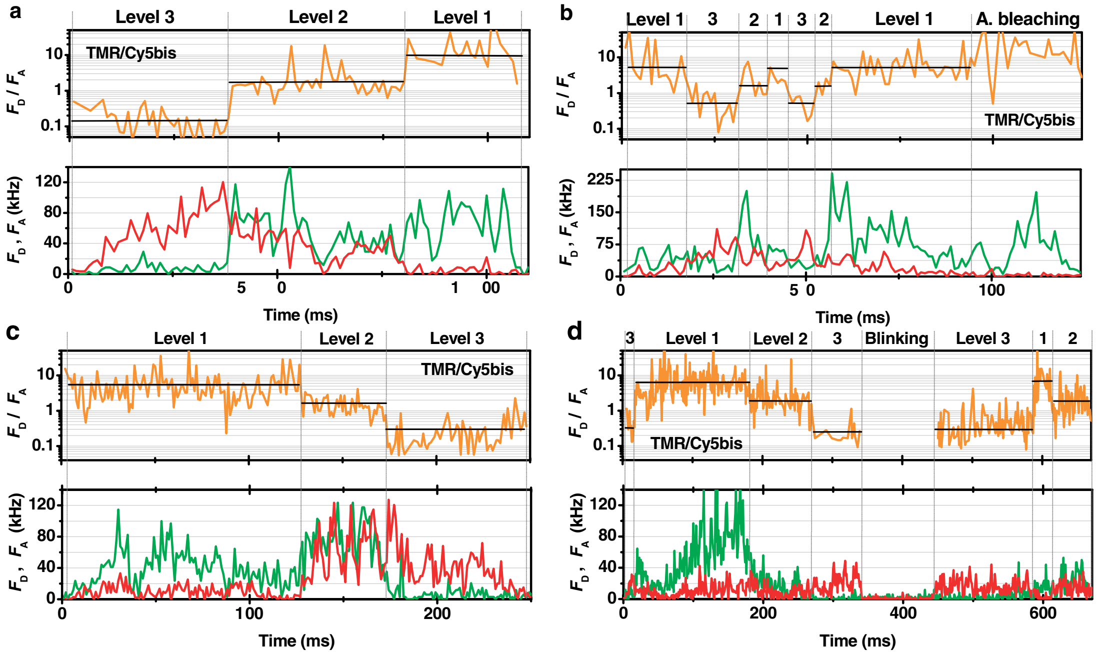

Supplementary Figure 2: Photon bursts of single FRET-labeled F_0F_1-ATP synthases in liposomes during ATP hydrolysis (**a**, **b**), and during ATP synthesis (**c**, **d**). FRET donor is TMR, FRET acceptor is Cy5bis in all traces. Corrected fluorescence intensity traces of the donor, F_D, and acceptor, F_A, are shown in green and red, respectively, corrected intensity ratios F_D/F_A are depicted in orange with a time window of 1 ms. Three distinct FRET levels are attributed (1, 2 or 3) at the top of the figures. Black horizontal lines indicate the mean FRET levels taken from the histrogram, vertical lines mark beginning and end of a level. In trace (**b**), the enzyme exhibits short dwell times for a FRET level, i.e. fast ATP turnover is depicted. In trace (**d**), photophysical fluorophore blinking after 340 ms interrupts the detection of FRET states for approximately 100 ms before ongoing ATP synthesis is demonstrated by interchanging FRET levels.

Anal Bioanal Chem (2007) 387:71–82
DOI 10.1007/s00216-006-0917-0

ORIGINAL PAPER

Monitoring dynamic systems with multiparameter fluorescence imaging

Volodymyr Kudryavtsev · Suren Felekyan · Anna K. Woźniak · Marcelle König · Carl Sandhagen · Ralf Kühnemuth · Claus A. M. Seidel · Filipp Oesterhelt

Received: 17 July 2006 / Revised: 5 October 2006 / Accepted: 9 October 2006 / Published online: 12 December 2006

Abstract A new general strategy based on the use of multiparameter fluorescence detection (MFD) to register and quantitatively analyse fluorescence images is introduced. Multiparameter fluorescence imaging (MFDi) uses pulsed excitation, time-correlated single-photon counting and a special pixel clock to simultaneously monitor the changes in the eight-dimensional fluorescence information (fundamental anisotropy, fluorescence lifetime, fluorescence intensity, time, excitation spectrum, fluorescence spectrum, fluorescence quantum yield, distance between fluorophores) in real time. The three spatial coordinates are also stored. The most statistically efficient techniques known from single-molecule spectroscopy are used to estimate fluorescence parameters of interest for all pixels, not just for the regions of interest. Their statistical significance is judged from a stack of two-dimensional histograms. In this way, specific pixels can be selected for subsequent pixel-based subensemble analysis in order to improve the statistical accuracy of the parameters estimated. MFDi avoids the need for sequential measurements, because the registered data allow one to perform many analysis techniques, such as fluorescence-intensity distribution analysis (FIDA) and fluorescence correlation spectroscopy (FCS), in an off-line mode. The limitations of FCS for counting molecules and monitoring dynamics are discussed. To demonstrate the ability of our technique, we analysed two systems: (i) interactions of the fluorescent dye Rhodamine 110 inside and outside of a glutathione sepharose bead, and (ii) microtubule dynamics in live yeast cells of *Schizosaccharomyces pombe* using a fusion protein of Green Fluorescent Protein (GFP) with Minichromosome Altered Loss Protein 3 (Mal3), which is involved in the dynamic cycle of polymerising and depolymerising microtubules.

Keywords Multiparameter fluorescence imaging · Fluorescence correlation spectroscopy · FCS · Confocal microscopy · Lifetime imaging · Microtubules

Introduction

To understand the processes that occur in cells in detail, there is a need for methodologies that reveal molecular organisation at high temporal and spatial resolutions. One would like to know molecular concentrations and the dynamics of molecular diffusion or transport, as well as spatially resolved molecular interactions with specific partners, the aggregation state and the stoichiometries of the aggregates. Optical microscopy and labelling techniques have developed rapidly in the last few years and are now approaching the ability to provide such data [1, 2]. In particular, fluorescence microscopy is a sensitive, specific and noninvasive method that allows one to assess biochemical information associated with living cells [3]. The increase in sensitivity achieved over the last few years and the use of fluorescent proteins have made fluorescence microscopy an extremely powerful tool. Multiparameter fluorescence imaging, the combination of confocal microscopy with multichannel, time-resolved single-photon counting, has made it possible to gather all of the spectroscopic information accessible for each pixel of an image. The combination of imaging methods with spectroscopic analysis can allow data to be collected on many parameters

---

V. Kudryavtsev · S. Felekyan · A. K. Woźniak · M. König · C. Sandhagen · R. Kühnemuth · C. A. M. Seidel (✉) · F. Oesterhelt (✉)
Lehrstuhl für Molekulare Physikalische Chemie, Heinrich-Heine-Universität Düsseldorf,
Universitätsstraße 1,
40225 Düsseldorf, Germany
e-mail: cseidel@gwdg.de
e-mail: Filipp.Oesterhelt@uni-duesseldorf.de

simultaneously, increasing the information content per image, which often is crucial to the accurate assessment of function.

Fluorescence microscopy techniques reveal biochemical information

The primary characteristics exhibited by a fluorophore are its intensity, fluorescence lifetime and anisotropy. Polarisation-dependent lifetime imaging (rFLIM) allows rotational correlation times to be derived from local anisotropies. These rotational correlation times provide information about the volumes and shapes of the molecular complexes [4].

The spectroscopic properties of the fluorophores provide information on the local molecular environment and so they also tell us about direct molecular interactions. Fluorescence resonance energy transfer (FRET) between two proteins in close proximity that are labelled with a donor and an acceptor fluorophore, respectively, leads to a decrease in donor emission and the sensitized emission of the acceptor. A major advantage of FRET is that it allows interactions to be detected in real time and changes to be observed down to the millisecond regime [5–7]. For quantitative FRET measurements, which are a prerequisite for the calculation of intermolecular distances, the fraction of labelled molecules that form a FRET complex has to be determined. For intensity-based FRET measurements, this has been achieved through the independent excitation of donor and acceptor fluorophores and by comparing the fluorescence signals that result from direct excitation and from excitation via FRET [8]. Since FRET also results in donor fluorescence lifetime quenching, the transfer efficiency can be estimated directly from lifetime images. This technique has the advantage that the concentrations of free and complexed molecules can be estimated directly from a biexponential lifetime decay model [9]. Also several other methods have been developed to estimate the efficiency of the energy transfer and thus detect molecular interactions and distances between the labelled donor and acceptor molecules [10].

Beside complexation and supramolecular structures, knowledge of the intracellular mobility of molecules is also crucial. Different tracking methods have been developed for directly observing the translational movements of single particles. Fast circular scanning of a laser focus gives time-resolved information about the position of a single particle, which can then be used to track its motion in 3-D [11]. Another method uses fast CCD imaging to localize individual particles like viruses [12] or even proteins labelled with single fluorophores [13, 14].

Faster movements of fluorescently labelled molecules can be studied via the resulting signal fluctuations in confocal measurements. Many different methods have been developed to derive information about the molecular dynamics from these fluctuations [15]. Fluorescence correlation spectroscopy (FCS) allows molecular concentrations and mobility parameters to be measured, and two-color fluorescence cross-correlation spectroscopy (FCCS) allows molecular interactions to be detected [16]. The dependence of the signal-to-noise ratio on different measurement conditions has been studied extensively [17]. FCS can be applied to covalently labelled molecules and to fluorescent proteins [18]. The autofluorescence background must be taken into account when applying the technique to cells in order to obtain accurate concentrations [19]. It was shown that two-photon excitation (2PE) minimizes photobleaching in spatially restrictive cellular compartments and thereby preserves long-term signal acquisition [20]. When diffusion is restricted to small cytosolic compartments, this must be considered when calculating mobility parameters. Different models have been developed to account for this effect [21].

Instead of analysing the intensity fluctuations at a fixed position, it is possible to scan the focus through the sample while detecting the fluctuating signal. The fluctuations contain both temporal and spatial information about the sample. The analysis of the fluorescence signal obtained from a detection volume by scanning a laser beam with a circular scan trajectory across a flowing dye solution allowed the direction and speed of the solution and the positions of immobilized particles to be determined [22]. Scanning FCS was also applied to the analysis of surface-bound molecules [23] and membrane dynamics [24], and it can be used as a tool for testing the resolution and sensitivity of a confocal microscope [25].

Images obtained with a standard laser-scanning microscope contain a time structure that can be exploited to measure the dynamics of molecules in solution and in cells [26]. Image correlation spectroscopy (ICS) analyses the temporal and spatial correlation between neighbouring pixels or successive images and allows molecular diffusion constants to be calculated in the microsecond to second regime [27, 28]. The direction of molecular movements can be determined due to the spatial information associated with the diffusion. This was applied to GFP-labelled membrane proteins for protein velocity mapping [29, 30].

FCS has proven to be a powerful technique with single-molecule sensitivity. Recently, it has found a complementary technique in the form of fluorescence intensity distribution analysis (FIDA), which has been used very successfully in biotechnology and bioanalytics [31–35]. There are several combinations of FIDA with other techniques, such as FILDA (time-correlated single-photon counting) and FIMDA (FCS). FIDA is especially suited to calculating precise brightness values of species, even in a complex mixture.

To conclude, a variety of distinct and complementary fluorescent techniques can be used in confocal microscopy to study bimolecular interactions [36]. Therefore, it is a logical extension to develop a measurement technique which allows for the simultaneous acquisition of the full fluorescence data for each pixel of an image. In this way, a series of measurements, which can be especially difficult to obtain for live cells or tissue, can be replaced by a single measurement.

Principles of multiparameter fluorescence imaging (MFDi)

Multiparameter fluorescence detection (MFD) is a technique that has been applied in single-molecule fluorescence spectroscopy. It allows for the simultaneous measurement of the full fluorescence information. Using a pulsed linear polarized laser, Widengren et al. have distinguished 16 differently labelled molecules in a single data set [37]. The absorption and fluorescence, $F(\lambda_A, \lambda_F)$, fluorescence brightness and quantum yield, Φ_F, fluorescence lifetime, τ [38–43], and anisotropy, r [44], are the five intrinsic properties of a fluorophore that are accessible in a multiparameter fluorescence detection (MFD) experiment (see Fig. 1). These "chromophore parameters" can be deduced from the time-resolved detection of the five observables of the chromophore, which serves as a tool that reports on its local environment. Moreover, there are at least three system parameters, such as the fluorophore separation (FRET and probability distribution analysis, PDA), the time evolution of the system (e.g. FCS), and the absolute intensity (which reflects the fluorophore concentration).

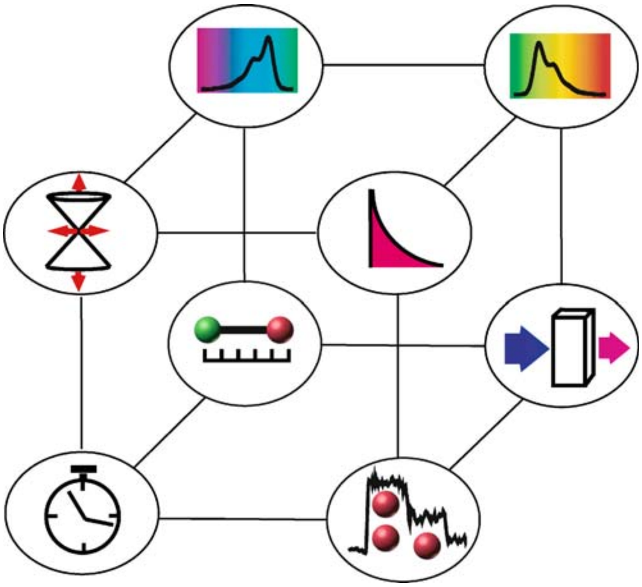

Fig. 1 The multiple dimensions of fluorescence data. Fluorescence properties at the front side of the cube (starting at the upper left corner, with clockwise rotation): fundamental anisotropy, fluorescence lifetime, fluorescence intensity, time; for the back side of the cube: excitation spectrum, fluorescence spectrum, fluorescence quantum yield, and distance between fluorophores

Due to the low number of photons detected, efficient algorithms for estimating fluorescence parameters [37, 45] close to their statistical shot noise limit were established. Moreover, multidimensional analysis offers the advantage of increased sensitivity when detecting distinct species in a heterogeneous ensemble. These methods have been applied to freely diffusing molecules [37, 46, 47] and to imaging [48].

In single-molecule fluorescence spectroscopy, we have analysed photon bursts due to the transit of a molecule. The photon bursts can be defined as packages of photons which are randomly distributed along the time axis. When imaging, a pixel is interpreted as a photon package that is well-defined by the scanning track. All known single-molecule techniques can be applied to photon packages defined by pixels instead of burst coordinates.

Figure 2 shows the basic principles of MFDi. For each pixel in Fig. 2a, all fluorescence parameters including the signal intensity are known. However, it is quite difficult to judge the statistical significance of the observed spread in fluorescence parameter values for all pixels in parameter images. Thus, it is useful to generate fluorescence parameter histograms for a given set of pixels (image). In MFDi, it is possible to display pairs of parameters in two-

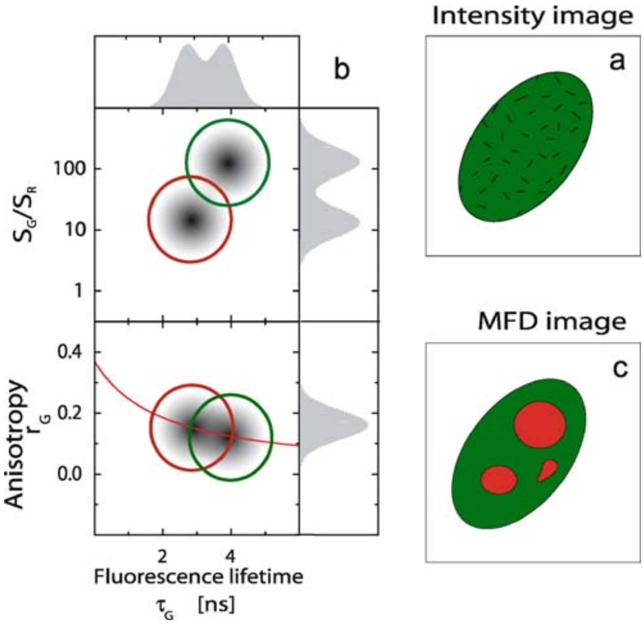

Fig. 2 **a**–**c** Representation of the features of MFD imaging. **a** The intensity image of the cell shows a rather homogeneous distribution of fluorescence inside the cell. **b** The sorting of pixels into a histograms according to various calculated parameters allows one to better distinguish between different species (e.g. green and red). **c** The two species in the cell can subsequently be distinguished and information about variations in the conditions in the cell can be obtained

dimensional frequency histograms where the number of pixels is displayed in a colour scheme (black corresponds to the highest value). Moreover, the corresponding one-dimensional histograms are given as projections. Figure 2b displays as an example a stack of 2-D histograms, which are important in FRET measurements [47]. Here the fluorescence lifetime of the donor dye τ_G is plotted against the ratio of signals in the green and red channels S_G/S_R and the fluorescence anisotropy r_G. In this way, the heterogeneity of a set of pixels for a given image or a series of images is easily monitored. By selecting a subpopulation of pixels (green and red circles, respectively) and displaying them in a joint image, more detailed spatial and fluorescence information of validated statistical significance is obtained for the image of the cell (Fig. 2c).

To further reduce the noise when determining fluorescence parameters, it is useful to perform a subensemble analysis, as shown in Fig. 3. Figure 3a displays the fluorescence decay for a single pixel, which is characterised by a high noise level, so that only a single fluorescence lifetime of 3.9 ns can be estimated using a maximum likelihood estimator [49]. If, however, a fluorescence arrival time histogram is accumulated for a subensemble of selected pixels, the noise is reduced and a much higher level of accuracy can be reached (Fig. 3b), which allows one to detect more than a single fluorescent species. Besides a scattered background (10%), the fitted model function has two fluorescent components with lifetimes of τ_{long}=4.5 ns (64%) and τ_{short}=0.6 ns (36%). Considering the fast scanning speed of confocal laser scanning microscopy, high accuracy FLIM can only be attained for the analysis of a pixel subensemble, not for a single pixel. MFDi shows that speed and accuracy are not mutually exclusive, but that they can be combined in a single measurement when suitable data acquisition and analysis is used. Similar arguments can be also applied to FCS [50], where FCS has been successfully applied to single-particle analysis. However, in commercial instruments, FCS measurements are often only available for regions of interest and cannot be obtained simultaneously for all pixels during scanning. Figure 3c displays a FCS curve calculated from photons detected in a single pixel using an integration time of 20 ms. It is evident that the curve has an amplitude >1 and a bunching term in the range of 0.1–1 ms. The statistical significance of this observation is validated by the pixel subensemble analysis shown in Fig. 3d.

To conclude, even if the noise is high for correlation curves of single pixels, it is still possible to derive statistically meaningful correlation functions by subensemble averaging. We also tested the influence of different pixel integration times on the correlation function in the following way. We analysed data that were taken continuously at one spot and simulated different pixel integration time windows by cutting the fluorescence traces into many small pieces and calculating individual correlation curves for all windows. If the mean fluorescence signal is constant

Fig. 3 **a**–**d** Pixelwise and pixel-selective analysis. Fluorescence lifetime decay of a single pixel (**a**) and of a selected set of pixels (**b**). The *solid line* corresponds to the fitted model function, while the *dashed line* indicates the instrumental response function. Correspondingly, correlation curves are calculated for a single pixel (**c**) as well as for a selected set of pixels (**d**)

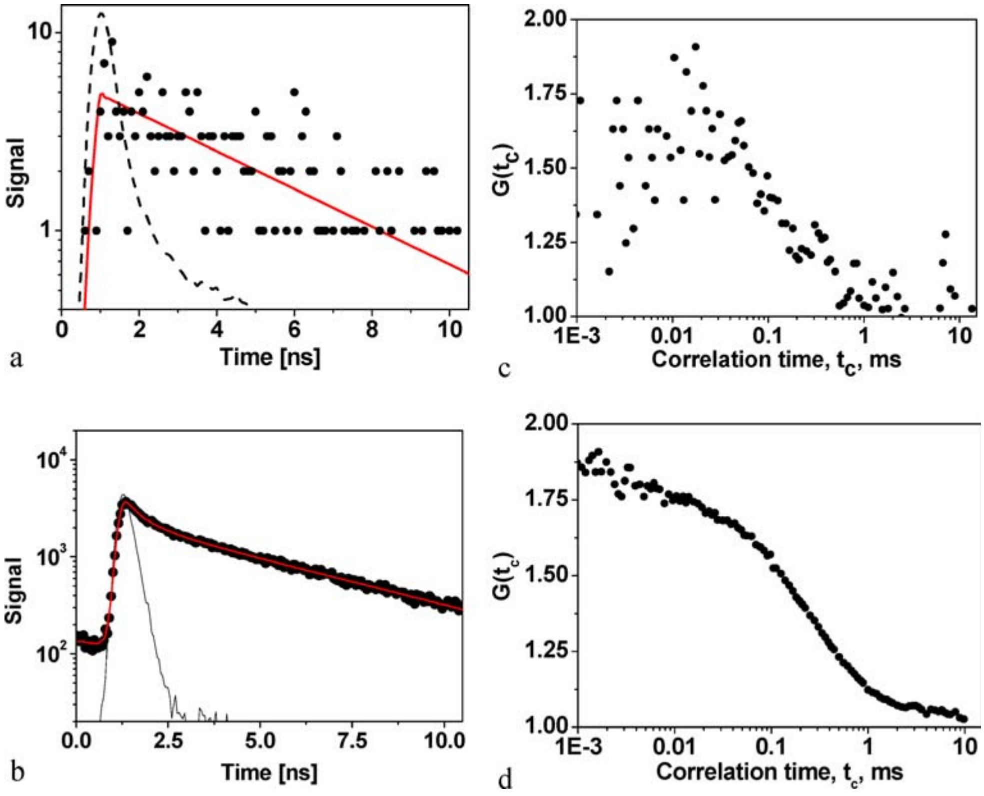

over time (no photobleaching), the average of all curves for a given integration time shows the same correlation as the complete trace, i.e. even if the size of the pixel integration time window is too small to measure the full decay of the correlation curve, the data are still sufficient to obtain the correct shape and absolute amplitude. If data from single pixel are too noisy, diffusion times and amplitudes can be calculated via subensemble analysis by averaging the correlation curves from several pixels.

As discussed above, it is obvious that images obtained with standard laser-scanning microscopes contain a time structure that can be exploited to measure the dynamics of molecules in solution and in cells [26]. Image correlation spectroscopy (ICS) analyses the temporal and spatial correlation between neighbouring pixels or successive images and allows molecular diffusion constants to be calculated in the microsecond to second timescale [27, 28]. The simulation shown in Fig. 4 illustrates that the data structure of MFDi is also suitable for fast scanning if no long term drifts occur. The part of the correlation curve at short correlation times (blue) is limited by the pixel integration time. The part of the correlation curve at long correlation times (red) is defined by the time that the laser takes to return to a given pixel. In our case, the gap in the correlation curve is equivalent to the time needed to take one image. Thus, a series of repeated scans (resulting in a series of images) is necessary to calculate the shown correlation curve.

Fast resonance scanners have become commercially available recently, and these have pixel integration times as short as several hundreds of nanoseconds. Here, the complete signal from one pixel is obtained by integrating several cycles. In this way, the time gap is shifted from milliseconds or seconds to microseconds, and the translational diffusion term in the correlation function will not be disturbed.

Finally, it is important to mention that the above methods will be also applicable for cases with slow cellular dynamics (not shown in Fig. 4). However, the slow drift will be reflected in an additional bunching term, which occurs on longer timescales.

Experimental

Set-up

All of the measurements were conducted with a homemade confocal fluorescence microscope. We excited the samples with the 476.5 nm line (yeast cells) or the 496 nm line (glutathione sepharose beads) of a linearly polarized, pulsed argon ion laser (Coherent, Inc., Santa Clara, CA, USA), which was focused in an inverted microscope (IX 70, Olympus, Hamburg, Germany) using a 60× water immersion objective (NA=1.2). The light emitted was collected in the same objective and successively separated into its parallel- and perpendicularly polarised components (VISHT11, Gsänger, Planegg, Germany) and into its green and red components (620DCLX beam splitter, AHF, Tübingen, Germany). The detected spectra are limited using bandpass filters: HQ 533/46, AHF in the green and HQ 730/140, AHF in the red spectral ranges, respectively

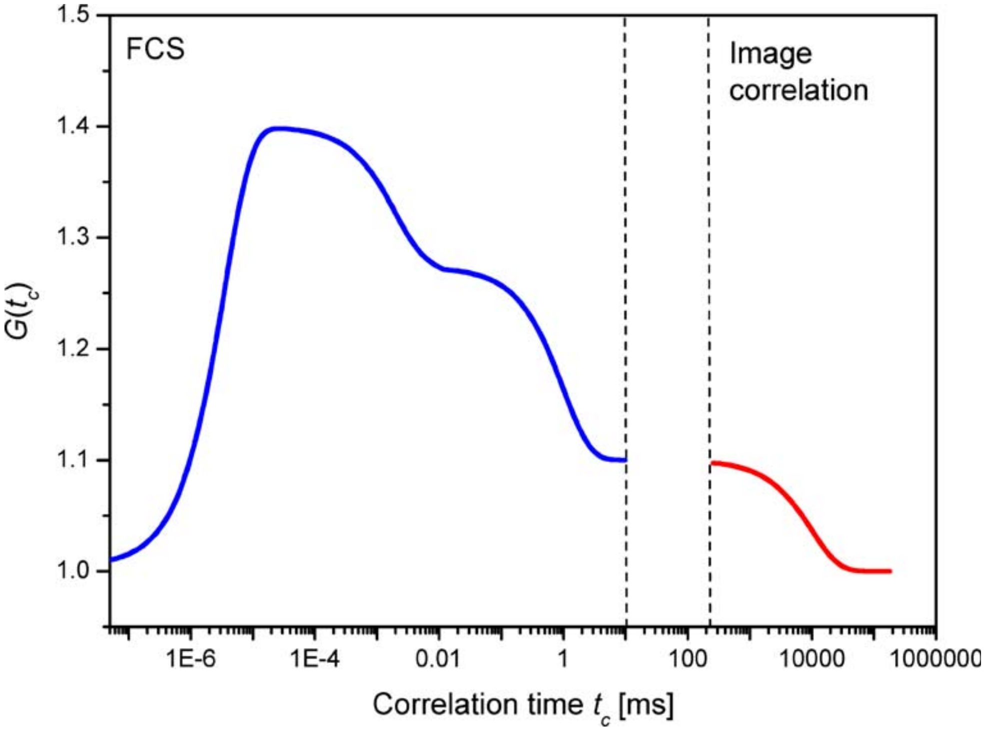

Fig. 4 Schematic representation of the full correlation curve: The *blue* curve is calculated from a large set of TCSPC data and corresponds to a full-range FCS; the *red* curve represents image correlation

(Chroma Technologies, Rockingham, VT, USA). The photons were detected by avalanche photodiodes (SPCM-AQR, Perkin-Elmer, Wellesley, MA, USA) and counted with PC plug-in cards (SPC132, Becker & Hickl, Berlin, Germany). A detailed description of the MFD set-up can be found in [37, 47, 48, 51].

Scanning To generate MFD images, the sample was moved in a stepwise manner relative to the confocal volume. For this purpose, the sample was mounted on a closed-loop piezo-controlled x,y-scanner (Physik Instrumente, Karlsruhe, Germany) and moved perpendicularly to the optical axis. The pixel size is therefore defined by the step size of the scan. The resolution is restricted by diffraction, and in our case incomplete illumination of the objective. The diameter of the detection volume was approximately 500 nm for the experiments presented here, which corresponds to an FCS diffusion time for rhodamine 110 (Rh110) of 60 µs. Before the actual scanning, the sample is wide-field-illuminated to adjust the z-position. The confocal volume is manually positioned in the centre of the object. The scanning process is controlled via software written in Visual C++. The program generates additional electronic pulses during pixel and row leaps, which are saved in two supplementary router channels of the SPC 132 board. These signals enable the picture to be reconstructed and the individual photons in each pixel to be evaluated.

Sample preparation

Preparation of gel beads for imaging To image Rh110 inside and outside of the polymeric beads (glutathione sepharose beads, Pharmacia, Peapack, NJ, USA), the dye and the beads were mixed and incubated for five minutes to allow the fluorophores to diffuse into the beads. In order to prevent movement of the beads during the scan, they were (locally) fixed by clamping the sample between two cover slides.

Preparation of yeast cells for imaging For life cell analysis, *Schizosaccharomyces pombe* yeast cells that express the Mal3-pk-GFP fusion protein were prepared as described in [52]. They were kindly provided by the group of Ursula Fleig at the University of Düsseldorf. The yeast cells were grown in Edinburgh minimal medium (EMM) to exponential phase. To fix the yeast cells on cover slips, *Griffonia simplicifolia* lectine was allowed to adsorb onto standard glass from a solution of 0.02 mg/ml for ten minutes. The glass was then gently rinsed with EMM and yeast cells were allowed to adsorb on the surface for approximately 15 min. This resulted in the firm attachment of the cells; no lateral movement could be detected over the course of the optical imaging.

Data analysis

The data registration and processing of MFD has been described in detail [37, 46, 48, 51]. In brief, four storage parameters are saved for each detected photon: (i) the spectral range, λ_F, of the detected fluorescence (green or red); (ii) the polarization of the signal photon (parallel or perpendicular) with respect to the linear polarization of the excitation laser; (iii) the arrival time of the signal photon relative to the incident laser pulse; and (iv) the time between photons, Δt.

During the imaging, additional “pixel” and “line” SYNC signals are introduced using two more router channels by the instrument control software in order to define pixel coordinates in a photon signal stream. Once a pixel is identified, the average green and red count rates, S_G and S_R, are calculated by dividing the number of registered photons by the pixel integration time. The arrival times of the photons in the pixel are used to generate fluorescence decay histograms for each of the four detection channels (green parallel, $G_{\|}$, green perpendicular, $G_{\perp}$, red parallel, $R_{\|}$, red perpendicular, $R_{\perp}$. The fluorescence lifetime, τ, and anisotropy, r, are determined for further analysis (as well as correlation curves), as given below.

Single-pixel fluorescence lifetime The signal decay histogram registered in the green detection range was described by scattered light and fluorescence decay with a single component. The normalized model pattern, M, of the total signal was computed, which contains variable fractions, γ, of scattered background, B, and fluorescence, F.

$$M_i(\tau,\gamma,s) = (1-\gamma)F_i + \gamma B_i \tag{1}$$

Fluorescence lifetimes were calculated using a maximum likelihood estimator, as described in [44], which has been shown to be the most statistically efficient.

Fluorescence anisotropy The anisotropy was primarily analysed in the green range. The steady-state anisotropy is formally given by $r_G = \int_0^\infty r_G(t)F_G(t)dt \Big/ \int_0^\infty F_G(t)dt$, where $r_G(t) = \frac{F_{G\|}(t) - F_{G\perp}(t)}{F_{G\|}(t) + 2\cdot F_{G\perp}(t)}$ is the time-dependent anisotropy, and $F_{G\|}(t)$ and $F_{G\perp}(t)$ are the fluorescence detected with polarizations parallel and perpendicular to that of the excitation light, respectively. $F_G(t) = F_{G\|}(t) + 2F_{G\perp}(t)$ is the total fluorescence intensity.

In this study, the anisotropy of the fluorescence detected from a single molecule in the green channels was determined as described by Schaffer et al. [44]. After determining the fraction of background signal γ, the background-corrected anisotropy is calculated via $r_G = \frac{gF_{G\|} - F_{G\perp}}{(1-3l_2)gF_{G\|} + (2-3l_1)F_{G\perp}}$, where $F_{G\perp}$ and $F_{G\|}$ are the average fluorescence count rates detected within a pixel with polarizations parallel and perpendicular to that of the excitation light, respectively. Correction factors (l_1= 0.0308 and l_2=0.0368) were applied in order to take into account the polarization mixing due to the objective lenses of the microscope [53]. g=1.05 compensates for the slightly different detection efficiencies of the two detection channels.

Correlation analysis The value of the correlation function $G(t_c)$ for the correlation time t_c for each pixel is calculated based on the algorithm described by Felekyan at al. [54], using the time-dependent fluorescence intensities in two detection channels, $F_1(t)$ and $F_2(t)$,

$$G(t_c) = \frac{\langle F_1(t)F_2(t+t_c)\rangle}{\langle F_1(t)\rangle \cdot \langle F_2(t)\rangle} = \frac{\left(\frac{\sum\limits_i F_1(t_i)F_2(t_i+t_c)}{\min\left(t_1^{\max}, t_2^{\max}-t_c\right)}\right)}{\left(\frac{\sum\limits_i F_1(t_i)}{t_1^{\max}}\right)\cdot\left(\frac{\sum\limits_j F_2(t_j)}{t_2^{\max}}\right)} \tag{2}$$

Therefore $\min\left(t_1^{\max}, t_2^{\max} - t_c\right)$ returns the smaller number of $t_1^{\max}$ and $t_2^{\max} - t_c$, and $t_1^{\max}$ and $t_2^{\max}$ are the time-bin numbers of the last photons in detection channels 1 and 2, respectively. Equation 2 is applicable for cases where the measurement time window is significantly bigger than the correlation time of interest. However, this is not the case for imaging, where the integration time of approached pixel T is on the order of the correlation time t_c used. Therefore, intensity values for the time trace with bin width t_{bin} must be used to calculate the mean intensities. For these cases, a corrected algorithm is applied to calculate the mean intensity. The pixel integration time T and the correlation time t_c can be expressed by the corresponding bin integer numbers N_T and N_c for a given time bin t_{bin}: T=$t_{bin}N_T$ and t_c=$t_{bin}N_c$. In this way, the number of intensities used in the calculation is given by N_T–N_c.

$$G(t_c) = \frac{\frac{1}{(N_T-N_c)}\sum\limits_{i=1}^{N_T-N_c} F_1(t_i)\cdot F_2(t_i+t_c)}{\frac{1}{N_T-N_c}\sum\limits_{i=1}^{N_T-N_c} F_1(t_i)\cdot\frac{1}{N_T-N_c}\sum\limits_{i=N_c}^{N_T} F_2(t_i+t_c)} \tag{3}$$

For each correlation curve, the following characteristic parameters were determined:

The mean correlation amplitude, g_m, of the correlation function, $G(t_c)$, is defined for a certain range of correlation times, $t_c(c_{start})$ to $t_c(c_{end})$, where the correlation amplitude reached saturation (Eq. 4).

$$g_m = \frac{\sum\limits_{c_{start}}^{c_{end}} G(c_i)}{c_{end} - c_{start}} \tag{4}$$

The correlation decay time, t_m, is a descriptive parameter and is calculated using a geometric approximation to reduce shot noise. Considering that the correlation times t_c have a pseudo-logarithmic time axis, where the values are ordered in a linear array of time channels c_i, we first calculate the mean channel number c_m, which is then converted by linear interpolation to the corresponding correlation decay time t_m (Eq. 5).

$$c_m = \frac{\sum\limits_i (G(c_i) - 1)}{g_m - 1} \tag{5}$$

Calculation of concentrations There are two ways to calculate the concentration of fluorescent molecules. First, the average number of fluorescent particles N_P that diffuse through the confocal volume can be calculated from the correlation amplitude of the FCS [54]. Second, the number of emitting fluorophores N_F can be deduced from the fluorescence intensity F by taking the brightness Q of the dye into account. These two methods have been applied to the analysis of the bead images (Fig. 5). The number $N_{F(in)}$ of fluorophores in the confocal volume inside the bead is calculated according to

$$N_{F(in)} = \frac{S_{in} - B_{in}}{Q_{in}} = \frac{F_{in}}{Q_{in}} \tag{6}$$

where S_{in}=183.7 kHz is the average fluorescence intensity inside the bead and B_{in}=11.3 kHz is the average background intensity measured in a bead without Rh110.

The brightness (i.e. signal counts per molecule) Q_{in} inside the bead is estimated by extrapolation, using the brightness outside the bead Q_{out} as a reference value. The latter must be corrected in order to account for the fluorescence quenching observed within the bead.

$$Q_{in} = Q_{out} \cdot \frac{\tau_{in}}{\tau_{out}} \tag{7}$$

The correction factor τ_{in}/τ_{out} results from the linear relationship between the fluorescence quantum yield Φ_F and the fluorescence lifetime τ, which is given by $\Phi = k_F\tau$, where k_F is the intrinsic rate constant for fluorescence. The average fluorescence lifetimes (τ_{in}=3.68 ns and τ_{out}=4.15 ns) were calculated by fitting all photon data for the respective selected pixels. Constant background is also taken into account, which could not be done for the single pixel lifetime analysis.

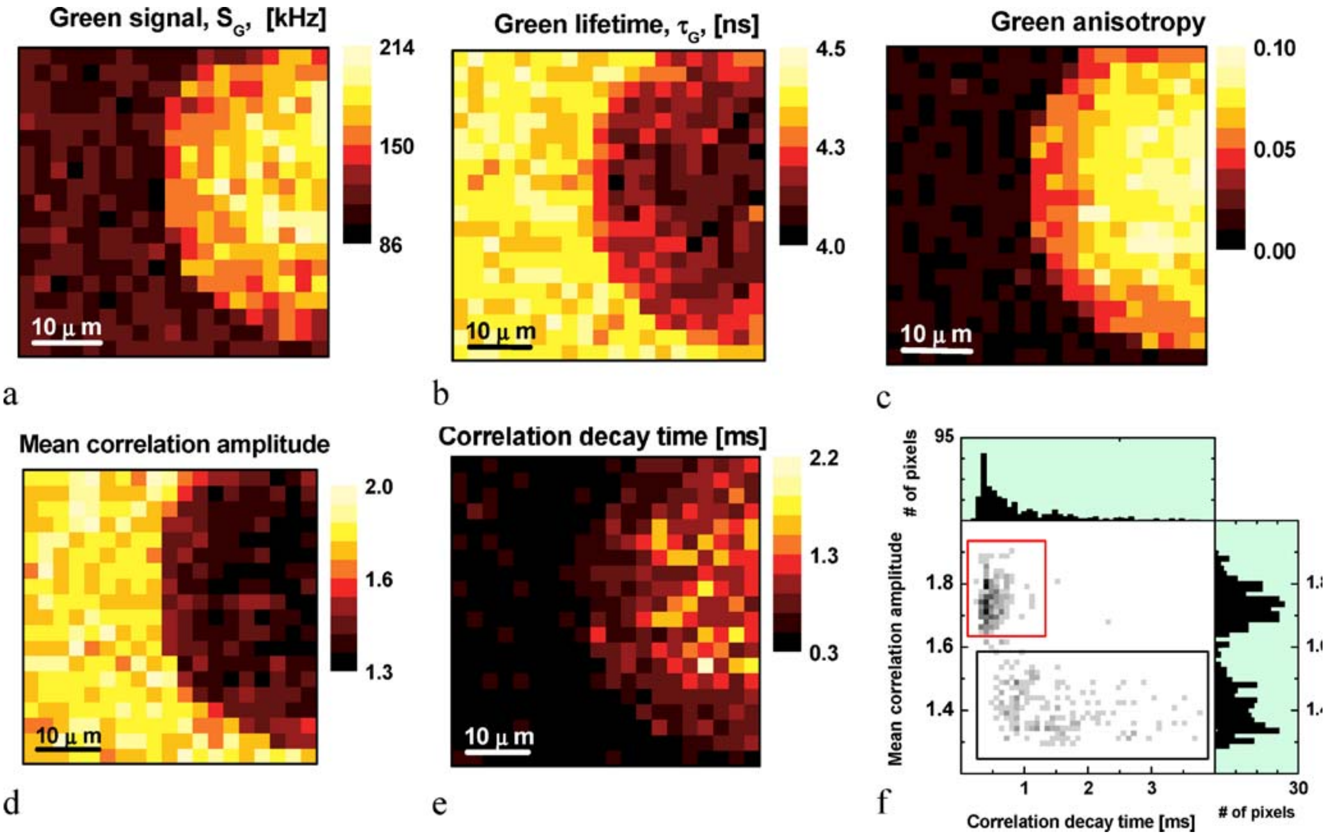

Fig. 5 **a**–**f** MFD imaging of the Rh110 dye located inside and outside a glutathione sepharose bead. The bead is located to the right-hand side of the pictures (the round shape). The following MFD parameters have been calculated: **a** green signal, S_G; **b** green lifetime, τ_G; **c** green anisotropy, r_G; **d** mean correlation amplitude; **e** correlation decay time. **f** A 2-D histogram of the single pixel values from pictures **d** and **e**. The correlation amplitude is plotted against the correlation decay time. The corresponding one-dimensional histograms are given as projections. The *black box* highlights the pixels inside the bead, the *red* one corresponds to the pixels outside the bead. The integration time per pixel is 300 ms

With an average signal per pixel of S_{out}=111.4 kHz, a background B_{out}=1.98 kHz and t $N_{P(out)}$=1.3 fluorophores in the confocal volume, as derived from the FCS, the brightness of the Rh110 outside the bead amounts to Q_{out}=81 kHz/molecule. The number of fluorophores in the focus is thus calculated to be $N_{F(in)}$=2.40 assuming the fluorophores do not aggregate outside the bead.

Results

MFDi

Mobility of fluorophores in different environments To demonstrate the ability of our multiparameter fluorescence imaging (MFDi) technique, we analysed a test system that exhibits spatial variation of molecular mobility. We used a model system of glutathione sepharose beads pressed between two cover slides, which allowed the fluorophore Rh110 to diffuse inside the bead too. Figure 5 shows five images for the different fluorescence parameters of the green detection channels: the green signal S_G (a), the fluorescence lifetime τ_G (b), the steady-state anisotropy r_G (c), the mean correlation amplitude (d) and the correlation decay time (e), all calculated from a single MFD image scan.

The intensity image (Fig. 5a) shows that the bead is brighter than the surroundings, which indicates an accumulation of fluorescent dyes inside the bead.

Due to the interaction with the polymer network, their fluorescence (Fig. 5b) is quenched. The fluorescence lifetime is reduced from τ_{out}=4.15 ns outside the bead to τ_{in}=3.68 ns inside the bead. The anisotropy image (Fig. 5c) shows higher r values inside the bead than outside. The average anisotropies for the selected areas inside and outside the bead are found to be 0.02 and 0.086, respectively. Using a value for the fundamental anisotropy r_0=0.375 in the Perrin equation $(\rho = r\,\tau/(r_0 - r))$ yields mean rotational correlation times of ρ_{out}=0.23 ns and ρ_{in}=1.1 ns. Thus, the reduced rotational mobility proves directly that the dye interacts with the polymer network.

For the anisotropy, intensity and fluorescence lifetime, an increased influence of the polymer matrix is visible when moving from the edge towards the centre of the bead. This may originate from the fact that the beads were clamped between two cover slides to fix them for stable imaging. This results in a compression of the polymer beads to approximately half of their thickness, which increases the polymer density, mainly at the centre of the bead. Performing the pixel-wise fluorescence correlation analysis, we obtain information about the number of fluorescent particles in the confocal volume via the correlation amplitude in each pixel. The mean correlation amplitude image (Fig. 5d) shows the change in concentration between the surroundings and the inside of the bead. Since the correlation amplitude is given by the inverse of the number of molecules in the focal volume, the lower amplitude inside the bead demonstrates the accumulation of fluorophores, which is consistent with the higher intensity inside the bead.

Simultaneously, we also obtain the image for the correlation decay time, which reflects the diffusion coefficient of the fluorophore in the different surroundings (Fig. 5e). This image clearly proves that translational diffusion is restricted, as indicated by longer correlation decay times within the bead, which is in accordance with the reduced rotational diffusion measured by the increase in the anisotropy.

In the fluorescence parameter images, it is quite difficult to analyse the statistical properties of the values at each pixel. In MFDi, it is possible to display pairs of parameters in two-dimensional frequency histograms, where the number of pixels is displayed in a colour scheme, and black corresponds to the highest value. Figure 5f displays the 2-D histogram for the correlation amplitude versus the correlation decay time, and the corresponding one-dimensional histogram is given as a projection. The two populations are clearly visible here; the population of free dye (red box) has a much smaller distribution of correlation decay times t_m compared to those inside the bead (black box), and this can only be seen in the 2-D histogram. The very broad t_m distribution of dyes inside the bead cannot be explained by statistical variations alone, and thus nicely reflects the heterogeneity of the microenvironments inside the bead.

Using the average correlation amplitudes of the selected areas outside the bead, the number of diffusing particles $N_{P(out)}=1.3$ in the confocal volume can be calculated [54]. Moreover, the fluorescence intensity is proportional to the number of fluorophores N_F emitting in the confocal volume. If the sample consisted of diffusing particles containing n fluorophores, the number of fluorophores N_F estimated from the fluorescence intensity would be n times the number of particles calculated according to the correlation amplitude. From the fluorescence intensity inside the bead, we calculate the number of fluorophores in the confocal volume to be $N_{F(in)}=2.4$ (see the “Data analysis” section), which agrees well with the number of diffusing particles $N_{P(in)}=2.5$. This result indicates that the fluorophores do not aggregate.

It is known that the calculation of exact concentrations from a fluorescence correlation analysis is limited by several uncertainties, such as: (1) the shape and size of the confocal detection volume, which can vary with the local index of refraction; (2) variations in the contribution from the background. Nevertheless, our results show that the accuracy obtained from the FCS calculation is high enough to decide, based on a comparison between the intensity and correlation amplitude images, whether particles contain one or more than one fluorophore. This is highly relevant, especially when studying the interactions of labelled proteins in cells.

Imaging the distribution and diffusion of GFP-labelled Mal3 proteins in yeast cells

We applied the multiparameter fluorescence imaging technique to single cells of fusion yeast *Schizosaccharomyces pombe* that express the GFP-labelled Mal3 protein. Yeast cells undergo a very dynamic cycle involving the polymerisation and depolymerisation of microtubules, which grow from the center of the cell towards its edges [55, 56].

The Mal3 protein assembles along microtubule, preferentially localizing at the growing ends of particles, promoting the initiation of microtubule growth and preventing degradation catastrophes. At the cell ends, the microtubule tip-associated Mal3 particles disappear, and this is followed by rapid microtubule degradation. This process allows the cell to target the cell ends, helping to maintain cellular bipolarity.

We applied MFDi to this highly dynamic system to show its ability to provide enhanced insight into cellular systems compared to simple intensity images. Time series taken with the MFDi system (data not shown) showed the typical rapid microtubule polymerisation and subsequent degradation, which took place within minutes. The imaged cell shown in Fig. 6 is in a state that occurs shortly after cell division, and it exhibits a septum in the centre, as indicated by the low fluorescence intensity.

We selected one image for detailed analysis. This shows the microtubule in the polymerising phase, where bright particles can be seen at the growing tips, which contain a high concentration of bound Mal3-pk-GFP. Besides these bright spots, a weaker fluorescence is visible in the rest of the cell due to the presence of Mal3-pk-GFP that not bound to the microtubule. Due to the high concentration of Mal3-pk-GFP and the low excitation intensity of 1.7 μW, the contribution from the autofluorescence background in the green channel does not dominate (Fig. 6a) (see below). In

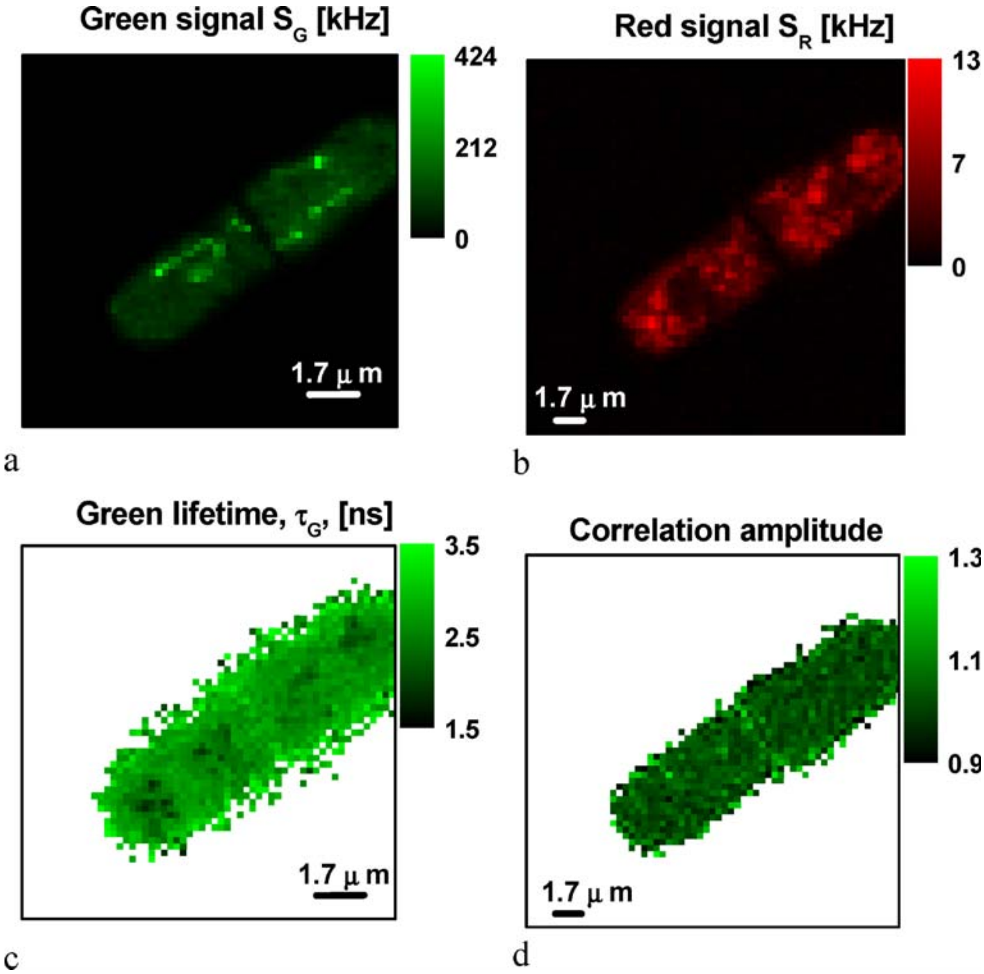

Fig. 6 MFD imaging of Mal3-pk-GFP proteins in *Schizosaccharomyces pombe* yeast cells. Intensity image of **a** the green signal, S_G and **b** the red signal, S_R; **c** green fluorescence lifetime, τ_G; **d** correlation amplitude. The cells were excited at 1.7 µW. The integration time per pixel was 20 ms

the simultaneously detected signal for the red channel, a significant contribution from red autofluorescence is visible (resulting from green excitation), which shows cellular structures. In the centre of the lower part of the cell, a vacuole structure is visible.

Because of the high rotational correlation time of GFP itself, which is longer than its fluorescence lifetime [57], the anisotropy does not increase strongly due to a decreased rotational movement upon interaction of the Mal3-pk-GFP protein with other protein complexes. Accordingly, we found the same anisotropy value, 0.26, throughout the whole cell, which is slightly smaller than the steady-state anisotropy of 0.32 [6, 44]. We only found variations at decreased fluorescence intensities at the border of the cell, where the calculated anisotropy values vary more strongly due to shot noise [44]. Interestingly, a decrease in anisotropy due to possible homo fluorescence energy transfer is not visible, not even for the areas of highest Mal3-pk-GFP concentration in the particles at the microtubule ends. This indicates that the different Mal3-pk-GFP proteins do not interact directly within these particles and they also do not form multimers (within a distance of approximately 8 nm) when they are not bound to the microtubules.

Figure 7a shows a 2-D histogram where the ratio of green to red intensity (S_G/S_R) is displayed versus the fluorescence lifetime τ_G for all individual pixels. A typical lifetime of 2.6 ns was found for most of the pixels, which is also slightly smaller than the mean GFP fluorescence lifetime of approximately 3 ns. Moreover, at intensity ratio smaller than 10, an additional species becomes visible that exhibits a shorter lifetime of approximately 2.2 ns. Note that this species would not have been detected from the 1-D histogram of fluorescence lifetime. They can easily be picked out in the intensity image for the yeast cell shown in Fig. 7b by assigning a red colour scale to the selected pixels only. Locally different fluorescence lifetimes might indicate variations in the surroundings when using fluorophores sensitive to pH or other parameters. However, while the GFP shows a pH-sensitive transition between a bright and a dark state that affects its average brightness, this does not strongly affect its fluorescence lifetime.

This shows that the simultaneous measurement of several parameters is crucial to the detection of systematic errors in quantitative fluorescence imaging and the correct interpretation of the images. The analysis of all pixel data in two-dimensional histograms highlights systematic

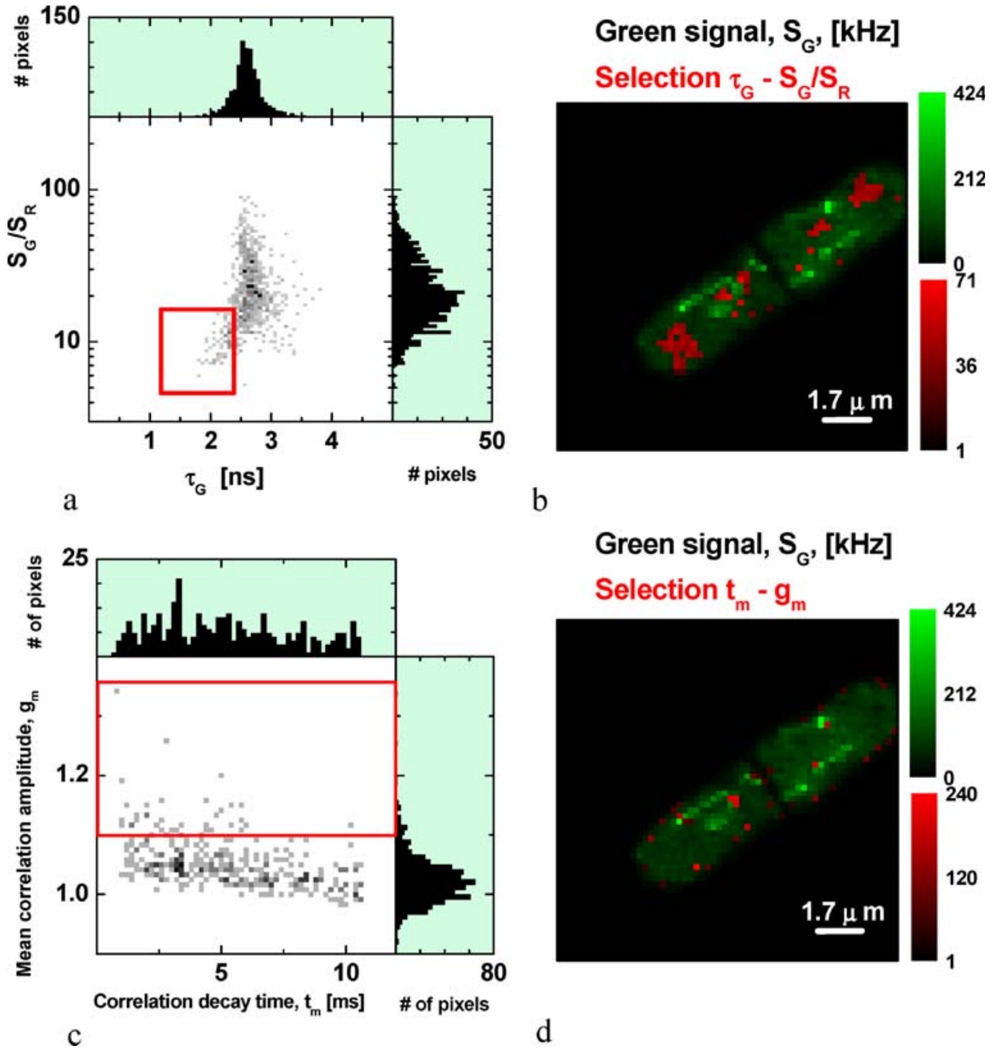

Fig. 7 **a**–**d** MFD imaging of Mal3-pk-GFP proteins in *Schizosaccharomyces pombe* yeast cells. Selection of subspecies according to their MFD parameters. **a** Selection of a short-lifetime, τ_G, low green-to-red intensity ratio, S_G/S_R, species in a 2-D histogram (*red box*), corresponding to a high amount of autofluorescence. **b** The species is highlighted by using a red colour scale in the green signal MFD image. **c** Another selection was made by choosing a high correlation amplitude species. **d** Again, the selection is highlighted by using a red colour scale in the green signal MFD image. The cells were excited at 1.7 μW. The integration time per pixel was 20 ms

trends, especially in the case of high noise due to low photon counts.

Figure 6d shows the fluorescence correlation amplitudes calculated for each individual pixel. Due to the short measurement time of 20 ms per pixel, and thus the relatively low number of photons per pixel of approximately 1500, the image shows considerable noise. We obtain an average amplitude of 1.03 from the 2-D histogram of correlation amplitude g_m vs. correlation decay time t_m (Fig. 7c), while the correlation decay times for the Mal3-pk-GFP protein show a broad distribution in the range of several milliseconds. This is consistent with the diffusion time of free GFP in aqueous buffer (approximately 0.4 ms), which was calculated from reference experiments (data not shown). Due to the high concentration of proteins and cellular components, the mobility of Mal3-pk-GFP within the cell will be reduced.

The 2-D histogram shows few pixels (9.5%) with amplitudes above 1.10. Due to the high noise, one must be careful when interpreting single pixel amplitudes. However, Fig. 7d shows the locations of the selected pixels displayed with a red colour scale in the intensity image. It is evident that the selected pixels are not randomly distributed in the cell. Two classes of pixels are detectable: (i) those located at the bright ends of the microtubules, and (ii) those located at the edge of the cell. While the high amplitudes at the edge of the cell may be due to fluctuations resulting from low photon counts, this notion does not hold for the bright pixels inside the cell.

In this respect, it is important to note that the correlation amplitude is strongly increased if the signal changes during the measurement time window of the pixel. Such a change in intensity within the measurement time window occurs at positions of high fluorescence intensity contrast due to the delayed approach of a new pixel in the closed-loop operation mode of the piezo scanner. To avoid the corruption of the calculated correlation parameters that would result from this relative movement of the confocal detection volume, one can easily exclude the photons taken in the first several ms from the data analysis. On the other hand, this would lead to increased noise due to lower photon counts, or it would require that the image recording time be increased. However, for most of the pixels within the cell, where the intensity contrast is not high, we found that this interference with the calculated correlation amplitude was small compared to the noise resulting from low photon counts.

Acknowledgements We thank Ursula Fleig and Christoph Beuter for their generous support. They provided the cells and prepared these cell samples for imaging. We thank Stanislav Kalinin for helping us to find appropriate and statistically stable parameters to describe noisy FCS curves. We thank Stefan Marawske for helping us to perform live cell measurements. We thank Alexander Gaiduk for helping us to establish MFD imaging. CS gratefully acknowledges financial support from the BMBF Biofuture grant 0311865 and the SFB 590, Heinrich-Heine-University Düsseldorf.

References

1. Giepmans BNG, Adams SR, Ellisman MH, Tsien RY (2006) Science 312:217–224
2. Xie XS, Yu J, Yang WY (2006) Science 312:228–230
3. Wouters FS, Verveer PJ, Bastiaens PIH (2001) Trends Cell Biol 11:203–211
4. Truong K, Ikura M (2001) Curr Opin Struct Biol 11:573–578
5. Sekar RB, Periasamy A (2003) J Cell Biol 160:629–633
6. Meyer BH, Segura JM, Martinez KL, Hovius R, George N, Johnsson K, Vogel H (2006) Proc Natl Acad Sci USA 103:2138–2143
7. Hoppe A, Christensen K, Swanson JA (2002) Biophys J 83:3652–3664
8. Bastiaens PIH, Squire A (1999) Trends Cell Biol 9:48–52
9. Jares-Erijman EA, Jovin TM (2003) Nature Biotechnol 21:1387–1395
10. Clayton AH, Hanley QS, Arndt-Jovin DJ, Subramaniam V, Jovin TM (2002) Biophys J 83:1631–1649
11. Levi V, Ruan Q, Kis-Petikova K, Gratton E (2003) Biochem Soc Trans 31:997–1000
12. Seisenberger G, Ried MU, Endreß T, Büning H, Hallek M, Bräuchle C (2001) Science 294:1929–1932
13. Schütz GJ, Axmann M, Freudenthaler S, Schindler H, Kandror K, Roder JC, Jeromin A (2004) Microsc Res Tech 63:159–167
14. Kues T, Dickmanns A, Lührmann R, Peters R, Kubitscheck U (2001) Proc Natl Acad Sci USA 98:12021–12026
15. Thompson NL, Lieto AM, Allen NW (2002) Curr Opin Struct Biol 12:634–641
16. Bacia K, Schwille P (2003) Methods 29:74–85
17. Saffarian S, Elson EL (2003) Biophys J 84:2030–2042
18. Kohl T, Schwille P (2005) Adv Biochem Eng Biotechnol 95:107–142
19. Brock R, Hink MA, Jovin TM (1998) Biophys J 75:2547–2557
20. Schwille P, Haupts U, Maiti S, Webb WW (1999) Biophys J 77:2251–2265
21. Gennerich A, Schild D (2000) Biophys J 79:3294–3306
22. Skinner JP, Chen Y, Müller JD (2005) Biophys J 89:1288–1301
23. Xiao Y, Buschmann V, Weston KD (2005) Anal Chem 77:36–46
24. Ruan Q, Cheng MA, Levi M, Gratton E, Mantulin WW (2004) Biophys J 87:1260–1267
25. Balaji J, Maiti S (2005) Microsc Res Tech 66:198–202
26. Rocheleau JV, Wiseman PW, Petersen NO (2003) Biophys J 84:4011–4022
27. Digman MA, Sengupta P, Wiseman PW, Brown CM, Horwitz AR, Gratton E (2005) Biophys J 88:L33–L36
28. Digman MA, Brown CM, Sengupta P, Wiseman PW, Horwitz AR, Gratton E (2005) Biophys J 89:1317–1327
29. Hebert B, Costantino S, Wiseman PW (2005) Biophys J 88:3601–3614
30. Kolin DL, Costantino S, Wiseman PW (2006) Biophys J 90:628–639
31. Palo K, Brand L, Eggeling C, Jäger S, Kask P, Gall K (2002) Biophys J 83:605–618
32. Kask P, Palo K, Fay N, Brand L, Mets Ü, Ullmann D, Jungmann J, Pschorr J, Gall K (2000) Biophys J 78:1703–1713
33. Kask P, Palo K, Ullmann D, Gall K (1999) Proc Natl Acad Sci USA 96:13756–13761
34. Palo K, Mets Ü, Jäger S, Kask P, Gall K (2000) Biophys J 79:2858–2866
35. Fries JR, Brand L, Eggeling C, Köllner M, Seidel CAM (1998) J Phys Chem A 102:6601–6613
36. Becker W, Bergmann A, Haustein E, Petrasek Z, Schwille P, Biskup C, Kelbauskas L, Benndorf K, Klöcker N, Anhut T, Riemann I, König K (2006) Microsc Res Tech 69:186–195
37. Widengren J, Kudryavtsev V, Antonik M, Berger S, Gerken M, Seidel CAM (2006) Anal Chem 78:2039–2050
38. Edman L, Mets Ü, Rigler R (1996) Proc Natl Acad Sci USA 93:6710–6715
39. Maus M, Cotlet M, Hofkens J, Gensch T, De Schryver FC, Schaffer J, Seidel CAM (2001) Anal Chem 73:2078–2086
40. Bowen BP, Scruggs A, Enderlein J, Sauer M, Woodbury N (2004) J Phys Chem A 108:4799–4804
41. Enderlein J, Sauer M (2001) J Phys Chem A 105:48–53
42. Tellinghuisen J, Goodwin PM, Ambrose WP, Martin JC, Keller RA (1994) Anal Chem 66:64–72
43. Enderlein J, Goodwin PM, van Orden A, Ambrose WP, Erdmann R, Keller RA (1997) Chem Phys Lett 270:464–470
44. Schaffer J, Volkmer A, Eggeling C, Subramaniam V, Striker G, Seidel CAM (1999) J Phys Chem A 103:331–336
45. Antonik M, Felekyan S, Gaiduk A, Seidel CAM (2006) J Phys Chem B 110:6970–6978
46. Eggeling C, Berger S, Brand L, Fries JR, Schaffer J, Volkmer A, Seidel CAM (2001) J Biotechnol 86:163–180
47. Rothwell PJ, Berger S, Kensch O, Felekyan S, Antonik M, Wöhrl BM, Restle T, Goody RS, Seidel CAM (2003) Proc Natl Acad Sci USA 100:1655–1660
48. Gaiduk A, Kühnemuth R, Antonik M, Seidel CAM (2005) ChemPhysChem 6:976–983
49. Zander C, Sauer M, Drexhage KH, Ko DS, Schulz A, Wolfrum J, Brand L, Eggeling C, Seidel CAM (1996) Appl Phys B 63:517–523
50. Eggeling C, Schaffer J, Seidel CAM, Korte J, Brehm G, Schneider S, Schrof W (2001) J Phys Chem A 105:3673–3679
51. Kühnemuth R, Seidel CAM (2001) Single Mol 2:251–254
52. Browning H, Hackney DD, Nurse P (2003) Nat Cell Biol 5:812–818
53. Koshioka M, Saski K, Masuhara H (1995) Appl Spectrosc 49:224–228
54. Felekyan S, Kühnemuth R, Kudryavtsev V, Sandhagen C, Becker W, Seidel CAM (2005) Rev Sci Instrum 76:083104
55. Busch KE, Brunner D (2004) Curr Biol 14:548–559
56. Kerres A, Vietmeier-Decker C, Ortiz J, Karig I, Beuter C, Hegemann J, Lechner J, Fleig U (2004) Mol Biol Cell 15:5255–5267
57. Striker G, Subramaniam V, Seidel CAM, Volkmer A (1999) J Phys Chem B 103:8612–8617

Anal. Chem. **2006,** *78,* 2039−2050

Single-Molecule Detection and Identification of Multiple Species by Multiparameter Fluorescence Detection

Jerker Widengren,*,†,‡ Volodymyr Kudryavtsev,‡,§ Matthew Antonik,§ Sylvia Berger,§,∥ Margarita Gerken,†,⊥ and Claus A. M. Seidel*,§

Department of Applied Physics, Royal Institute of Technology, Albanova University Center, 10691 Stockholm, Sweden, and Lehrstuhl für Molekulare Physikalische Chemie, Heinrich-Heine Universität Düsseldorf, Universitätsstrasse 1, D-40225 Düsseldorf, Germany

Two general strategies are introduced to identify and quantify single molecules in dilute solutions by employing a spectroscopic method for data registration and specific burst analysis, denoted multiparameter fluorescence detection (MFD). MFD uses pulsed excitation and time-correlated single-photon counting to simultaneously monitor the evolution of the eight-dimensional fluorescence information (fundamental anisotropy, fluorescence lifetime, fluorescence intensity, time, excitation spectrum, fluorescence spectrum, fluorescence quantum yield, distance between fluorophores) in real time and allows for selection of specific events for subsequent analysis. Using the multiple fluorescence dimensions, we demonstrate a dye labeling scheme of oligonucleotides, by which it is possible to identify and separate 16 different compounds in the mixture via their characteristic pattern by MFD. Such identification procedures and multiplex assays with single-molecule sensitivity may have a great impact on screening of species and events that do not lend themselves so easily to amplification, such as disease-specific proteins and their interactions.

Assays enabling detection and identification of minute amounts of biomolecules have attracted a strong interest in the last years. In the biomedical field, the ability to detect and identify disease-specific proteins in low numbers, specific for an incipient cancerous disease or a bacterial or viral infection, can provide detailed early-stage diagnoses. Likewise, technologies for sensitive, precise, and accurate detection of the genetic bases underlying onset of diseases and variations in drug responses (pharmacogenetics) and exposure to toxic agents (toxicogenetics) are likely to have a dramatic impact on future diagnostics and (individualized) pharmacological treatments.[1]

Such pharmacogenetical and toxicogenetical differences can often be attributed to single base-pair variations in the genome, so-called single-nucleotide polymorphisms, which are of particular interest to detect and identify.[2] Over the past decade, fluorescence-based techniques for molecular studies have shown remarkable progress. Fluorescence-based platforms have been developed for sensitive and high-throughput detection and identification of nucleic acids, proteins, and other biomolecules.[3] These platforms often take advantage of the specificity of naturally occurring enzymes and recognition molecules, such as in Taqman genotyping. By using molecular beacons, aptamers, and monoclonal antibodies, the molecules searched for can be presented to arrays of target molecules in a highly parallelized manner.[4]

The exquisite sensitivity of fluorescence detection has made detection, identification, and characterization of single molecules possible. This not only enables fundamental scientific studies of dynamic and conformational properties of single biomolecules,[5] it also provides a potential to establish molecular profiles, with an ultimate level of sensitivity, of species present at very low concentrations or quantities.[6−9]

For nucleic acid analysis, single-molecule techniques make it possible to circumvent amplification steps, thereby avoiding quantification difficulties due to small differences in efficiencies of amplifications from sample to sample and from one thermal cycle to another, as experienced, for example, for PCR-based assays. Several fluorescence-based approaches have also been reported for single-molecule DNA sequencing.[9−16] However, single-molecule sensitivity may have an even greater impact on

---

* Corresponding authors. E-mail: jerker@biomolphysics.kth.se.

† Royal Institute of Technology.

‡ Contributed equally.

§ Heinrich-Heine Universität Düsseldorf.

∥ Present address: Fluka Chemie GmbH, Industriestrasse 25, CH-9471 Buchs, Switzerland.

⊥ Present address: 3. Physikalisches Institut, Pfaffenwaldring 57, D-70550 Stuttgart, Germany.

(1) Ross, J. S.; Ginsburg, G. S. *DDT* **2002**, *7*, 859−64.

(2) Pfost, D. R.; Boyce-Jacino, M. T.; Grant, D. M. *Trends Biotechnol.* **2000**, *18*, 334−8.

(3) Eggeling, C.; Brand, L.; Ullmann, D.; Jager, S. *DDT* **2003**, *8*, 632−41.

(4) Shi, M. M. *Clin. Chem.* **2001**, *47*, 164−72.

(5) Moerner, W. E.; Fromm, D. P. *Rev. Sci. Instrum.* **2003**, *74*, 3597−619.

(6) Knemeyer, J.-P.; Marmé, N.; Sauer, M. *Anal. Chem.* **2000**, *72*, 3717−24.

(7) Anazawa, T.; Matsunaga, H.; Yeung, E. S. *Anal. Chem.* **2002**, *74*, 5033−8.

(8) Herten, D. P.; Tinnefeld, P.; Sauer, M. *Appl. Phys. B* **2000**, *71*, 765−71.

(9) Tinnefeld, P.; Sauer, M. *Angew. Chem., Int. Ed.* **2005**, *44*, 2642−71.

(10) Neuweiler, H.; Sauer, M. *Anal. Chem.* **2005**, *77*, 178A−85A.

(11) Scheffler, S.; Sauer, M.; Neuweiler, H. *Z. Phys. Chem.* **2005**, *219*, 665−78.

(12) Jett, J. H.; Keller, R. A.; Martin, J. C.; Marrone, B. L.; Moyzis, R. K.; Ratliff, R. L.; Seitzinger, N. K.; Shera, E. B.; Stewart, C. C. J. *J. Biomol. Struct. Dyn.* **1989**, *7*, 301−9.

(13) Werner, J. H.; Cai, H.; Jett, J. H.; Reha-Krantz, L.; Keller, R. A.; Goodwin, P. M. *J. Biotechnol.* **2003**, *102*, 1−14.

10.1021/ac0522759 CCC: $33.50

the screening of species and events that do not lend themselves so easily to amplification, such as disease-specific proteins and their interactions.[11,17]

In recent years, the characterization of molecules in single-molecule fluorescence detection measurements has step by step been established for the different fluorescence parameters. Spectral properties of absorption and fluorescence, $F(\lambda_A, \lambda_F)$,[18] fluorescence brightness and quantum yield, Φ_F,[19] fluorescence lifetime, τ,[20−26] and anisotropy, r,[27,28] are the five intrinsic properties of a fluorophore that are accessible in a multiparameter fluorescence detection (MFD) experiment (see Figure 1). These "chromophore parameters" can be deduced from the time-resolved detection of the five observables of the chromophore, which now serves as a tool to report on its local environment.

Considering molecular systems, changes in fluorescence parameters of a single coupled fluorophore sometimes do not provide enough information for molecular identification or for more detailed investigations of molecular interactions. Further information can be obtained on a single-molecule level by having more than one fluorophore per particle involved, thereby increasing the possibilities to determine stoichiometries and interactions of individual particles from photon densities and coincidences.[29,30] Moreover, the use of two fluorescing reporters also makes it possible to determine structural features of particles via Förster fluorescence resonance energy transfer (FRET).

In FRET, the energy from an excited donor fluorophore, D, is nonradiatively transferred to an acceptor fluorophore, A, by a strongly distance-dependent dipole−dipole coupling. Via the measured FRET efficiency, long-range molecular distance information can be provided, in a range of 20−100 Å, which is not covered by virtually any other solution technique.[31−33] FRET is taken advantage of in a number of screening procedures, providing information about changes in inter- and intramolecular distances that take place as an effect of the specific molecular interaction that is screened for.[34] When performed at the single-molecule level, FRET studies can yield information about heterogeneities in terms of conformations and conformational dynamics that are unavailable from ensemble measurements.[35] With a donor−acceptor distance approaching or exceeding 100 Å, the FRET efficiency typically is so small that the fluorescence from the acceptor can be determined only by additional direct excitation such as two-photon[36] or two-color excitation in a cw or alternating mode (ALEX).[37] Then the simultaneous presence of the two dyes, significant for an interaction or binding event, can be determined by cross-correlation,[36] colocalization,[38] or two-dimensional fluorescence intensity distribution analysis.[39]

Following the ideas of Förster, it is obvious that the fluorescence has multiple characteristic parameters that can be exploited to yield specific identification by a multiplex analysis.[40−43] In view

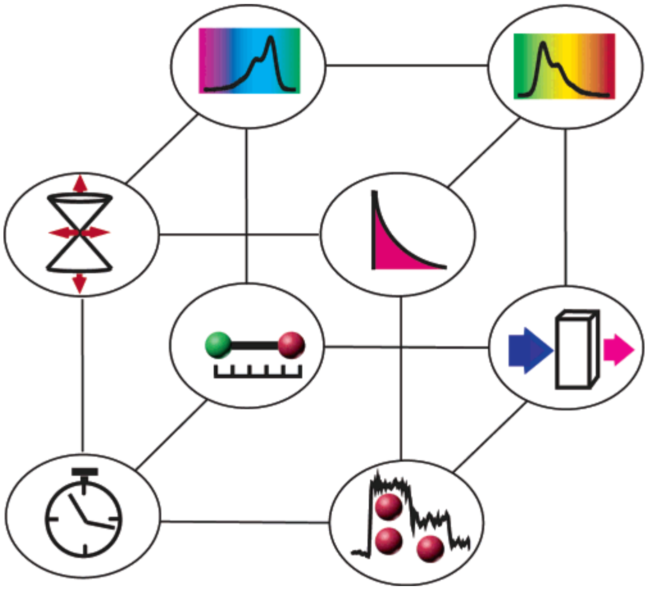

Figure 1. Multiple dimensions of the fluorescence. Sketches for fluorescence properties at the front side of the cube (starting at the upper left corner with clockwise rotation): fundamental anisotropy, fluorescence lifetime, fluorescence intensity, time; backside: excitation spectrum, fluorescence spectrum, fluorescence quantum yield, and distance between fluorophores.

---

(14) Sauer, M.; Angerer, B.; Ankenbauer, W.; Földes-Papp, Z.; Gobel, F.; Han, K. T.; Rigler, R.; Schulz, A.; Wolfrum, J.; Zander, C. *J. Biotechnol.* **2001**, *86*, 181−201.

(15) Dörre, K.; Brakmann, S.; Brinkmeier, M.; Han, K. T.; Riebeseel, K.; Schwille, P.; Stephan, J.; Wetzel, T.; Lapczyna, M.; Stuke, M.; Bader, R.; Hinz, M.; Seliger, H.; Holm, J.; Eigen, M.; Rigler, R. *Bioimaging* **1997**, *5*, 139−52.

(16) Braslavsky, I.; Hebert, B.; Kartalov, E.; Quake, S. R. *Proc. Natl. Acad. Sci. U.S.A.* **2003**, *100*, 3960−4.

(17) Sauer, M.; Zander, C.; Müller, R.; Ullrich, B.; Drexhage, K. H.; Kaul, S.; Wolfrum, J. *Appl. Phys.* **1997**, *65*, 427−31.

(18) Tamarat, P.; Maali, A.; Lounis, B.; Orrit, M. *J. Phys. Chem.* **2000**, *104*, 1−16.

(19) Kask, P.; Palo, K.; Ullmann, D.; Gall, K. *Proc. Natl. Acad. Sci. U.S.A.* **1999**, *96*, 13756−61.

(20) Zander, C.; Sauer, M.; Drexhage, K. H.; Ko, D. S.; Schulz, A.; Wolfrum, J.; Brand, L.; Eggeling, C.; Seidel, C. A. M. *Appl. Phys. B* **1996**, *63*, 517−23.

(21) Edman, L.; Mets, Ü.; Rigler, R. *Proc. Natl. Acad. Sci. U.S.A.* **1996**, *93*, 6710−5.

(22) Maus, M.; Cotlet, M.; Hofkens, J.; Gensch, T.; De Schryver, F. C.; Schaffer, J.; Seidel, C. A. M. *Anal. Chem.* **2001**, *73*, 2078−86.

(23) Bowen, B. P.; Scruggs, A.; Enderlein, J.; Sauer, M.; Woodbury, N. *J. Phys. Chem. A* **2004**, *108*, 4799−804.

(24) Enderlein, J.; Sauer, M. *J. Phys. Chem. A* **2001**, *105*, 48−53.

(25) Tellinghuisen, J.; Goodwin, P. M.; Ambrose, W. P.; Martin, J. C.; Keller, R. A. *Anal. Chem.* **1994**, *66*, 64−72.

(26) Enderlein, J.; Goodwin, P. M.; van Orden, A.; Ambrose, W. P.; Erdmann, R.; Keller, R. A. *Chem. Phys. Lett.* **1997**, *270*, 464−70.

(27) Ha, T.; Laurence, T. A.; Chemla, D. S.; Weiss, S. *J. Phys. Chem. B* **1999**, *103*, 6839−50.

(28) Schaffer, J.; Volkmer, A.; Eggeling, C.; Subramaniam, V.; Striker, G.; Seidel, C. A. M. *J. Phys. Chem. A* **1999**, *103*, 331−6.

(29) Schmidt, T.; Schütz, G. J.; Gruber, H. J.; Schindler, H. *Anal. Chem.* **1996**, *68*, 4397−401.

(30) Weston, K. D.; Dyck, M.; Tinnefeld, P.; Muller, C.; Herten, D. P.; Sauer, M. *Anal. Chem.* **2002**, *74*, 5342−9.

(31) Lilley, D. M. J.; Wilson, T. J. *Curr. Opin. Chem. Biol.* **2000**, *4*, 507−17.

(32) Selvin, P. R. *Nat. Struct. Biol.* **2000**, *7*, 730−4.

(33) van der Meer, B. W.; Cooker, G.; Chen, S. Y. *Resonance Energy Transfer: Theory and Data*; VCH Publishers: New York, 1994.

(34) Karlstrom, A.; Nygren, P. A. *Anal. Biochem.* **2001**, *295*, 22−30.

(35) Ha, T. *Methods* **2001**, *25*, 78−86.

(36) Heinze, K. G.; Koltermann, A.; Schwille, P. *Proc. Natl. Acad. Sci. U.S.A.* **2000**, *97*, 10377−82.

(37) Kapanidis, A. N.; Laurence, T. A.; Lee, N. K.; Margeat, E.; Kong, X. X.; Weiss, S. *Acc. Chem. Res.* **2005**, *38*, 523−33.

(38) Lacoste, T. D.; Michalet, X.; Pinaud, F.; Chemla, D. S.; Alivisatos, A. P.; Weiss, S. *Proc. Natl. Acad. Sci. U.S.A.* **2000**, *97*, 9461−6.

(39) Kask, P.; Palo, K.; Fay, N.; Brand, L.; Mets, Ü.; Ullmann, D.; Jungmann, J.; Pschorr, J.; Gall, K. *Biophys. J.* **2000**, *78*, 1703−13.

(40) Förster, T. *Fluoreszenz organischer Verbindungen*, Vandenhoeck & Ruprecht: Göttingen, Germany, 1951.

(41) Förster, T. *Ann. Phys.* **1948**, *2*, 55−75.

(42) Lakowicz, J. R. *Principles of Fluorescence Spectroscopy*, 2nd ed.; Kluwer Academic/Plenum Publishers: New York, 1999.

(43) Valeur, B. *Molecular Fluorescence: Principles and Applications*; Wiley-VCH Verlag: Weinheim, Germany. 2002.

of the additional information that can be extracted from a molecule having two or more fluorophores coupled to it, it is reasonable to add additional fluorescence dimensions to the five "chromophore parameters" stated above. With reference to Figure 1, we argue that the fluorescence parameter space can under appropriate conditions be considered to be at least eight-dimensional, adding three "system/environmental parameters" [(fluorophore) stoichiometry, (fluorophore) coupling, and time (at time scales other than that of excitation and emission to and from the excited singlet state)] to the above five "chromophore" parameters. It is noteworthy, that the two dyes can interfere with the fluorescence of one another by time-dependent intrinsic (e.g., transitions to and from photophysical states other than the singlet ground and excited states) or extrinsic (e.g., quenching or other chemical reactions influencing the fluorescence) processes.

Given that the FRET efficiency is reflected in several of the fluorescence parameters of the donor and acceptor fluorophores, a multidimensional and simultaneous registration of the fluorescence parameters from both the fluorophores can therefore increase both precision and accuracy. Moreover, since local effects also influence the fluorescence properties of the fluorophores, a multidimensional registration of the fluorescence can increase the certainty with which differences in the measured parameters due to true changes in the FRET efficiency and the interdye distances can be distinguished from differences due to local effects.[44,45] MFD has recently been successfully applied at the single-molecule level to study heterogeneities in conformations and conformational dynamics of HIV-1 reverse transcriptase:primer/template complexes[46] as well as to reveal a dynamic equilibrium between closed and open forms of the SNARE protein syntaxin-1, with possible implications for the regulation of membrane fusion of synaptic vesicles.[47]

The aim of this study is not to deliver a detailed analysis of specific molecular dynamic processes. Rather, it presents an investigation to what extent FRET-active compounds can be identified on the single-molecule level utilizing MFD and the differences in the detected fluorescence parameters of the molecules. It has previously been shown that single fluorescently labeled mononucleotides, with a specific fluorophore labeled to each of four different types of mononucleotides, can be detected and identified using spectrally resolved time-correlated single-photon counting.[48]

Here, we combine single-molecule identification based on fluorophore label identity with identification based on differences in intramolecular distances (donor-to-acceptor distances). Single molecules are analyzed, as they are freely diffusing in to and out of a confocal detection volume in a homogeneous sample. This approach offers both advantages and disadvantages, compared to the detection of surface-immobilized molecules. On one hand, the investigated molecules undertake different trajectories through the detection volume, which leads to a distribution of both the experienced excitation intensities and the interrogation times. This generates a variation of the brightness and duration of the fluorescence bursts, and many fluorescence bursts are too small to unequivocally be identified as a single-molecule event. MFD, including burst detection and subsequent offline data analysis, is useful in obtaining a sample survey, based only on those single-molecule events that have a long pathway through the detection volume.[49] The information content, in terms of the number of fluorescence photons detected per molecule, is limited by the dwell times, which typically cannot be extended maximally, until the fluorophore marker(s) eventually is (are) bleached. The great advantage of this homogeneous assay format is very good statistics on the investigated sample with several thousands of analyzed molecules, which is easily obtained. Moreover, for surface-immobilized molecules, evidently no information on the diffusion properties of the investigated molecules can be obtained. In addition, in an inhomogeneous assay, molecular and fluorescence marker properties can be significantly influenced by the immobilization itself. Immobilization also does not fulfill the demand for single-molecule detection and identification of molecules without the need for prior separation or manipulation steps. However, the MFD approach presented here is also fully employable and useful for a wide range of molecules, regardless whether immobilization is used or not.

In this study, 12 identical oligonucleotides, differing in the combination of dyes labeled to them, but also in the distance between the two dyes, were measured separately at the single-molecule level. To simulate a mixture measurement, the results of the burstwise analysis, which contain the fluorescence parameters for each molecule of all 12 species, were combined into a single data set. This postmeasurement mixing is possible because, in single-molecule measurements, the burst events are independent of each other, and the order of the events plays no role in the analysis. We introduce two different approaches for how individual molecules among samples of 12 differently labeled oligonucleotides can be identified. They both rely on sequential separations in different two-dimensional parameter space projections, or along several one-dimensional parameter axes.

In the first approach, a graphical analysis is performed to display the MFD features visually. The starting point is to arrange all detected molecules into a series of multidimensional histograms, based on the measured fluorescence parameters from each individual molecule. Within the total collection of detected molecules, and from the differences in the fluorescence parameters detected among the molecules, we show how it is possible to separate and identify the different types of oligonucleotides. Also shown is the possibility to discriminate against impurities, free dyes, and oligonucleotides labeled only with a single donor dye, yielding all in all 16 different compounds that are identified.

In the second approach, a mathematical procedure is applied that converts the above stepwise graphical analysis into a one-step computer algorithm. We introduce an identification algorithm that compares the measured fluorescence parameters for each detected molecule with the probability distributions for the

---

(44) Eggeling, C.; Berger, S.; Brand, L.; Fries, J. R.; Schaffer, J.; Volkmer, A.; Seidel, C. A. M. *J. Biotechnol.* **2001**, *86*, 163−80.

(45) Kühnemuth, R.; Seidel, C. A. M. *Single Mol.* **2001**, *2*, 251−4.

(46) Rothwell, P. J.; Berger, S.; Kensch, O.; Felekyan, S.; Antonik, M.; Wöhrl, B. M.; Restle, T.; Goody, R. S.; Seidel, C. A. M. *Proc. Natl. Acad. Sci. U.S.A.* **2003**, *100*, 1655−60.

(47) Margittai, M.; Widengren, J.; Schweinberger, E.; Schröder, G. F.; Felekyan, S.; Haustein, E.; König, M.; Fasshauer, D.; Grubmüller, H.; Jahn, R.; Seidel, C. A. M. *Proc. Natl. Acad. Sci. U.S.A.* **2003**, *100*, 15516−21.

(48) Lieberwirth, U.; Arden-Jacob, J.; Drexhage, K. H.; Herten, D. P.; Müller, R.; Neumann, M.; Schulz, A.; Siebert, S.; Sagner, G.; Klingel, S.; Sauer, M.; Wolfrum, J. *Anal. Chem.* **1998**, *70*, 4771−9.

(49) Fries, J. R.; Brand, L.; Eggeling, C.; Köllner, M.; Seidel, C. A. M. *J. Phys. Chem. A* **1998**, *102*, 6601−13.

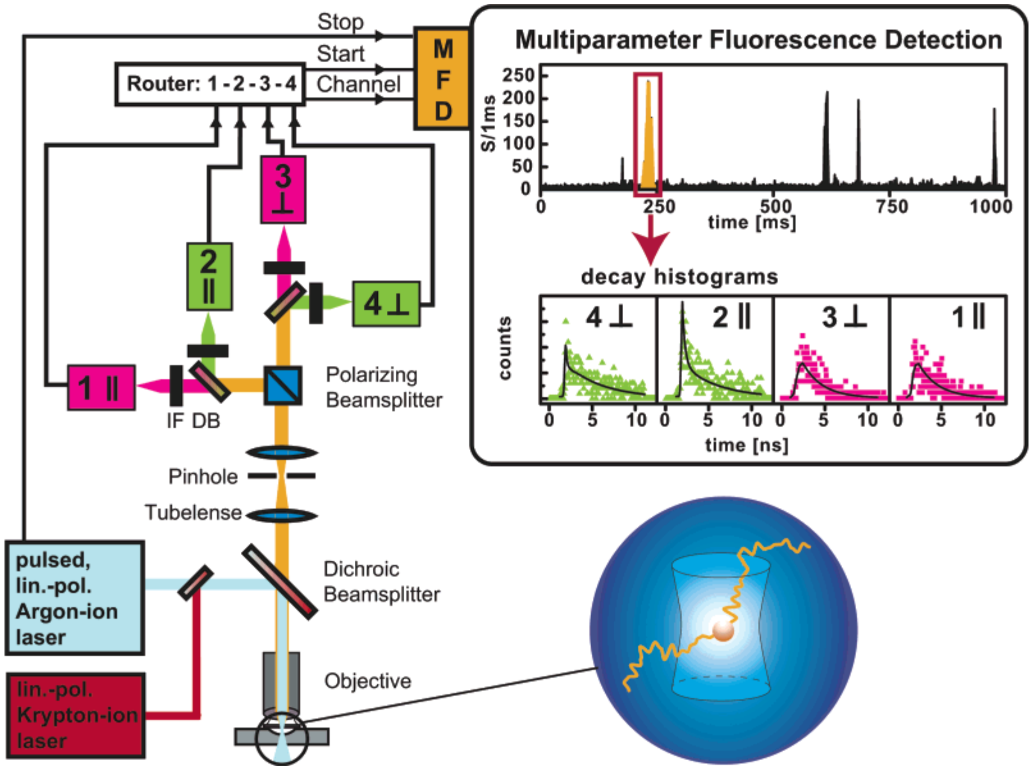

Figure 2. Four-channel confocal setup for simultaneous detection of spectral range, λ_F fluorescence intensity *S*, lifetime τ, anisotropy *r*. Abbreviations: IF, interference filter; DB, dichroic beam splitter.

corresponding parameters for all different possible species. The comparison is performed for several independent parameters or parameter combinations. The approach can be shown to offer fast, stable, and reliable species identification and to determine concentration profiles of molecular species with high fidelity.

Based on these results, we suggest confocal single-molecule spectroscopy using MFD as a useful tool for qualitative analysis revealing the presence of multiple distinct molecules in a sample. This study demonstrates the precision and accuracy with which single molecules can be detected, identified, and analyzed and with which concentration profiles of multiple molecular species can be determined, with possible implications for diagnostics of profiles of different molecules, their presence and interactions.[9−11]

METHODS AND MATERIALS

Setup. The confocal microscopy arrangement used in this study is depicted in Figure 2. The setup has basic features similar to those previously presented for applications of ultrasensitive fluorescence spectroscopy.[50,51] Freely diffusing molecules are excited by a pulsed, linearly polarized argon ion laser emitting at 514 nm (Sabre, Coherent, Palo Alto, CA) with a repetition rate of 73 MHz and an excitation power of 558 μW. In addition, there is the option to use a linear polarized krypton ion laser emitting at 647 nm (Sabre, Coherent) for two-color excitation experiments. The two lasers are not yet synchronized. After reflection by a dual-band dichroic mirror (DCLP510, AHF Analysentechnik), the laser beam is focused by a microscope objective (Olympus 60×, NA 1.2, water immersion). The fluorescence is collected and then refocused by the same objective to the image plane, where a pinhole is placed (radius 100 μm). From a FCS diffusion time of free rhodamine 6G (Rh6G) dye of $\tau_D = 256$ μs, the detection volume can be estimated to be ~1 fL. After passage through the pinhole, the fluorescence is separated by a polarizing beam splitter, based on its direction of polarization with respect to that of the laser beam. The fluorescence is then divided by a dichroic beam splitter (510DCLX, AHF Analyzentechnik) into the fractions originating from the acceptor [cyanine 5 (Cy5) or BODIPY650 (BP650/665)] and donor (cyanine 3 (Cy3) or Rh6G fluorophores). Subsequently, band-pass filters are used (HQ730/140 by AHF Analyzentechnik for Cy5 and BP650/665; HQ575/70 by AHF Analyzentechnik for Cy3, Rh6G) to discriminate the two fractions of the collected fluorescence from scattered laser light. Each of the fractions of the fluorescence light is then detected by an avalanche photodiode (SPCM AQ-141, EG&G Vaudreuil, Quebec, Canada), the output pulses of which are processed online by a PC-BIFL-card with a routing unit (SPC 432 Becker&Hickl GmbH, Berlin, Germany) in the MFD mode.

MFD. The data registration and processing of MFD has been described in detail.[44] In brief, using the setup depicted in Figure 2, each detected photon can be characterized by four parameters: (i) spectral range, λ_F, of the detected fluorescence (green or red); (ii) the polarization of the signal photon (parallel or perpendicular) with respect to the linear polarization of the excitation laser; (iii) the arrival time of the signal photon relative to the incident laser pulse; and (iv) the interphoton time, Δt, to the preceding signal photon.

---

(50) Rigler, R.; Mets, Ü.; Widengren, J.; Kask, P. *Eur. Biophys. J.* **1993**, *22*, 169−75.

(51) Eggeling, C.; Fries, J. R.; Brand, L.; Günther, R.; Seidel, C. A. M. *Proc. Natl. Acad. Sci. U.S.A.* **1998**, *95*, 1556−61.

A single molecule diffusing through the laser focus generates a burst of fluorescence photons. Thus, a single-molecule event (burst) can be separated from background via small interphoton times. In addition to a criterion based on a maximum interphoton time of 0.0493 ms, bursts also had to contain a minimum total number of detected photons, here set to 120, to be registered as a molecular event. Once a single-molecule event is identified, average green and red count rates of the burst, S_G and S_R, are calculated by dividing the number of registered photons by the individual burst duration times. Arrival times of the photons in the selected burst are used to generate fluorescence decay histograms for each of the four detectors (green parallel, $G_{\|}$, green perpendicular, $G_{\perp}$, red parallel, $R_{\|}$, red perpendicular, $R_{\perp}$). With further analysis, the parameters lifetime, τ, and anisotropy, r, for each spectral range are determined.[28] The anisotropy was primarily analyzed in the green range. The steady-state anisotropy is formally given by

$$r_G = \int_0^{\infty} r_G(t) F_G(t)\, dt \Big/ \int_0^{\infty} F_G(t)\, dt$$

where

$$r_G(t) = \frac{F_{G\|}(t) - F_{G\perp}(t)}{F_{G\|}(t) + 2F_{G\perp}(t)}$$

is the time-dependent anisotropy, and where $F_{G\|}(t)$ and $F_{G\perp}(t)$ are the donor fluorescence detected with a polarization parallel and perpendicular to that of the excitation light, respectively. $F_G(t) = F_{G\|}(t) + 2F_{G\perp}(t)$ is the total detected donor fluorescence intensity. In this study, the anisotropy of the fluorescence detected from a single molecule in the green channels was determined as by Schaffer et al.,[28] from

$$r_G = \frac{GS_{G\|} - S_{G\perp}}{(1 - 3l_2)GS_{G\|} + (2 - 3l_1)S_{G\perp}}$$

where $S_{G\|}$ and $S_{G\perp}$ are the average donor fluorescence count rates detected within a burst, with a polarization parallel and perpendicular to that of the excitation light, respectively. Correction factors, $l_1 = 0.0308$ and $l_2 = 0.0368$ were applied in order to take into account mixing of polarizations by the microscope objective lenses.[52] $G = 0.964$ compensates for slightly different detection efficiencies in the two detection channels.

The signal registered in the green detection range was described by scattered light and fluorescence decay with a single component. Thereby the fluorescence lifetimes were calculated using a maximum likelihood estimator as described in refs 28 and 53, which has been shown to be statistically most efficient. The standard deviations of the obtained fluorescence lifetimes of ±15% are equivalent to the expected shot noise limit, if the registered photon numbers and the fractions of scattered light were considered.

The results of the MFD measurements were presented by plotting the frequency of occurrence of certain pairs of parameter values in two-dimensional histograms, where increasing frequency is coded by the gray-scale level. To use the full dynamic range of MFD and to show also minor populations of molecules, we present *Z*-magnified views with a single peak level above a specified level indicated in yellow (the specific level is given in the captions of Figures 4−9). Raw data from several measurement sessions were combined into a single complete measurement set for further analysis.

Sample. For our studies, a deoxyoligonucleotide N1 containing 27 nucleobases in a random sequence was synthesized using the standard phosphoamidite technology: 5′-d(TTG AAA ACG AGA GAG ACA TAA ACG ATC). The 5′-d of this deoxyoligonucleotide was labeled via a C6 amino link either with the *N*-hydroxysuccinimide ester of Cy3 (Amersham Pharmacia Biotech) or Rh6G (Molecular Probes, Eugene, OR) as donor dye. Using a postlabeling reaction, the acceptor dyes BP650/665 (Molecular Probes) or Cy5 (Amersham Pharmacia Biotech) were covalently attached to an 5′-C6-amino-2′d**T** at a defined position (with 9, 13, or 17 base pairs (bp) between the linked dyes) on the complementary deoxyoligonucleotide N2: 5′-d(GAT CGT TTA **T**GT C**T**C TC**T** CGT TTT CAA). The oligonucleotides were double HPLC-purified and additionally PAGE-purified. All synthesis and purification was done by IBA GmbH (Göttingen, Germany). Hybridization was performed in a buffer containing 180 mM NaCl, 12 mM sodium citrate, and 25 μM $MgCl_2$ (pH 7.5). To obtain the FRET-active molecules, complementary donor- and acceptor-labeled strands (N1 and N2) were mixed in a 1:1 ratio and slowly cooled from 95 to 20 °C. In all experiments, we used a sodium phosphate buffer with 180 mM NaCl, 10 mM NaH_2PO_4/Na_2HPO_4, and 400 μM sodium ascorbate (pH 7.5). The following 16 molecules were analyzed: Cy3−Cy5 (9, 13, or 17 bp), Cy3−BP650/665 (9, 13, or 17 bp), Cy3−oligonucleotide, Rh6G−Cy5 (9, 13, or 17 bp), Rh6G−BP650/665 (9, 13, or 17 bp), Rh6G−oligonucleotide, and two fluorescent impurities of unknown structures **I1** and **I2**.

RESULTS AND DISCUSSION

Spectrofluorometric and Time-Correlated Single-Photon-Counting (TCSPC) Measurements. The labeled single-stranded oligonucleotides were investigated in a spectrofluorometer (Jobin-Yvon Fluorolog 3) with respect to the excitation and fluorescence spectra of the dyes attached to them. The fluorescence lifetimes were investigated by TCSPC, performed by the MFD instrumentation (Figure 2) at concentrations of ~100 pM. In the TCSPC experiments, the donor (Rh6G, Cy3) and the acceptor (Cy5, BP650/665) dyes were excited by the argon ion (514 nm) and the krypton ion (647 nm) laser, respectively. The measured fluorescence lifetimes of the dyes and their maximum absorption and emission wavelengths are given in Table 1 and the spectra in Figure 3.

MFD Measurements and Strategy for Systematic Selection of Species. The different oligonucleotides were measured and analyzed burstwise with respect to all their fluorescence parameters on the single-molecule level by MFD, as described in Methods and Materials. For each type of dye-labeled oligonucleotide, the detected molecules were measured and sorted into a multidimensional cumulative histogram, based on the determined

---

(52) Koshioka, M.; Saski, K.; Masuhara, H. *Appl. Spectrosc.* **1995**, *49*, 224−8.

(53) Brand, L.; Eggeling, C.; Zander, C.; Drexhage, K. H.; Seidel, C. A. M. *J. Phys. Chem. A* **1997**, *101*, 4313-21.

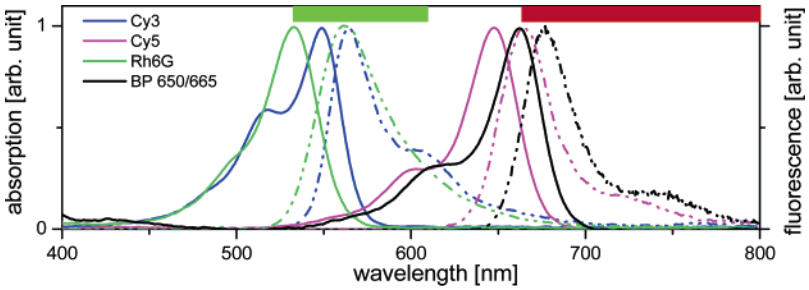

Figure 3. Absorption (solid line) and emission (dashed line) spectra of Rh6G, Cy3, Cy5, and BP650/665 dyes. Bars on the top indicate transmission range of the filters for single-molecule spectroscopy.

Table 1. Lifetimes and Abs/Flu Wavelengths

dye label at oligonucleotide	τ (ns)[a]	λ_{Abs}/λ_F (nm)	spectral detection (nm)
Rh6G	4.0	534/564	535−605
Cy3	0.8[b]	550/565	535−605
BP650/665	4.3	663/678	665−800
Cy5	1.0	649/665	665−800

[a] Fluorescence parameters of the free dyes are given. [b] The experimentally measured fluorescence lifetimes using the latest avalanche photodiodes (APDs) of the Series "AQR" are increased due to a count rate-dependent jitter by ~10%. The listed τ values are corrected for this effect, but the τ-histograms shown in Figures 4−9 were not corrected for this effect. [c] Surprisingly the Cy3-labeled DNA samples contain large amounts of a fluorescent species with a fluorescence lifetime of 1.5 ns. It is classified as an impurity because it is not quenched by FRET as the species with $\tau = 0.8$ ns. It is assumed that the species with $\tau = 1.5$ ns are not attached to the oligonucleotide.

fluorescence parameters. The fluorescence bursts from all the different oligonucleotides were then arranged into one joint histogram.

In Figure 4, a two-dimensional projection of this histogram is shown, where the fluorescence bursts from all the measured compounds have been arranged with respect to their count rates in the green and red emission ranges, S_G and S_R.

Even though recording takes place at the single-molecule level, which should in principle provide the possibility to reveal subpopulations within an ensemble of molecules, it is clear that at least a characterization based on only S_G and S_R is in this case not sufficient to identify the different subpopulations. From this histogram, it is also not possible to extract from how many different compounds the data have been recorded. To demonstrate the full dynamic range of MFD, we present Z-magnified views with the last level indicated in uniform yellow (see Figures 4 and 6−9), which focuses the dynamic range of the gray scale to the border zones between the different populations.

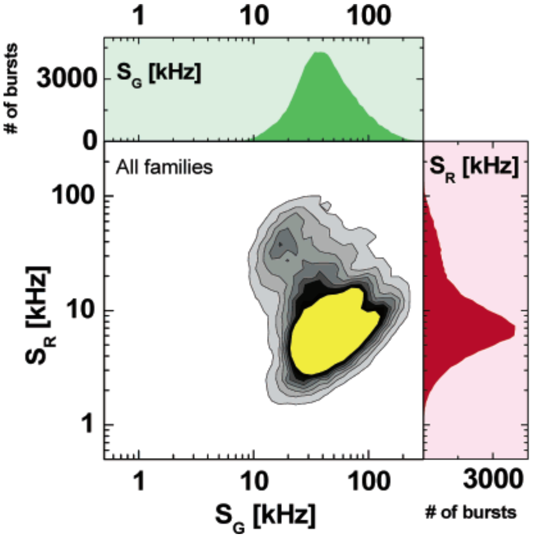

Figure 4. Cumulative histogram of all compounds. Green signal, S_G, is plotted versus red signal, S_R. Frequency is coded by gray scale. To visualize small subpopulations, a Z-magnified view is presented, where all frequencies above 0.2 of the maximum are displayed in yellow as a single level. Total number of molecules $A_{total} = 92\,694$.

To better distinguish between the species, we follow a procedure where the subpopulations are identified based on a set of parameters and where a systematic selection of subpopulations within different ranges of the detected parameters will be performed in subsequent steps. The general rationale for this multistep selection procedure is that the different compounds differ distinctly from each other with respect to at least one measurable parameter or that combinations of parameter values can be used to enhance differences between compounds that do not differ distinctly with respect to a single parameter. In this study, differences between the compounds in rotational mobilities (characterized by different anisotropies, r_G, for free and labeled fluorophores), FRET efficiencies (different dye-to-dye distances reflected in S_G, S_R, τ_G, and τ_R), and differences due to the identities of the donor and acceptor dye labels (S_G, S_R, τ_G, τ_R), or differences in combinations of the parameters are exploited within the frame of this general strategy for systematic selection. As shown in Table 1, donor dyes (Rh6G, Cy3) and acceptor dyes (BP650/665, Cy5) with long and short fluorescence lifetimes, respectively, have been chosen for the green and the red spectral windows. Based on their characteristic fluorescence lifetimes, four distinct oligonucleotide families (Rh6G−BP650/665, Rh6G−Cy5, Cy3−BP650/665, Cy3−Cy5) with different DA distances have been studied.

Graphical MFD Analysis. Step 1: Selection in the r_G versus τ_G Parameter Plane. As a first step, the multidimensional cumulative histogram was projected onto a two-dimensional histogram, with the bursts sorted with respect to the measured fluorescence anisotropy, r_G, and the fluorescence lifetimes, τ_G, of their donor fluorophores ($r_G-\tau_G$ histogram). Given its formal expression (see Methods and Materials), it is clear that r_G will increase with shorter fluorescence lifetimes. This is illustrated in the $r_G-\tau_G$ histogram of Figure 5. For comparison, lines corresponding to mean rotational correlation times ρ of 0.2, 2.0, and 7.0 ns are included, which are calculated from the Perrin equation, $r_G = r_0/(1 + \tau/\rho)$, using a fundamental anisotropy $r_0 = 0.375$.

In view of the broad range of fluorescence lifetimes covered, the observed anisotropy, broadened by shot noise, is also very

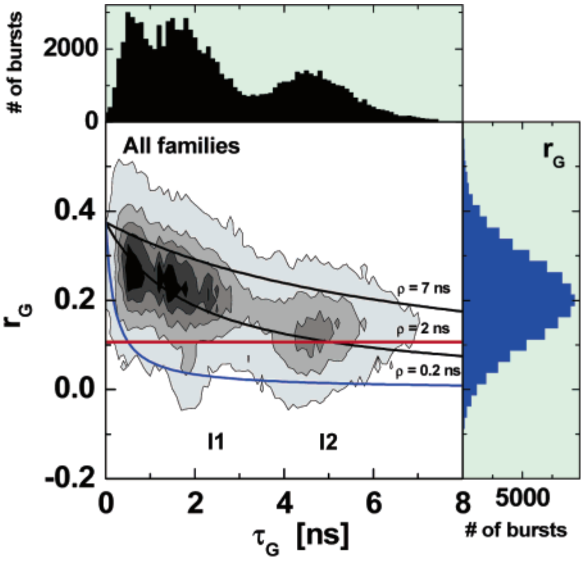

Figure 5. Green lifetime, τ_G, plotted versus anisotropy, r_G, together with an overlaid Perrin equation computed for three rotational correlation times (0.2, 2, 7 ns). Molecules under the red line were excluded from further analysis. Total number of molecules A_{total} = 92 628.

wide. The anisotropies of the major subpopulations consisting of the donor dyes linked to the oligonucleotides are well described by a mean rotational correlation time of $\rho = 2.0$ ns. However, there are two subpopulations, marked as **I1** and **I2**, with fluorescence lifetimes $\tau_G = 1.8$ and 4 ns, which have very small mean rotational correlation times of ~0.2 ns (blue line). The small rotational correlation time is evidence for the existence of free impurities, which emit in the green spectral range and are not subject to FRET-mediated quenching of their fluorescence.

Based on this, a limit was defined such that only labeled oligonucleotides with $r_G > 0.107$ (red line) were selected for further analysis. The highly rotationally mobile fluorescent impurities **I1** and **I2** could thus be sorted out with high certainty. Their rotational correlation times were short enough not to be attributed to the rotation of donor-labeled oligonucleotides, but rather to free dyes.

Generation of Characteristic Patterns. In the present qualitative analysis, we aim at detection of the presence of an individual subpopulation. For this, we generated characteristic patterns of different individual species of donor–acceptor-labeled oligonucleotides. These characteristic patterns guide the definition of the areas in various parameter planes as belonging to a particular species. We generated specific patterns for all two-dimensional parameter planes by analyzing the individual subpopulations separately. In addition to free dye molecules, fractions of molecules that are not labeled at all or that are not completely labeled remain in practically all labeling procedures. To show the features distinguishing fully labeled molecules from incompletely labeled ones, we refer to the cumulative histograms of the individual oligonucleotide species from which free dye molecules have been sorted out by use of the criterion of step 1. Panels A–C in Figure 6 show three typical two-dimensional histograms, with oligonucleotides labeled with Rh6G (donor) and Cy5 (acceptor) with different distances between the labeling sites. The measurements can be evaluated by depicting the ratios of their signal intensities detected in the green (S_G) divided by those in the red (S_R) wavelength range, S_G/S_R, along the ordinate, and their donor fluorescence lifetimes, τ_G, along the abscissa.

It can be seen from these $S_G/S_R-\tau_G$ histograms that the fractions of oligonucleotides that are not labeled with acceptor dyes can be clearly distinguished from those labeled with both dyes. For oligonucleotides that were labeled with both donor and acceptor dyes (DA-oligonucleotides), FRET-mediated quenching of the donor fluorescence and a concomitant FRET-sensitized fluorescence of the acceptor dye will occur when the donor dye is excited by laser light at 514 nm. With higher FRET efficiencies, increasingly lower ratios of S_G/S_R and shorter τ_G appear. DA-oligonucleotides accumulate in distinct fractions with lower S_G/S_R and shorter τ_G, well separable from oligonucleotides, having just a donor fluorophore labeled to them (D-oligonucleotides). Acceptor-labeled oligonucleotides (A-oligonucleotides) are practically not excited at an excitation wavelength of 514 nm and are thus not detectable in the current experiment.

Further, for DA-oligonucleotides labeled with the same donor–acceptor dye pair, the positions of the population of DA-oligo-

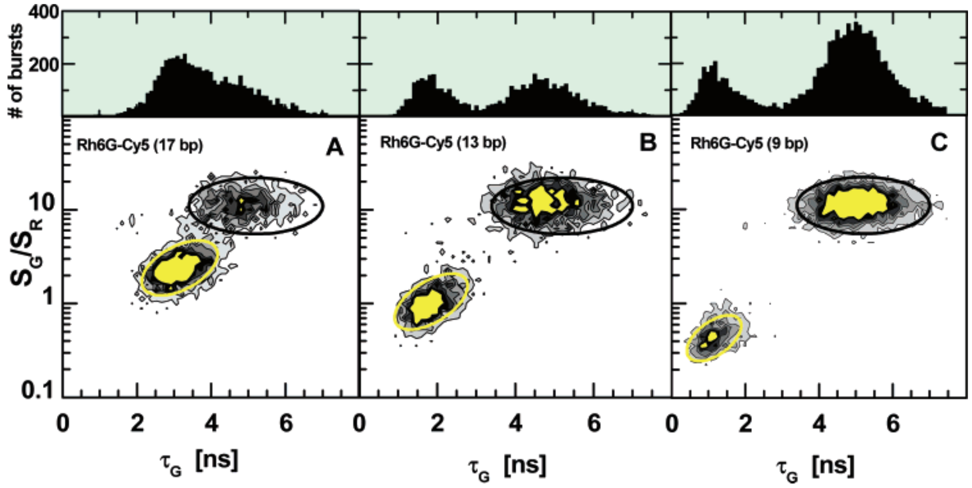

Figure 6. Green lifetime, τ_G, plotted versus fluorescence count rate ratio, S_G/S_R, for individual populations of oligos labeled with Rh6G (donor) and Cy5 (acceptor) with different distances between the labeling sites [17 (A), 13 (B), and 9 base pairs (C)]. Black ellipses show patterns for donor-only-labeled oligos, yellow ellipses for oligos labeled with both donor and acceptor. Z-Magnified view, where all frequencies above 0.4 of the maximum are displayed in yellow as a single level. Total number of molecules: (A) A_{total} = 5856, (B) A_{total} = 4768, and (C) A_{total} = 9804.

nucleotides in the histograms differ distinctly depending on the dye-to-dye distance (distances between the two dyes in Figure 6A, B, and C of 17, 13, and 9 base pairs, respectively). The differences of the individual histograms should thus provide patterns from which it is possible to separate D-oligonucleotides from DA-oligonucleotides and to distinguish between the DA-oligonucleotides in the joint histograms via their specific FRET efficiencies defined by the distances between the labeling sites of their donor and acceptor fluorophores.

For this graphical analysis, it is sufficient to approximate the characteristic patterns by variable ellipses with characteristic colors for the four families of DA oligonucleotides [Rh6G−BP650/665 (magenta), Rh6G−Cy5 (yellow), Cy3−BP650/665 (orange), Cy3−Cy5 (olive)] and for the D-oligonucleotides of Rh6G and Cy3 (black). The size of these elliptic patterns in the contour plots is defined by the area in which the frequency is 20% of the maximum value or higher. For histograms containing a mixture of species, such elliptic patterns guide the definition of areas within which the different individual species are confined.

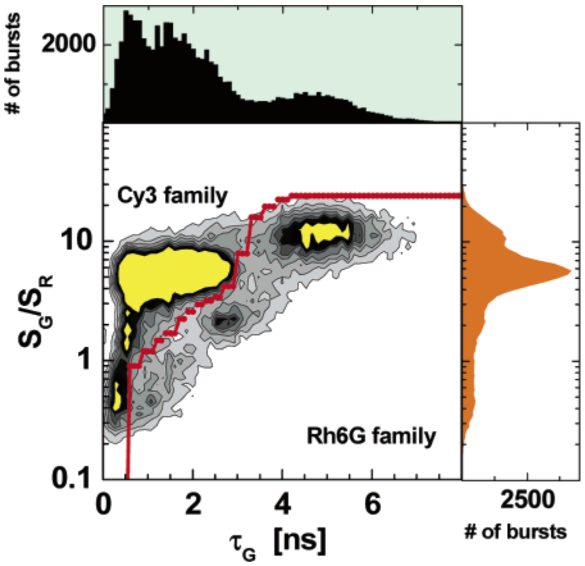

Figure 7. Green lifetime, τ_G, plotted versus fluorescence signal ratio, S_G/S_R, for all measured compounds. Red line shows separation between populations of oligos labeled with Rh6G and Cy3 dyes. *Z*-Magnified view, where all frequencies above 0.2 of the maximum are displayed in yellow as a single level. Total number of molecules A_{total} = 74 758.

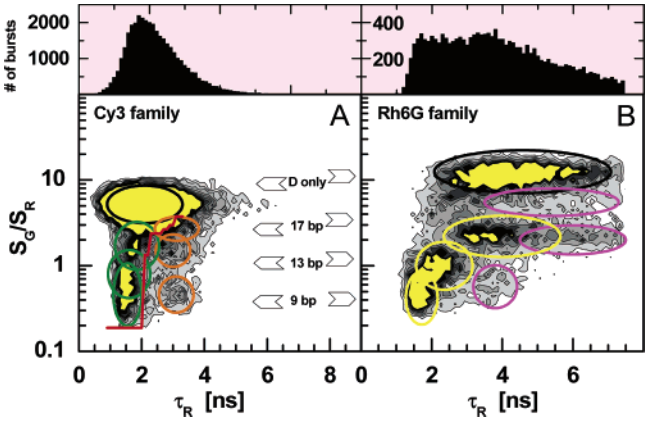

Figure 8. Red decay time, τ_R, plotted versus fluorescence signal ratio, S_G/S_R, for oligos, labeled with Cy3 (A) and Rh6G (B) donor dyes. Green ellipses indicate patterns for Cy3−Cy5 populations; orange, Cy3−BP650/665 populations; yellow, Rh6G−Cy5 populations; pink, Rh6G−BP650/665 populations; black, donor-only-labeled oligos. Red line shows separation between Cy3−BP650/665 and Cy3−Cy5 populations. *Z*-Magnified view, where all frequencies above 0.075 of the maximum are displayed in yellow as a single level. Total number of molecules: (A) A_{total} = 37 275; (B) A_{total} = 14 398.

Step 2: Selection in the S_G/S_R versus τ_G Parameter Plane. After separation of free dyes from the mixture in step 1 above, differences in the macroscopic fluorescence properties of the fluorophores (Table 1) were exploited in sequential steps to separate the subpopulations of the remaining oligonucleotides. First, the oligonucleotides were separated into two main groups based on the differences in the intrinsic fluorescence lifetimes of their donor fluorophores [Rh6G (4 ns) and Cy3 (0.8 ns)]. This was performed by displaying the detected oligonucleotides in a S_G/S_R versus τ_G histogram. As mentioned above, higher efficiencies of FRET generate increasingly lower ratios of S_G/S_R and shorter τ_G. However, irrespective of the degree of quenching of the donor dye due to FRET, oligonucleotides labeled with Rh6G can be separated from those labeled with Cy3. This separation is possible by virtue of the distinct differences in the measured τ_G between the molecules, which follows from the prominent difference in the intrinsic lifetimes of the two donor fluorophores. The separation of Cy3-labeled oligonucleotides from their Rh6G-labeled counterparts is indicated by a red line in Figure 7.

Step 3: Selection in the S_G/S_R versus τ_R Parameter Plane. Following the separation of oligonucleotides based on the intrinsic donor fluorescence lifetimes (Figure 7), oligonucleotides labeled with either Cy3 or Rh6G as donors were separated with respect to what acceptor dye was attached to them. This separation step is possible due to a large difference in the intrinsic lifetimes of the two acceptor dyes Cy5 (1.0 ns) and BP650/665 (4.3 ns) (see Table 1). In Figure 8A and B, the histograms selected based on the different intrinsic donor lifetimes of the Cy3- and Rh6G-labeled oligonucleotides according to step 2 are each projected in a plane defined by the ratio S_G/S_R and the measured decay time in the red detection channels, τ_R. Here, a clear distinction can be seen for those oligonucleotides labeled with BP650/665 (4.3 ns) as the acceptor dye from those with Cy5 (1.0 ns). Disregarding the effect of the duration of the laser excitation pulses (which is subject to deconvolution), the measured acceptor fluorescence intensity is a convolution product of the donor and acceptor fluorescence intensity decay following a Dirac pulse, i.e.,

$$F_A(t) \propto \int_0^t \exp(-t'/\tau_D)\,\exp(-(t-t')/\tau_A)\,dt'$$

for monoexponential fluorescence decays, where τ_D and τ_A are the lifetimes of the donor and acceptor dyes, respectively. In contrast to the determination of the donor fluorescence lifetime from the complete fluorescence response curve, it is at present sufficient that only the decaying part of the complex fluorescence response of the acceptor is judged by a single-exponential decay without deconvolution having a characteristic signal decay time, τ_R.[54] Short D−A distances generate short donor lifetimes and, thus, also a shorter time over which excitation by energy transfer to the acceptor dye can take place. Consequently, for oligonucle-

---

(54) Eggeling, C.; Schaffer, J.; Seidel, C. A. M.; Korte, J.; Brehm, G.; Schneider, S.; Schrof, W. *J. Phys. Chem. A* **2001**, *105*, 3673−9.

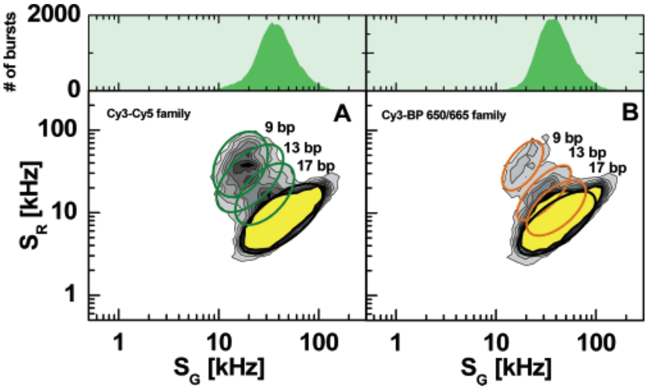

Figure 9. Green fluorescence signal, S_G, plotted versus red signal, S_R, for Cy3−Cy5 populations (A) and Cy3−BP650/665 populations (B). Green ellipses indicate patterns for Cy3−Cy5 populations and orange, Cy3−BP650/665 populations. *Z*-Magnified view, where all frequencies above 0.06 of the maximum are displayed in yellow as a single level. Total number of molecules: (A) A_{total} = 29 035; (B) A_{total} = 29 306.

otides with shorter D−A distances, typically a shorter time interval passes after the excitation pulse until the acceptor dye is excited and subsequently fluoresces, although the intrinsic fluorescence lifetime of the acceptor remains the same. This effect can most clearly be seen for those oligonucleotides having Rh6G as a donor dye (Figure 8B), since the absolute changes in fluorescence lifetime upon FRET are larger with Rh6G than with Cy3, due to the shorter intrinsic fluorescence lifetime of Cy3. Likewise, with a relatively short intrinsic fluorescence lifetime of the acceptor dye, the relative effect of convolution by the donor fluorescence decay is more prominent and distinct, as can be seen for the Rh6G−Cy5-labeled oligonucleotides in Figure 8B. Considering the specific patterns, all DA combinations of the Rh6G family can easily be distinguished, which allows for the simultaneous detection of seven oligonucleotides: Rh6G−Cy5 (9, 13, and 17 bp), Rh6G−BP650/665 (9, 13, and 17 bp), and Rh6G−oligonucleotide (D-oligonucleotide).

Step 4: Selection in the S_R versus S_G Parameter Plane. As indicated in Figure 8A, a separation relying on D−A distances can be difficult when based solely on the S_G/S_R versus τ_R projection. Considering the Cy3 family, a substantial overlap of the oligonucleotides with different D−A distances can be noticed. For the case of overlap between populations of different species, additional projections can be used to increase the specificity of the separation of the different species from each other. In Figure 9A and B, the projections of the Cy3−Cy5 and Cy3−BP650/665 populations, both included in Figure 8A, are after separation (indicated by the red line in Figure 7A) plotted along S_G and S_R. In this case, this projection provides an additional criterion, enabling an improved separation of the oligonucleotides labeled with Cy3 as a donor and either Cy5 (olive) or B650 (orange) as an acceptor, based on their D−A distances. In this way, the remaining seven oligonucleotides are identified: Cy3−Cy5 (9, 13, and 17 bp), Cy3−BP650/665 (9, 13, and 17 bp), and Cy3−oligonucleotide (D-oligonucleotide).

Quantitative Identification of the Detected Molecules Using a Pattern Recognition Algorithm of Fluorescence Parameter Sets. The visual identification procedure, performed in sequential steps, as outlined above, forms the principal basis of an automated identification procedure that can determine the relative fractions of each species. The accuracy of such an approach would ideally be limited only by the ability to identify properly single-molecule bursts for each species in the data. In the following section, we present a procedure, which exploits the multidimensionality of the measured data and which lends itself well for fast, stable, and reliable species identification of the detected species.

Procedure. The core of the procedure is the estimation of the probability, $\Psi(m|\{\upsilon_{k\ \text{exp}}\}_\alpha)$. It states the probability that a detected molecule α, possessing a set of *K* independent experimentally determined fluorescence parameter values, $\{\upsilon_{1\ \text{exp}}... \upsilon_{K\ \text{exp}}\}$, belongs to species *m* out of *N* different species with the index $n = 1$ to *N*. In the *K*-dimensional set $\{\upsilon_{k\ \text{exp}}\}_\alpha$, each of the *K* values corresponds to a unique fluorescence parameter, e.g., lifetime, anisotropy, etc.

As an intermediate step in determining Ψ, it is first necessary to determine a set of $K \times N$ probability distributions, $\{P_{k,m}(\upsilon_k), k = 1 \text{ to } K, n = 1 \text{ to } N\}$, which describes the probability that a molecule known to be of species *m* has a value for the *k*th fluorescence parameter given by υ_k (or more precisely, has a value that falls into a bin centered around υ_k). In this report, the $P_{k,m}(\upsilon_k)$ distributions are generated from histograms obtained from the same MFD data used to determine the characteristic patterns above (for example, see 1D projections in Figure 6), whereby the DA-oligonucleotides were first separated from the D-oligonucleotides and impurity species. The relevant histograms are normalized such, that for each species *m* and parameter *k*, $\sum_\upsilon P_{k,m}(\upsilon_k) = 1$ (remembering that the values for υ are restricted to a finite set of bin centers). The probability $\Psi(m|\{\upsilon_{k\ \text{exp}}\}_\alpha)$ is calculated from the set of distributions $\{P_{k,m}(\upsilon_{k\ \text{exp}})\}$ as follows:

$$\Psi(m|\{\upsilon_{k\text{exp}}\}_\alpha) = \frac{\prod_{k=1}^{K} P_{k,m}(\upsilon_{k\text{exp}})}{\sum_{n=1}^{N}\prod_{k=1}^{K} P_{k,n}(\upsilon_{k\text{exp}})} \qquad (1)$$

This ratio expresses the probability of a molecule from species *m* displaying the particular set of parameters $\{\upsilon_{k\ \text{exp}}\}$ (calculated in the numerator) relative to the probability that the set $\{\upsilon_{k\ \text{exp}}\}$ will be displayed by *any* of the *N* species (denominator). In the absence of conformational dynamics (which is here the case), shot noise limited distributions for the individual parameters are measured. For each individual molecule α, a set of *N* probabilities, $\{\Psi(1|\{\upsilon_{k\ \text{exp}}\}_\alpha)... \Psi(N|\{\upsilon_{k\ \text{exp}}\}_\alpha)\}$, is calculated by eq 1 using the set of experimentally determined fluorescence parameters for that molecule, $\{\upsilon_{1\ \text{exp}}... \upsilon_{K\ \text{exp}}\}_\alpha$. Since a molecule must belong to one of the *N* species, $\sum_n \Psi(n|\{\upsilon_{k\ \text{exp}}\}_\alpha) = 1$ for each molecule α. The molecule is then classified as belonging to that species *m* for which $\Psi(m|\{\upsilon_{k\ \text{exp}}\}_\alpha)$ is the highest.

For each of the $n_d = 1, \cdot, m, \cdot, N$ DA-oligonucleotide data sets, a histogram was generated that counted how many molecules in that data set were assigned to each of the *N* species. By normalizing the sum of each of these histograms to unity, we obtain the classification probability $\Omega(m|n_d)$ stating the probability that a molecule of the data set n_d (i.e., originating from species $n = m$) is classified as species *m*. By restricting analysis to a single data set n_d, the classification probability $\Omega(m|n_d)$ can be defined

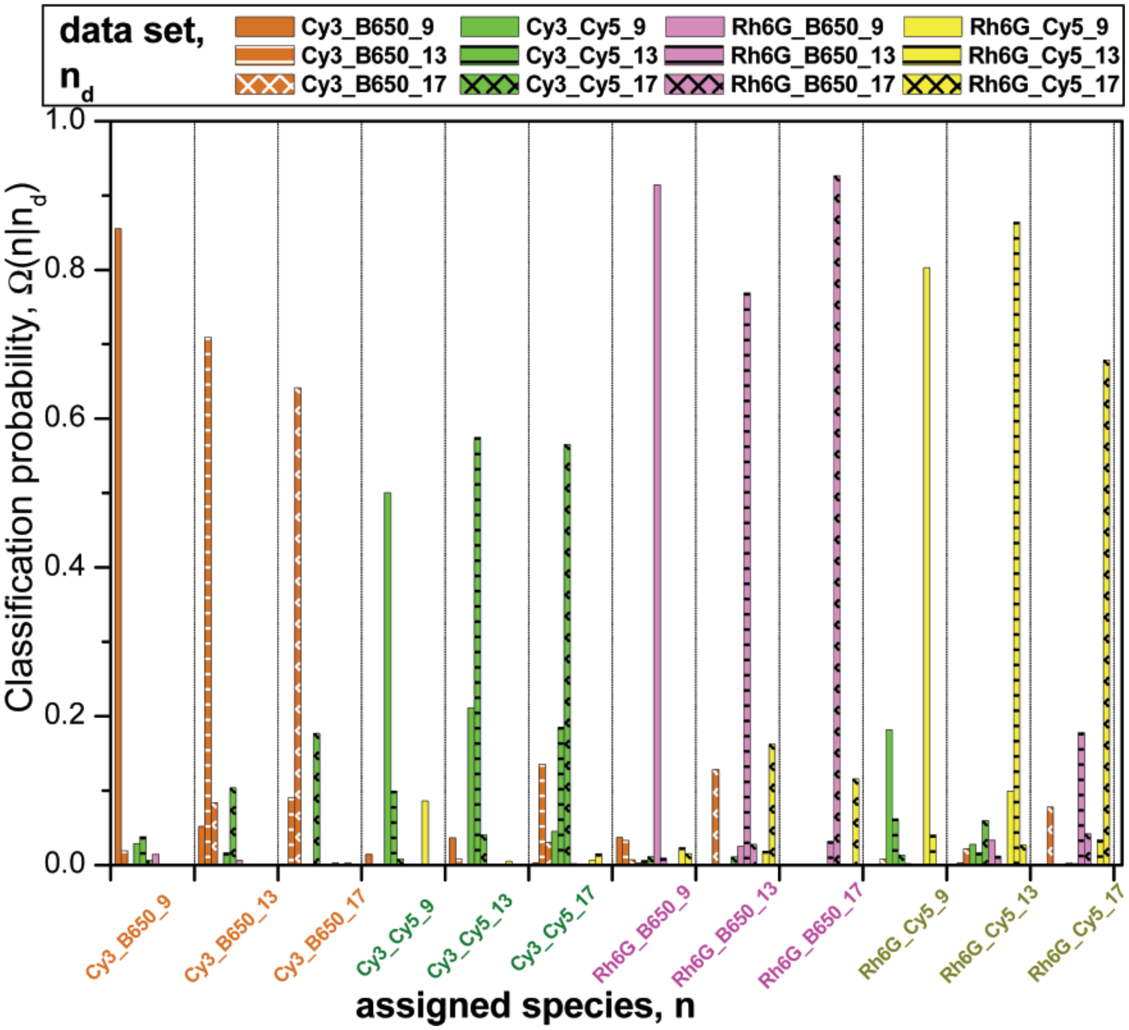

Figure 10. Classification probability, $\Omega(n|n_\mathrm{d})$, that an DA-oligonucleotide molecule of the data set n_d is classified as a species n. Calculations were based on the procedure, described in the text, using four fluorescence dimensions: green lifetime, τ_G, green anisotropy, r_G, red decay time, τ_R, and signal intensity ratio, $S_\mathrm{G}/S_\mathrm{R}$. (For detailed values see Supporting Information, Table 1).

as $\Omega(m|n_d) = a_m/\sum_{n=1}^{N} a_n$, where $\{a_{n=1}; \ldots a_N\}$ are the numbers of molecules from data set n_d assigned to species m.

Classification of Single Molecules. In Figure 10, the classification probabilities obtained for each of the $N = 12$ DA-oligonucleotide species are shown. If $\Omega(n=n_d|n_d) = 1$, then we have no errors in classification. However, not all of the molecules of an individual data set n_d are indeed classified as belonging to species m, i.e., $\Omega(m=n_\mathrm{d}|n_\mathrm{d}) < 1$. This error is due to overlap of the one-dimensional probability distributions, $P_{k,n}$, between the different species. However, by increasing the number of dimensions, K, the classification confidence can be improved. The classification probabilities shown in Figure 10 use four fluorescence dimensions: green lifetime, τ_G, green anisotropy, r_G, red signal decay time, τ_R, and signal intensity ratio, $S_\mathrm{G}/S_\mathrm{R}$. Analyzing $\Omega(m|n_\mathrm{d})$ in Figure 10, the likelihood that a molecule of data set is properly assigned to a species (i.e., the correct classification, $\Omega(n=n_\mathrm{d}|n_\mathrm{d})$ always dominates over the other classification probabilities $\Omega(n\neq n_\mathrm{d}|n_\mathrm{d})$ and exceeds 0.5 for all data sets with n_d.

Analysis of an Ensemble of Molecules. In general, having a definition for the classification probabilities $\Omega(n=1|n_\mathrm{d})$ to $\Omega(n=N|n_\mathrm{d})$ for a given data set n_d with a separate species n allows us to generalize the definition for a_n to include all of the analyzed data sets. The frequency histogram for the classification of corresponding single molecules can be predicted with the frequency of the assigned molecules described by $\vec{a}=\{a_{n=1}; \ldots a_N\}$, where the total number of detected molecules A_total is given by $\sum_{n=1}^{N} a_n$. Due to shot noise broadened fluorescence parameters, the patterns overlap, which has the consequence that the recognition of single molecules cannot be perfect (Figure 10). Because of these statistical classification problems in the first step, which can be described by error probabilities, we now analyze all molecules together in a second step and improve the classification on the basis of the knowledge of the mean classification error. In this way, a much better result for the number of detected molecules of the ensemble c_n is obtained than at the single-molecule level.

The actually calculated numbers for each species in this mixture $\vec{c} = \{c_{n=1}; \ldots c_N\}$ are obtained by solving the following system of linear equations with the classification probabilities $\Omega(n|n_\mathrm{d})$ and the experimentally obtained numbers of assigned molecules $\vec{a}$.

$$\begin{bmatrix} \Omega(n=1|n_\mathrm{d}=1) & \ldots & \Omega(n=1|n_\mathrm{d}=N) \\ \ldots & \ldots & \ldots \\ \Omega(n=N|n_\mathrm{d}=1) & \ldots & \Omega(n=N|n_\mathrm{d}=N) \end{bmatrix} \begin{bmatrix} c_{n=1} \\ \ldots \\ c_N \end{bmatrix} = \begin{bmatrix} a_{n=1} \\ \ldots \\ a_N \end{bmatrix} \quad (2)$$

Finally, we want to give an example for the substantial improvement by using eq 2 to reliably calculate ensemble numbers of the analyzed molecules. Therefore, we analyzed an independently measured test sample with a total number $A_{total} = 4143$ molecules, which contained three of the 12 DA-oligonucleotides. For the discussion of the results we normalize the molecule numbers $\vec{a}$ and $\vec{c}$ by A_{total} defining relative fractions of experimentally assigned molecules $\vec{a}_r$ and relative species fractions calculated for the ensemble $\vec{c}_r$, respectively. The actual sample composition $\vec{c}_{rsample} = [a_3(\text{Cy3}-\text{BP650/665 (17 bp)}) = 0.33;\ a_4(\text{Cy3}-\text{Cy5 (9bp)}) = 0.35;\ a_{12}(\text{Rh6G}-\text{Cy5 (17bp)}) = 0.32\}$ is very well recovered by our single-molecule counting analysis $\vec{c}_{ranalysis} = \{a_3 = 0.32;\ a_4 = 0{,}35;\ a_6 = 0.01;\ a_8 = -0.01;\ a_{11} = -0.01;\ a_{12} = 0.34\}$. Please note that in the following analysis we list only coefficients for the relative species fractions, which are not equal to zero. The negative fractions of $\vec{c}_{ranalysis}$ are solely the result of the mathematical solution and have of course no chemical meaning. In contrast to $\vec{c}_{ranalysis}$, please note that the fractions obtained in the first step by the single-molecule classification $\vec{a}_r = \{0.01;\ 0.03;\ \mathbf{0.21},\ \mathbf{0.17};\ 0.08;\ 0.03;\ 0.01;\ 0.09;\ 0.04;\ 0.06;\ 0.02;\ \mathbf{025}\}$ (eq 1) indicate a level of misclassification of up to 10%, which results in false positive and false negative classified molecules on the single-molecule level. This result is equivalent to the case of the overlap of ellipses for different species in the graphical analysis (e.g., Figure 8). However, using eq 2, $\vec{a}_r$ is converted with high accuracy to $\vec{c}_{ranalysis}$ in the second step of the single-molecule counting analysis. The comparison of $\vec{c}_{rsample}$ with $\vec{c}_{ranalysis}$ indicates a very low statistical noise level of only 1−2%.

CONCLUSIONS AND OUTLOOK

The purpose of this study was to demonstrate the feasibility and huge dynamic range of single-molecule measurements for identifying a larger number of different species, based on multiparameter detection and a multidimensional single-molecule counting analysis. By MFD, free dye molecules and incompletely labeled species could be excluded from the analysis, and in all 16 different compounds (four families of DA-oligonucleotides, Cy3−Cy5, Cy3−BP650/665, Rh6G−Cy5, and Rh6G−BP650/665, each with 9-, 13-, and 17-bp separation between the dyes, D-oligonucleotides labeled with Cy3 or Rh6G, impurities) were separated, based on the multidimensional information contained in the fluorescence of the analyzed molecules.

Following arrangement of the detected molecules into a multidimensional cumulative histogram, identification of the different species was first demonstrated by use of sequential two-dimensional projections of the histogram in different parameter planes, employing different "borderlines" between the populations projected in each plane. However, apart from this visual approach demonstrating the feasibility, we also show that a more quantitative identification procedure can be employed, based on an algorithm that offers fast and automated species identification with reasonable fidelity on a single-molecule level. This approach can also regenerate concentration profiles of species in a mixed sample with very high accuracy, and there is still a clear potential for implementing additional criteria and procedures. Apart from the "traditional" "chromophore" fluorescence parameters providing the criteria for the species identification in this study, fluctuation analysis of the fluorescence intensity (such as fluorescence correlation spectroscopy) or some other parameter of the detected fluorescence) can yield additional independent parameters. To such characteristic fluctuation parameters, within the category of parameters referred to as "environment/system parameters" above, belong triplet-state transitions,[55] trans−cis isomerization,[56] charge transfer,[57] or even transport properties.[54] In a recent study, the determination of up to 14 different parameters from one individual molecule was claimed, including transition rates to and from the triplet state and spatial parameters.[58] In MFD, fluctuation analysis of the detected fluorescence within selected bursts is possible. The use of MFD and additional parameters extracted from fluctuation analysis to identify different individual molecules will be reported elsewhere. Recently, Bowen et al. implemented neural networks for classifying fluorescence from individual molecules in a mixture. A neural network was constructed and trained to identify molecules based on fluorescence lifetime data and was shown to perform better than (nonideal more complex data) or equal to (ideal data) a maximum likelihood estimator (MLE) approach.[23] Here "ideal" means, that the data could be well described by the MLE by assuming, for example, a single-exponential decay. By use of identification procedures of this kind, applied in the multiparameter space, it is reasonable to believe that the number of species that can be separated from each other, and the specificity with which this can be done, can be increased even further. Apart from extensions in the extraction and processing of information from the emitted fluorescence, further operations can also be added on the excitation side, extending the degrees of freedom with respect to which single molecules can be analyzed. Recently, Kapanidis et al. reported the use of alternating direct laser excitation of both donor and acceptor fluorophores on single diffusing molecules. This enables both an interdye distance-dependent and distance-independent intensity ratio of the analyzed molecules, the latter based on labeling stoichiometry.[59] MFD lends itself well for the introduction of an alternating excitation scheme, with two or several laser lines. In general, given the flexible concept of MFD, in terms of possible schemes of excitation, the emission characterization, and the data processing steps, the potential for further improvements is large, and the modifications can be tailored to the specific species to be identified. The presented study thus only indicates a fundamental level at which single-molecule detection and identification can be performed using the MFD approach.

Finally, it is important to mention that an analysis of a sample, where the analyzed fluorescence bursts have been selected from the fluorescence intensity time trace via an intensity threshold criterion, can give only a qualitative picture on the sample composition, because the chance of bright molecules to be selected and to be subsequently analyzed is higher than that of less bright molecules. However, the multidimensional single-molecule counting analysis performed here is very well suited to check for the presence of even very small amounts of analyte molecules yielding a qualitative sample survey. Moreover, Fries et al.[49] have shown that the analysis of the obtained burst size distributions allows one to identify fluorescent sample molecules

---

(55) Widengren, J.; Mets, Ü.; Rigler, R. *J. Phys. Chem.* **1995**, *99*, 13368−79.
(56) Widengren, J.; Schwille, P. *J. Phys. Chem. A* **2000**, *104*, 6416−28.
(57) Widengren, J.; Dapprich, J.; Rigler, R. *Chem. Phys.* **1997**, *216*, 417−26.
(58) Prummer, M.; Sick, B.; Renn, A.; Wild, U. P. *Anal. Chem.* **2004**, *76*, 1633−40.
(59) Kapanidis, A. N.; Lee, N. K.; Laurence, T. A.; Doose, S.; Margeat, E.; Weiss, S. *Proc. Natl. Acad. Sci. U.S.A.* **2004**, *101*, 8936−41.

also in a quantitative manner. Thus, the introduced method of multidimensional single-molecule counting harbors the potential for a complete characterization and quantitative analysis of a highly diluted sample in homogeneous assays.

ACKNOWLEDGMENT

Financial support by BMBF Biofuture 0311865 is gratefully acknowledged. Enno Schweinberger is acknowledged for assisting with the design of oligonucleotides. Suren Felekyan, Stanislav Kalinin, and Wajih Al-Soufi are acknowledged for helpful theoretical discussions and for providing important analytical software. J.W. acknowledges support from the Swedish Board for Internationalization of Higher Education and Science (STINT), The Swedish Research Council (VR), and the Swedish Cancer Foundation.

SUPPORTING INFORMATION AVAILABLE

Additional information as noted in text. This material is available free of charge via the Internet at http://pubs.acs.org.

Received for review December 23, 2005. Accepted January 3, 2006.

AC0522759

Supplement materials for

Single molecule detection and identification of multiple species by multiparameter fluorescence detection.

Jerker Widengren [1†], Volodymyr Kudryavtsev [2†], Matthew Antonik [2], Sylvia Berger [2,4],*
Margarita Gerken [3], Claus A. M. Seidel [2]*

Table 1 presents the classification probability, $\Omega(n|n_d)$, that a DA-oligonucleotide molecule of the data set n_d (shown as rows in Table 1) is classified as species n (columns). Based on the values of the Table 1, Figure 10 of the manuscript text is plotted as follows: the X-axis of the plot corresponds to the assigned species, n, and the colored texture above the plot corresponds to the originating datasets, n_d. A vertical colored texture bar corresponding to each n_d appears in each of the 12 areas of Figure 10, and represents the fraction of molecules from n_d which is classified as belonging to species n. Therefore, the sum of all identical color texture bars in Figure 10 (representing a single row in Table 1) is unity, whereas the sum of all bars in a particular region (columns in Table 1) need not be unity.

Dataset\species	Cy3_B650_9	Cy3_B650_13	Cy3_B650_17	Cy3_Cy5_9	Cy3_Cy5_13	Cy3_Cy5_17	Rh6G_B650_9	Rh6G_B650_13	Rh6G_B650_17	Rh6G_Cy5_9	Rh6G_Cy5_13	Rh6G_Cy5_17
Cy3_B650_9	0.85521	0.05208	0	0.01458	0.03646	0.00312	0.0375	0	0	0.00104	0	0
Cy3_B650_13	0.01917	0.70919	0.09055	0	0.00859	0.13549	0.03305	0.00066	0	0	0.0033	0
Cy3_B650_17	0	0.08423	0.6413	0	0.00037	0.03066	0.00702	0.12819	0.00074	0.00776	0.0218	0.07795
Cy3_Cy5_9	0.02912	0.00104	0	0.50052	0.21109	0.04541	0.00312	0	0	0.18198	0.02773	0
Cy3_Cy5_13	0.03809	0.01632	0.0006	0.09976	0.57497	0.18561	0.00605	0	0	0.06227	0.01632	0
Cy3_Cy5_17	0.00656	0.10394	0.17724	0.00821	0.04048	0.56565	0.01149	0.01094	0	0.01313	0.05963	0.00274
Rh6G_B650_9	0.01461	0.00626	0	0	0	0.00209	0.9144	0.02505	0	0.00209	0.0334	0.00209
Rh6G_B650_13	0	0	0	0	0	0	0.00945	0.7689	0.03179	0	0.01203	0.17784
Rh6G_B650_17	0	0	0.00312	0	0	0	0	0.0281	0.92662	0	0	0.04215
Rh6G_Cy5_9	0	0.00061	0	0.08634	0.0049	0.00612	0	0	0	0.80282	0.0992	0
Rh6G_Cy5_13	0	0	0.00305	0.00076	0	0.01523	0.02361	0.01904	0	0.04037	0.86443	0.03351
Rh6G_Cy5_17	0	0	0.00037	0	0	0	0.01563	0.16263	0.11574	0	0.0268	0.67882

Table 1. Classification probability, $\Omega(n|n_d)$, that an DA-oligonucleotide molecule of the data set n_d (rows) is classified as a species n (columns). Calculations were based on the procedure, described in the text, using 4 fluorescence dimensions: green lifetime, τ_G, green anisotropy, r_G , red decay time, τ_R, and signal intensity ratio, S_G/S_R.

REVIEW OF SCIENTIFIC INSTRUMENTS **76**, 083104 (2005)

Full correlation from picoseconds to seconds by time-resolved and time-correlated single photon detection

S. Felekyan, R. Kühnemuth,[a] V. Kudryavtsev, and C. Sandhagen
Lehrstuhl für Molekulare Physikalische Chemie, Heinrich Heine Universität Düsseldorf,
40225 Düsseldorf, Germany

W. Becker
Becker & Hickl GmbH, Nahmitzer Damm 30, 12277 Berlin, Germany

C. A. M. Seidel
Lehrstuhl für Molekulare Physikalische Chemie, Heinrich Heine Universität Düsseldorf,
40225 Düsseldorf, Germany

(Received 11 March 2005; accepted 8 May 2005; published online 21 July 2005)

We present an advanced time-correlated single photon counting (TCSPC) technique that delivers traditional fluorescence correlation (FCS) or cross correlation (FCCS) and fluorescence lifetime data simultaneously. Newly developed electronics allow for detection and registration of single photon events over time periods of hours with picoseconds accuracy. Subsequent software-correlation yields correlation curves covering more than 12 orders of magnitude in time. At the same time, the original data, containing all information accessible by single photon counting techniques, can be analyzed conventionally according to common single molecule fluorescence techniques. Potential applications of the new technique using pulsed or cw laser excitation are discussed. © *2005 American Institute of Physics.* [DOI: 10.1063/1.1946088]

I. INTRODUCTION

If photons are emitted by thermal sources or by fluorescence of a large number of molecules the emission events are independent. The photons appear randomly, and the distribution of the time distance between subsequent photons drops exponentially with increasing time distance.

For light generated by nonlinear effects, by quantum dots,[1–3] or by the fluorescence of single molecules[4–8] this is not necessarily the case. When a single molecule has absorbed a photon it cannot absorb and emit a second photon until it has not returned to the electronic ground state. Thus, the photons exhibit an antibunching phenomenon with a time constant defined by the fluorescence lifetime and excitation rate. Investigation of these effects requires the detection and correlation of single photons on the ps and ns scale.

Fluorescence correlation spectroscopy (FCS) exploits the autocorrelation between the fluorescence intensities in different time intervals.[9–12] A confocal or two-photon setup is used to achieve a sample volume of the order of 0.1–1 fl. At a concentration of $10^{-9}-10^{-11}$ mol/l only a few molecules are in the focus. Processes like diffusion, conformational changes or intersystem crossing cause a fluctuation of the number of fluorescing molecules in the sample volume and therefore a fluctuation in the fluorescence intensity.

FCS can be combined with simultaneous detection in different wavelength intervals and for different polarization.[13–15] Cross-correlation of the fluorescence signals of different fluorophores (FCCS) in biological systems then delivers direct information about the colocalization of the fluorophore molecules, about conformational dynamics in FRET active molecules, and via rotational correlation times about the size and shape of labelled proteins and aggregates and about the mobility in membrane structures.[16]

A large number of fluorescence markers are available that bind to specific protein and lipid structures. In particular, cells can be transfected with green fluorescent protein (GFP) mutants resulting in a well-defined localisation of fluorophores in defined subunits of the cells.[17,18] Even quantum dots have been shown to bind covalently to cellular proteins and antibodies.[19–22] If different protein structures are marked with different fluorophores FCCS shows whether the structures are linked or diffuse independently. Typical FCS and FCCS effects happen on a time scale from several nanoseconds to milliseconds.

Clusters of proteins and dyes can change their conformation, which, in turn, induces changes in the fluorescence quantum efficiency, i.e., fluorescence intensity and fluorescence lifetime, and the fluorescence anisotropy.[13–15] Fluctuations of the quantum efficiency can be due to changes in the quenching efficiency, or, if two dyes with overlapping emission and absorption spectra are used, by fluorescence resonance energy transfer (FRET).[23–25] Fluctuations of the quantum efficiency cause a similar FCS signature as the fluctuation of the number of molecules in the excited sample volume. The effects can, however, be distinguished even in the case of similar time constants if the fluorescence lifetime or the characteristic antibunching time is recorded simultaneously with the FCS. Fluorescence lifetime in conjunction with spectral information can also be used to distinguish between different dyes and dye-protein clusters.[26–29]

---

[a] Author to whom correspondence should be addressed; electronic mail: Ralf.Kuehnemuth@uni-duesseldorf.de

The common technique for FCS recording is the "hardware correlator." The device registers single photon events with a time-resolution in the ns range and correlates the detection times in an internal signal processor. The standard technique for fluorescence lifetime and antibunching experiments is time-correlated single photon counting (TCSPC).[30] Both techniques can, of course, be used in combination to obtain independent FCS and lifetime data for the dye and protein under investigation.[11,12] The drawback is that the lifetime data are not obtained from exactly the same molecules as the FCS data, and lifetime fluctuations cannot be correlated with the fluctuations in the FCS data.

Fully parallel recording of FCS/FCCS and fluorescence lifetime information or antibunching requires a technique that records the fluorescence photons in several independent detection channels and covers a time range of many seconds with picosecond resolution. Furthermore, it must record photon rates up to several 10^5/s virtually without counting loss. We will show that advanced TCSPC techniques developed in the last few years[31–33] can be extended to the recording of FCS, FCCS, fluorescence lifetime, and antibunching effects.

II. EXPERIMENT

A. Hardware

1. Time-correlated single photon counting (TCSPC)

Conventional time-correlated single photon counting is based on the measurement of the detection times of individual emitted photons with respect to the time of the excitation. Excitation is achieved with a periodical light source.[30] The method makes use of the fact that for low level, high repetition rate signals the detection rate is much lower than the excitation pulse rate. Therefore, the detection of several photons per excitation pulse can be neglected. By building up a histogram of the photon detection times the waveform of the detected signal is obtained. Although this principle looks complicated at first glance, it has a number of striking benefits:

(a) The time resolution of TCSPC is limited by the transit time spread, not by the width of the output pulse of the detector. Even early TCSPC systems delivered an instrument response of less than 60 ps FWHM.[34,35] With modern microchannel plate photomultipliers (MCP-PMTs) an instrument response width of less than 30 ps is achieved.[33]

(b) TCSPC has a near-perfect counting efficiency and therefore achieves optimum signal-to-noise ratio for a given number of detected photons.[36–38]

A severe drawback of classic TCSPC instruments was their slow signal processing electronics. The dead time after the detection of a photon was of the order of 10 μs, which resulted in a maximum useful count rate of the order of 50 $\times 10^3$ s^{-1}. Another limitation was the low repetition rate of the light sources used in early TCSPC experiments. The low repetition rate resulted in severe pile-up, i.e., detection of several photons per signal period, and limited the applicable count rates to even lower values.[30] These limitations can be considered a feature of the nuclear instrumentation module (NIM) electronics and the light sources used in early TCSPC experiments. A more general problem of the classic TCSPC technique is, however, that it is intrinsically one-dimensional. Only one waveform of one light signal at one spot of a sample is recorded at a time.

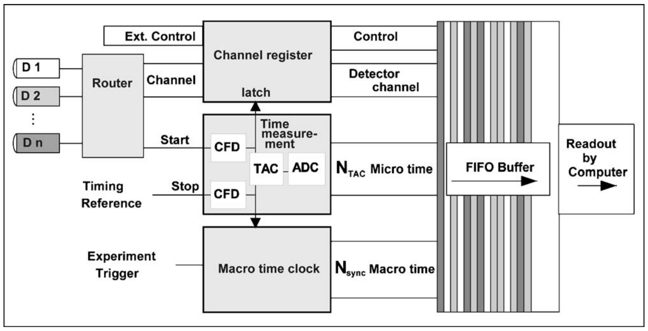

FIG. 1. Block diagram of one TCSPC channel. D1 through Dn, detectors; CFD, constant fraction discriminator; TAC, time-to-amplitude converter; ADC, analog-to-digital converter.

Advanced TCSPC techniques use new time-conversion principles that have resulted in a decrease of the dead time by a factor of about 100.[29,33] Moreover, advanced TCSPC is based on a multidimensional recording process, i.e., records the photon density not only as a function of the time in the signal period, but also over other parameters, such as the wavelength, polarization, location within a scanning area, and the time from the start of the experiment.[13,15,27,39,40] A variant of the multidimensional TCSPC technique does not build up photon distributions but stores the full information about each individual photon. The mode is called time-tag or FIFO mode. The device used for this work can be configured to deliver either multidimensional histograms of the photon density or time-tag data. The architecture of the device in the time-tag mode is shown in Fig. 1.

One or several light signals are detected simultaneously by a number of photomultiplier tubes (PMTs) or single-photon avalanche photodiodes (SPADs). The recording of the signals is based on the general presumption of TCSPC that the detection of several photons per signal period is unlikely. Under this condition simultaneous detection of several photons in different detectors can be considered unlikely as well. Therefore, the single-photon pulses of all detectors can be processed by a single TCSPC channel. A "router" combines the single photon pulses in one common timing pulse line, and, simultaneously, delivers a digital "channel" signal that indicates which detector delivered the current photon pulse.[33] When the TCSPC device detects the photon pulse it writes the corresponding channel word into a channel register. Several additional bits can be read simultaneously with the channel word and be used to synchronize the recording with the experiment.

The single photon pulses from the detectors are used as start pulses for the time-measurement block. The time-measurement block employs the traditional architecture of TCSPC. The single-photon pulses and the timing-reference pulses are fed through constant-fraction discriminators (CFD), to remove the amplitude jitter from the timing information. The time between the single-photon pulses and the

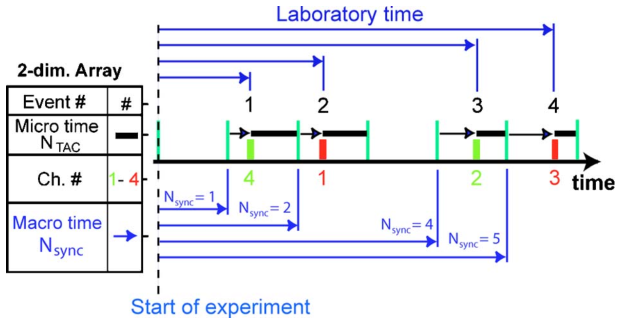

FIG. 2. (Color online) Data structure in the FIFO mode. For each photon micro time (TAC channel N_{TAC}), macro time (sync counter N_{sync}), and detection channel number are recorded.

timing reference is converted into a voltage by a time-to amplitude converter (TAC). The voltage delivered by the TAC is converted into a digital data word by the analog-to-digital converter (ADC). The delivered data word defines the micro time, i.e., the arrival time of the detected photon relative to the reference pulse, by the specified number of micro time channels, N_{TAC}. The width of a micro time channel is usually a few picoseconds. Compared to traditional NIM devices the ADC is more than 100 times faster. The high speed is obtained by a modified dithering technique. The technique adds an auxiliary signal to the ADC input, which is later subtracted from the output data word. Each photon signal is therefore converted at a different location on the ADC characteristic, resulting in a cancellation of the nonuniformity of the channel width.[29,33] Consequently, the accuracy requirements to the ADC are relaxed, and extremely fast ADC chips can be used. Together with a speed-optimized TAC a dead time as low as 100 ns is reached.

The laboratory time elapsed from the start of the experiment is obtained by combining the micro and macro time information of the measurement (Fig. 2). The macro time is measured by the number of periods of a clock oscillator, or, alternatively, the number of TAC stop periods from an external "experiment trigger" pulse, N_{sync}.

The memory of the TCSPC device is configured as a first-in-first-out (FIFO) buffer. When a photon is detected the micro time, the macro time, and the data in the channel register are written into the FIFO. The output of the FIFO is written continuously, and the data are written into the memory or on the hard disk of the host computer.

The time-tag mode is particularly useful for single molecule spectroscopy to combine analyses which use the micro and macro time information.[15] Fluorescence correlation curves (FCS) are obtained by correlating the macro times of one, fluorescence cross-correlation curves by correlating the macro times of different detectors. The fluorescence lifetime can be included in the analysis by building up histograms of the micro time. Fluorescence intensity distribution analysis (FIDA) (Ref. 41) is possible by analyzing the frequency of the counts in consecutive macro time intervals. FIDA can be combined with analyzing of the average micro times (fluorescence intensity and lifetime distribution analysis, FILDA).[42] Burst-integrated fluorescence lifetime (BIFL) analyzes the lifetime and the count numbers in the individual burst delivered by single molecules.[14,27,43] Antibunching results are obtained by using the usual Hanbury-Brown and Twiss setup[7,44] and connecting one detector to the start, the other to the stop input of the TCSPC device (Fig. 3).

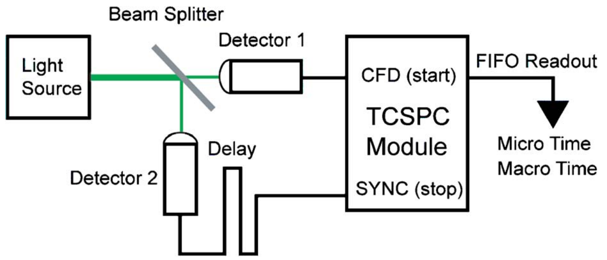

FIG. 3. (Color online) Hanbury-Brown and Twiss setup (Ref. 43) with a single TCSPC module. A single TAC is started and stopped by two detectors.

In all these applications the counting efficiency of the recording system is an important parameter. The standard deviation of the results of FIDA and BIFL depends on the square root of the number of photons detected within the sampling time interval or the burst time. For FCS and antibunching the signal-to-noise ratio even depends linearly on the number of recorded photons. More important, correct results of FCS, FIDA, and BIFL experiments are only obtained if the counting efficiency is constant within the expected range of burst count rates. There are several ways a TCSPC setup may lose photons. The most obvious one is the limited efficiency of the optical system and of the detector (see below, Experimental Setup and Detectors). The TCSPC device itself may lose photons by the classic pile-up effect, and by counting loss in the dead time after the recording of a previously detected photon.

The dead time in typical TCSPC devices is "nonparalyzing," i.e., a photon lost in the dead time of a previous one does not cause new dead time. Moreover, for a TAC stop period shorter than the dead time the counting efficiency covers both the loss by the dead time and the loss by pile-up. For a continuous input signal the counting efficiency, E, is given by the ratio of the recorded count rate, r_{rec}, and the detected count rate, r_{det}, and can be related to the dead time t_d,[40,45]

$$E = \frac{r_{\mathrm{rec}}}{r_{\mathrm{det}}} = \frac{1}{1 + r_{\mathrm{det}} t_d}. \tag{1}$$

The dead time of the TCSPC modules used for this work is 100–125 ns. In a single molecule experiment the burst count rates under reasonable excitation conditions usually do not exceed $5 \times 10^5\ \mathrm{s}^{-1}$, the maximum count rates in the presented data were $3 \times 10^5\ \mathrm{s}^{-1}$. The corresponding counting loss is 5%–6% and does therefore not result in noticeable distortion of the results.

Another nonideal effect to be considered is the distortion of the photon distribution by pile-up. Pile-up is caused by the detection of a second photon within one TAC stop period. For a single-exponential fluorescence decay, the pile-up adds virtual lifetime components of $\tau/2$, $\tau/3 \ldots \tau/n$ to the correct lifetime, τ.[40] The resulting mean intensity-weighted lifetime is approximately

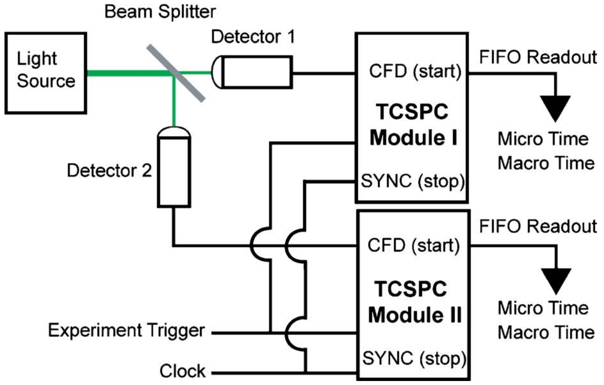

FIG. 4. (Color online) Dual module setup with synchronized data acquisition.

$$\tau_{\mathrm{mean}i} \approx \tau(1-p/4) \quad \text{for } p < 0.1, \tag{2}$$

with p being the average number of photons per TAC stop period. For the TAC stop period of 13.6 ns used in the experiments described below the pile-up results in a lifetime error of less than 0.2% up to the highest expected count rates in a burst of 5×10^5 s^{-1}.

2. Dual-channel TCSPC setup

A single TCSPC channel of the architecture shown in Fig. 1 is unable to correlate photons of different detectors within times shorter than the dead time. Correlation of shorter times can, in principle, be obtained by giving the signals different delays.[46] If the delay difference for the individual detectors is larger than the dead time of the board, then photons that are detected simultaneously can be recorded separately. However, the photons must be identified by their macro time differences which is only possible if the count rate is low. Another way of fast correlation is the antibunching experiment (Fig. 3). The photon pulses of one or several start detectors are correlated against the pulses of one stop detector. The setup easily yields correlation down to the IRF width of the detectors. The time scale of the correlation is, however, limited by the TAC range. The recording can, in principle, be combined with a FCS recording obtained consecutively in the same TCSPC channel or simultaneously in a second one. However, continuous correlation from the time scale of antibunching to the time scale of diffusion effects is not obtained this way.

To overcome these limitations we used two synchronized TCSPC boards (SPC-132, custom design, two modified boards of a four board SPC-134 system, Becker & Hickl, Berlin). The general setup is shown in Fig. 4.

The events detected in the two detectors are processed in separate TCSPC boards. Both modules use the same timing reference signal at their TAC stop inputs. For experiments with pulsed excitation the timing reference signal is derived from the laser pulse sequence. For continuous excitation an artificial reference signal from a pulse generator was used.

To obtain synchronized, i.e., comparable macro times in both channels the macro time clocks of both channels must be driven by the same clock source. Moreover, the recording must be started synchronously in both channels. We use the TAC stop signal as a mother clock of the macro time and start both channels synchronously via their experiment trigger inputs. Thus, every photon is assigned to a defined TAC stop period. The events recorded in both modules are used to calculate a single cross correlation function on a continuous laboratory time scale from picoseconds to milliseconds or seconds, the length of the continuous single photon traces only being limited by the computer memory.

This calculation is described in Sec. II B. For the calculation the following problems needed to be solved: (1) The time measurement in the TACs is independent of the macro time measurement. This results in independent time scales, and different relations of "time zero" of the TACs referred to the macro time transitions. (2) The time scales of both TACs may be different by about 1% and the start and stop delays may be different by a few 100 ps. (3) Due to the finite bandwidth of the TAC circuitry the first few ns of the TAC characteristic are nonlinear. In the majority of TCSPC applications the nonlinear region can easily be avoided by using an appropriate TAC offset and the corresponding signal delay. This is not possible when a continuous macroscopic time axis needs to be constructed, i.e., when the photons falling in the nonlinear part cannot be discarded. In the correlation measurements presented here the nonlinearity leads to periodic distortion of the effective time axis. A reduction of these distortions by software is described in Sec. II B 1.

3. Detectors

In general, detectors for TCSPC should have a gain high enough to resolve single photon events, a short transit time spread, and high quantum efficiency. The detector gain and the intrinsic delay must be stable up to a count rate of several 10^6 photons per second.

For fluorescence correlation, the quantum efficiency is even more essential. When the detection events are correlated the number of coincidences per time interval drops with the square of the photon number. Thus, the signal-to-noise ratio of the correlation spectrum depends linearly on the rate of photons—not on the square root as for a fluorescence decay curve. Another complication is afterpulsing. Almost any detector has an increased probability to deliver a background pulse for some time after the detection of a photon. Afterpulsing in PMTs is caused by ion feedback and probably dynode fluorescence and glass scintillation. In avalanche photodiodes afterpulses appear when trapped carriers from a previous avalanche are released. Typical afterpulsing time constants are of the order of a few hundred ns, which makes afterpulsing hard to distinguish from triplet effects. The dual detector configurations described above substantially reduce the effect of afterpulsing on the FCS results by applying cross-correlation analysis.

To date there is no detector that is really suitable for correlation experiments down to the picosecond range. Single photon avalanche photodiodes, in principle, are able to yield a high quantum efficiency (exceeding 65% at 650 nm) (Ref. 45) and a good time resolution.[47–49] Unfortunately, the commonly used Perkin Elmer SPCM-AQR modules have a poor timing performance. The width of the TCSPC instrument response was found to vary strongly from module to module (we have measured FWHM between

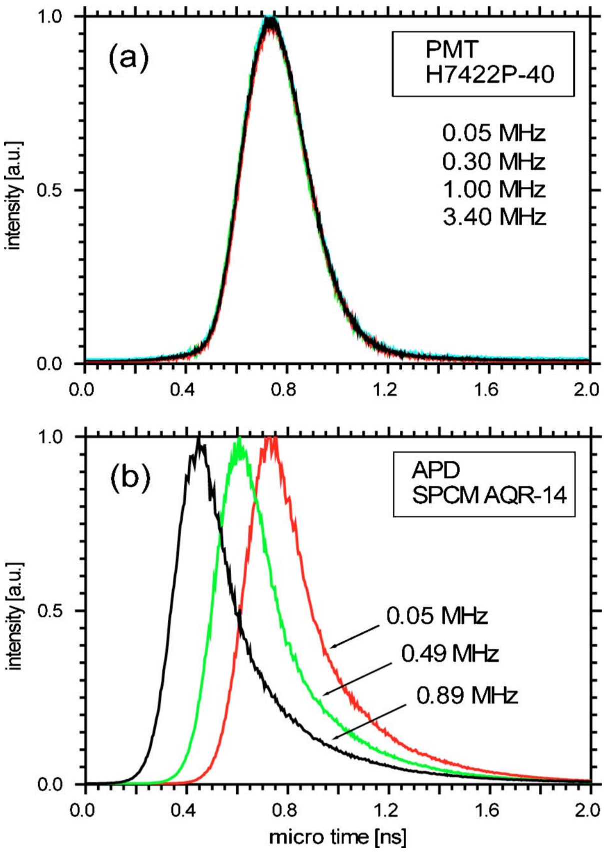

FIG. 5. (Color online) TCSPC Instrument response functions, measured with Becker and Hickl SPC-132 or SPC-630 TCSPC modules. (a) H7422P-40: 3.4 MHz, 1 MHz, 0.3 MHz, 0.05 MHz. Diode laser @ 650 nm (BHL-600, Becker and Hickl). (b) SPCM-AQR-14: count rates 0.05 MHz (right), 0.49 MHz (middle), and 0.89 MHz (left). Modelocked Ar-ion laser at 496 nm (Coherent).

190 ps and 620 ps in about 12 different tested modules) and depends on the wavelength (not shown). For all tested modules we measured a strong dependence of the postion of the IRF on the count rate [Fig. 5(b)], which makes experiments with fluctuating signals cumbersome or impossible to be analyzed quantitatively. Recently, a technical modification of the Perkin Elmer SPCM-AQR modules was shown to yield much better time responses than the ones tested.[50] The dead time of the SPCM-AQR can be estimated from the curves of the counting efficiency versus count rate given by the manufacturer.[45] The dead time is about 50 ns and thus of the same order as for the TCSCPC modules.

An alternative detector is the Hamamatsu H7422P-40 PMT.[51] Due to its GaAsP cathode it has a quantum efficiency approaching 40% around 450 nm, and a relatively short and stable TCSPC instrument response [Fig. 5(a)].

4. Experimental setup

The experiments are carried out with a confocal epi-illuminated setup based on an Olympus IX70 inverted microscope (Fig. 6).

The fluorescent molecules are excited by a linearly polarized argon-ion-laser (Innova Sabre, Coherent) at 496 nm, either active-mode-locked (73.5 MHz, 150 ps) or in cw mode. The HF-source for the mode-locker serves as the common time base for sync (TAC stop signal) and the macro time counter for both SPC-132 counting boards. The laser is focused into the sample by a NA=1.2 water-immersion objective lens (UPLAPO 60×, Olympus, Hamburg, Germany).

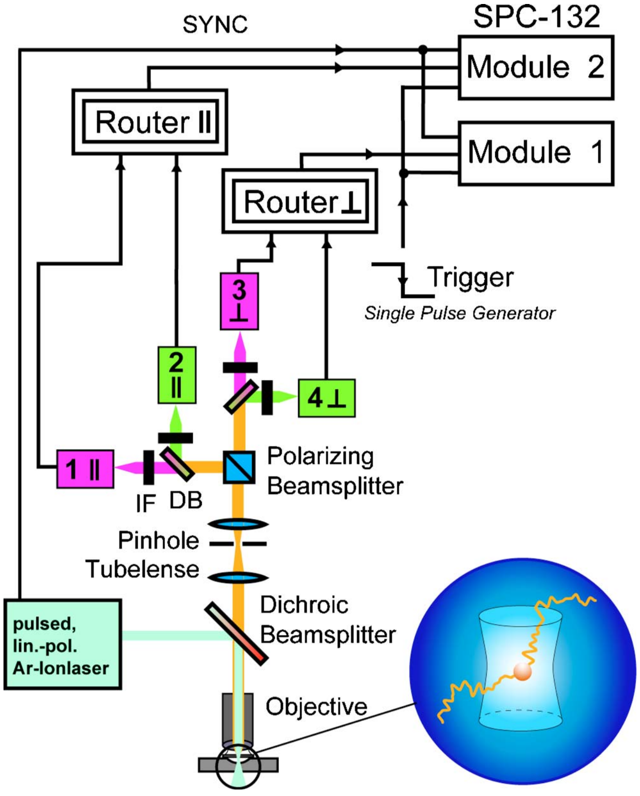

FIG. 6. (Color online) Four-channel (detectors 1–4) setup for simultaneous detection of fluorescence intensity F, lifetime τ, anisotropy r, and spectral range λ.

The fluorescence is collected by the same lens and separated from the excitation by a polychroic beamsplitter (488/636 PC, AHF, Tübingen, Germany). A confocal pinhole of 100 μm diameter and the slightly underfilled objective yield a detection volume element of approximately 1 μm diameter and 2 fl size, as determined by fluorescence correlation spectroscopy.[13] The collected fluorescence photons are divided first into its parallel and perpendicular components by a polarizing beamsplitter cube (VISHT11, Gsänger, Planegg, Germany), then by dichroic beamsplitters (Q 595 LPXR, AHF) into wavelength ranges below and above 595 nm. Fluorescence bandpass filters (HQ533/46, AHF) block residual laser light and reduce Raman scattering from the solvent.

The detectors used were photomultiplier tubes with GaAsP photocathodes (H7422P-40, Hamamatsu, Germany) or single photon avalanche diodes (SPCM-AQR-14, Perkin Elmer, Germany). Only detectors in postion 2 and 4 were used for the experiments presented here. Detectors in position 1 and 3 are available for optional two color coincidence or fluorescence resonance energy transfer (FRET) experiments with doubly dye-labelled samples.

5. Samples and sample preparation

All measurements were made on freely diffusing Rhodamine 110 molecules (Radiant Dyes, Wermelskirchen, Germany) in aqueous solution. The dye was diluted in dou-

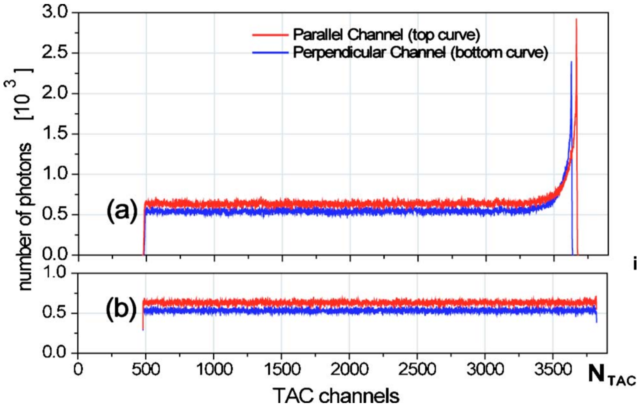

FIG. 7. (Color online) TAC-histograms. (a) Original histograms diplaying nonlinearities in both channels/boards. (b) Corresponding linearized histograms.

bly distilled deionized water to nanomolar concentrations. The pure solvent did not contain any detectable fluorescent impurities. All samples were air-saturated and have been investigated at room temperature (295 K).

B. Software

All software was written in LabVIEW (version 7.0, National Instruments) containing C++ subroutines.

1. Time-axis generation and TAC linearization

Laboratory time. For the FCS/FCCS curve generation it is required to restore the exact laboratory time from start of the experiment with ps resolution for each photon from the saved data. For this purpose we used the macro- and micro-(TAC) time information of each event for the generation of a combined arrival time with TAC resolution (see Fig. 2):

$$t_{\mathrm{lab}} = t_{\mathrm{sync}} \cdot N_{\mathrm{sync}} + t_{\mathrm{TAC}} \cdot N_{\mathrm{TAC}}, \qquad (3)$$

where t_{lab} is the laboratory time since the start of the experiment, t_{sync} is the time between the synchronization pulses, N_{sync} is the macro time counter (number of SYNC pulses since the start of the experiment), t_{TAC} is the calibrated width of a TAC channel in ns, and N_{TAC} the number of TAC-channels between a photon and the previous sync pulse. The combination of the time axes is only possible when the master clock for the macro timer (t_{sync}) and the stop signal for the TAC (t_{TAC}) are the same, as achieved in our dual channel TCSPC setup.

Nonlinearity. Any nonlinearity of the TAC characteristic will cause periodic distortions in the reconstructed time axis, as dicussed before. We correct for these—reproducible—artefacts by applying a rebinning algorithm to yield equal time-bins, which makes use of a calibration table containing calibration factors for each channel of the two TACs.

The first step in the generation of this linearization table is the acquisition of TAC histograms consisting of at least 10^6 randomly distributed photons to record the characteristic for each TAC with sufficient accuracy. To preserve the original factory-set calibration of the TAC the approximately linear part of the histograms is used to calculate a mean number of counts per channel, n_{mean} [i.e., from channels 550–3000 in Fig. 7(a)]. Within the shot-noise limit the counts in every channel, $n(k)$, of an ideal TAC should equal this number of photons. The deviations observed in practice for certain regions of the full range will be corrected for as follows:

The TAC histogram is normalized with n_{mean}. The obtained numbers, $n(k)/n_{\mathrm{mean}}$, represent the deviation from the mean of the width of the corresponding TAC channel. From these relative bin-widths a table of corrected times, $N_{\mathrm{TAC}}^{\mathrm{fract}}(i)$, for each channel i is generated by defining

$$N_{\mathrm{TAC}}^{\mathrm{fract}}(i) = f \sum_{k=0}^{i} \frac{n(k)}{n_{\mathrm{mean}}}, \qquad (4)$$

where $n(k)/n_{\mathrm{mean}}$ is the measured width of the nonlinear bins and f a stretching factor. The factor f was needed to avoid gaps in the time axis, i.e., to make the TAC scales of both modules identical and match the macro time spacing by correcting the slight and unavoidable variations in the individual calibrations. It corrects for inaccuracies in the TAC calibration which usually is performed by the manufacturer only for the linear part. As a result of this stretching/shrinking each TAC range yields the same number of channels required to fill the lag between two SYNC pulses with bins of the calibrated width [in our case 3343 bins of 4.069 ps ($=t_{\mathrm{TAC}}$) for a 13.6 ns ($=t_{\mathrm{sync}}$) time window]. The corrected times for each TAC bin, $N_{\mathrm{TAC}}^{\mathrm{fract}}(i)$, still refer to the units of the original time-bins but are rational numbers and no longer integers. Since efficient and fast correlation of the data requires equal time bins (see below) a rebinning of the photons has to be performed.

Rebinning of photons. The next step of the linearization process is the redistribution of the photons on the time axis from the original nonlinear TAC bins, i, into corresponding bins of equal width, N_{TAC}. A relative width $n(k)/n_{\mathrm{mean}} > 1$ suggests a division of that particular bin into smaller bins. A redistribution of single photons is performed one by one according to the calculated probability of the photon belonging to a certain corrected time-bin. To this end a random number, u, is assigned to the considered photon and, after beeing multiplied by the respective bin-width, added to the corrected time of the previous bin,

$$N_{\mathrm{TAC}} = N_{\mathrm{offset}} + \lceil N_{\mathrm{TAC}}^{\mathrm{fract}}(i-1) + u(N_{\mathrm{TAC}}^{\mathrm{fract}}(i) - N_{\mathrm{TAC}}^{\mathrm{fract}}(i-1)) \rceil \quad \text{with } i > N_{\mathrm{offset}}, \qquad (4')$$

where $0 \leq u < 1$ is a random number generated by the standard LabVIEW random number generator, N_{offset} the number of empty TAC channels [about 500 in Fig. 5(a)] and $\lceil\,\rceil$ increases the enclosed argument to the nearest higher integer. N_{TAC} gives the new channel number for the considered photon.

The result of the linearization is demonstrated in Fig. 7. Histograms of fluorescence of Rhodamine 110 solutions excited by polarized cw laser light and detected in the two perpendicularly polarized channels are displayed before and after the linearization procedure [Figs. 7(a) and 7(b), respectively].

Synchronization of the board specific switching points of the macro time counter with the TAC time scale. Besides the TAC nonlinearity a second property of the analog circuitry potentially producing artefacts in the combined time axis is

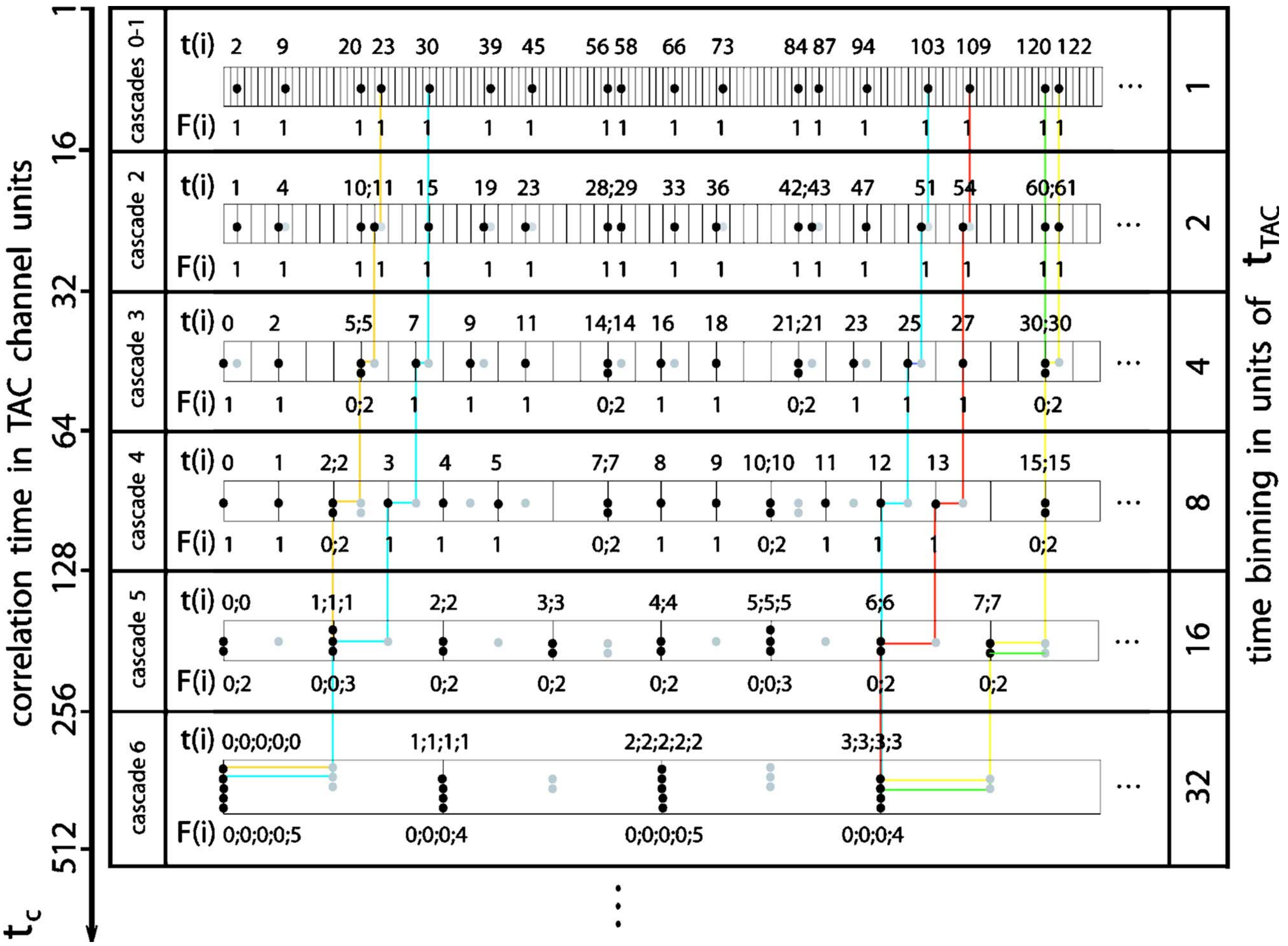

FIG. 8. (Color online) Architecture of the rebinning algorithm.

an offset between TAC ramp and macro timer. Despite the use of a single external clock signal to "simultaneously" advance the macro time counters and stop the TACs of both boards, internal delays in general cause a switching of the macro timer not exactly at the end of a TAC ramp but rather during the ramp and different for both modules. As a result, an identical photon train simultaneously arriving at both boards, i.e., a single detector signal split by a powersplitter, would occasionally generate "photon pairs" stamped with identical TAC time but a macro time differing by one count. The corresponding Δt histogram for short times $[|\Delta t = t_{\text{lab}}(\text{det }1) - t_{\text{lab}}(\text{det }2)| < 100\text{ ns}]$ would peak at $\Delta t = 0$ but also show satellites $\Delta t = \pm t_{\text{sync}}$. Moving by software of the switching points of both modules to the same end of the TAC ramp vastly reduces these satellites. Allthough a complete correction was not possible due to a slight jitter of the counting electronics, the remaining uncertainty was less than five TAC channels of 4.069 ps width each.

2. Software correlation

In FCS, fluctuations, $\delta F(t)$, of the fluorescence intensity, $F(t)$, with time, t, around an equilibrium value, $\langle F\rangle$, $(\delta F(t) = F(t) - \langle F\rangle)$ are statistically investigated by calculating the normalized second order autocorrelation function, $G^{(2)}(t_c)$. In practice the fluorescence signal is often split and directed onto two separate detectors to overcome deadtime problems of the detectors and associated electronics. The resulting two signals are then cross-correlated to yield the correlation curve, with the correlation or lag time t_c,

$$G^{(2)}(t_c) = \frac{\langle F_1(t)F_2(t+t_c)\rangle}{\langle F_1\rangle\langle F_2\rangle} = 1 + \frac{\langle \delta F_1(t)\delta F_2(t+t_c)\rangle}{\langle F_1\rangle\langle F_2\rangle}. \quad (5)$$

A multi-tau software correlator was developed to correlate the data. The algorithm uses the asynchronous single photon intensity information of the TCSPC data without requiring the construction of a multichannel scaler (MCS) trace, as needed for conventional intensity correlation algorithms. As shown previously,[52–54] this is the most efficient way to correlate single photon data at low or moderate count rates.

The TCSPC data allows recovery of the photon detection laboratory time with the accuracy of the TAC channel calibration time (4.069 ps in our experiments). From $t_{\text{sync}} = t_{\text{TAC}} \cdot N_{\text{TAC}}^{\max}$ ($N_{\text{TAC}}^{\max}$ is the number of TAC channels within one macrotiming clock cycle t_{sync}) and Eq. (3) it follows that also the laboratory times t_{lab} of the photon detection are integer multiples of the TAC channel calibration time t_{TAC}. This "single photon MCS trace" differs from conventional MCS traces by containing only the time information of the registered photons instead of intensity information for equally spaced bins. In this way the same information is stored in a much more efficient way, equivalent to only saving the filled bins and not the much more frequent empty ones. Our fast correlation algorithm makes use of this fact.

Correlation of the data with full (ps) time resolution up to the milliseconds or seconds range would still require enormous computation time and at the same time gain little information. Therefore a reduction of the time resolution for larger correlation times t_c was carried out using a multi tau scheme. Calculation of $G^{(2)}(t_c)$ with pseudologarithmically spaced lag times was first proposed by Schätzel[55,56] and then used in commercial hardware correlators. An equivalent procedure was adopted by our algorithm. Here a fixed number N_c of time bins with equal spacing (one cascade) is followed by consecutive cascades with bin-widths that, starting with the third cascade, double each time.

The number of equal time-bins per cascade can be chosen arbitrarily in the algorithm. For the full correlation curves presented in this paper we used the number of correlation times per cascade $N_c=8$, in analogy with the standard design of commercial hardware-correlators. This results in the following array of lag times in units of t_{TAC} for the first four cascades: $\{t_c\}=\{(1,2,\ldots,7,8),(9,10,\ldots,15,16),(18,20,\ldots,30,32),(36,40,\ldots,60,64)\ldots\}$. The general analytical representation of this array of lag times $t_c(k)$ is

$$t_c(k)=\begin{cases}1 & \text{if} \quad k=0\\ t_c(k-1)+1 & \text{if} \quad 0<k<2N_c\\ t_c(k-1)+2^{\lfloor (k/N_c)-1\rfloor} & \text{if} \quad k\geqslant 2N_c\end{cases} \tag{6}$$

where $\lfloor\,\rfloor$ returns the integer part of the enclosed expression, which for $k>2N_c$ is $K-1$, with K being the cascade number.

Our algorithm works directly on two arrays of laboratory times $t_1(i)$ and $t_2(j)$, which for the first two cascades correspond to single photon events. As a consequence of the time binning multiple events per bin for cascades $K\geqslant 2$ are possible. To take that into account, in parallel to the two arrays of laboratory times $t_1(i)$ and $t_2(j)$ an additional pair of arrays $F_1(i)$ and $F_2(j)$ is generated which carries the photon number or intensity information. The initial values for the first two cascades are $F_1(i)=F_2(j)=1$. The algorithm runs in a cycle for each cascade to find the coincident photons for the corresponding range of lag times. For a given element i in array $F_1(i)$ the corresponding bin in $F_2(j)$ is found via its associated time in the range from $t_2^{\mathrm{start}}(K,N_c,t_1(i))$ to $t_2^{\mathrm{end}}(K,N_c,t_1(i))$:

$$\begin{aligned} t_2^{\mathrm{start}}&=\frac{t_c(k=KN_c)}{b}+t_1(i) \qquad \text{with the binning factor} \quad b=\begin{cases}1 & \text{if} \quad K=0\\ 2^{K-1} & \text{if} \quad K>0.\end{cases}\\ t_2^{\mathrm{end}}&=t_2^{\mathrm{start}}+N_c\end{aligned} \tag{7}$$

The number of cascades is defined by the maximum correlation time chosen by the user, which can be up to one-fifth of the length of the data set.

For the correlation an array $P(t_c)$ containing the sums of the products of the photon numbers for each lag time, i.e., the number of pairs, is generated,

$$P(t_c)=\sum F_1(t_1(i))F_2(t_1(i)+t_c). \tag{8}$$

Starting with the first element of the first channel $F_1(t_1(i=0))$, the algorithm searches an element in the second channel $F_2(t_2(j))$ in the range $t_2^{\mathrm{start}}\leqslant t_2(j)<t_2^{\mathrm{end}}$. It then generates the possible products $F_1(t_1(i))F_2(t_1(i)+t_c)$ in that cascade and adds them to their corresponding bins $P(t_c)$, with $t_c=t_2(j)-t_1(i)=t_c(t_2(j)-t_2^{\mathrm{start}}+KN_c)$.

After completing the first two cascades rebinning of the data has to be performed. For the following cascades the widths of the time-bins of both channels are doubled each time by dividing the elements of the time arrays t_1 and t_2 by 2. Since these values are stored as 64 bit integers, the divison by 2 is performed by a right-shift. Elements of the intensity arrays $F_1(t_1(i))$ and $F_2(t_2(j))$, that as a result now belong to the same laboratory time bin, are grouped:

$$\left.\begin{aligned}F_{i+1}(K)&=F_i(K-1)+F_{i+1}(K-1)\\ F_i(K)&=0\end{aligned}\right\}\quad \text{for } t_i(K)=t_{i+1}(K). \tag{9}$$

The application of Eq. (9) is schematically displayed in Fig. 8.

The values $G^{(2)}(t_c)$ of the second order cross-correlation of the two intensity channels, F_1 and F_2, are obtained by normalizing $P(t_c)$:

$$\begin{aligned}G^{(2)}(t_c)&=\frac{\langle F_1(t)F_2(t+t_c)\rangle}{\langle F_1(t)\rangle\cdot\langle F_2(t)\rangle}\\ &=\frac{\left(\dfrac{\sum_i F_1(t_i)F_2(t_i+t_c)}{\min(t_1^{\max},t_2^{\max}-t_c)}\right)}{\left(\dfrac{\sum_i F_1(t_i)}{t_1^{\max}}\right)\cdot\left(\dfrac{\sum_j F_2(t_j)}{t_2^{\max}}\right)}=\frac{\left(\dfrac{P(t_c)}{t_{\mathrm{cor}}}\right)}{\left(\dfrac{N_1}{t_1^{\max}}\right)\left(\dfrac{N_2}{t_2^{\max}}\right)}.\end{aligned} \tag{10}$$

N_1 and N_2 are the total numbers of photons in channel 1 and 2, $\min(t_1^{\max},t_2^{\max}-t_c)=t_{\mathrm{cor}}$ returns the smaller number of $t_1^{\max}$ and $(t_2^{\max}-t_c)$, and $t_1^{\max}$ and $t_2^{\max}$ are the time-bin numbers of the last photons in detection channels 1 and 2, respectively. Please note that for the different cascades $t^{\max}$ is expressed in different multiples of t_{TAC}. Thus the normalization by $t^{\max}$

automatically compensates for the different numbers of possible pairs of bins in the different time binnings. Since in this paper we focus on short time correlations, symmetrical normalization as in Eq. (10) was chosen to reduce computation time. As shown previously, noise reduction by in general more appropriate asymmetrical normalization becomes significant only at larger lag times.[57]

More sophisticated techniques like time-gated correlation[14] which selects photons according to their arrival time after pulsed laser excitation for correlation analysis, or selective correlation,[15] i.e., selection of specific single-molecule events in a fluorescence time trace, are implemented in the software and can be applied as well.

3. FCS modelling

Continuous wave (cw) excitation. Every process leading to statistical fluctuations in the fluorescence signal (e.g., quenching kinetics, triplet formation, diffusion) will induce a characteristic decay or rise time in the correlation curve. For independent, i.e. uncorrelated processes their contribution is additive to the complete correlation curve. If translational diffusion, triplet formation and single molecule photon antibunching are the only noticeable processes causing fluorescence intensity fluctuations, the normalized correlation function, $G^{(2)}(t_c)$, can be approximated by the sum of a diffusional term $G_D(t_c)$, a characteristic triplet term $G_T(t_c)$ and an antibunching term $G_A(t_c)$, scaled with the mean reciprocal particle number $(1/N)$ in the detection volume element and superimposed on the poissonian contribution $G(\infty)=1$,[58,59]

$$
\begin{aligned}
G^{(2)}(t_c) &= 1 + \frac{1}{N}\left[G_D(t_c) + G_T(t_c) + G_A(t_c)\right] \\
&= 1 + \frac{1}{N}\left[\left(\frac{1}{1+(t_c/t_D)}\right)\left(\frac{1}{1+\left(\frac{\omega_0}{z_0}\right)^2 (t_c/t_D)}\right)^{1/2} \right. \\
&\quad + \frac{T}{m(1-T)}\exp(-t_c/t_T) - \frac{1}{m(1-T)} \\
&\quad \left. \times\exp(-t_c/t_A)\right]. \qquad (11)
\end{aligned}
$$

This model assumes a three-dimensional Gaussian shaped volume element with spatial distribution of the detection probabilities: $w(x,y,z)=\exp(-2(x^2+y^2)/\omega_0^2)\exp(-2z^2/z_0^2)$. The $1/e^2$ radii in x and y or in z direction are denoted by ω_0 or z_0, respectively. The characteristic diffusion time t_D can be used to estimate the diffusion coefficient D: $t_D=\omega_0^2/4D$. From the equilibrium fraction of molecules in the triplet state, T_{eq}, and the triplet correlation time, t_T, the rate constants for intersystem crossing, k_{ISC}, and triplet decay, k_T, can be derived. The characteristic rise time of the antibunching term t_A is the reciprocal sum of the rate constants for excitation k_{01} and fluorescence decay k_0: $t_A=1/(k_{01}+k_0)$. A variable m is included to take into account the possibility of multiple independent fluorophores per diffusing particle. A possible uncorrelated background due to darkcounts or scatter is not considered here but should be taken into account for quantitative interpretation of the amplitude $1/N$.[60]

For freely diffusing molecules with a single fluorophore $(m=1)$, the amplitude of the correlation curve at time zero, $G(0)$, is equal to 1 and independent on the number of molecules in the sample volume. For $m>1$, e.g., for multiply labelled molecules, complexes, etc. this no longer holds. From Eq. (11) it follows:

$$
G^{(2)}(0) = 1 + \frac{1}{N}\left[1 - \frac{1}{m}\right] > 1. \qquad (12)
$$

This effect can be used to estimate the number of independent fluorophores per particle.

Pulsed excitation and short-time correlation. For simultaneous lifetime and correlation measurements pulsed excitation is required. The nonclassical photonbunches of the laser light will result in a train of equally spaced correlation peaks superimposed on the correlation function, broadened by the fluorescence lifetime $[\tau=(k_0)^{-1}]$ and the instrumental response function (IRF). Due to the pseudologarithmic time-binning used in the software correlation this modulation vanishes at higher times due to averaging of many excitation periods.

In the constant time-binning regime and assuming single exponential decay of the detected fluorescence, a sum of shifted exponentials can be used to fit the data,[61]

$$
\begin{aligned}
G^{(2)}(t_c) &= C_{i=0}\exp\left(-\frac{|t_c - t_0|}{\tau_d}\right) \\
&\quad + \sum_{i=1}^{n} C_i\left(\exp\left(-\frac{|t_c - t_0 + it_L|}{\tau_d}\right)\right. \\
&\quad \left. + \exp\left(-\frac{|t_c - t_0 - it_L|}{\tau_d}\right)\right). \qquad (13)
\end{aligned}
$$

C_i are the amplitudes of the central/lateral peaks, t_0 a possible offset between detection channels, t_L the time between laser pulses, and τ_d the signal decay time, which for negligible width of the IRF equals the fluorescence lifetime. The amplitudes C_i can be related to the normalized correlation amplitude values $G(i\cdot t_L)$ that would be measured in a cw experiment at $t_c=i\cdot t_L$ by Eq. (14),

$$
G(i\cdot t_L) = C_i\frac{2\tau_d}{t_L}. \qquad (14)
$$

At high repetition rates, i.e., with spacings between the laser pulses of the order of the fluorescence decay time, the peaks in the correlation curve partially overlap. In this case only fitting of a model function like Eq. (13) allows one to approximately resolve coincident photon pairs originating from excitation pulses with defined spacing. By that means the undisturbed correlation amplitude at time zero, $G(0)$, can be calculated which, e.g., is necessary to determine the number of independent emitters with Eq. (12).

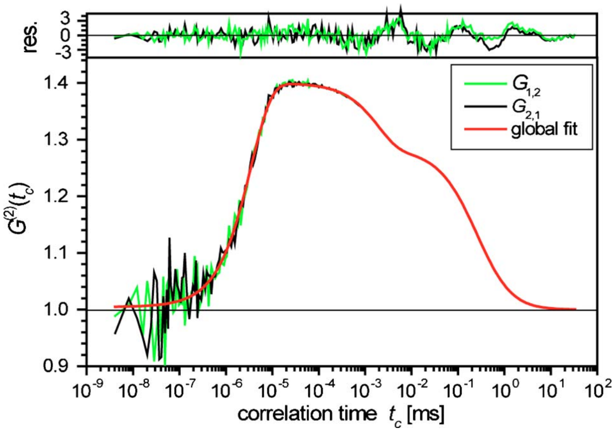

FIG. 9. (Color online) Correlation curves $G_{1,2}$ and $G_{2,1}$ of Rhodamine 110 aqueous solutions. Excitation at 496 nm, measured with PMT detectors. Recording time 16 min. Fit to Eq. (11) ($N=3.5$, $z_0/\omega_0=1.5$, $t_D=0.3$ ms, $T=0.29$, $t_T=1.9$ μs, $m=1.02$, $t_A=3.5$ ns).

At reduced repetition rates, i.e., $t_L \gg \tau_d$, correlation of the macro-times or building histograms of coincident photons[46] is sufficient to calculate $G(0)$. A quantitative interpretation still requires knowledge of the complete correlation curve, e.g., the degree of triplet excitation T and other dark states and, for investigations of mobile emitters, the number of independently diffusing particles N. Reducing the repetition rate to avoid overlapping decays reduces the time resolution and, in case the observation time is limited, also the efficiency of the experiment. In these cases high repetition rate laser excitation followed by analysis of the correlation curves with Eqs. (13) and (14) might be an alternative.

Fitting of the above model functions to the data is performed by a Levenberg-Marquardt routine. Constant weighting was applied for correlation curves with equal time-binning, while for variable binning according to Eq. (7) a modified procedure based on the work of Koppel was applied.[60]

III. RESULTS

A. Continuous wave (cw) excitation

1. Full correlation

Complete correlation curves generated from single photon data ranging from picoseconds up to 35 ms are shown in Fig. 9. Here Rh110 solutions were excited by cw laser light and the fluorescence was detected with Hamamatsu H7422P-40 photomultipliers. A pseudologarithmic binning procedure was used starting with the highest time resolution at a correlation time $t_c=4.069$ ps. To demonstrate the symmetry of the setup both cross-correlations $G_{1,2}$ and $G_{2,1}$ are presented. For Rh110, a small molecule with a rotational correlation time that is short on the time scale of its excited state lifetime and as a consequence exhibiting a very small steady state anisotropy, no measurable differences between both cross-correlations are to be expected. The experimental curve is well reproduced by a weighted fit to the model function [Eq. (11)] which neglects rotational effects. Slight deviations of both correlation curves at longer times that can be seen in the residuals are expected and can be explained by partial singlet and triplet saturation as well as photobleaching caused by the relatively high mean excitation power ($I_0/2$) (Ref. 62) of 90 kW/cm^2. The detected count rate added from both channels was 526 kHz, which by normalizing to the mean number of Rh110 molecules in the detection volume element of $N=3.5$ corresponds to 150 kHz per molecule.

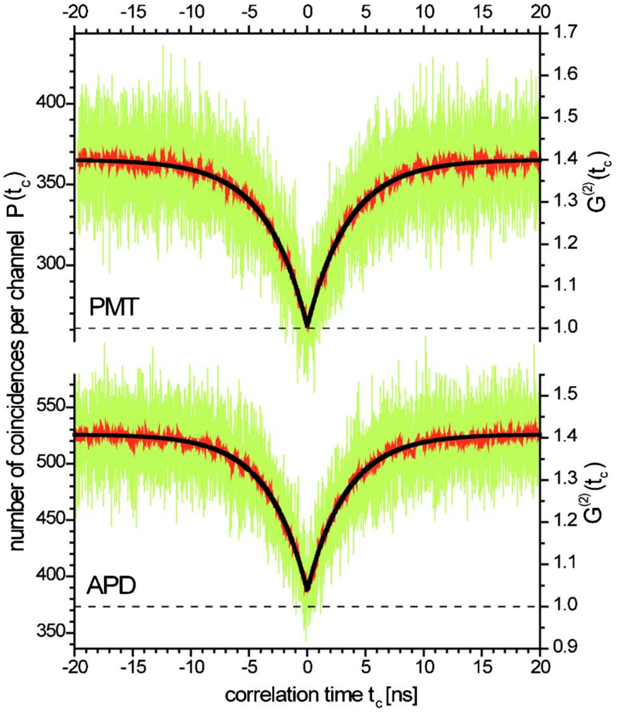

FIG. 10. (Color online) Short-time correlation curves of Rhodamine 110 aqueous solutions measured with PMT (top) and APD detectors (bottom). Experimental conditions as in Fig. 9. Recording time is 16 min. Fit to Eq. (11) (black line): antibunching time $t_A=3.6$ ns (PMT) and $t_A=3.4$ ns (APD), $m=1.01$ (PMT) and $m=1.10$ (APD).

The high excitation power is also denoted by the observed mean triplet population of 29%. No artefacts around 13.6 ns are observed, confirming the accurate combination of the micro- and the macroscopic time information to a unified time axis.

2. Short time regime: Dual board data acquisition

Many of the possible experimental artefacts discussed above will manifest in the short time regime of a correlation curve. This part of the correlation curve is dominated by photon antibunching from single Rh110 molecules. The normalized amplitude at zero delay, $G^{(2)}(t_c=0)$, is expected to approach one for single emitters freely diffusing in solution. A thorough investigation of the times between $-20\text{ ns} < t_c < 20\text{ ns}$, covering the critical region around the junction of the micro- and the macro-time axis at 13.6 ns, recalculated from the data taken with H7422P-40 PMTs and shown in Fig. 9, is presented in Fig. 10 (top). Besides the data acquisition electronics mainly detector performance affects the signal quality. For a comparison we recorded data with Perkin Elmer SPCM AQR-14 avalanche photodiodes under otherwise comparable experimental conditions (Fig. 10, bottom).

To generate the curves two settings in the correlation software had to be used that have not been described previously: (1) Our correlation algorithm only uses positiv correlation times ($t_c \geqslant 0$). To facilitate computation, channel 2 was given an artificial positive offset which was subtracted after correlation. This way the whole time intervall shown with positive and negative correlation times between $-20\ \text{ns} < t_c < 20$ ns could be calculated in one run. (2) The curves were calculated with the full (electronical) time resolution of 4.069 ps by setting N_c to a number sufficiently large to have the desired time range fall inside the first two cascades, by that means avoiding time-binning. For the data in Fig. 10 a cascade size of $N_c = 5000$ and an offset for channel 2 of $\Delta t_2 = 5000$ was used.

The number of coincidences per channel in a correlation experiment, $P(t_c)$, is calculated from Eq. 8. The fit (black line) as well as the smoothed data (dark grey) confirm the inferior time resolution of the APDs as compared to the PMTs: the correlation of the APD data cannot reproduce the amplitude at $t_c = 0$ of $G(0) = 1$, as would be expected for freely diffusing single fluorophores and is found with the PMTs. This cannot be attributed to the timing jitter of the detectors: The full width at half maximum (FWHM) of the instrumental response functions (IRF) was measured to be around 0.30 ns for the PMT detectors and 0.19 and 0.23 ns for the APDs used (Fig. 5). Besides an increased afterpulsing probability for the APDs (not shown, afterpulsing does not significantly affect the shape of the cross-correlation curves), the main origin of the poorer performance of the APDs is their unstable IRF which drifts with count rate (Fig. 5(b). The time constant of the drift was found to be of the order of 0.1 s (not shown).

In some experiments at low light levels APDs could still be the better choice. APDs can achieve much higher quantum efficiencies (QE) than PMTs over wide wavelength ranges. Based on the count rate per molecule (180 kHz vs 150 kHz in our experiment) we find a 20% higher sensitivity for our APDs compared to the PMTs in the wavelength range around 533 nm (see Figs. 10 and 11; the manufacturers specifications for typical modules at 580 nm would predict a difference around 40%[45,51]). When the dominant source for uncertainty in the determination of the characteristic antibunching time is shot-noise the detectors with the highest QE should be preferred.

3. Short time regime: Single board data acquisition

The common way to obtain interphoton arrival time histograms for short delay times t_d, which are equivalent to the cross-correlation curves in Fig. 10 employs a Hanbury-Brown and Twiss (HBT) setup as shown in Fig. 3. Here only a single TAC is used to directly record t_d, therefore not requiring the construction of synchronized macroscopic time-axes (Fig. 11).

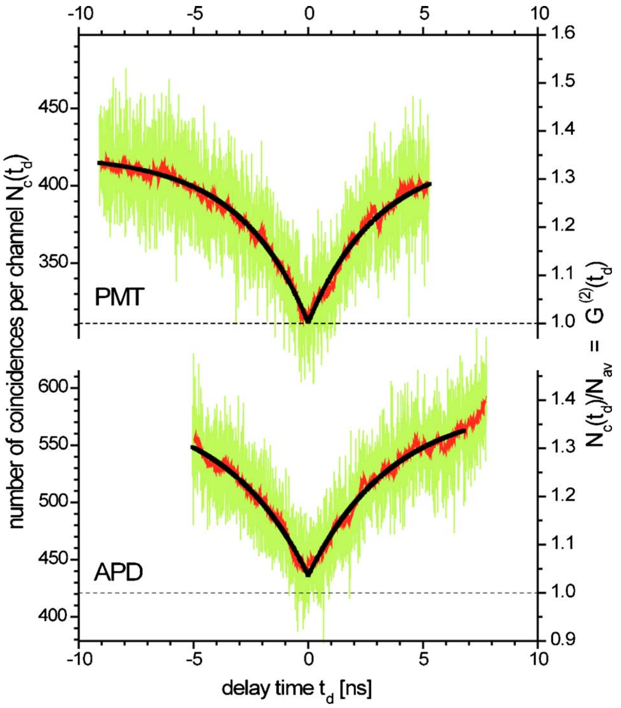

FIG. 11. (Color online) Δt (TAC) histograms of Rhodamine 110 aqueous solutions measured with PMT (top) and APD detectors (bottom). Recording time in 14 min. Fit to Eq. (11) (black line): antibunching time $t_A = 3.0$ ns (PMT) and $t_A = 3.7$ ns (APD).

Data were recorded in the histogram mode of the board, i.e., only the number of stop events per TAC channel $N_c(t_d)$ but no macro time information was stored. Normalization to obtain the correlation amplitude was done by dividing $N_c(t_d)$ by the average number of coincidences N_{av} that are expected for poissonian noise. N_{av} was calculated from the mean countrate by Eq. (15),

$$N_{av} = \left(\frac{F}{t} \right)^2_{av} t_{TAC} t_{exp}, \tag{15}$$

with $(F/t)_{av}$ being the mean count rate per detection channel, t_{TAC} the TAC channel width, and t_{exp} the total data acquisition time. The mean number of fluorophores N in the detection volume element was determined to $N = 4.0$ by separate FCS preceding the HBT experiment. Having countrates per molecule comparable to the FCS experiment (Fig. 10), the higher number of coincidences per channel in the HBT experiment can be explained by the slightly higher concentration.

Compared to the recording and correlation of high resolution photon time traces the comparably simple HBT arrangement has a number of drawbacks: (1) Depending on the length of the TAC ramp only a limited time range is accessible. The same TAC setting as in Fig. 10, i.e., a bin-width of 4.069 ps, was used in Fig. 11. (2) In principle, as with the used electronics, macro time recording of the photons that stop the TAC is possible. Since this is only a small fraction of the total number of photons detected by both detectors, (long-time) correlation curves generated from these data would be correspondingly noisy. In the classical HBT experiment the macro time information is lost. Consequently the full correlation curve and therefore information about fluorophore concentrations is in general not available. (3) Electronic interference between the two channels destorting the time axis can be seen on the smoothed curve (dark grey) and is harder to minimize in a single board setup than in a dual board experiment.

The antibunching time t_A from all four experiments (Figs. 10 and 11) is in average 3.4 ns±10%, the HBT-data having the bigger error due to the smaller time-window available for fitting. From $t_A = 1/(k_{01}+k_0)$ and the excitation rate constant $k_{01} = \sigma_{01} \cdot I_0/2 \cdot \lambda/hc$, with λ/hc being the wavelength of the exciting light divided by Planck's constant and the speed of light, the known absorption cross section σ_{01} can now be used to predict t_A.[63] For a fluorescence lifetime of $(k_0)^{-1} = 4.01$ ns, an applied mean excitation intensity of $I_0/2 = 90$ kW/cm^2 at a wavelength of $\lambda = 496$ nm and an absorption cross section for Rh110 in water of $\sigma_{01} = 2.62 \times 10^{-16}$ cm^2 at that wavelength[64] we obtain $t_A = 3.24$ ns. This is well within the experimental error of our measured value. The limited instrumental resolution was not taken into account in this consideration; its effect was estimated to be smaller than the scattering of the experimental values for the antibunching relaxation times but would make the difference between prediction and mean experimental value even smaller.

B. Pulsed excitation

cw experiments can, via measuring of antibunching relaxation times, yield information about the fluorescence lifetimes but requires knowledge of the excitation rates. The more direct and, for a given number of detected photons statistically far more accurate way to determine lifetimes employs pulsed excitation. In the following we will discuss its effect on the correlation curves.

In fluorescence experiments with pulsed laser excitation the system is probed at the repetition rate of the light source as opposed to random excitation with a cw light source. Consequently, for time intervals of the order of or smaller than the pulse distance, correlation of the data results in significantly different FCS curves for the two excitation modes. As shown for Rhodamine 110 solutions (Fig. 12), the pulse train of the excitation pulses is reflected in the statistics of the emitted photons. The highly correlated fluorescence signal results in correlation curves exhibiting strong bunching/antibunching behavior at time scales of the laser repetition rates.

Fluorescence was detected with APDs after excitation by pulsed laser light at 496 nm and a repetition rate of 73.5 MHz. The mean intensity was set to 24 kW/cm^2, the mean number of Rh110 molecules in the confocal volume element was $N = 5.4$.

1. Fluorescence decay

Histogramming the photon arrival times t_{mic} (micro time $t_{\mathrm{mic}} = t_{\mathrm{TAC}} \cdot N_{\mathrm{TAC}}$) yields fluorescence decay curves F_{par} and F_{perp} for the parallel and perpendicular detection channel, respectively. Assuming isotropic distribution of the molecules the total fluorescence signal decay $F_{\mathrm{tot}}(t_{\mathrm{mic}})$ can be reconstructed by Eq. (16),.

$$F_{\mathrm{tot}}(t_{\mathrm{mic}}) = (1 - 3l_2)F_{\mathrm{par}}(t_{\mathrm{mic}}) + (2 - 3l_1)gF_{\mathrm{perp}}(t_{\mathrm{mic}}). \quad (16)$$

The correction factors $l_1 = 0.0308$, $l_2 = 0.0368$ compensate for mixing of polarizations in the high N.A. objective.[13,65] The g-factor (in our case $g = 0.91$) corrects intensities for slight anisotropies in the individual detection efficiencies of the different channels and was experimentally determined by tail fitting of the decay curves $F_{\mathrm{par}}(t_{\mathrm{mic}})$ and $F_{\mathrm{perp}}(t_{\mathrm{mic}})$. A total fluorescence decay $F_{\mathrm{tot}}(t_{\mathrm{mic}})$ is shown in Fig. 12(a) together with a fitted single exponential, taking into account superposition of decays from previous pulses.[66] The APD modules used in this experiment showed significant afterpulsing. Afterpulsing occurs on timescales larger than the detector dead-time and generates a flat offset in the TAC histogram. To account for that a constant offset F_{offs} was used and in the fit added to the time-dependent fluorescence signal $F_{\mathrm{flu}}(t_{\mathrm{mic}})$ $[F_{\mathrm{tot}}(t_{\mathrm{mic}}) = F_{\mathrm{offs}} + F_{\mathrm{flu}}(t_{\mathrm{mic}})]$. The offset in Fig. 12(a) amounts to 5.8% of the total signal. The fluorescence lifetime was found to be $\tau = 4.01$ ns.

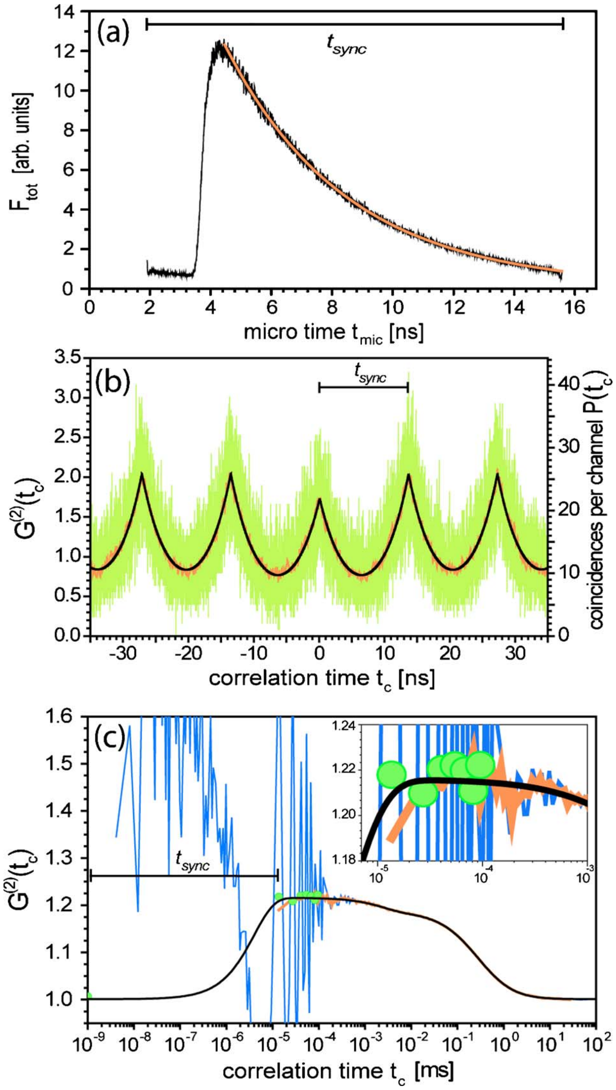

FIG. 12. (Color online) MFD of Rhodamine 110 aqueous solutions with APD detectors, pulsed excitation at 496 nm, mean intensity is 24 kW/cm^2. Recording time is 40 s. t_{sync} is the synchronisation signal for the macro time counter and is obtained from the modelocker of the pulsed laser. (a) Micro time t_{mic} histogram showing fluorescence decay (black) with single exponential fit (red). Fit results: $\tau = 4.01$ ns, $F_{\mathrm{offs}} = 0.0206$. (b) Short-time correlation curves (green) with 50 point average (red) and fit to Eq. (13) (black). Time channel width is 4.069 ps. Fit results: $C_0 = 1.48$, $C_1 = 1.81$, $C_2 = 1.80$, $t_{\mathrm{del}} = 13.6$ ns, $\tau_d = 4.14$ ns. A linear offset was set to 0.113 (see text). (c) Full correlation curve (blue) with macro time correlation curve (red), short-time correlation amplitudes from Eq. (14) (green dots), and simulation according to Eq. (11) (black). Simulation parameters: $N = 5.4$, $z_0/\omega_0 = 2.0$, $t_D = 0.3$ ms, $T_{\mathrm{eq}} = 0.135$, $t_T = 2.4$ μs, $m = 1.01$, $t_A = 4.0$ ns. The insert shows an enlarged part of the time regime around the intersection of micro and macro time axes.

2. Short-time correlation

The FCS for lag times between $-100\ \text{ns} < t_c < 100\ \text{ns}$ is shown in Fig. 12(b) (light grey) together with a fit to Eq. (13) (black) and a smoothed curve of the data (dark grey). The amplitude at $t_c=0$, corresponding to the central peak, is smaller than at the lateral peaks as a result of single molecule photon antibunching, but does no longer represent the absolute minimum of the FCS as in the case of cw excitation. By setting an offset to 0.113, corresponding to the measured offset of 5.8% in the fluorescence decay [Fig. 12(a)] a decay time for the correlation peaks of $t_d=4.14$ ns was found. t_d is expected to be slightly larger than τ derived from the fluorescence decay analysis since no deconvolution with the instrumental response function was performed and in the FCS two IRF (one per channel) enter to broaden the signal.

The contrast of the pulse pattern in this time regime is a function of the experimental conditions and will vanish, for a given fluorescence lifetime, at high repetition rates ($t_L \ll \tau_d$) or at low instrumental resolution ($t_L \ll \text{FWHM}_{\text{IRF}}$).

3. Full correlation

For pseudologarithmic binning (multiple tau correlation) the long-time portion of the full correlation resembles a cw experiment [Fig. 12(c)]. Here the time-bins cover (and average) many excitation periods. A fit to Eq. (11) for $t_c > 10^{-4}$ ms, extrapolated to shorter times with fixed parameters $t_A=4.0$ ns and $m=1$ is shown as a black overlay in the figure. Correlation of the macro-times yields a low-resolution curve starting at 13.6 ns (red). The first points of this curve with spacings of 13.6 ns suffer from overlapping of the fluorescence decays originating from adjacent laser pulses. Here fitting of the the short-time correlation curve [Fig. 12(b)] and application of Eq. (14) yields more accurate results by taking these artefacts into account (dots). The amplitude at time zero ($t_c=0$) as it would be expected in a cw experiment is indicated at $t_c=10^{-9}$ ms. In pulsed experients with high repetition rates this amplitude can only be derived in the described way and is not available by macro-time correlation.

The three different ways to analyse the data from pulsed excitation can give information (1) via correlation, about molecular and photophysical dynamics with a time resolution of the pulse distance, (2) via decay analysis, about fluorescence lifetime and faster rotational correlation times, and (3) at $t_c=0$, i.e., in the photon antibunching regime, about coincident photons and numbers of independent fluorophores.

IV. POTENTIAL APPLICATIONS

We have developed an improved time-correlated single photon counting (TCSPC) technique for simultaneous fluorescence lifetime and correlation experiments that allows calculation of the full correlation curve from the same photons emitted from single, or very few, molecules. The method offers two main advantages for experiments at low concentrations over conventional single molecule fluorescence detection:

(1) The rotational correlation times of large macromolecules, which are much bigger than the fluorescence lifetimes are now accessible in a TCSPC experiment with high time resolution. Many Proteins exhibit rotational correlation times between 10 and 100 ns. In comparison, the fluorophores commonly used (like Rhodamine 110) have fluorescence lifetimes around 4 ns. Accessing the rotational diffusion via commercial hardware correlators on the other hand is at present limited to time resolutions of 5 ns or worse. The presented technique is bridging the gap between anisotropy decay analysis and currently available commercial correlators.

(2) The number of independent fluorophores on a single molecule can be determined (e.g., the number of monomers in a complex) by measuring coincident photons simultaneously with all other fluorescence parameters. Alternatively, in suitable systems photophysical processes like singlet-singlet-annihilation or singlet-triplet-annihilation[67] can be studied with high precision. Besides applications in the investigation of multichromophoric entities, this technique, which is based on the quantum mechanical phenomenon of antibunching, might also be promising for applications in molecular biology.

The technique is applicable to immobilized molecules as well as to solutions of fluorophores. In heterogeneous samples species selective correlation analysis is possible after sorting single molecule events by software.

ACKNOWLEDGMENT

This work was supported by the BMBF (Bio-Future Award, Grant No. 0311865) and the Volkswagen-Stiftung.

[1] P. Michler, A. Imamoglu, M. D. Mason, P. J. Carson, G. F. Strouse, and S. K. Buratto, Nature (London) **406**, 968 (2000).

[2] R. M. Thompson, R. M. Stevenson, A. J. Shields, I. Farrer, C. J. Lobo, D. A. Ritchie, M. L. Leadbeater, and M. Pepper, Phys. Rev. B **64**, 201302 (2001).

[3] Z. L. Yuan, B. E. Kardynal, R. M. Stevenson, A. J. Shields, C. J. Lobo, K. Cooper, N. S. Beattie, D. A. Ritchie, and M. Pepper, Science **295**, 102 (2002).

[4] B. Lounis and W. E. Moerner, Nature (London) **407**, 491 (2000).

[5] C. Zander, M. Sauer, K. H. Drexhage, D. S. Ko, A. Schulz, J. Wolfrum, L. Brand, C. Eggeling, and C. A. M. Seidel, Appl. Phys. B **63**, 517 (1996).

[6] P. Tinnefeld, K. D. Weston, T. Vosch, M. Cotlet, T. Weil, J. Hofkens, K. Müllen, F. C. De Schryver, and M. Sauer, J. Am. Chem. Soc. **124**, 14310 (2002).

[7] T. Basché, W. E. Moerner, M. Orrit, and H. Talon, Phys. Rev. Lett. **69**, 1516 (1992).

[8] W. P. Ambrose, P. M. Goodwin, J. Enderlein, D. J. Semin, J. C. Martin, and R. A. Keller, Chem. Phys. Lett. **269**, 365 (1997).

[9] N. L. Thompson, in *Topics in Fluorescence Spectroscopy*, edited by J. R. Lakowicz (Plenum, New York, 1991), pp. 337–378.

[10] R. Rigler and J. Widengren, in *BioScience*, edited by B. Klinge and C. Owman (Lund University Press, Lund, 1990), pp. 180–183.

[11] P. Schwille, S. Kummer, A. A. Heikal, W. E. Moerner, and W. W. Webb, Proc. Natl. Acad. Sci. U.S.A. **97**, 151 (2000).

[12] A. A. Heikal, S. T. Hess, G. S. Baird, R. Y. Tsien, and W. W. Webb, Proc. Natl. Acad. Sci. U.S.A. **97**, 11996 (2000).

[13] J. Schaffer, A. Volkmer, C. Eggeling, V. Subramaniam, G. Striker, and C. A. M. Seidel, J. Phys. Chem. A **103**, 331 (1999).

[14] C. Eggeling, S. Berger, L. Brand, J. R. Fries, J. Schaffer, A. Volkmer, and C. A. M. Seidel, J. Biotechnol. **86**, 163 (2001).

[15] C. Eggeling, J. R. Fries, L. Brand, R. Günther, and C. A. M. Seidel, Proc. Natl. Acad. Sci. U.S.A. **95**, 1556 (1998).

[16] P. Schwille, F. J. Meyer-Almes, and R. Rigler, Biophys. J. **72**, 1878 (1997).

[17] R. Y. Tsien, Annu. Rev. Biochem. **67**, 509 (1998).

[18] J. Zhang, R. E. Campbell, A. Y. Ting, and R. Y. Tsien, Nat. Rev. Mol. Cell Biol. **3**, 906 (2002).

[19] W. C. W. Chan and S. M. Nie, Science **281**, 2016 (1998).

[20] X. Michalet, F. F. Pinaud, L. A. Bentolila, J. M. Tsay, S. Doose, J. J. Li, G. Sundaresan, A. M. Wu, S. S. Gambhir, and S. Weiss, Science **307**, 538 (2005).

[21] X. Y. Wu, H. J. Liu, J. Q. Liu, K. N. Haley, J. A. Treadway, J. P. Larson, N. F. Ge, F. Peale, and M. P. Bruchez, Nat. Biotechnol. **21**, 41 (2003).

[22] W. C. W. Chan, J. D. Maxwell, X. Gao, R. E. Bailey, M. Han, and S. Nie, Curr. Opin. Biotechnol. **13**, 40 (2002).

[23] A. A. Deniz, M. Dahan, J. R. Grunwell, T. J. Ha, A. E. Faulhaber, D. S. Chemla, S. Weiss, and P. G. Schultz, Proc. Natl. Acad. Sci. U.S.A. **96**, 3670 (1999).

[24] M. Margittai, J. Widengren, E. Schweinberger, G. F. Schröder, S. Felekyan, E. Haustein, M. König, D. Fasshauer, H. Grubmüller, R. Jahn, and C. A. M. Seidel, Proc. Natl. Acad. Sci. U.S.A. **100**, 15516 (2003).

[25] A. A. Deniz, T. A. Laurence, G. S. Beligere, M. Dahan, A. B. Martin, D. S. Chemla, P. E. Dawson, P. G. Schultz, and S. Weiss, Proc. Natl. Acad. Sci. U.S.A. **97**, 5179 (2000).

[26] C. Zander, K. H. Drexhage, K. T. Han, J. Wolfrum, and M. Sauer, Chem. Phys. Lett. **286**, 457 (1998).

[27] R. Kühnemuth and C. A. M. Seidel, Single Mol. **2**, 251 (2001).

[28] M. Prummer, C. G. Hübner, B. Sick, B. Hecht, A. Renn, and U. P. Wild, Anal. Chem. **72**, 443 (2000).

[29] W. Becker, H. Hickl, C. Zander, K. H. Drexhage, M. Sauer, S. Siebert, and J. Wolfrum, Rev. Sci. Instrum. **70**, 1835 (1999).

[30] D. V. O'Connor and D. Phillips, *Time-Correlated Single Photon Counting* (Academic, New York, 1984).

[31] W. Becker, A. Bergmann, C. Biskup, T. Zimmer, N. Kloecker, and K. Benndorf, Proc. SPIE **4620**, 79 (2002).

[32] W. Becker, K. Benndorf, A. Bergmann, C. Biskup, K. Koenig, U. Tirlapur, and T. Zimmer, Proc. SPIE **4431**, 94 (2001).

[33] W. Becker, A. Bergmann, H. Wabnitz, D. Grosenick, and A. Liebert, Proc. SPIE **4431**, 249 (2001).

[34] I. Yamazaki, N. Tamai, H. Kume, H. Tsuchiya, and K. Oba, Rev. Sci. Instrum. **56**, 1187 (1985).

[35] D. Bebelaar, Rev. Sci. Instrum. **57**, 1116 (1986).

[36] R. M. Ballew and J. N. Demas, Anal. Chem. **61**, 30 (1989).

[37] M. Köllner and J. Wolfrum, Chem. Phys. Lett. **200**, 199 (1992).

[38] J. Carlsson and J. Philip, Proc. SPIE **4622**, 70 (2002).

[39] W. Becker, A. Bergmann, M. A. Hink, K. König, K. Benndorf, and C. Biskup, Microsc. Res. Tech. **63**, 58 (2004).

[40] W. Becker, *Advanced Time-Correlated Single Photon Counting Techniques* (Springer, New York, 2005).

[41] P. Kask, K. Palo, D. Ullmann, and K. Gall, Proc. Natl. Acad. Sci. U.S.A. **96**, 13756 (1999).

[42] K. Palo, L. Brand, C. Eggeling, S. Jäger, P. Kask, and K. Gall, Biophys. J. **83**, 605 (2002).

[43] M. Prummer, B. Sick, A. Renn, and U. P. Wild, Anal. Chem. **76**, 1633 (2004).

[44] R. Hanbury-Brown and R. Q. Twiss, Nature (London) **177**, 27 (1956).

[45] *Datasheet Single Photon Counting Module*, *SPCM-AQR Series* (Perkin-Elmer Optoelectronics, Kirkland, Quebec, Canada, 2004).

[46] K. D. Weston, M. Dyck, P. Tinnefeld, C. Muller, D. P. Herten, and M. Sauer, Anal. Chem. **74**, 5342 (2002).

[47] P. A. Ekstrom, J. Appl. Phys. **52**, 6974 (1981).

[48] S. Cova, A. Lacaita, M. Ghioni, G. Ripamonti, and T. A. Louis, Rev. Sci. Instrum. **60**, 1104 (1989).

[49] H. Yang, G. B. Luo, P. Karnchanaphanurach, T. M. Louie, I. Rech, S. Cova, L. Y. Xun, and X. S. Xie, Science **302**, 262 (2003).

[50] S. Cova, M. Ghioni, A. Lotito, I. Rech, and F. Zappa, J. Mod. Opt. **51**, 1267 (2004).

[51] *Datasheet Photosensor Modules, H7422 Series* (Hamamatsu Photonics Deutschland, Germany, 2004).

[52] M. Wahl, I. Gregor, M. Patting, and J. Enderlein, Opt. Express **11**, 3583 (2003).

[53] T. Wohland, R. Rigler, and H. Vogel, Biophys. J. **80**, 2987 (2001).

[54] D. Magatti and F. Ferri, Rev. Sci. Instrum. **74**, 1135 (2003).

[55] K. Schätzel, Inst. Phys. Conf. Ser. **77**, 175 (1985).

[56] K. Schätzel and R. Peters, Proc. SPIE **1430**, 109 (1991).

[57] K. Schätzel, M. Drewel, and S. Stimac, J. Mod. Opt. **35**, 711 (1988).

[58] Ü. Mets, in *Fluorescence Correlation Spectroscopy*, edited by R. Rigler and E. L. Elson (Springer, Berlin, 2001), pp. 346–359.

[59] J. Widengren, in *Fluorescence Correlation Spectroscopy*, edited by R. Rigler and E. L. Elson (Springer-Verlag, Berlin, 2001), pp. 276–301.

[60] D. E. Koppel, Phys. Rev. A **10**, 1938 (1974).

[61] A. Beveratos, S. Kuhn, R. Brouri, T. Gacoin, J.-P. Poizat, and P. Grangier, Eur. Phys. J. D **18**, 191 (2002).

[62] C. Eggeling, J. Widengren, R. Rigler, and C. A. M. Seidel, Anal. Chem. **70**, 2651 (1998).

[63] Ü. Mets, J. Widengren and R. Rigler, Chem. Phys. **218**, 191 (1997).

[64] C. Eggeling, Ph.D. Thesis, Georg-August-Universität Göttingen, Germany (1999).

[65] M. Koshioka, K. Saski, and H. Masuhara, Appl. Spectrosc. **49**, 224 (1995).

[66] M. Maus, M. Cotlet, J. Hofkens, T. Gensch, F. C. De Schryver, J. Schaffer, and C. A. M. Seidel, Anal. Chem. **73**, 2078 (2001).

[67] J. Hofkens, M. Cotlet, T. Vosch, P. Tinnefeld, K. D. Weston, C. Ego, A. Grimsdale, K. Müllen, D. Beljonne, J. L. Bredas, S. Jordens, G. Schweitzer, M. Sauer, and F. De Schryver, Proc. Natl. Acad. Sci. U.S.A. **100**, 13146 (2003).

Declaration

I declare that the following thesis has been completed independently, without illegitimate help and has not been submitted previously for a degree.

Volodymyr Kudryavtsev,

Düsseldorf, 12.12.2006